

KINETIC MODELING OF GAS-PHASE PHENOL  
HYDRODEOXYGENATION OVER Ag/TiO<sub>2</sub> CATALYST  
VIA TGA-FTIR BASED MICROREACTOR

ANDREW NG KAY LUP

FACULTY OF ENGINEERING  
UNIVERSITY OF MALAYA  
KUALA LUMPUR

2019

**KINETIC MODELING OF GAS-PHASE PHENOL  
HYDRODEOXYGENATION OVER Ag/TiO<sub>2</sub> CATALYST  
VIA TGA-FTIR BASED MICROREACTOR**

**ANDREW NG KAY LUP**

**THESIS SUBMITTED IN FULFILMENT OF THE  
REQUIREMENTS FOR THE DEGREE OF DOCTOR OF  
PHILOSOPHY**

**FACULTY OF ENGINEERING  
UNIVERSITY OF MALAYA  
KUALA LUMPUR**

**2019**

**UNIVERSITY OF MALAYA**  
**ORIGINAL LITERARY WORK DECLARATION**

**Name of Candidate : ANDREW NG KAY LUP**

**Matric No. : KHA150076**

**Name of Degree : Doctor of Philosophy (Ph.D.)**

**Title of Project Paper/Research Report/Dissertation/Thesis (“this Work”):**

**KINETIC MODELING OF GAS-PHASE PHENOL HYDRODEOXYGENATION  
OVER Ag/TiO<sub>2</sub> CATALYST VIA TGA-FTIR BASED MICROREACTOR**

**Field of Study: Reaction Engineering**

**I do solemnly and sincerely declare that:**

- (1) I am the sole author/writer of this Work;
- (2) This Work is original;
- (3) Any use of any work in which copyright exists was done by way of fair dealing and for permitted purposes and any excerpt or extract from, or reference to or reproduction of any copyright work has been disclosed expressly and sufficiently and the title of the Work and its authorship have been acknowledged in this Work;
- (4) I do not have any actual knowledge nor do I ought reasonably to know that the making of this work constitutes an infringement of any copyright work;
- (5) I hereby assign all and every rights in the copyright to this Work to the University of Malaya (“UM”), who henceforth shall be owner of the copyright in this Work and that any reproduction or use in any form or by any means whatsoever is prohibited without the written consent of UM having been first had and obtained;
- (6) I am fully aware that if in the course of making this Work I have infringed any copyright whether intentionally or otherwise, I may be subject to legal action or any other action as may be determined by UM.

Candidate’s Signature

Date:

Subscribed and solemnly declared before,

Witness’s Signature

Date:

Name:

Designation:

# KINETIC MODELING OF GAS-PHASE PHENOL HYDRODEOXYGENATION OVER Ag/TiO<sub>2</sub> CATALYST VIA TGA-FTIR BASED MICROREACTOR

## ABSTRACT

Bio-oil produced from biomass pyrolysis is a potential source for liquid fuel. However, bio-oil has high oxygen content due to its complex mixture of oxygen-containing compounds which results in deleterious properties such as lower heating value, corrosion and chemical instability of liquid fuel. Phenolics are some of the major O-containing constituents commonly found in lignocellulosic biomass derived bio-oil. Thus, phenolic hydrodeoxygenation (HDO) is a process required for bio-oil upgrading into high quality liquid fuel. In this study, gas-phase hydrodeoxygenation of phenol over Ag/TiO<sub>2</sub> catalyst at atmospheric pressure was conducted as a model compound approach in investigating the reaction mechanism and kinetics of oxygen removal from phenolics. Physicochemical properties of Ag/TiO<sub>2</sub> catalyst were investigated to explore its potential as hydrodeoxygenation catalyst. The results showed that the metal-support interaction of Ag/TiO<sub>2</sub> enabled hydrogen spillover phenomenon and synergistic interaction of acid and metal sites which are fundamental in catalyzing adsorption and activation of phenolics and hydrogen during hydrodeoxygenation. Reduction study of Ag/TiO<sub>2</sub> by hydrogen also showed that Ag<sub>2</sub>O undergoes single-step reduction to form Ag which can be described using unimolecular decay model. Sample encapsulation technique was also proposed in this study to lengthen the release of vaporized phenol sample in microreactor. The delayed volatiles release phenomenon was enhanced by using metal capsule with higher material hardness and smaller surface area for sample evaporation. By using cylindrical tin capsule, significant release of vaporized phenol was extended up to 454—554 K which is above its boiling point. This finding is useful in enabling better catalyst activation and kinetic study of catalytic solid-gas reaction over a larger temperature range but at a fixed reactant amount. FTIR and GC-MS

analyses showed the conversion of phenol into benzene as major product over Ag/TiO<sub>2</sub> catalyst at atmospheric pressure condition. The proposed kinetic model for the phenol HDO network over Ag/TiO<sub>2</sub> confirmed the occurrence of phenol hydrogenolysis and hydrogenation; cyclohexanol dehydration and hydrogenation of benzene and cyclohexene. The reaction rates increase with the following order:  $r_1$  (phenol hydrogenolysis) <  $r_2$  (phenol hydrogenation) <  $r_5$  (benzene hydrogenation) <  $r_3$  (cyclohexanol dehydration) <  $r_4$  (cyclohexene hydrogenation). Both phenol hydrogenolysis and hydrogenation steps are the respective rate-limiting steps for DDO (direct deoxygenation) and HYD (hydrogenation-dehydration) pathways of phenol hydrodeoxygenation over Ag/TiO<sub>2</sub>. Application of transition state theory has also indicated formation of more orderly activated complexes in the elementary reaction steps as indicated by the negative entropy change of activation. The proposed kinetic model was able to describe quantitative and qualitative observations in this work with a reasonable agreement and would be a useful tool for kinetic and mechanistic understanding of surface reactions of phenol HDO over supported transition metal catalysts. Successive hydrodeoxygenation runs (4 h) showed no significant degradation in catalytic and physicochemical properties of Ag/TiO<sub>2</sub> catalyst. The accumulation of oxidized Ag metal species and coke deposits on Ag/TiO<sub>2</sub> catalyst after each HDO run can be removed via H<sub>2</sub>-activation and calcination in air at 553 K with at least 98.9% removal efficiency.

Keywords: Kinetic modeling, TGA-FTIR, phenol, Ag/TiO<sub>2</sub>, gas-phase hydrodeoxygenation.

**PEMODELAN KINETIK HIDROPENYAHOKSIGENAN FENOL FASA GAS  
ATAS MANGKIN Ag/TiO<sub>2</sub> MELALUI MIKROREAKTOR BERASASKAN**

**TGA-FTIR**

**ABSTRAK**

Bio-minyak yang dihasilkan daripada pirolisis biomas merupakan sumber yang berpotensi untuk bahan api cecair. Walau bagaimanapun, bio-minyak mempunyai kandungan oksigen yang tinggi disebabkan oleh campuran kompleks sebatian beroksigen yang akan mengakibatkan sifat bahan api cecair yang memudaratkan seperti nilai pemanasan yang rendah, kakisan dan ketidakstabilan kimia. Fenolik merupakan konstituen beroksigen yang utama dan seringkali dikandung dalam bio-minyak yang diperoleh daripada biomas lignoselulosa. Oleh itu, hidropenyahoksigenan fenolik merupakan proses penting untuk menaik taraf bio-minyak kepada bahan api cecair yang berkualiti tinggi. Dalam kajian ini, hidropenyahoksigenan fenol fasa gas pada tekanan atmosfera melalui pemangkin Ag/TiO<sub>2</sub> telah dilaksanakan sebagai kaedah sebatian model dalam mengkaji mekanisme dan kinetik tindakbalas penyahoksigenan fenolik. Sifat-sifat fizikokimia pemangkin Ag/TiO<sub>2</sub> telah dikaji untuk menerokai potensinya sebagai pemangkin hidropenyahoksigenan. Hasil kajian menunjukkan bahawa interaksi logam-sokongan pemangkin Ag/TiO<sub>2</sub> membolehkan fenomena tumpahan hidrogen dan interaksi sinergi antara tapak asid dan logam yang penting untuk memangkin penjerapan dan pengaktifan fenolik dan hidrogen semasa hidropenyahoksigenan. Kajian reduksi Ag/TiO<sub>2</sub> oleh hidrogen juga menunjukkan bahawa Ag<sub>2</sub>O mengalami reduksi berlangkah tunggal untuk menghasilkan Ag yang dicirikan oleh *unimolecular decay model*. Teknik pengkapsulan sampel juga dicadangkan dalam kajian ini untuk memanjangkan pengeluaran sampel fenol yang disejat dalam mikroreaktor. Fenomena pengeluaran sampel meruap yang dilambatkan juga dipertingkatkan dengan menggunakan kapsul logam yang kekerasan bahan tinggi dan keluasan permukaan kecil untuk penyejatan sampel.

Penggunaan kapsul logam stanum berbentuk silinder juga memanjangkan pengeluaran sampel fenol yang disejat kepada 454—554 K yang melebihi takat didih fenol. Dapatan ini ialah penting untuk pengaktifan pemangkin yang lebih baik dan kajian kinetik tindakbalas pemangkinan pepejal-gas yang merentangi julat suhu yang lebih besar tetapi dengan kuantiti bahan tindak balas yang sama. Analisis FTIR dan GC-MS menunjukkan pengubahan fenol kepada benzena sebagai produk utama oleh pemangkin Ag/TiO<sub>2</sub> pada keadaan tekanan atmosfera. Model kinetik HDO fenol oleh pemangkin Ag/TiO<sub>2</sub> mengesahkan hidrogenolisis dan hidrogenasi fenol; dehidrasi sikloheksanol dan hidrogenasi benzena dan sikloheksena. Kadar tindakbalas meningkat dengan susunan berikut:  $r_1$  (hidrogenolisis fenol) <  $r_2$  (hidrogenasi fenol) <  $r_5$  (hidrogenasi benzena) <  $r_3$  (dehidrasi sikloheksanol) <  $r_4$  (hidrogenasi sikloheksena). Hidrogenolisis dan hidrogenasi fenol merupakan langkah tindakbalas pengehadan kadar untuk DDO dan HYD proses. Aplikasi *transition state theory* menunjukkan formasi *activated complexes* yang lebih teratur dalam setiap langkah tindak balas asas berdasarkan perubahan entropi pengaktifan yang negatif. Model kinetik ini berupaya menerangkan permhatian kuantitatif dan kualitatif dalam kajian ini dengan ketepatan yang munasabah dan berguna untuk pemahaman kinetika dan mekanistika tindak balas permukaan untuk HDO fenol atas pemangkin logam transisi yang disokong. Pemangkin Ag/TiO<sub>2</sub> tidak menunjukkan degradasi ketara dalam sifat pemangkin dan fizikokimia selepas diguna untuk 4 jam eksperimen penyahoksigenan berturut-turut. Penimbunan spesies logam Ag yang teroksidasi dan deposit kok di pemangkin Ag/TiO<sub>2</sub> selepas setiap eksperimen HDO boleh dialihkan melalui H<sub>2</sub>-pengaktifan dan pengkalsinan di udara pada 553 K dengan sekurang-kurangnya 98.9% kecekapan penyingkiran.

Kata kunci: Pemodelan kinetik, TGA-FTIR, fenol, Ag/TiO<sub>2</sub>, hidropenyahoksigenan fasa

gas

## ACKNOWLEDGEMENTS

First and foremost, I want to thank my God for all that he has ordained and given in my life. The Lord has been my unerring counsel in times of uncertainties, my solace in times of tumult, my comforter in times of sorrow, my strength in times of weariness and my joy in every season.

I would also like to thank Professor Dr. Wan Mohd Ashri Wan Daud for giving me this research opportunity and also guiding me through this journey of life as a doctorate candidate. I express my gratitude to my institution, University of Malaya (UM) for the opportunity to pursue a Ph.D. in chemical engineering.

To my family, I thank you for everything. Even as I write this sentence, I am reminded of how time had indeed passed so quickly, of my former days and my past glorious moments at University of Malaya. Now here I am, ready to move onto the next chapter of my life with a heart of mixed feelings. However, in all of these, I remembered one thing with all my heart that if it is not for God, this zero-to-hero journey would not have been made possible. Under the sun and the rain, God is ever sovereign and every strand of joy and sorrow had a place within the tapestry of His grace. So, through every season of life, I will choose to say, “Thy perfect will in thy perfect way and timing”.

“As for man, his days are like grass—

he blooms like a flower of the field;

when the wind has passed over, it vanishes,

and its place remembers it no more.

But from everlasting to everlasting

the loving devotion of the LORD extends to those who fear Him,

and His righteousness to their children’s children.”



## TABLE OF CONTENTS

Abstract .....	iii
Abstrak .....	v
Acknowledgements .....	vii
Table of Contents .....	viii
List of Figures .....	xiv
List of Tables .....	xviii
List of Symbols and Abbreviations.....	xxi
List of Appendices .....	xxvii
<b>CHAPTER 1: INTRODUCTION.....</b>	<b>1</b>
1.1 Research background.....	1
1.2 Problem statement .....	3
1.3 Objectives of research.....	5
1.4 Workflow of research .....	7
1.5 Scope of research.....	8
1.6 Importance of proposed research.....	9
1.7 Outline of thesis .....	9
<b>CHAPTER 2: LITERATURE REVIEW.....</b>	<b>12</b>
Part A: A review on reaction mechanisms of metal-catalyzed deoxygenation process in bio-oil model compounds	
2.1 Introduction.....	12
2.2 Deoxygenation process of model compounds .....	13
2.2.1 Phenolics .....	15
2.2.2 Furans .....	32

2.2.3	Ethers.....	43
2.2.4	Carboxylic acids.....	48
2.2.5	Aldehydes and ketones.....	52
2.2.6	Alcohols.....	57
2.3	Deoxygenation reactivity of model compounds.....	61
Part B: A review on reactivity of heterogeneous metal catalysts for deoxygenation of bio-oil model compounds		
2.4	Introduction.....	66
2.5	Metal catalysts in deoxygenation processes.....	67
2.5.1	Effect of metal element.....	68
2.5.1.1	Pt-based catalyst.....	68
2.5.1.2	Ni-based catalyst.....	73
2.5.1.3	Pd-based catalyst.....	77
2.5.1.4	Cu-based catalyst.....	81
2.5.1.5	Mo-based catalyst.....	85
2.5.1.6	Co-based catalyst.....	90
2.5.1.7	Zn-based catalyst.....	94
2.5.1.8	Ru-based catalyst.....	97
2.5.1.9	Re-based catalyst.....	101
2.5.1.10	Ir-based catalyst.....	104
2.5.1.11	Zr-based catalyst.....	107
2.5.1.12	Fe-based catalyst.....	110
2.5.1.13	W-based catalyst.....	114
2.5.1.14	Sn-based catalyst.....	118
2.5.1.15	Ga-based catalyst.....	121
2.5.1.16	Rh-based catalyst.....	124

2.5.1.17	Cs-based catalyst .....	127
2.5.1.18	Mg-based catalyst .....	130
2.5.1.19	Overview .....	131
2.5.2	Effect of metal loading and dispersion .....	133
2.5.3	Effect of support and its metal-support interaction .....	135
2.5.4	Effect of preparation method and condition .....	138
2.6	Catalyst selection criteria for deoxygenation .....	142
2.7	Discussion on hydrodeoxygenation scenarios .....	146
2.7.1	Titania supported silver catalyst for phenol hydrodeoxygenation .....	146
2.7.2	Phenol hydrodeoxygenation as catalytic gas-solid reaction .....	148
<b>CHAPTER 3: SYNERGISTIC INTERACTION OF METAL-ACID SITES FOR</b>		
<b>PHENOL HYDRODEOXYGENATION OVER BIFUNCTIONAL</b>		
<b>AG/TIO<sub>2</sub> NANOCATALYST .....</b>		
<b>150</b>		
3.1	Introduction.....	150
3.2	Experimental.....	152
3.2.1	Materials .....	152
3.2.2	Synthesis of Ag/TiO <sub>2</sub> catalysts .....	153
3.2.3	Characterization of Ag/TiO <sub>2</sub> catalysts .....	153
3.2.4	Catalytic reactivity test .....	155
3.3	Results and discussion .....	156
3.3.1	Physical properties of Ag/TiO <sub>2</sub> catalysts .....	156
3.3.1.1	Textural properties .....	156
3.3.1.2	XRD analysis.....	157
3.3.1.3	Morphology and topography .....	161
3.3.2	Chemical properties of Ag/TiO <sub>2</sub> catalysts .....	163
3.3.2.1	Elemental analysis and mapping .....	163

3.3.2.2	NH <sub>3</sub> -TPD and Py-FTIR analysis .....	165
3.3.2.3	H <sub>2</sub> -TPD analysis .....	169
3.3.3	HDO activity of Ag/TiO <sub>2</sub> catalysts .....	176
3.4	Conclusion .....	178

#### **CHAPTER 4: TEMPERATURE-PROGRAMMED REDUCTION OF SILVER(I)**

##### **OXIDE IN TITANIA SUPPORTED SILVER CATALYST UNDER**

##### **H<sub>2</sub> ATMOSPHERE .....**

4.1	Introduction.....	180
4.2	Theory .....	183
4.2.1	Determination of reduction rate equation.....	183
4.2.2	Calculation of TPR patterns .....	185
4.2.3	Determination of reduction activation energy.....	186
4.2.4	Determination of reduction mechanism .....	188
4.3	Experimental.....	190
4.3.1	Materials .....	190
4.3.2	Reduction experiments .....	190
4.4	Results and discussion .....	191
4.4.1	Effect of metal loading and particle size .....	191
4.4.2	Effect of heating rate .....	195
4.4.3	Reduction mechanism of Ag/TiO <sub>2</sub> catalyst.....	197
4.4.4	Mass transfer limitations .....	205
4.5	Conclusion .....	206

#### **CHAPTER 5: DELAYED VOLATILES RELEASE PHENOMENON AT**

##### **HIGHER TEMPERATURE IN TGA VIA SAMPLE**

##### **ENCAPSULATION TECHNIQUE .....**

5.1	Introduction.....	208
5.2	Theory .....	211
5.2.1	Thermodynamics of vaporization.....	211
5.2.2	Release of vaporized volatiles at higher temperatures .....	212
5.3	Experimental.....	215
5.3.1	Materials .....	215
5.3.2	Sample encapsulation technique.....	216
5.3.3	Volatilization of encapsulated sample.....	217
5.3.4	Catalytic gas-solid reaction .....	218
5.4	Results and discussion .....	219
5.4.1	Post-vaporization conditions .....	219
5.4.2	Delayed volatile release via sample encapsulation .....	220
5.4.3	Catalytic gas-solid reaction .....	227
5.5	Conclusion.....	229

**CHAPTER 6: ATMOSPHERIC HYDRODEOXYGENATION OF PHENOL AS  
PYROLYTIC OIL MODEL COMPOUND FOR HYDROCARBON  
PRODUCTION USING AG/TIO<sub>2</sub> CATALYST..... 230**

6.1	Introduction.....	230
6.2	Theoretical formalisms of elementary rate reaction .....	232
6.2.1	Collision theory .....	232
6.2.2	Transition state theory .....	236
6.2.2.1	Microscopic formulation .....	237
6.2.2.2	Macroscopic formulation .....	240
6.2.2.3	Surface reactions .....	242
6.3	Experimental.....	242
6.3.1	Chemicals .....	242

6.3.2	Catalyst preparation.....	243
6.3.3	Catalyst characterization .....	243
6.3.4	Catalytic measurement .....	244
6.3.4.1	Kinetic tests .....	244
6.3.4.2	Catalyst stability study .....	246
6.4	Results and discussion .....	246
6.4.1	Characterization of catalysts under study.....	246
6.4.2	Hydrodeoxygenation of phenol .....	248
6.4.3	Effect of reaction conditions .....	253
6.4.3.1	Effect of temperature.....	253
6.4.3.2	Effect of H <sub>2</sub> flow rate .....	254
6.4.3.3	Effect of WHSV .....	255
6.4.4	Mechanisms and kinetics.....	257
6.4.5	Catalyst recycling test .....	262
6.4.5.1	Catalyst stability.....	262
6.4.5.2	Catalyst activity.....	264
6.5	Conclusion.....	265
<b>CHAPTER 7: CONCLUSIONS AND RECOMMENDATIONS.....</b>		<b>267</b>
7.1	Conclusions.....	267
7.2	Recommendations for future works.....	270
References .....		272
List of Publications and Papers Presented .....		316
Appendix .....		324

## LIST OF FIGURES

Figure 1.1	: Detailed workflow of research.....	7
Figure 2.1	: Production of liquid fuels from lignocellulosic biomass.....	13
Figure 2.2	: Molecular structures of phenolic model compounds.....	16
Figure 2.3	: Reaction pathways of phenol HDO: A) HYD and DDO pathways, B) Tautomerization-deoxygenation pathway .....	18
Figure 2.4	: Phenol HDO over Ni/HZSM-5 and Ni/ $\gamma$ -Al <sub>2</sub> O <sub>3</sub> -HZSM-5 catalysts....	25
Figure 2.5	: Reaction pathways of HDO of guaiacol, phenol and anisole .....	29
Figure 2.6	: Molecular structures of furanic model compounds .....	33
Figure 2.7	: Adsorption modes of furfural on metal surfaces .....	33
Figure 2.8	: Reaction pathway of 2-methyltetrahydrofuran deoxygenation .....	38
Figure 2.9	: Mechanism of C( <i>sp</i> <sup>3</sup> )—O bond cleavage in benzofuran HDO starting from 2,3-dihydrobenzofuran.....	39
Figure 2.10	: Molecular structures of aromatic ether model compounds.....	44
Figure 2.11	: Mechanism of E1 elimination of diisopropyl ether .....	45
Figure 2.12	: Molecular structures of acid model compounds .....	49
Figure 2.13	: Molecular structures of carbonyl model compounds.....	53
Figure 2.14	: Deoxygenation of acetophenone into ethylcyclohexane .....	53
Figure 2.15	: Reaction network of benzaldehyde HDO .....	54
Figure 2.16	: Molecular structures of alcohol model compounds.....	58
Figure 2.17	: Regeneration of oxygen vacant site in molybdenum oxide catalyst during acetone deoxygenation .....	87
Figure 2.18	: HDO mechanism of guaiacol over Co/SiO <sub>2</sub> catalyst.....	91
Figure 2.19	: HDO of <i>m</i> -cresol over Ga-based zeolite catalyst .....	122
Figure 2.20	: Deoxygenation of methyl octanoate over CsNaX zeolite catalyst ....	128
Figure 2.21	: Conversion of lignocellulosic biomass into valorized deoxygenated products.....	132

Figure 3.1	: A) N <sub>2</sub> adsorption-desorption isotherms and B) respective pore size distributions of samples with different Ag loadings: (a) TiO <sub>2</sub> (calcined at 400 °C), (b) Ag/TiO <sub>2</sub> -1, (c) Ag/TiO <sub>2</sub> -3, (d) Ag/TiO <sub>2</sub> -5 and (e) Ag/TiO <sub>2</sub> -10 .....	157
Figure 3.2	: XRD patterns of (a) TiO <sub>2</sub> (calcined at 400 °C), (b) Ag/TiO <sub>2</sub> -1, (c) Ag/TiO <sub>2</sub> -3, (d) Ag/TiO <sub>2</sub> -5 and (e) Ag/TiO <sub>2</sub> -10 .....	160
Figure 3.3	: FESEM micrographs of calcined TiO <sub>2</sub> , Ag/TiO <sub>2</sub> -1, Ag/TiO <sub>2</sub> -3, Ag/TiO <sub>2</sub> -5 and Ag/TiO <sub>2</sub> -10 at 50 kX (a, b, c, d, e) and 100 kX (A, B, C, D, E) magnifications .....	162
Figure 3.4	: TEM micrographs of (A) calcined TiO <sub>2</sub> , (B) Ag/TiO <sub>2</sub> -1, (C) Ag/TiO <sub>2</sub> -3, (D) Ag/TiO <sub>2</sub> -5 and (E) Ag/TiO <sub>2</sub> -10 at 200 kX magnification.....	163
Figure 3.5	: Elemental mapping of Ti (green) and Ag (red) for Ag/TiO <sub>2</sub> -10 catalyst with FESEM micrographs of 10 kX and 40 kX magnifications.....	164
Figure 3.6	: NH <sub>3</sub> -TPD spectra of catalyst samples at 40 K/min (left) and Ag/TiO <sub>2</sub> -10 at different heating rates (right) .....	166
Figure 3.7	: Pyridine-FTIR spectra after desorption for: (A) Ag/TiO <sub>2</sub> with different Ag loadings at 770 K, (B) Ag/TiO <sub>2</sub> -10 at different outgassing temperatures.....	167
Figure 3.8	: Linear plot of ln (β/T <sub>p</sub> <sup>2</sup> ) versus 1/T <sub>p</sub> for (A) peak 1 and (B) peak 2 of Ag/TiO <sub>2</sub> -10 catalyst.....	169
Figure 3.9	: H <sub>2</sub> -TPD spectra of catalyst samples at 40 K/min (left) and Ag/TiO <sub>2</sub> -10 at different heating rates (right) .....	170
Figure 3.10	: Deconvoluted H <sub>2</sub> -TPD spectra of (a) TiO <sub>2</sub> , (b) Ag/TiO <sub>2</sub> -1, (c) Ag/TiO <sub>2</sub> -3, (d) Ag/TiO <sub>2</sub> -5 and (e) Ag/TiO <sub>2</sub> -10 .....	172
Figure 3.11	: Linear plot of ln (β/T <sub>p</sub> <sup>2</sup> ) versus 1/T <sub>p</sub> for A) peak 1, B) peak 2 and C) peak 3 of Ag/TiO <sub>2</sub> -10 catalyst .....	175
Figure 4.1	: Algorithm for determination of Ag/TiO <sub>2</sub> reduction mechanism .....	189
Figure 4.2	: (a) TPR profiles of TiO <sub>2</sub> and Ag/TiO <sub>2</sub> samples at 20 K/min heating rate. (b) Effect of particle size on reduction temperature .....	192
Figure 4.3	: TPR profiles of Ag/TiO <sub>2</sub> -10 catalyst with different heating rates.....	196
Figure 4.4	: Temperature-programmed “Arrhenius plots” for Ag <sub>2</sub> O reduction (Ag/TiO <sub>2</sub> -10): (A) first peak; (B) second peak.....	197
Figure 4.5	: Calculated TPR patterns for peak 1 (i) and 2 (ii) based on reduction models: (a) three-dimensional nucleation based on Avrami-Erofeev	



	equation; (b) two-dimensional nucleation based on Avrami-Erofeev equation; (c) phase boundary controlled contracting cylinder; (d) phase boundary controlled contracting sphere; (e) unimolecular decay; (f) three-dimensional diffusion.....	200
Figure 4.6	: Comparison of TPR patterns: (a) experimental result using Ag/TiO <sub>2</sub> -10 at 30 K/min, (b) first measured reduction peak obtained via peak deconvolution, (c) second measured reduction peak obtained via peak deconvolution, (d) simulation result of first peak using unimolecular decay model, (e) simulation result of second peak using unimolecular decay model.....	201
Figure 5.1	: Delayed release of vaporized sample via encapsulation.....	214
Figure 5.2	: Schematics of sample encapsulation concept for catalytic gas-solid reaction with standard sample (left) and encapsulated sample (right) in TGA.....	215
Figure 5.3	: Hermetically sealed pans containing liquid samples: Tin cylinder (left), Tin pan (middle) and Aluminum pan (right).....	217
Figure 5.4	: Gas-phase reduction of phenol to benzene over Ag/TiO <sub>2</sub> catalyst without and with sample encapsulation technique.....	219
Figure 5.5	: Conditions of metal capsules: stock (left), before (middle) and after (right) experiment.....	220
Figure 5.6	: TG (left) and DTG (right) curves of Al pan encapsulated guaiacol vaporization at different heating rates.....	222
Figure 5.7	: TG (left) and DTG (right) curves of Al pan encapsulated phenol and guaiacol vaporization at 50 K/min.....	223
Figure 5.8	: Vapor pressure of phenol and guaiacol at different temperatures based on Antoine equation.....	223
Figure 5.9	: TG (left) and DTG (right) curves of encapsulated phenol vaporization at 50 K/min.....	226
Figure 5.10	: Phenol release rates (left) and product evolution during phenol reduction (right): (A) unreacted phenol and (B) benzene without sample encapsulation; (C) unreacted phenol and (D) benzene with sample encapsulation.....	228
Figure 6.1	: N <sub>2</sub> adsorption-desorption isotherms of Ag/TiO <sub>2</sub> and TiO <sub>2</sub> .....	247
Figure 6.2	: (A) SEM and (B) TEM images of Ag/TiO <sub>2</sub> catalyst.....	248

Figure 6.3	: Reaction scheme of phenol hydrodeoxygenation .....	249
Figure 6.4	: FTIR absorbance spectra for phenol and HDO product mixtures. HDO conditions: 553 K, 1 atm, $W_{\text{cat}} = 0.23$ g, $WHSV = 5.09$ h <sup>-1</sup> , 5 mL/min H <sub>2</sub> flow.....	250
Figure 6.5	: Effect of H <sub>2</sub> flow rate on A) cyclohexane and benzene selectivity, B) phenol conversion at 454, 495 and 553 K. HDO conditions: 1 atm, 230 mg catalyst, 5.09 h <sup>-1</sup> WHSV .....	255
Figure 6.6	: Effect of WHSV on phenol conversion at 454, 495 and 530 K. HDO conditions: 1 atm, 5 mL/min H <sub>2</sub> flow.....	256
Figure 6.7	: Parity plots of experimental and calculated reaction rates of Step 1, 2, 3, 4 and 5.....	261
Figure 6.8	: TEM images of spent Ag/TiO <sub>2</sub> catalyst after 4 h of reaction.....	264
Figure 6.9	: XRD diffractograms of fresh and spent Ag/TiO <sub>2</sub> catalysts .....	264

## LIST OF TABLES

Table 2.1	: Comparison of HDO reaction pathways.....	20
Table 2.2	: Normalized oxophilicity scale of several elements .....	26
Table 2.3	: Deoxygenation process for phenolic compounds commonly found in bio-oil .....	31
Table 2.4	: Values of equilibrium, rate and adsorption constants for furfural deoxygenation to 2-methylfuran.....	36
Table 2.5	: Deoxygenation process for furanic compounds commonly found in bio-oil.....	43
Table 2.6	: Deoxygenation process for ethers commonly found in bio-oil .....	48
Table 2.7	: Deoxygenation process for acids commonly found in bio-oil.....	51
Table 2.8	: Kinetic terms of benzaldehyde HDO on different catalysts in hexane ..	55
Table 2.9	: Deoxygenation process for carbonyl compounds commonly found in bio-oil .....	57
Table 2.10	: Deoxygenation process for alcohols commonly found in bio-oil .....	61
Table 2.11	: C—O bond dissociation energies (BDE) of O-containing model compounds at 298 K .....	65
Table 2.12	: Deoxygenation processes using Pt-based catalysts .....	71
Table 2.13	: Deoxygenation processes using Ni-based catalysts .....	75
Table 2.14	: Deoxygenation processes using Pd-based catalysts .....	80
Table 2.15	: Deoxygenation processes using Cu-based catalysts.....	84
Table 2.16	: Deoxygenation processes using Mo-based catalysts.....	89
Table 2.17	: Deoxygenation processes using Co-based catalysts.....	93
Table 2.18	: Deoxygenation processes using Zn-based catalysts .....	96
Table 2.19	: Deoxygenation processes using Ru-based catalysts.....	100
Table 2.20	: Deoxygenation processes using Re-based catalysts .....	103
Table 2.21	: Deoxygenation processes using Ir-based catalysts.....	106

Table 2.22	: Deoxygenation processes using Zr-based catalysts.....	109
Table 2.23	: Deoxygenation processes using Fe-based catalysts .....	113
Table 2.24	: Deoxygenation processes using W-based catalysts.....	117
Table 2.25	: Deoxygenation processes using Sn-based catalysts .....	120
Table 2.26	: Deoxygenation processes using Ga-based catalysts.....	123
Table 2.27	: Deoxygenation processes using Rh-based catalysts.....	126
Table 2.28	: Deoxygenation processes using Cs-based catalysts .....	129
Table 2.29	: Deoxygenation process of bio-oil model compounds over metal-based catalysts .....	132
Table 2.30	: Effect of impregnation and drying conditions on metal distribution within pore.....	140
Table 2.31	: Deoxygenation processes over metal-based catalysts .....	144
Table 2.32	: Catalyst supports for deoxygenation process .....	145
Table 2.33	: Reactor features .....	149
Table 3.1	: Physicochemical properties of TiO <sub>2</sub> and Ag/TiO <sub>2</sub> samples .....	157
Table 3.2	: NH <sub>3</sub> -TPD analysis of Ag/TiO <sub>2</sub> catalysts .....	167
Table 3.3	: H <sub>2</sub> -TPD analysis of TiO <sub>2</sub> support and Ag/TiO <sub>2</sub> catalysts.....	173
Table 3.4	: Comparison of various HDO catalysts in terms of acid and metal site densities .....	176
Table 3.5	: Catalytic performance of Ag/TiO <sub>2</sub> -10 catalyst for phenol HDO. Reaction conditions: Pressure = 1 atm, W <sub>cat</sub> = 230 mg, 100 mL/min 5% H <sub>2</sub> /N <sub>2</sub> flow, WHSV = 5.09 h <sup>-1</sup> .....	178
Table 3.6	: Effect of Ag loading on catalyst performance. Reaction conditions: Pressure = 1 atm, T = 500 K, W <sub>cat</sub> = 230 mg, 100 mL/min 5% H <sub>2</sub> /N <sub>2</sub> flow, WHSV = 5.09 h <sup>-1</sup> .....	178
Table 4.1	: $f(\alpha)$ and $g(\alpha)$ of reduction models.....	186
Table 4.2	: Physicochemical properties of Ag/TiO <sub>2</sub> catalyst.....	190
Table 4.3	: TPR results of Ag/TiO <sub>2</sub> catalysts at 20/K min heating rate .....	193
Table 4.4	: $A$ and FWHM values of the two reduction peaks calculated by using $E = 73.35$ kJ/mol, $T_{\max} = 393.8$ K for first peak; $E = 81.71$ kJ/mol, $T_{\max} =$	

	495 K for second peak at $\beta = 30$ K/min .....	199
Table 4.5	: Reduction kinetic parameters of Ag/TiO <sub>2</sub> -10 at 20 K/min at maximum reduction rate .....	202
Table 4.6	: Comparison of Ag <sub>2</sub> O reduction models .....	204
Table 5.1	: Dimensions of metal capsules .....	216
Table 6.1	: Partition function of each mode .....	240
Table 6.2	: Physicochemical properties of Ag/TiO <sub>2</sub> catalyst.....	247
Table 6.3	: IR bands for functional group identification .....	250
Table 6.4	: HDO products of phenol over Ag/TiO <sub>2</sub> as determined by GC-MS.....	253
Table 6.5	: Kinetic data for gas-phase phenol hydrodeoxygenation network on Ag/TiO <sub>2</sub> catalyst with their 95% confidence intervals. HDO conditions: 454 K, 1 atm, WHSV = 5.1 h <sup>-1</sup> , H <sub>2</sub> /phenol molar ratio = 1 .....	259
Table 6.6	: Adsorption equilibrium parameters for reactants in phenol hydrodeoxygenation network on Ag/TiO <sub>2</sub> catalyst and their 95% confidence intervals at 454 K .....	260
Table 6.7	: Total coke and oxidized silver contents of spent catalyst as obtained from TGA. HDO conditions of each 1 h run: 553 K, 1 atm, W <sub>cat</sub> = 2.0 g, WHSV = 0.59 h <sup>-1</sup> , 200 mL/min 5% H <sub>2</sub> /N <sub>2</sub> gas flow .....	262
Table 6.8	: Physicochemical properties of spent Ag/TiO <sub>2</sub> catalyst after 4 h of reaction .....	263
Table 6.9	: Product analysis of each HDO run. HDO conditions of each 1 h run: 553 K, 1 atm, W <sub>cat</sub> = 2.0 g, WHSV = 0.59 h <sup>-1</sup> , 200 mL/min 5% H <sub>2</sub> /N <sub>2</sub> gas flow .....	265

## LIST OF SYMBOLS AND ABBREVIATIONS

$\alpha$	:	Reduction percentage of solid reactant
$\beta$	:	Heating rate, K/min
$\Delta_r E_{m,0}^\ddagger$	:	Standard molar activation energy of activation, kJ/mol
$\Delta_i G$	:	Gibbs free energy change of <i>i</i> th reaction, kJ/mol
$\Delta_i G_m$	:	Molar Gibbs free energy change of <i>i</i> th reaction, kJ/mol
$\Delta_r G_m^\ddagger$	:	Molar Gibbs free energy change of activation, kJ/mol
$\Delta H_i$	:	Adsorption enthalpy of species <i>i</i> , kJ/mol
$\Delta_r H_m^\ddagger$	:	Molar enthalpy change of activation, kJ/mol
$\Delta_r S_m^\ddagger$	:	Molar entropy change of activation, J/mol.K
$\varepsilon_r$	:	Total energy level at <i>r</i> th level, eV
$\varepsilon_r^T$	:	Translational energy level at <i>r</i> th level, eV
$\varepsilon_r^R$	:	Rotational energy level at <i>r</i> th level, eV
$\varepsilon_r^V$	:	Vibrational energy level at <i>r</i> th level, eV
$\varepsilon_r^{El}$	:	Electronic energy level at <i>r</i> th level, eV
$\eta$	:	Internal effectiveness factor
$\theta_i$	:	Fractional coverage of species <i>i</i>
$\theta_p$	:	Surface coverage at peak temperature
$\mu_{ij}$	:	Reduced mass of <i>i</i> and <i>j</i> molecular species
$\rho$	:	Steric factor
$\sigma$	:	Polar substituent parameter (Hammett equation)
$\sigma_c$	:	Constriction factor
$\sigma_i$	:	Sticking probability of species <i>i</i>
$\sigma_{ij}$	:	Cross section of reaction between <i>i</i> and <i>j</i> molecular species

$\tilde{\tau}$	:	Tortuosity
$\phi_n$	:	Thiele modulus of $n$ th reaction order
$\phi_p$	:	Porosity
$A$	:	Pre-exponential factor
$C_i$	:	Concentration of species $i$ , mol/dm <sup>3</sup>
$C_{i,0}$	:	Initial concentration of species $i$ , mol/dm <sup>3</sup>
$C_{W-P}$	:	Weisz-Prater criterion
$\bar{D}$	:	Average particle size, nm
$\bar{D}_p$	:	Average pore size, nm
$D_e$	:	Effective diffusivity, nm <sup>2</sup> /s
$(D_K)_i$	:	Knudsen diffusivity of species $i$ , nm <sup>2</sup> /s
$E_a$	:	Activation energy, kJ/mol
$E_d$	:	Desorption activation energy, kJ/mol
$E_s$	:	Steric substituent parameter (Taft equation)
$E_\sigma$	:	Polar substituent parameter (Taft equation)
$f(\alpha)$	:	Reduction model
$F_i$	:	Flow rate of species $i$ , mol/s
$F_{i,0}$	:	Initial flow rate of species $i$ , mol/s
$g_r$	:	Total degeneracy of $r$ th energy level state
$g_r^T$	:	Translational degeneracy of $r$ th energy level state
$g_r^R$	:	Rotational degeneracy of $r$ th energy level state
$g_r^V$	:	Vibrational degeneracy of $r$ th energy level state
$g_r^{El}$	:	Electronic degeneracy of $r$ th energy level state
$G(i, T)$	:	Gibbs free energy of species $i$ at temperature $T$ , kJ/mol

$G_m(i, T)$	:	Molar Gibbs free energy of species $i$ at temperature $T$ , kJ/mol
$h$	:	Planck constant, m <sup>2</sup> .kg/s
$k_B$	:	Boltzmann constant, m <sup>2</sup> .kg/K.s <sup>2</sup>
$k_i$	:	Rate constant of $i$ th reaction, mol/dm <sup>3</sup> .s
$k_{i,0}$	:	Initial rate constant of $i$ th reaction, mol/dm <sup>3</sup> .s
$K_i$	:	Adsorption equilibrium constant of species $i$ , kPa <sup>-1</sup>
$K^\ddagger$	:	Quasi-equilibrium constant of activation, dm <sup>3</sup> /mol
$M_i$	:	Molecular mass of species $i$ , g/mol
$n_i$	:	Number of moles of species $i$ , mol
$N_A$	:	Avogadro constant, mol <sup>-1</sup>
$N_i$	:	Number of $i$ molecules
$\Theta$	:	Normalized oxophilicity
$p_i$	:	Partial pressure of species $i$ , kPa
$P_{i,0}$	:	Initial partial pressure of species $i$ , kPa
$q$	:	Molecular partition function
$q_m$	:	Molar partition function, mol <sup>-1</sup>
$q_i^T$	:	Translational partition function of species $i$
$q_i^R$	:	Rotational partition function of species $i$
$q_i^V$	:	Vibrational partition function of species $i$
$q_i^{El}$	:	Electronic partition function of species $i$
$Q$	:	Total canonical partition function
$r_i$	:	Reaction rate of $i$ th reaction, mol/dm <sup>3</sup> .s
$R$	:	Ideal gas constant, kJ/mol.K
$S_{BET}$	:	Specific surface area (BET), m <sup>2</sup> /g
$S_i$	:	Selectivity of species $i$



$t$	:	Time, s or h
$T$	:	Temperature, K
$T_p$	:	Peak temperature, K
$\bar{v}_r$	:	Average relative mean velocity of molecules, m/s
$V_{cat}$	:	Volume of catalyst bed, mm <sup>3</sup>
$V_{micro}$	:	Volume of micropores, cm <sup>3</sup> /g
$V_{meso}$	:	Volume of mesopores, cm <sup>3</sup> /g
$W_{cat}$	:	Catalyst weight, mg
$X_i$	:	Conversion of species $i$
$Z_{ij}$	:	Collision frequency between $i$ and $j$ molecular species
2-MF	:	2-methylfuran
2-MP	:	2-methylpentane
Ag <sub>2</sub> O	:	Silver(I) oxide
Ag/TiO <sub>2</sub>	:	Titania supported silver catalyst
AES	:	Auger electron spectroscopy
Al <sub>2</sub> O <sub>3</sub>	:	Aluminum oxide
AOS	:	Average oxidation state
BDE	:	Bond dissociation energy
BET	:	Brunauer-Emmett-Teller theory
BJH	:	Barrett-Joyner-Halenda analysis
CeO <sub>2</sub>	:	Cerium oxide
CNFs	:	Carbon nanofibres
CNTs	:	Carbon nanotubes
CUS	:	Coordinative unsaturated sites
DDO	:	Direct deoxygenation pathway

DFT	:	Density functional theory
DTG	:	Differential thermogravimetry
DSC	:	Differential scanning calorimetry
EDX	:	Energy-dispersive X-ray spectroscopy
FAL	:	Furfural
Fe <sub>2</sub> O <sub>3</sub>	:	Iron(III) oxide
FESEM	:	Field emission scanning electron microscopy
FOL	:	Furfuryl alcohol
FWHM	:	Full width at half maximum height
GC	:	Gas chromatography
HDO	:	Hydrodeoxygenation
HDS	:	Hydrodesulfurization
HMF	:	5-hydroxymethylfurfural
HPLC	:	High performance liquid chromatography
HYD	:	Hydrogenation-dehydration pathway
ICP-OES	:	Inductively coupled plasma optical emission spectrometry
<i>iPrOH</i>	:	Isopropyl alcohol
IR	:	Infrared spectroscopy
LFER	:	Linear free energy relationship
MIBK	:	Methyl isobutyl ketone
MS	:	Mass spectrometry
MTHF	:	2-methyltetrahydrofuran
OMC	:	Ordered mesoporous carbon
rGO	:	Reduced graphene oxide
SiO <sub>2</sub>	:	Silicon dioxide
TCD	:	Thermal conductivity detector

TEM	:	Transmission electron microscopy
TG	:	Thermogravimetry
TGA	:	Thermogravimetric analysis
TGA-FTIR	:	Thermogravimetric-Fourier Transform Infrared Coupling System
THF	:	Tetrahydrofuran
TiO <sub>2</sub>	:	Titanium(IV) oxide
TOF	:	Turnover frequency
TPD	:	Temperature-programmed desorption
TPR	:	Temperature-programmed reduction
TST	:	Transition state theory
VC	:	Vanadium carbide
XRD	:	X-ray diffraction analysis
ZnO	:	Zinc oxide
ZrO <sub>2</sub>	:	Zirconium(IV) oxide

## LIST OF APPENDICES

Appendix A : Evaluation of mass transfer effects using Weisz-Prater criterion.....	324
Appendix B : Derivation of phenol HDO kinetic model.....	329

University of Malaya

## CHAPTER 1: INTRODUCTION

### 1.1 Research background

Biomass is a renewable energy source which has been extensively researched on and utilized over these several decades. The high demand of energy resources, the search for an environmentally friendlier energy source and the abundance of biomass feedstock were some of the major reasons for the rapid development of biomass-based energy industry. Lignocellulosic biomass is a common biomass feedstock used to produce bio-oil through pyrolysis process. The pyrolysis process involves thermal decomposition of biomass feedstock in the absence of oxygen (Abnisa & Wan Daud, 2014). During pyrolysis, biomass components such as cellulose, hemicellulose and lignin undergo thermal degradation to form a complex mixture of more than 400 different oxygen-containing compounds such as phenolics, furans, acids, alcohols, carbonyls, esters and ethers (Bu et al., 2012).

Bio-oil has the prospect of being used as a viable source for liquid fuel. However, a typical bio-oil has high oxygen content which leads to its deficiencies in being used as liquid fuel. Issues such as high corrosivity, low heating value and thermal instability were often attributed to the presence of oxygenated compounds within bio-oil. Therefore, bio-oil upgrading process is an essential step required to convert bio-oil into a deoxygenated liquid fuel which is comparable with fossil fuels. In addition, bio-oil upgrading process is also important as it functions as a platform for the valorization of precursors into high-added value products which are of great importance to other industries (Jacobson et al., 2013). Bio-oil upgrading process can be achieved through deoxygenation which is a process of removing oxygen atoms from a chemical compound. Unlike crude oil which requires hydrodesulfurization treatment due to its high sulfur content, bio-oil has negligible sulfur content and only requires deoxygenation treatment to reduce its oxygen content. The deoxygenation treatment of

bio-oil is challenging as it involves oxygen removal from O-containing compounds with minimal hydrogen consumption and maximized retention of carbon in deoxygenated products (Asadieraghi et al., 2014). These requirements were necessary to ensure the treatment is economical and the upgraded bio-oil has a high fuel rating.

In the light of this matter, extensive studies were done by numerous researchers on the deoxygenation of various model compounds of bio-oil over assorted kinds of metal catalysts. For phenolic model compounds, their deoxygenation process is also equivalently termed as hydrodeoxygenation in which the latter connotes the requirement of H<sub>2</sub> for phenolic deoxygenation. The studies involved the investigation of the nature of deoxygenation process itself and also the performances of metal catalysts. The study of the nature of deoxygenation process involved the discovery and the understanding of reaction pathways, reaction kinetics or mechanisms, and product compositions (He & Wang, 2012). Likewise, the study of metal catalyst performance entailed the analyses of the catalytic effects, electronic interactions by metal and catalytic parameters in terms of yield, conversion, selectivity, turnover frequency and activity (Chaudhari et al., 2013). Examples of deoxygenation model compounds commonly studied were phenol (Yoosuk et al., 2012; Zhao et al., 2011), cresols (Ausavasukhi et al., 2012; Wang et al., 2014a), anisole (Zhu et al., 2011), guaiacol (Bykova et al., 2014; Hong et al., 2014a), furfural (McManus & Vohs, 2014; Yu et al., 2014), dibenzofuran (Cecilia et al., 2013), glycerol (Jin et al., 2013), palmitic acid (Ding et al., 2015), propanoic acid (Chen et al., 2012b), etc. Model compounds were often selected to be studied because they existed in large proportion in bio-oil. Model compound study is beneficial because it can independently elucidate the kinetics and the reaction mechanisms associated with the model compound of that particular functionality under a particular reaction condition. However, real feed study is also important as it accounts for the bulk, synergistic or inhibitive effects which

arose from the intertwining interactions of the complex mixtures (Choudhary & Phillips, 2011).

Nevertheless, there are still some existing problems associated with metal catalysis in deoxygenation. In regard to this aspect, there are still many deoxygenation processes in which their actual metal-catalyzed reaction mechanisms have yet to be rigorously elucidated. Numerous works have been done to understand more vividly on the reaction mechanisms through techniques such as kinetic studies, microkinetic modeling, lumped kinetic modeling or density functional theory. However, these works were done based on elementary approximated reactions or assumptions of kinetic parameters and conditions due to the associated difficulties in determining the accurate dynamics of elementary processes at catalytic sites (Chaudhari et al., 2013). Thus, there is still a great need to further study on the adsorbed species at catalytic sites and their respective elementary reactions in order to determine the rigorous kinetic models or governing rate laws which accurately elucidate the reaction mechanism.

## **1.2 Problem statement**

As mentioned earlier, aside from determining accurate reaction kinetics and mechanisms of deoxygenation, one of the major studies in this field is the search for an excellent deoxygenation catalyst. Previous investigations by other researchers have focused on the use of zeolite based and supported metal catalysts for deoxygenation process. Both catalyst categories were reported to show good deoxygenation activity for various O-containing compounds due to their bifunctional metal-acid properties (Rezaei et al., 2015). However, high surface acidity in zeolite catalysts has also been known to favor secondary condensation reactions which would lead to severe catalytic coking (To & Resasco, 2015). Thus, mild acid supports such as  $\text{Al}_2\text{O}_3$ ,  $\text{TiO}_2$ ,  $\text{ZrO}_2$  and  $\text{CeO}_2$  may

offer better coking resistance while having optimal acid sites for hydrogenolysis in deoxygenation. Likewise, there were many transition metals being used in past studies on deoxygenation such as Co, Cu, Fe, Ga, Ir, Mo, Ni, Pd, Pt, Re, Rh, Ru, Sn, W, Zn and Zr. The use of transition metals in deoxygenation was also favored as they contained metal sites which effectively promote adsorption and activation of hydrogen. However, one of the limitations of transition metals such as Co, Ir, Pd, Pt, Re, Rh and Ru is their high material cost which would be a major challenge to their applications at commercial scale. Silver, on the other hand, is categorized with Cu, Fe, Ni, Ti and Zn as low cost transition metals (Sá & Śrębowata, 2016) and its studies on deoxygenation in regard to its physicochemical properties and metal-support interaction are sparse and varying in their results. Silver-based catalyst would certainly offer higher commerciality should it be found to exhibit excellent phenolic deoxygenation activity as compared with other transition metal deoxygenation catalysts.

The study on bio-oil upgrading mechanism is intricate as it involves multiple deoxygenation process of various O-containing compounds which might have bulk, synergistic or inhibitive effects which arose from the intertwining interactions of the complex mixtures (Choudhary & Phillips, 2011). Phenolics are one of the major compounds in bio-oil (Diebold, 2000; Zhang et al., 2007; Mullen & Boateng, 2008; Abnisa et al., 2014) which pose greater challenge in their oxygen removal due to the higher  $C_{AR}(sp^2)$ —OH bond energy (Furimsky, 2000). Among the phenolic compounds, phenol has the simplest functionality which enables a focused study on the scission of  $C_{AR}(sp^2)$ —OH bond to be done effectively. Other phenolics are actually made up of one or more phenol with additional functional groups which still consist of the targeted  $C_{AR}(sp^2)$ —OH bond for scission during HDO. Thus, by studying HDO mechanism of phenol in a model compound study, these results can be extrapolated for HDO model



compound study of other phenolics which eventually enables a better understanding of phenolics deoxygenation in bio-oil.

Pre-volatilization of sample for catalytic solid-gas reaction is prominent in volatile samples. This undesirable effect will cause an unstandardized contact of volatilized samples with the catalyst bed over a range of reaction temperature which would subsequently affect the analysis of reaction kinetics. Thus, a technique to standardize the release of volatile sample at a definite temperature over catalyst bed is important to ensure proper catalyst activation and accurate reaction kinetics analysis.

### **1.3 Objectives of research**

This research endeavored to obtain scientific understandings on the potential of Ag/TiO<sub>2</sub> as catalyst for phenol hydrodeoxygenation; the mitigation of sample pre-volatilization in catalytic solid-gas reaction for improving reaction kinetic data analysis; the reaction mechanism and kinetics of phenol hydrodeoxygenation over Ag/TiO<sub>2</sub> catalyst. The detail objectives and approaches are as followed:

*1) To investigate the effects of physicochemical properties of Ag/TiO<sub>2</sub> catalyst on its potential as phenol hydrodeoxygenation catalyst.*

This study attempted to explore whether Ag/TiO<sub>2</sub> has the fundamental properties for phenol hydrodeoxygenation. These fundamental properties are oxophilicity, acidity, hydrogen sticking probability and reducibility of supported metal catalyst. Other physicochemical properties of a typical supported metal catalyst were also investigated and compared.

*2) To analyze the interaction of Ag/TiO<sub>2</sub> catalyst with hydrogen and its reduction kinetics.*

This study focused on how Ag/TiO<sub>2</sub> is being reduced in the presence of hydrogen which would give further insights on its interaction with hydrogen during hydrodeoxygenation. Reduction model of Ag/TiO<sub>2</sub> was also determined in regard to thermodynamic and topochemical aspects of reduction.

- 3) *To develop an efficient sample volatilization condition via sample encapsulation technique for the analysis of gas-phase phenol hydrodeoxygenation mechanism and kinetics over Ag/TiO<sub>2</sub> catalyst in TGA-FTIR microreactor.*

This study sought to develop a technique for volatilizing sample at higher temperature to ensure better catalyst activation during its contact with gaseous reactants. The second part of this study involved the application of this technique in gas-phase phenol hydrodeoxygenation over Ag/TiO<sub>2</sub> catalyst for the analysis of its kinetics, mechanism and effect of reaction conditions on HDO products formation. The mechanistic model of phenol hydrodeoxygenation was also sought to be determined in order to quantify the adsorption, surface reaction and desorption occurring at the catalytic interface during phenol hydrodeoxygenation.

## 1.4 Workflow of research

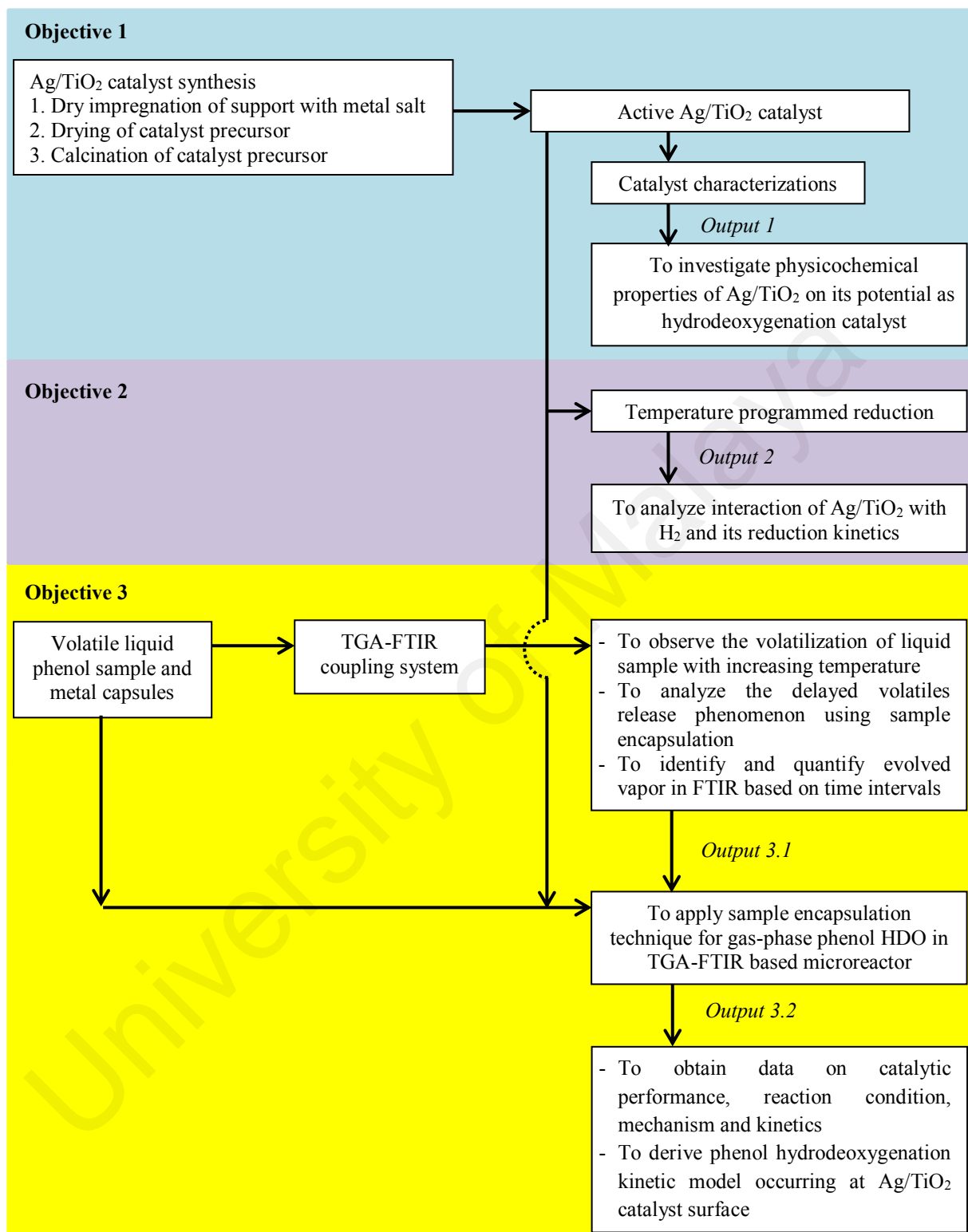


Figure 1.1: Detailed workflow of research

Figure 1.1 shows the overall procedures employed in performing the research of this thesis. The first investigation of this research is to determine the potential of titania supported silver catalysts for phenol hydrodeoxygenation. Since titania supported silver catalyst has not been used in catalyzing phenol hydrodeoxygenation, it is imperative to investigate its physicochemical properties and their effects on the hydrodeoxygenation ability of Ag/TiO<sub>2</sub> catalyst. The second work aimed to investigate the reducibility of Ag/TiO<sub>2</sub> by H<sub>2</sub> via TPR technique. By deriving the reduction kinetics of Ag/TiO<sub>2</sub>, further understanding on its interaction with hydrogen during hydrodeoxygenation can be elucidated.

For the first part of the third study, the phenomenon of phenolics volatilization in the microreactor was also examined to understand its role during the vapor phase reaction. Subsequently, hydrodeoxygenation of phenol will be conducted using the tested Ag/TiO<sub>2</sub> catalyst and the developed reaction setup in order to obtain quantitative kinetic models on its surface reaction.

## **1.5 Scope of research**

This research focused on model compound approach to derive hydrodeoxygenation kinetics and mechanism of phenolics in bio-oil over supported metal catalyst. Therefore, phenol was chosen as the phenolic model compound in this study because phenol is one of the main O-containing constituents in bio-oil. Titania supported silver catalyst was synthesized and used in this reaction study as it is one of the supported metal catalysts that is yet to be thoroughly investigated and applied as hydrodeoxygenation catalyst. The studies on physicochemical properties and reduction of Ag/TiO<sub>2</sub> focused on parameters such as metal loading, surface area, phase composition, acidity, metal site density and reducibility; and their effects on the catalytic ability of Ag/TiO<sub>2</sub> for

hydrodeoxygenation. Parameters of catalyst synthesis and activation such as preparation method, preparation conditions, drying conditions and calcination conditions were set constant in this study. The parameters of catalyst synthesis and activation were selected based on the justifications found within literature. The optimum Ag/TiO<sub>2</sub> catalyst was then further used for reaction study and kinetic modeling. All hydrodeoxygenation experiments were performed using a microreactor in TGA-FTIR equipment at atmospheric pressure and vapor phase. The effects of H<sub>2</sub>/phenol ratio, temperature and catalyst amount on the yield of deoxygenated product are also described in this study. The kinetic modeling of phenol hydrodeoxygenation over Ag/TiO<sub>2</sub> catalyst focuses only on experimental reaction data to analyze the surface reaction chemistry.

### **1.6 Importance of proposed research**

- a) The search for an effective metal-based catalyst for hydrodeoxygenation in terms of its catalytic activity and cost in order to enhance the commerciality of hydrodeoxygenation as bio-oil upgrading process.
- b) To find a precise and effective technique to measure reaction kinetics data at a higher resolution of time and minimized sample pre-volatilization.
- c) This research will contribute to the understanding of hydrodeoxygenation mechanism and kinetics of real bio-oil based on the scientific knowledge obtained from model compound study of phenol hydrodeoxygenation.

### **1.7 Outline of thesis**

This thesis follows the article style format as mentioned in the University of Malaya guidelines. All of the studies which were presented in this thesis have been submitted to several ISI-indexed academic journals for publications. The overall outline and the

content framework of this thesis are presented in this section. This thesis consists of seven thematic chapters and each chapter is as follows:

**Chapter 1:** This chapter explores on research background, problem statement, research objectives, research workflow, research scope, research importance and outline of thesis.

**Chapter 2:** This chapter presents on a comprehensive literature review and major discussions regarding deoxygenation process over supported metal catalysts from several points of view such as model compounds and mechanisms in Part A and metal catalysts in Part B. The obtained information was necessary to aid in the selection of a potential supported metal catalyst, i.e. titania supported silver catalyst, which is still fairly new in HDO field of study. In addition, several outlooks based on studies in literature are also given in this chapter. The first part of this chapter has been published in *Applied Catalysis A: General* (Kay Lup, A. N., Abnisa, F., Wan Daud, W. M. A. and Aroua, M. K. (2017). *A review on reaction mechanism of metal-catalyzed deoxygenation process in bio-oil model compounds. Applied Catalysis A: General, 541: 87-106*). The second part of this chapter has been published in *Journal of Industrial and Engineering Chemistry* (Kay Lup, A. N., Abnisa, F., Wan Daud, W. M. A. and Aroua, M. K. (2017). *A review on reactivity and stability of heterogeneous metal catalysts for deoxygenation of bio-oil model compounds. Journal of Industrial and Engineering Chemistry, 56: 1-34*).

**Chapter 3:** Synergistic interaction of metal-acid sites for phenol hydrodeoxygenation over bifunctional Ag/TiO<sub>2</sub> nanocatalyst. This chapter describes the work for the first objective. This study has been published in *Chinese Journal of Chemical Engineering* (Kay Lup, A. N., Abnisa, F., Wan Daud, W. M. A. and Aroua, M. K. (2018). *Synergistic interaction of metal-acid sites for phenol hydrodeoxygenation over bifunctional Ag/TiO<sub>2</sub>*

*nanocatalyst. Chinese Journal of Chemical Engineering. DOI: 10.1016/j.cjche.2018.08.028).*

**Chapter 4:** Temperature programmed reduction of silver(I) oxide in titania supported silver catalyst under H<sub>2</sub> atmosphere. This chapter addresses the second objective. This study has been received in revised form by Journal of the Chinese Chemical Society.

**Chapter 5:** Delayed volatiles release phenomenon at higher temperature in TGA via sample encapsulation technique. This chapter addresses the first part of the third objective. This study has been published in *Fuel* (Kay Lup, A. N., Abnisa, F., Wan Daud, W. M. A. and Aroua, M. K. (2018). *Delayed volatiles release phenomenon at higher temperature in TGA via sample encapsulation technique. Fuel, 234: 422-429).*

**Chapter 6:** Atmospheric hydrodeoxygenation of phenol as pyrolytic oil model compound for hydrocarbon production using Ag/TiO<sub>2</sub> catalyst. This chapter addresses the second part of the third objective. This study has been published in *Asia-Pacific Journal of Chemical Engineering* (Kay Lup, A. N., Abnisa, F., Wan Daud, W. M. A. and Aroua, M. K. (2019). *Atmospheric hydrodeoxygenation of phenol as pyrolytic oil model compound for hydrocarbon production using Ag/TiO<sub>2</sub> catalyst. Asia-Pacific Journal of Chemical Engineering, DOI: 10.1002/apj.2293).*

**Chapter 7:** This chapter gives a summary of the important results and the main conclusions in regard to the research objectives. Recommendations on future works are also provided in this chapter.

## CHAPTER 2: LITERATURE REVIEW

### Part A: A Review on Reaction Mechanisms of Metal-Catalyzed Deoxygenation Process in Bio-Oil Model Compounds

#### 2.1 Introduction

Bio-oil is a potential liquid fuel source which can be produced through the pyrolysis of biomass. Catalytic deoxygenation is an instrumental step for the defunctionalization of bio-oil which will result in liquid fuel which is of lower oxygen content and higher heating value. Numerous studies were done to investigate the deoxygenation mechanisms and the kinetics of various bio-oil model compounds. In this section, heterogeneous metal-catalyzed deoxygenation mechanisms of oxygenated model compounds with functional groups such as phenolics, furans, ethers, carboxylic acids, aldehydes, ketones and alcohols were compared and discussed. The limitations, benefits and feasibilities of such mechanisms were also presented in this section. The discussions on the classes of model compounds and the bonding configurations of oxygenated compounds have also shown that there is a strong correlation between these parameters and the reaction pathways. Hence, this section presents a summary of the model compound based approach researches which would be useful in correlating such knowledge with the actual bio-oil deoxygenation process. Several outlooks on the deoxygenation reactivity of model compounds were also presented in this section based on the studies on the literatures.



## 2.2 Deoxygenation process of model compounds

Deoxygenation process is one of the integral treatments required to upgrade bio-oil into liquid fuel (Figure 2.1). This is because pyrolysis of biomass will lead to the fragmentation and the depolymerization reactions of hemicellulose, cellulose and lignin-based compounds into acids, ketones, aldehydes, alcohols, ethers, esters, furans, sugars and phenolic compounds which are oxygen-containing compounds. Thus, numerous studies on acids, ketones, aldehydes, alcohols, esters, ethers and phenols were done to investigate their deoxygenation processes.

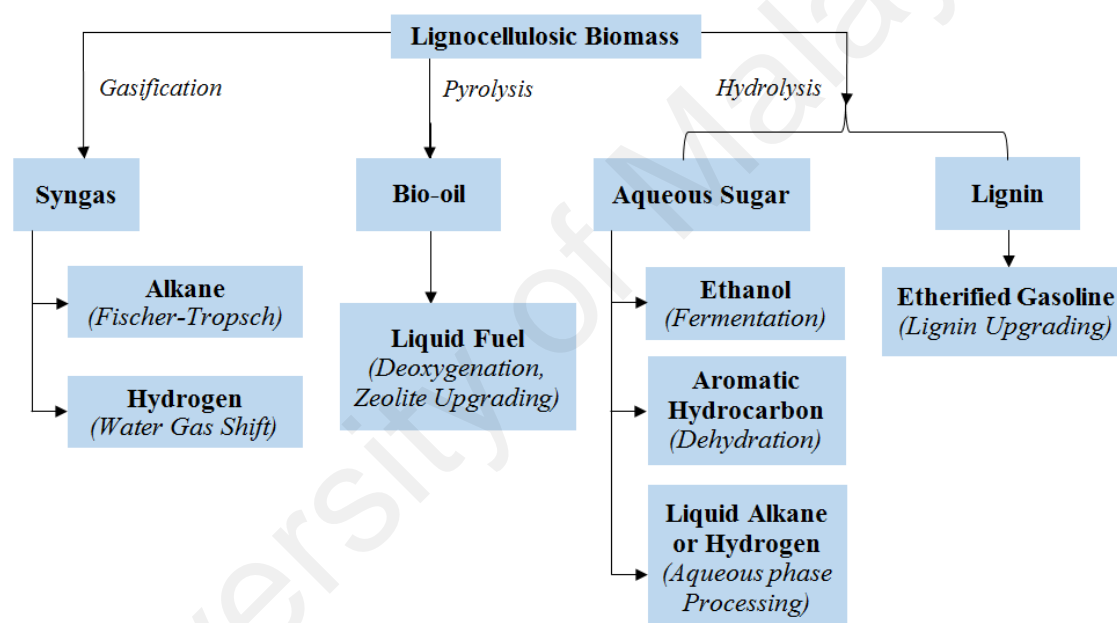


**Figure 2.1: Production of liquid fuels from lignocellulosic biomass (Huber & Dumesic, 2006)**

Numerous studies were also done by researchers to analyze the types of oxygenated compounds and their respective abundances within the bio-oils. For instance, Mullen and Boateng (2008) have studied on the compositions of oxygenated compounds in bio-oils obtained from Switchgrass and Alfalfa (Early bud and full flower) and reported the percentages of oxygenated compounds to be at 11.93 wt%, 9.35 wt% and 12.01 wt%

respectively. Likewise, a review by Zhang et al. (2007) also reported the bio-oil obtained from *P. Indicus* prawn species contained 73.43 vol% of total oxygenated compounds. The relative abundances of oxygenated compounds in bio-oils vary as the bio-oils originate from different biomass sources. Nevertheless, these studies jointly showed the presence of some of the common oxygenated compounds such as phenolics, furans, ethers, carboxylic acids, aldehydes, ketones, alcohols and esters existing in significant proportion within bio-oils. With such analyses, the selections of suitable model compounds for deoxygenation processes were done in past studies, by focusing on model compounds which were of high abundance in bio-oils (Choudhary & Phillips, 2011).

Deoxygenation can be classified into several reaction pathways. In this section, the deoxygenation pathways to be discussed are hydrodeoxygenation, decarboxylation, decarbonylation, dehydration and demethoxylation. Hydrodeoxygenation is a deoxygenation process which uses hydrogen with pressure of up to 20 MPa (Bruycker et al., 2014) for the direct scission of C—O bond. Decarboxylation and decarbonylation also remove oxygen atoms by the respective removal of CO<sub>2</sub> and CO molecules, resulting in the simultaneous loss of one carbon atom. Likewise, dehydration also involves oxygen removal through the formation of H<sub>2</sub>O from reacting molecule while demethoxylation involves oxygen abstraction through the removal of methoxy group (—OCH<sub>3</sub> group) from the compound.

The reaction pathway of deoxygenation varies due to the different types of oxygen-containing functional groups which were being targeted for oxygen abstraction. For instance, decarboxylation abstracts oxygen from carboxylic acids in the form of CO<sub>2</sub> while decarbonylation abstracts oxygen from ketones, aldehydes and carboxylic acids in the form of CO. Likewise, dehydration abstracts oxygen from hydroxyl group (—OH group) in alcohol while demethoxylation abstracts oxygen from methoxy group (—

OCH<sub>3</sub> group) from ether compounds. Despite the variations in reaction pathway and by-product, the aforementioned reactions are deoxygenation processes as they involve the abstraction of oxygen to produce deoxygenated compound as the major product.

### 2.2.1 Phenolics

Phenols or phenolic compounds are categorized as a group of chemical compounds containing at least one hydroxyl group (—OH) directly bonded to a benzene ring. Phenolic compounds are commonly found in bio-oil (up to 55 vol%) (Abnisa et al., 2014; Diebold, 2000) due to the breakdown of lignin-based compounds during the pyrolysis of biomass (Ausavasukhi et al., 2012). Samanya et al. (2012) reported that the high level of phenols will increase the instability and acidity of bio-oils. Figure 2.2 shows phenolic compounds which are present in bio-oil such as phenol, cresol, ethylphenol, catechol, resorcinol, guaiacol, vanillin and eugenol (Furimsky, 2000).

Hydrodeoxygenation is the main reaction involved in the abstraction of oxygen from the aromatic rings of phenolic compounds. The HDO of phenolic compound proceeds through three distinct pathways which are direct deoxygenation route (DDO) (Boullosa-Eiras et al., 2014), hydrogenation-dehydration route (HYD) (Zhao et al., 2011) and tautomerization-deoxygenation route (de Souza et al., 2015; Nie & Resasco, 2014). The DDO pathway involves a direct scission of the C<sub>AR</sub>(sp<sup>2</sup>)—OH bond by hydrogenolysis to yield deoxygenated aromatics as major products while the HYD pathway involves firstly the hydrogenation of aromatic ring and followed by the dehydration of hydroxyl group from the C<sub>cyclic</sub>(sp<sup>3</sup>)—OH bond to yield deoxygenated cyclic compounds as major product (Figure 2.3). The DDO pathway is more advantageous than the HYD pathway because DDO does not require the hydrogenation of aromatic rings for oxygen abstraction. Hence, DDO pathway will consume lesser H<sub>2</sub> (Hensley et al., 2015) and

will produce aromatic products of higher octane ratings which are more suitable for fuel blending purposes (Mochizuki et al., 2014; Zanuttini et al., 2013). However, DDO pathway becomes more feasible at higher reaction temperature range due to the higher energy required to cleave the  $C_{AR}(sp^2)-OH$  bond as compared with the  $C_{cyclic}(sp^3)-OH$  bond in which their respective bond energies are 468 kJ/mol and 385 kJ/mol (Furimsky, 2000; Nie et al., 2014).

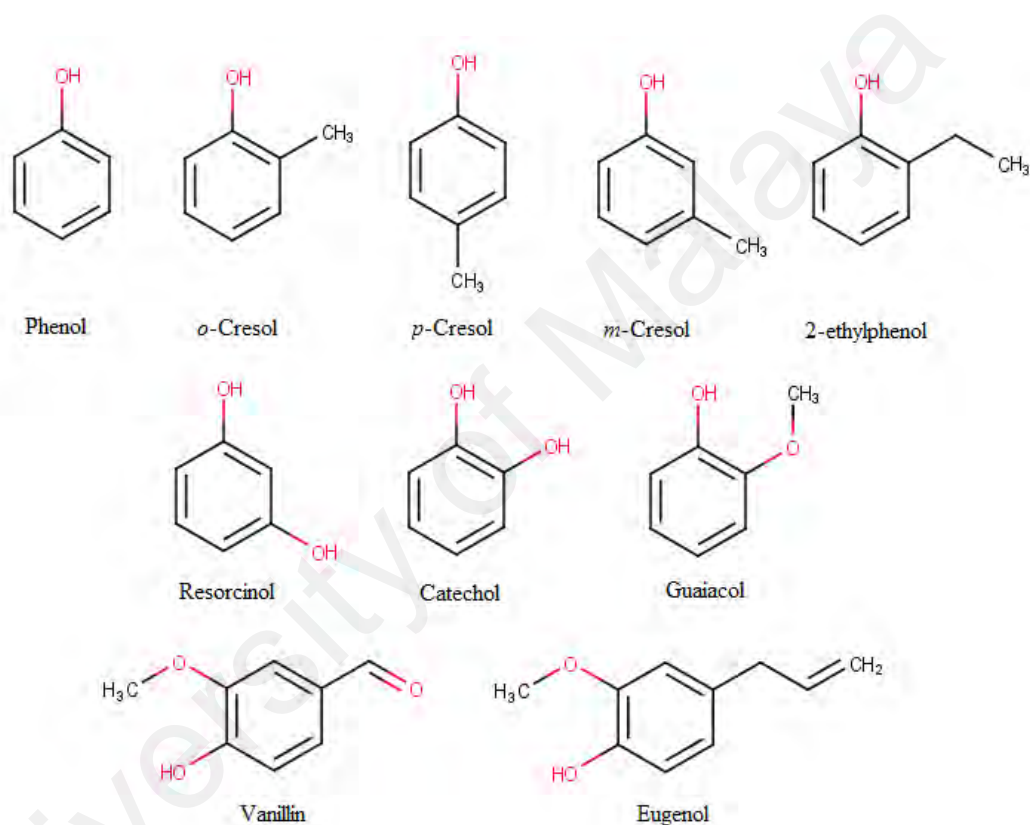


**Figure 2.2: Molecular structures of phenolic model compounds**

The preference for DDO pathway at higher temperature was also attributed to the thermodynamic limitations of phenyl ring hydrogenation for HYD pathway at higher temperature. According to the work by Gutierrez et al. (2009), phenyl ring hydrogenation is the major pathway at 373 K whereas deoxygenation (DDO pathway) is the major pathway at 573 K. Gutierrez et al. (2009) noted that the hydrogenation of aromatic ring is dependent on the availability of adsorbed hydrogen on catalyst surface.

Since H<sub>2</sub> adsorption on catalyst surface is an exothermic reaction (Jiang et al., 2007), an increase in reaction temperature will change the H<sub>2</sub> sorption equilibrium which is the decrease in H<sub>2</sub> adsorption. Thus, the decrease in H<sub>2</sub> adsorption and surface coverage with the increase in temperature will result in the lower rate of phenyl ring hydrogenation. These findings were also reported by Derrouiche and Bianchi (2004) and Nimmanwudipong et al. (2011a). Keane and Patterson (1999) have also reported that H<sub>2</sub> adsorption activation energy is coverage dependent and increases when H<sub>2</sub> surface coverage decreases, which is also in corroboration with the thermodynamic limitations of phenyl ring hydrogenation at higher reaction temperature.

The third pathway of HDO involves firstly the tautomerization of phenolic compounds into a keto-enol equilibrium mixture. Tautomerization of phenolic compounds was proposed to be one of the pathways since the bonding of hydroxyl group with the aromatic ring is one of the characteristics of an enol compound. Several density functional theory (DFT) studies on phenolic tautomerization were explored for its possibility in which the studies have shown its energy barrier is lower than DDO pathway since tautomerization will alter the hybridized C(sp<sup>3</sup>)—O bond into C(sp<sup>2</sup>)—O bond of lower bond energy prior to the C—O bond scission (Hensley et al., 2015; Hernandez-Tamargo et al., 2017; Robinson et al., 2016a; Robinson et al., 2016b). Likewise, tautomerization pathway as one of the deoxygenation pathways was also reported in experimental studies when oxophilic metal catalysts were used such as Pt-Mo/Al<sub>2</sub>O<sub>3</sub>, Ni-Fe/SiO<sub>2</sub>, Pd/TiO<sub>2</sub>, Pd/ZrO<sub>2</sub> and Ru/TiO<sub>2</sub> (de Souza et al., 2015; Nelson et al., 2015; Nie et al., 2014; Robinson et al., 2016a). During tautomerization, the formation of highly unstable keto compounds will cause the facile C=O hydrogenation of keto compound and its subsequent dehydration to form a deoxygenated aromatic compound (de Souza et al., 2015). For example, phenol tautomerizes into 3,5-cyclohexadienone to form a keto-enol equilibrium mixture in this pathway. Then, the

3,5-cyclohexadienone keto compound undergoes C=O hydrogenation to form 3,5-cyclohexadienol which readily dehydrates to form benzene (Figure 2.3).

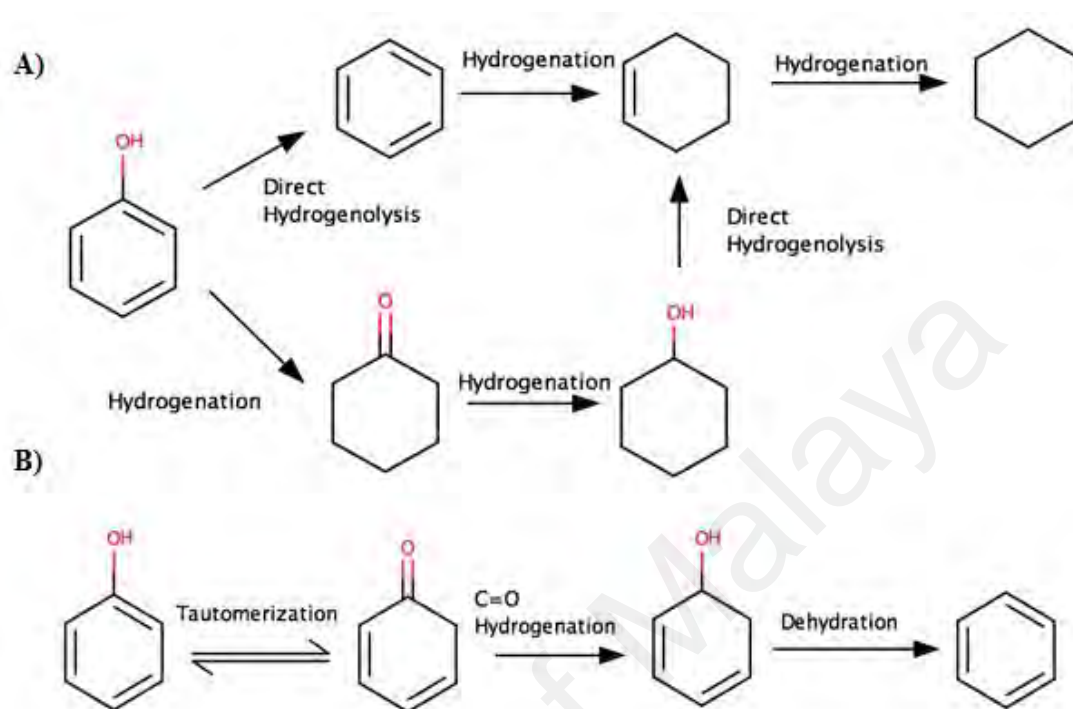


**Figure 2.3: Reaction pathways of phenol HDO: A) HYD and DDO pathways, B) Tautomerization-deoxygenation pathway (Badawi et al., 2013; de Souza et al., 2015; Kay Lup et al., 2017a)**

The type of reaction pathway undertaken during the HDO of phenolic compound is dependent on the type of metal catalyst, type of supports and reaction conditions such as temperature and partial pressure of hydrogen (He & Wang, 2012). In addition, the variation in the HDO pathway would also result in the formation of different deoxygenated compounds. For instance, the direct deoxygenation and the tautomerization-deoxygenation routes would result in the formation of deoxygenated aromatics such as benzene while the hydrogenation-dehydration route would result in the formation of deoxygenated cyclic compounds such as cyclohexane. Table 2.1 summarized on the major aspects of the pathways of HDO. It should also be noted that complexity of mechanism increases in the order of: DDO < HYD < Tautomerization

with HYD pathway having the highest H<sub>2</sub> consumption. HYD pathway also has stronger dependence on temperature and hydrogen pressure which would significantly affect H<sub>2</sub> surface coverage on catalyst surface for phenyl ring hydrogenation (Keane & Patterson, 1999).

University of Malaya

**Table 2.1: Comparison of HDO reaction pathways**

	Direct Deoxygenation (DDO)	Hydrogenation-Dehydration (HYD)	Tautomerization-Deoxygenation
Kinetics	Scission of C <sub>AR</sub> —O bond from phenyl ring	<ul style="list-style-type: none"> <li>- Phenyl ring hydrogenation</li> <li>- Scission of C—O bond from cyclohexanol</li> </ul>	<ul style="list-style-type: none"> <li>- Keto-enol tautomerization to form keto compound over oxophilic catalyst</li> <li>- C=O hydrogenation of keto compound</li> <li>- CH<sub>2</sub>—C—OH dehydration</li> </ul>
Hydrogen consumption	Hydrogen is required only for C—O bond scission. Thus, theoretical hydrogen consumption for DDO at 100% conversion will be 1 mol of H <sub>2</sub> per 1 mol of phenolic compound.	Hydrogen is required for C—O bond scission and hydrogenation of benzene ring. Thus, theoretical hydrogen consumption for HYD at 100% conversion will be 4 mol of H <sub>2</sub> per 1 mol of phenolic compound.	Hydrogen is required only for C=O bond hydrogenation of keto intermediate. Thus, theoretical hydrogen consumption for tautomerization-deoxygenation at 100% conversion will be 1 mol of H <sub>2</sub> per 1 mol of phenolic compound.
Temperature	<ul style="list-style-type: none"> <li>- Dominant at 573 K and above (Gutierrez et al., 2009)</li> <li>- Requires higher temperature to overcome the higher bond dissociation energy of C<sub>AR</sub>—O bond.</li> </ul>	<ul style="list-style-type: none"> <li>- Dominant at 373 K to 573 K (Gutierrez et al., 2009)</li> <li>- Higher temperature results in lower H<sub>2</sub> adsorption constant and lower H<sub>2</sub> availability for benzene ring hydrogenation</li> </ul>	Dominance of tautomerization pathway at a temperature range has not been warranted. However, phenolic deoxygenation which undergoes this pathway was done at the range of 573 K (de Souza et al., 2015; Nie et al., 2014).
Pressure	- DDO pathway was observed at 1.01 bar of H <sub>2</sub> pressure and above (Ausavasukhi et al., 2012; Ausavasukhi et al., 2009)	<ul style="list-style-type: none"> <li>- HYD pathway was observed at 15 bar of H<sub>2</sub> pressure and above (Echeandia et al., 2014; Platanitis et al., 2014)</li> <li>- Higher H<sub>2</sub> pressure at a fixed temperature results in higher H<sub>2</sub> adsorption on catalyst surface and higher H<sub>2</sub> availability for saturation of benzene ring (Keane &amp; Patterson, 1999)</li> </ul>	Tautomerization pathway was observed at 1.01 bar of H <sub>2</sub> pressure and above (de Souza et al., 2014; de Souza et al., 2015)
Major product	Deoxygenated aromatics such as benzene	Deoxygenated cyclic compounds such as cyclohexane	Deoxygenated aromatics such as benzene



Various metal catalysts have been used in past studies to investigate the HDO of phenolic compounds. Sulfided metal catalysts such as Co-Mo-S, Ni-Mo-S and Ni-W-S were some of the common catalysts being studied for HDO of phenolic compounds besides being commonly used as hydrodesulfurization (HDS) catalysts (Furimsky, 2000). In sulfided Mo-based catalysts, the MoS<sub>2</sub> functions as the active site for HDO and HDS reactions while Co and Ni act as promoters by donating electrons to Mo atoms (Wang et al., 2014a). The promoting effect by Co or Ni will then weaken the Mo—S bonds and generate sulfur vacant sites which are known as coordinatively unsaturated sites (CUS) (Mortensen et al., 2011). These vacant sites of MoS<sub>2</sub> exhibit Lewis acid character and act as the adsorption sites for oxygen while the S—H species on MoS<sub>2</sub> exhibit Brønsted acid character and act as proton donor to the adsorbed oxygenate compound (He & Wang, 2012). The scission of C—O bond within the protonated adsorbed molecule will then occur, forming a deoxygenated compound.

Romero et al. (2010) studied the HDO of 2-ethylphenol over a MoS<sub>2</sub>-based catalyst and proposed the mechanisms by DDO and HYD routes. The mechanisms showed that the phenolic molecule adsorbed vertically via the C<sub>AR</sub>—OH group in DDO pathway while it adsorbed horizontally via the aromatic ring in HYD pathway. The vertical adsorption mode would lead to the direct cleavage of C<sub>AR</sub>—OH bond via hydrogenolysis to form deoxygenated aromatics while the horizontal adsorption mode would lead to the hydrogenation of aromatic ring and subsequent dehydration to form deoxygenated cyclic hydrocarbons. The effect of adsorption mode of phenolic compounds on the difference in reaction pathway and product were also confirmed by other authors (Badawi et al., 2013; Wang et al., 2014a).

Both HYD and DDO pathways are possible to occur on CUS sites but DDO pathway is more promoted by Co promoter (Badawi et al., 2013) while HYD pathway is more

promoted by Ni promoter (Şenol et al., 2007). Badawi et al. (2013) had used Mo/ $\gamma$ -Al<sub>2</sub>O<sub>3</sub> and CoMo/ $\gamma$ -Al<sub>2</sub>O<sub>3</sub> sulfided catalysts for the HDO of phenol and 2-ethylphenol at 613 K and 7 MPa. Their results showed that the DDO/HYD selectivity ratios for phenol and 2-ethylphenol respectively increased from 0.11 to 0.34 and 0.30 to 1.04 when sulfided Mo/Al<sub>2</sub>O<sub>3</sub> catalyst was added with Co promoter. Yoosuk et al. (2012) have also shown that the addition of Ni (0.1 Ni/(Mo+Ni) molar ratio) to Mo-based sulfided catalyst would cause a decrease in DDO/HYD selectivity ratio from 1.9 to 0.3. The catalytic activities of sulfided catalysts for phenol HDO were also investigated by Platanitis et al. (2014) with the order of NiMo > CoMo > NiW when supported on  $\gamma$ -Al<sub>2</sub>O<sub>3</sub> or the order of CoMo > NiMo > NiW when supported on TiO<sub>2</sub> and with sulfided NiMo/ $\gamma$ -Al<sub>2</sub>O<sub>3</sub> being the most active one for HYD pathway.

Massoth et al. (2006) also proposed the kinetic model of the HDO of phenol over sulfided CoMo/ $\gamma$ -Al<sub>2</sub>O<sub>3</sub> in packed bed reactor based on Langmuir-Hinshelwood rate equation:

$$-\frac{dC_{phenol}}{d\tau} = \frac{k_1 K_{ads} C_{phenol} + k_2 K_{ads} C_{phenol}}{(1 + C_{phenol,0} K_{ads} C_{phenol})^2} \quad (2.1)$$

where  $C_{phenol}$  is phenol concentration,  $C_{phenol,0}$  is initial phenol concentration,  $k_1$  is DDO rate constant,  $k_2$  is HYD rate constant,  $K_{ads}$  is equilibrium constant for phenol adsorption on catalyst surface,  $\tau$  is residence time. The  $K_{ads}$ ,  $k_1$  and  $k_2$  constants for phenol HDO at 300 °C and 2.85 MPa were reported to be 2 m<sup>3</sup>/mol, 7 mol/kg.h and 40 mol/kg.h respectively, indicating that CoMo/ $\gamma$ -Al<sub>2</sub>O<sub>3</sub> catalyst preferentially catalyzes HYD pathway than DDO pathway. The  $K_{ads}$ ,  $k_1$  and  $k_2$  constants were also noted to increase when phenol contains a methyl substituent. These effects were attributed more to the electronic effects of methyl groups on phenol than their geometric restrictions, as

shown in the DFT study on the molecular orbitals of methyl-substituted phenols by Massoth et al. (2006).

Catalytic hydrodeoxygenation of phenolic compounds could also be carried out over transition metal catalysts. Among the transition metal catalysts being commonly studied were Co (Badawi et al., 2013), Cu (Jin et al., 2013; Sad et al., 2011), Fe (Hensley et al., 2014a; Kim et al., 2015), Mo (Ding et al., 2015; Ruinart de Brimont et al., 2012; Yoosuk et al., 2012), Ni (Bykova et al., 2014; Cecilia et al., 2013; Chen et al., 2015a; Iino et al., 2014; Zhao et al., 2012b), Pd (de Souza et al., 2015; Hong et al., 2014b; Zhao et al., 2011), Pt (Hellinger et al., 2015; Nie et al., 2014; Zanuttini et al., 2013; Zhu et al., 2011), Rh (Hong et al., 2014b), Ru (Chen et al., 2012b) and W (Hong et al., 2014a; Platanitis et al., 2014). The transition metal catalysts used could be in monometallic or bimetallic form with or without supports such as HBeta zeolite (Ausavasukhi et al., 2012), H-ZSM-5 zeolite (Zhao et al., 2012b), H-MFI-90 zeolite (Hellinger et al., 2015), reduced graphene oxide (rGO) (Jin et al., 2013), carbon nanotubes (CNTs) (Ding et al., 2015), ordered mesoporous carbon (OMC) (Kim et al., 2015), silica (Cecilia et al., 2013; Chen et al., 2015a; Iino et al., 2014), titania (Platanitis et al., 2014), alumina (Hong et al., 2014a; Zanuttini et al., 2013), zirconia (Chen et al., 2012b; de Souza et al., 2015) and hematite ( $\text{Fe}_2\text{O}_3$ ) (Hong et al., 2014b). The use of transition metal catalysts in HDO is of great interest due to the high  $\text{H}_2$  sticking probability and potential of transition metal in activating hydrogen (Hong et al., 2014b). Nevertheless, adsorption and activation of hydrogen by transition metal catalysts are temperature dependent as shown by Gutierrez et al. (2009), Derrouiche and Bianchi (2004) in the earlier part of this section. The mechanism of hydrodeoxygenation over supported transition metal catalysts generally involves the transition metal as  $\text{H}_2$  adsorption and activation sites (Bu et al., 2012; Mortensen et al., 2011) while the O-containing compound can be activated at the metal sites or the metal-support interface

(He & Wang, 2012). The saturation of activated hydrogen at metal site will induce hydrogen spillover over the metal-support interface site to hydrogenate the O-containing compound (Hong et al., 2014b; Moberg et al., 2010). The acidic sites of supports will then dehydrate the intermediate, forming deoxygenated compound (Foster et al., 2012).

In HDO reactions, transition metal catalysts are commonly supported on acidic supports because the reaction requires both metal sites and acidic sites of support for the respective activation of H<sub>2</sub> and O-containing compound. It has been inferred that metal sites catalyze hydrogenation while acidic sites (HY zeolite, HZSM-5,  $\gamma$ -Al<sub>2</sub>O<sub>3</sub>) catalyze alkylation, isomerization, dehydration and condensation reactions (Nimmanwudipong et al., 2011b). He and Wang (2012) have arranged the acidic supports in the order of decreasing acidity:  $\gamma$ -Al<sub>2</sub>O<sub>3</sub> >> TiO<sub>2</sub> > ZrO<sub>2</sub> > CeO<sub>2</sub>. An acidic support with higher acid site density will have a stronger catalytic effect on dehydration reaction. However, one must also consider the Lewis acid site density and the Brønsted acid site density as both have different functions. The Lewis acid site binds species to catalytic surface while the Brønsted acid site protonates the intermediate (Bykova et al., 2014). Zhao et al. (2012a) have studied the effect of acidic supports (HZSM-5,  $\gamma$ -Al<sub>2</sub>O<sub>3</sub>) on phenol HDO over supported Ni at 493 K and 5 MPa H<sub>2</sub>. Both Ni/HZSM-5 and Ni/ $\gamma$ -Al<sub>2</sub>O<sub>3</sub>-HZSM-5 samples favored the formation of cyclohexane through hydrogenation and dehydration reactions (Figure 2.4). However, the introduction of  $\gamma$ -Al<sub>2</sub>O<sub>3</sub> into HZSM-5 support had reduced the turnover frequency (TOF) of cyclohexanone and cyclohexene hydrogenation by almost half due to the decrease in Brønsted acid site density though Ni/ $\gamma$ -Al<sub>2</sub>O<sub>3</sub>-HZSM-5 achieved a higher catalytic activity due to higher Ni dispersion.

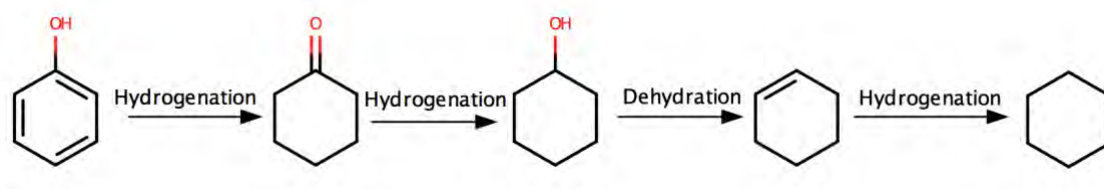


**Figure 2.4: HDO of phenol over Ni/HZSM-5 and Ni/ $\gamma$ -Al<sub>2</sub>O<sub>3</sub>-HZSM-5 catalysts (Zhao et al., 2012b)**

In discussing the effect of support on HDO reaction over transition metal catalyst, the oxophilicity of support is also worth mentioning. Oxophilicity is the tendency of a compound to form oxides by oxygen abstraction or hydrolysis. It was noted that transition metal catalyst supported on oxophilic supports such as ZrO<sub>2</sub> or TiO<sub>2</sub> exhibited higher selectivity towards aromatic products during HDO. The oxophilicity of support is fundamental for the tautomerization of phenolic compounds into a keto-enol mixture whereby the keto intermediates will be hydrogenated and dehydrated into an aromatic product (de Souza et al., 2015). The aforementioned result was consistent with the findings of Nie and Resasco (2014) in which the HDO of *m*-cresol was capable of forming toluene over Pt/ZrO<sub>2</sub> and Pt/TiO<sub>2</sub> which contain oxophilic supports. The oxophilicity of supports are very much dependent on the oxophilicity of metal elements which could be compared based on the normalized oxophilicity scale in Table 2.2 by Kepp (2016). An element that has higher normalized oxophilicity value will have stronger oxygen attraction than other element. Based on Table 2.2, it can be noted that supports such as C, TiO<sub>2</sub> and ZrO<sub>2</sub> are highly oxophilic supports with the oxophilicity order of: C > TiO<sub>2</sub> > ZrO<sub>2</sub> while metal catalyst such as V, W, Co, Fe, Ru and Sn were also noted to be oxophilic metals that are capable of facile oxygen abstraction.

**Table 2.2: Normalized oxophilicity scale of several elements (Kepp, 2016)**

Element	Normalized Oxophilicity, $\theta$	Element	Normalized Oxophilicity, $\theta$
C	1.4	Rh	0.3
Ti	1.0	Ag	0.2
V	0.8	Cu	0.2
W	0.8	Ni	0.2
Zr	0.8	Zn	0.2
Co	0.4	Pt	0.1
Fe	0.4	Au	0.0
Ru	0.4	Pd	0.0
Sn	0.4		

The *m*-cresol was also one of the main model compounds being studied for the HDO of phenolic compounds. HDO of *m*-cresol also occurs through DDO and HYD pathways to give toluene and methylcyclohexane as respective major products. Odebunmi and Ollis (1983b) have studied on HDO of *m*-cresol over sulfided CoMo catalyst with reactant feed containing *m*-cresol and *n*-heptyl mercaptan in hexadecane solvent. The liquid reactant feed was added with about 0.2 mol% of *n*-heptyl mercaptan to ensure sulfided CoMo catalyst remains in its sulfided form. The reaction was done in packed bed trickle reactor and a Langmuir-Hinshelwood kinetic model was developed:

$$F_c \frac{dX_c}{dW} = \frac{k_{HDO} K_H K_C C_C P_H}{(1 + K_C C_C + K_w C_w + K_S C_S)} \quad (2.2)$$

where  $F_c$  is *m*-cresol flow rate,  $dX_c/dW$  is change of *m*-cresol conversion with respect to catalyst weight,  $k_{HDO}$  is HDO rate constant,  $P_H$  is partial pressure of hydrogen;  $K_H$ ,  $K_C$ ,  $K_w$  and  $K_S$  are the respective adsorption constants of hydrogen, *m*-cresol, water and mercaptan;  $C_c$ ,  $C_w$  and  $C_s$  are the respective concentrations of *m*-cresol, water and mercaptan. By assuming negligible water inhibition ( $K_w C_w$  is negligible) and constant  $K_H P_H$ , Equation 2.3 can be expressed in the following form (Odebunmi & Ollis, 1983b):

$$\frac{W}{F_c} = - \left[ \frac{1 + K_C C_{co}}{k_{HDO} K_C C_{co}} \right] \ln(1 - X_c) \quad (2.3)$$

where  $F_{co}$  is initial *m*-cresol flow rate,  $W$  is catalyst weight,  $X_c$  is conversion of *m*-cresol,  $C_{co}$  is initial *m*-cresol concentration. The  $k_{HDO}$  and  $K_c$  values were reported to be  $4.5 \times 10^{-3}$  L/g<sub>cat</sub>.h and 8.43 L/mol respectively at 375 °C and 69 atm H<sub>2</sub> pressure. With the increase in temperature,  $k_{HDO}$  increases which indicates a higher *m*-cresol HDO rate while  $K_c$  decreases which indicates a lower surface coverage of *m*-cresol (Odebunmi & Ollis, 1983b).

Odebunmi and Ollis (1983a) have also investigated on the effect of substituent position of cresols on their relative reactivity and proposed the following HDO reactivity order: *m*-cresol > *p*-cresol > *o*-cresol. The higher deoxygenation reactivity of *meta*-substituted cresol as compared with *para*-substituted cresol can be attributed to the greater electron donating inductive effect by methyl group which is nearer to —OH group at *meta* position. Nevertheless, if the substituent is an electron withdrawing group, an opposite inductive effect would be predicted, causing a reversed relative reactivity of the *meta*- and *para*-substituted O-containing aromatics. Likewise, *ortho*-substituent has the strongest inductive effect among the other substitutions due to its closest proximity with the —OH group. In addition, *ortho*-substitution has also been commonly reported to cause steric effect besides inductive effect (Furimsky, 2000; Odebunmi & Ollis, 1983a; Santiago et al., 2016).

The quantitative analysis of substituent effect on HDO reaction could also be done using linear free energy relationships (LFERs). Among the prototypical examples are Hammett equation (Equation 2.4) (Hammett, 1937) and Taft equation (Equation 2.5) (Taft, 1952a; Taft, 1952b) which relate reaction rate with substituent type. Taft equation is more refined in a sense as it accounts for steric effect by *ortho*-substitution and polar effect of substituent while Hammett equation only accounts for polar effect of substituent which comprises of inductive, resonance and field effects (Hammett, 1937).

$$\log \frac{k}{k_o} = \sigma \rho \quad (2.4)$$

$$\log \frac{k}{k_o} = E_s + E_\sigma \rho \quad (2.5)$$

where  $k$  is reaction rate of substituted reactant,  $k_o$  is reaction rate of non-substituted reactant,  $\rho$  is reaction constant,  $\sigma$  is polar substituent parameter for Hammett equation (Equation 2.4),  $E_s$  and  $E_\sigma$  are steric and polar substituent parameters for Taft equation (Equation 2.5) respectively. The substituent parameters are unique to each substituent and its position. By comparing the values of  $\sigma$ ,  $E_s$  and  $E_\sigma$  for different substituents, the reactivity of different substituted reactants for the same reaction can then be compared quantitatively.

LFERs involving substituents such as —OH, —OCH<sub>3</sub>, —CH<sub>3</sub> and —H are indeed of great interest to the kinetic and reactivity studies for HDO of phenol, guaiacols and cresols. However, values of  $\sigma$ ,  $E_s$  and  $E_\sigma$  for various kind of substituent groups such as —OH, —OCH<sub>3</sub>, —CH<sub>3</sub>, —H, etc. as reported by Hammett (1937) and Taft (1952a; 1952b) were based on the hydrolysis and esterification of benzoate esters and may not be necessarily equivalent for phenolics HDO due to the different extent of steric effect on different reactions. Thus, LFERs study on phenolics for HDO process still remain as an unexplored area of research which might be insightful to the further understanding of the kinetics of phenolics HDO of various kind of substituents.

Figure 2.5 shows the possible reaction networks for the hydrodeoxygenation of phenol, guaiacol and anisole. A direct scission of C—O bond (DDO pathway) at hydroxyl and methoxy groups in guaiacol during HDO will respectively yield phenol and anisole. Thus, the HDO of guaiacol would require the direct scissions of both C—O bonds at hydroxyl and methoxy group in order to obtain benzene as the final deoxygenated aromatic product. The HDO of guaiacol may also proceed through HYD



pathway to produce deoxygenated cyclic compounds such as methylcyclohexane, cyclohexane or methylcyclopentane. Transalkylation can occur as side reaction whereby the alkyl group in methoxy group of guaiacol is transferred to another guaiacol to form products such as methylcatechol, 1,2-dimethoxybenzene or methylguaiacol.

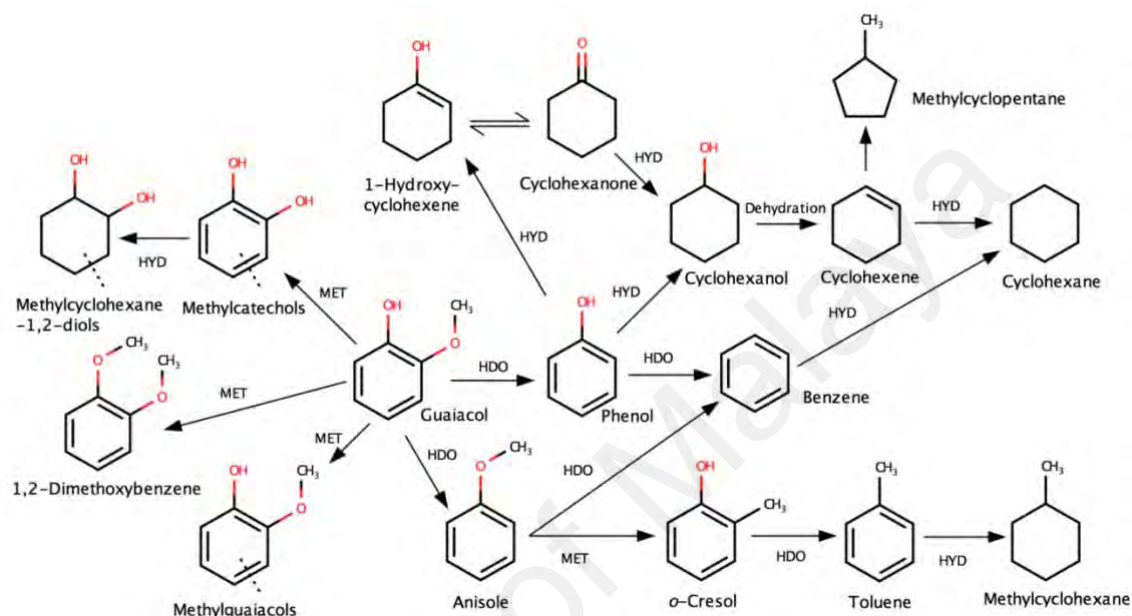


**Figure 2.5: Reaction pathways of HDO of guaiacol, phenol and anisole (Bykova et al., 2014)**

The type of catalyst is also one of the major factors in affecting the reaction mechanisms of phenolics deoxygenation. Transition metals such as Pt, Ni and Pd were known to have high H<sub>2</sub> sticking coefficient and induce hydrogen spillover effect (Hong et al., 2014b). For instance, Hensley et al. (2014a) have noted that Pd surface interacts more strongly with aromatic rings than with C—O and C=O bonds, causing the preferential hydrogenation of aromatic rings by palladium. With the use of such metal catalysts, hydrogenation of aromatic ring was often observed during phenolic deoxygenation, causing the formation of deoxygenated cyclic compounds to be favored. These observations were also in agreement with several phenolic deoxygenation studies done using transition metal catalysts (Echeandia et al., 2014; Nie & Resasco, 2014;

Shafaghat et al., 2016; Zhao et al., 2012a; Zhao et al., 2011). Likewise, several transition metals such as Fe, Ti, V and W are oxophilic in nature and showed higher affinity for C=O and C—O bonds. These properties would result in the oxophilic metal to preferentially activate C=O and C—O bonds through hydrogenation or hydrogenolysis instead of aromatic rings. Thus, deoxygenation catalysts with high oxophilicity were often noted to tautomerize the phenolics into deoxygenation aromatics through the formation of cyclohexanone intermediate without the saturation of aromatic rings (de Souza et al., 2015; Hensley et al., 2015; Nelson et al., 2015; Nie et al., 2014).

Acidic zeolites such as HBeta (Ausavasukhi et al., 2012), H-ZSM-5 (Zhao et al., 2012b), H-MFI-90 (Hellinger et al., 2015), HY (To & Resasco, 2015) and Al-MCM-41 (Tran et al., 2016) were known to deoxygenate phenolics through hydrodeoxygenation and transalkylation. Transalkylation of phenolics such as cresols is necessary for the removal of methyl group and oxygen to form benzene. The ability of transalkylation by zeolite is often attributed to its acidic sites (Tran et al., 2016). In addition, the difference in pore sizes of H-ZSM-5 and HBEA zeolites was also noted to produce significant steric effects in affecting the alkylation of phenol during deoxygenation (Zhao et al., 2012a).

Metal catalysts of sulfide, carbide, oxide, nitride and phosphide forms were also used in phenolic deoxygenation studies. Sulfided metal catalysts were some of the well-known deoxygenation catalysts for phenolics as discussed in the earlier part of this section. The presence of sulfur vacant sites within such catalysts often resulted in facile hydride transfer and oxygenates adsorption for an effective deoxygenation. Metal carbides were often noted to have the highest deoxygenation activity than the other forms, owing to their high oxophilicity which enabled them to directly cleave C—O and

C=O bonds (Sullivan et al., 2016). In addition, metal carbides were also found to undergo surface oxidation by water during reaction to form metal oxides which has a lower activity (Mortensen et al., 2015). The study on molybdenum carbide, nitride, phosphide and oxide catalysts for phenol HDO by Boullosa-Eiras et al. (2014) was one of the comprehensive studies which reported the effects of metal catalyst forms on the reaction itself. The catalysts of nitride and phosphide forms were noted to have slightly lower deoxygenation activity than the oxide forms. In addition, the phosphide catalyst was also reported to have higher hydrogenation and isomerization activities which resulted in the conversion of phenol to methylcyclopentane instead. Table 2.3 summarized on the major deoxygenated products formed from phenolic compounds which are commonly found in bio-oil samples. The information on the reaction pathway observed and the metal based catalysts used for the phenolic deoxygenation will be necessary for the appropriate catalyst selection in bio-oil upgrading and the effective valorization of desired deoxygenated aromatics.

**Table 2.3: Deoxygenation process for phenolic compounds commonly found in bio-oil**

Phenolics	Deoxygenated products	Metal-based catalysts	Reaction pathway	Ref.
Phenol	Benzene, cyclohexane	Co, Fe, Mo, Ni, W	Hydrodeoxygenation	(Badawi et al., 2013; Boullosa-Eiras et al., 2014; Mortensen et al., 2015; Shafaghat et al., 2016; Yang et al., 2009; Yoosuk et al., 2012; Zhao et al., 2012b)
2-Ethylphenol	2-Ethylcyclohexane, 2-ethylbenzene	Sulfided Mo with or without Co promoter	Hydrodeoxygenation	(Badawi et al., 2013; Romero et al., 2010)
4-Propylphenol	Propylbenzene	Pt with Au, Bi, Fe, Ga, In, Ir, Mo, Pd, Re, Sn or W as bimetallic catalysts	Hydrodeoxygenation	(Ohta et al., 2014)
Cresol	Benzene, toluene, xylene, cyclohexane	Co, Fe, Ga, Mo, Ni, Pt, Pd, Rh	Hydrodeoxygenation	(Ausavasukhi et al., 2012; Chen et al., 2015a; Hong et al., 2014b; Nie et al., 2014; Shafaghat et al., 2016; Wang et al., 2014a; Zanuttini et al., 2013)
Guaiacol	Benzene, toluene, xylene, cyclohexane	Co, Fe, Ni, Pd, Pt, Re	Hydrodeoxygenation	(Bykova et al., 2012; Hellinger et al., 2015; Hong et al., 2014a; Leiva et al., 2015a; Olcese et al., 2012; Shafaghat et al., 2016; Tran et al., 2016)

### 2.2.2 Furans

Furans are heterocyclic organic compounds which contain five-membered aromatic ring with four carbon atoms and at least one oxygen atom. Furanic compounds are some of the oxygenated compounds commonly found in bio-oil as the dehydration products of cellulose and hemicellulose fragments (Resasco & Crossley, 2015). Figure 2.6 shows some of the furanic compounds commonly found in bio-oil which are furan, tetrahydrofuran (THF), furanone, maleic anhydride, furfural, furfuryl alcohol, 5-hydroxymethylfurfural (HMF), benzofuran and dibenzofuran. For the deoxygenation of furfural, there are two main reaction pathways (He & Wang, 2012):

- 1) Decarbonylation of C=O bond to form furan and a subsequent hydrogenation to form tetrahydrofuran or ring opening reaction to form butane, butanol and butanone.
- 2) Hydrogenation of C=O bond to form furfuryl alcohol and a subsequent dehydroxylation to form 2-methylfuran.

Based on past studies, the deoxygenation pathway of furfural is dependent on the type of metal catalyst used. Sitthisa et al. (2011b) have investigated the furfural deoxygenation on Pd and PdCu catalysts in a tubular flow reactor at 230 °C and 1 atm. When Pd catalyst was used, furan and tetrahydrofuran were the major products, indicating decarbonylation as the major reaction pathway. When PdCu catalyst was used, 2-methylfuran was the major product instead, indicating hydrogenation pathway as the major reaction pathway. Sitthisa et al. (2011b) proposed that different type of metal catalyst would exhibit different electronic structures which would change the adsorption mode of the furfural on catalyst surface (Figure 2.7). With Pd catalyst, the  $\eta^1$ -(acyl) adsorption mode was stable enough to form an acyl intermediate which could readily be decarbonylated into furan. However, with PdCu catalyst, the addition of Cu

to form Pd-Cu alloy resulted in an electronic perturbation which reduced electron back-donating effect to the  $\pi$  delocalized system of furan ring in furfural (Sitthisa et al., 2011b). This would cause the  $\eta$ 1-(acyl) and  $\eta$ 2-(CO-aldehyde) adsorption modes to be unfavorable but  $\eta$ 1 (O-aldehyde) adsorption mode to be preferred for hydrogenation

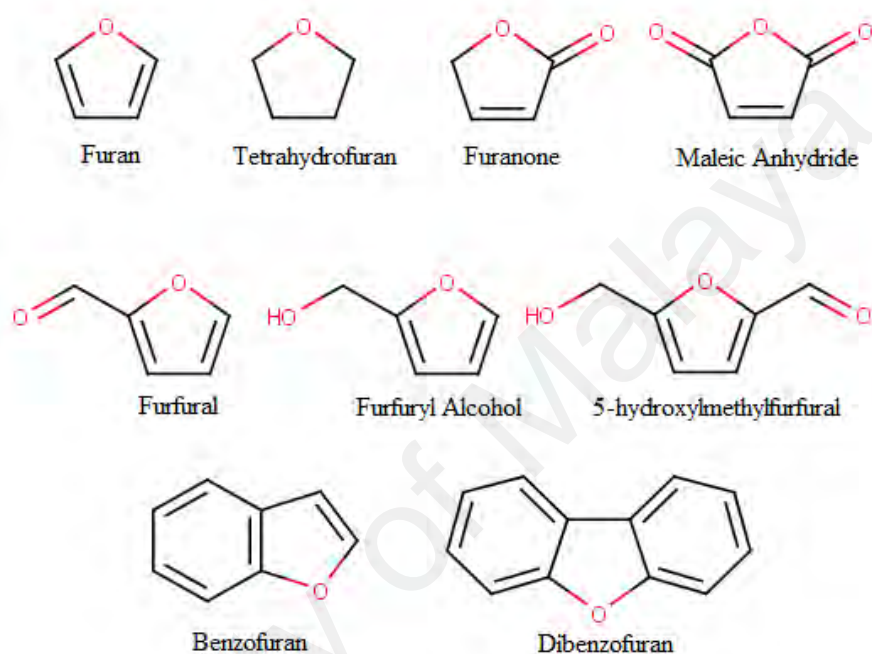


**Figure 2.6: Molecular structures of furanic model compounds**

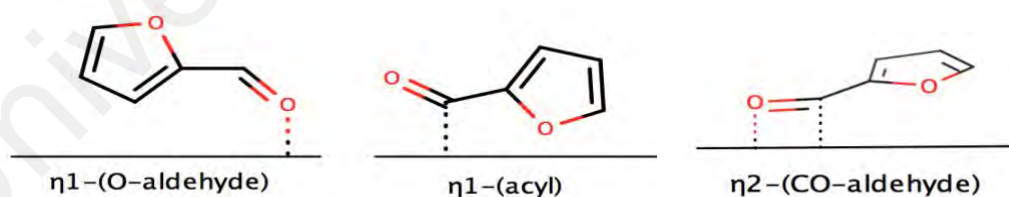


**Figure 2.7: Adsorption modes of furfural on metal surfaces (Sitthisa et al., 2011b)**

These results were in agreement with another furfural deoxygenation study by Sitthisa and Resasco (2011) where three separate Cu/SiO<sub>2</sub>, Pd/SiO<sub>2</sub> and Ni/SiO<sub>2</sub> catalysts were used instead. Sitthisa et al. (2011a) have also noted that the addition of Fe in Ni catalyst produces a combination of suppressing and promoting effects on its

catalytic activity. The deoxygenation of furfural on all four metal-based catalysts yielded different distribution of products (Sitthisa et al., 2011a; Sitthisa & Resasco, 2011):

- 1) For Cu-based catalyst, C=O bond hydrogenation was the main reaction pathway to form furfuryl alcohol and then dehydroxylation to 2-methylfuran. This was due to the preferred  $\eta^1$  (O-aldehyde) adsorption mode.
- 2) For Pd-based catalyst, decarbonylation was dominant due to the preferred  $\eta^1$ - (acyl) adsorption mode, leading to formation of furan. The strong Pd interaction with furan ring also led to the ring hydrogenation to produce tetrahydrofuran.
- 3) For Ni-based catalyst, it had the same preference as Pd-based catalyst to produce furan intermediate. However, the metal interaction with furan ring was even stronger in Ni than in Pd, causing the ring opening of furan to form butane, butanol and butanone.
- 4) For Fe-based catalyst, decarbonylation activity was suppressed while C=O bond hydrogenation and C—O bond hydrogenolysis were respectively promoted at low and high temperatures. The addition of Fe in Ni catalyst also showed some promoter effects. Fe is an oxophilic metal which has higher affinity for C=O and C—O bonds, thus resulting in the facile activation of these bonds for deoxygenation through hydrogenolysis or hydrogenation (Sitthisa et al., 2011a). The presence of Fe<sub>2</sub>O<sub>3</sub> due to Fe addition also generates acid sites which favor hydrogenolysis (Hensley et al., 2014a; Nie et al., 2014).

Sitthisa et al. (2011c) have also derived the kinetics of vapor phase furfural deoxygenation over Cu/SiO<sub>2</sub> catalyst in an isothermal tubular reactor based on Langmuir-Hinshelwood model, with the following assumptions:

- Molecular adsorption of furfural (FAL), furfuryl alcohol (FOL) and 2-methylfuran (2-MF)
- Dissociative hydrogen adsorption
- Adsorption sites are equivalent and independent of coverage
- Surface reaction is rate limiting step

$$r_{FAL} = -k_1 K_{FAL} P_{FAL} \theta_v + \frac{k_1}{K} K_{FOL} P_{FOL} \theta_v \quad (2.6)$$

$$r_{FOL} = k_1 K_{FAL} P_{FAL} - \left[ \frac{k_1}{K} K_{FOL} P_{FOL} \theta_v + k_2 K_{FOL} P_{FOL} \theta_v \right] \quad (2.7)$$

$$r_{2-MF} = k_2 K_{FOL} P_{FOL} \theta_v \quad (2.8)$$

$$\theta_v = \frac{1}{1 + K_{FAL} P_{FAL} + K_{FOL} P_{FOL} + K_{2-MF} P_{2-MF} + \sqrt{K_{H_2} P_{H_2}}} \quad (2.9)$$

where  $r_{FAL}$ ,  $r_{FOL}$  and  $r_{2-MF}$  are the respective formation rates of furfural, furfuryl alcohol and 2-methylfuran;  $K$  is equilibrium constant;  $K_i$  is adsorption constant of reactant  $i$ ;  $P_i$  is partial pressure of reactant  $i$ ;  $k_1$  is rate constant of furfural hydrogenation into furfuryl alcohol and  $k_2$  is rate constant of furfuryl alcohol dehydroxylation into 2-methylfuran (Sitthisa et al., 2011c). The values of equilibrium, rate and adsorption constants as reported by Sitthisa et al. (2011c) were shown in Table 2.4. Furfuryl alcohol dehydroxylation into 2-methylfuran was noted to be the rate determining step owing to the significantly smaller  $k_2$  value than  $k_1$  value (Sitthisa et al., 2011c). The high surface coverage of furfural on Cu/SiO<sub>2</sub> was also noted by its highest adsorption constant as compared with other intermediates, which is necessary for its effective deoxygenation. Likewise, the increase in rate constants and the decrease in adsorption constants with the increase of temperature were also indications of higher collision rate among reactant molecules at higher temperature.

The deoxygenation of furfuryl alcohol also had similar reaction pathways as furfural deoxygenation in which furfuryl alcohol could undergo dehydroxylation or hydrogenolysis to form 2-methylfuran in the presence of metal catalysts (He & Wang, 2012). As noted previously, metal catalyst such as Fe which contains acid sites will also result in the enhanced hydrogenolysis of furfuryl alcohol to 2-methylfuran. In addition, it was also reported that furfuryl alcohol was capable of producing levulinic acid in the presence of strong acids (Nakagawa et al., 2013; Resasco & Crossley, 2015). The production of levulinic acid from furfuryl alcohol involved a series of acid-catalyzed hydration and dehydration steps and a ring opening step.

**Table 2.4: Values of equilibrium, rate and adsorption constants for furfural deoxygenation to 2-methylfuran. Data obtained from (Sitthisa et al., 2011c)**

T (°C)	Equilibrium constant	Rate constant (mmol/g <sub>cat</sub> .h)		Adsorption constant (Torr <sup>-1</sup> )			
	<i>K</i>	<i>k</i> <sub>1</sub>	<i>k</i> <sub>2</sub>	<i>K</i> <sub>FAL</sub>	<i>K</i> <sub>FOL</sub>	<i>K</i> <sub>2-MF</sub>	<i>K</i> <sub>H<sub>2</sub></sub>
230	4.56	3.00	0.10	0.29	0.18	0.083	11.9 x 10 <sup>-5</sup>
270	2.98	5.93	0.24	0.12	0.11	0.063	4.2 x 10 <sup>-5</sup>
290	2.01	8.05	0.34	0.08	0.09	0.056	2.7 x 10 <sup>-5</sup>

Cheng and Huber (2011) have also studied the conversion of furans over zeolites. Several reactions were identified in this study: Diels-Alder condensation to form benzofuran; decarbonylation to form allene and oligomerization to form olefins and aromatics (Cheng & Huber, 2011). The deoxygenation of tetrahydrofuran (THF) over sulfided and reduced MoO<sub>3</sub>-CoO<sub>3</sub>/Al<sub>2</sub>O<sub>3</sub> catalysts were also studied by Furimsky (Furimsky, 1983). The study showed that butenes were the major products over sulfided catalyst while propylene and butadiene were the major products over reduced catalysts. In both cases, tetrahydrofuran vertically adsorbed onto the catalytic site, with the formation of temporary metal-oxygen bond. In addition, the ring opening of



tetrahydrofuran was also one of the key steps to produce paraffinic intermediates over both catalysts (Furimsky, 1983). For the reduced catalyst, intramolecular migration of H atom in THF was observed to be the pre-requisite step for the ring opening of THF. For sulfided catalyst, adsorption of external H<sub>2</sub> on sulfur site would instead be the pre-requisite step for the ring opening of THF.

Iino et al. (2014) have investigated on the deoxygenation of 2-methyltetrahydrofuran over a Ni<sub>2</sub>P/SiO<sub>2</sub> catalyst in a continuous-flow quartz reactor at 150—350 °C and 0.5 MPa. It was shown that *n*-pentane was the major product with a 99.8 mol% conversion of 2-methyltetrahydrofuran and an 85 mol% selectivity of pentane over Ni<sub>2</sub>P/SiO<sub>2</sub> catalyst at 350 °C. Based on Figure 2.8, the deoxygenation of 2-methyltetrahydrofuran was proposed to have proceeded through a ring opening step, hydrogenation-dehydration of C=O bond and hydrogenation of C=C bond to form *n*-pentane (Iino et al., 2014). The kinetics of vapor phase 2-methyltetrahydrofuran deoxygenation over Ni<sub>2</sub>P/SiO<sub>2</sub> catalyst was also derived based on Langmuir-Hinshelwood model with the following assumptions (Iino et al., 2014):

- Negligible adsorption of products on catalyst surface
- Surface reaction is rate limiting step
- All elementary reaction steps are irreversible

$$r = \frac{kK_{MTHF}P_{MTHF}\sqrt{K_{H_2}P_{H_2}}}{(1 + \sqrt{K_{H_2}P_{H_2}} + K_{MTHF}P_{MTHF})^2} \quad (2.10)$$

where  $r$  is formation rate of *n*-pentane,  $k$  is rate constant,  $K_i$  is adsorption constant of reactant  $i$ ,  $P_i$  is partial pressure of reactant  $i$  and  $MTHF$  is 2-methyltetrahydrofuran. The values of  $k$ ,  $K_{H_2}$  and  $K_{MTHF}$  at conditions of 300 °C and 0.5 MPa were reported to be 2.5 s<sup>-1</sup>, 10<sup>4</sup> kPa<sup>-1</sup> and 31 kPa<sup>-1</sup> respectively (Iino et al., 2014). The larger  $K_{H_2}$  value would

indicate a higher hydrogen surface coverage and adsorption on catalyst surface which resulted in a lower surface coverage of 2-methyltetrahydrofuran. Likewise, the higher hydrogen binding constant,  $K_{H_2}P_{H_2}$ , was reported to result in lower conversion of 2-methyltetrahydrofuran but an increase in selectivity of *n*-pentane (Iino et al., 2014).

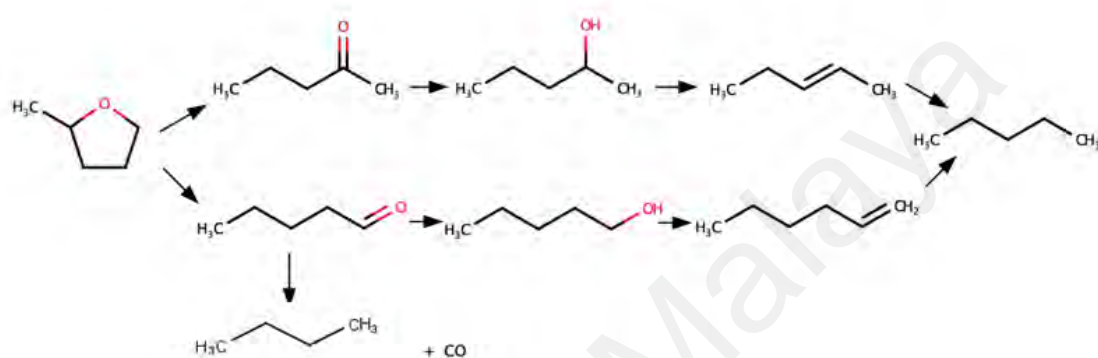


**Figure 2.8: Reaction pathway of 2-methyltetrahydrofuran deoxygenation (Iino et al., 2014)**

The deoxygenation of benzofuran in the presence of  $H_2$  over Pt/C (Dickinson et al., 2012), CoMo/ $Al_2O_3$  (Lee & Ollis, 1984), NiMo/ $Al_2O_3$  (Bunch & Ozkan, 2002; Edelman et al., 1988), NiMoP/ $Al_2O_3$  (Romero et al., 2009) and Ni<sub>2</sub>P-N/MCM-41 (Song et al., 2015) catalysts were also investigated. Past studies had shown the formation of ethylphenol and ethylbenzene as some of the major products obtained during deoxygenation of benzofuran. Benzofuran was proposed to undergo furanic ring hydrogenation to first form dihydrobenzofuran which then undergoes furanic ring opening to form 2-ethylphenol as the major intermediate. Further deoxygenation steps would then occur in 2-ethylphenol to form various products such as ethylbenzene, toluene, benzene, ethylcyclohexane and heptane. This reaction network was also proposed by many studies (Bunch & Ozkan, 2002; Dickinson et al., 2012; Romero et al., 2009; Song et al., 2015), indicating there is a good corroboration among the results.

In addition, further study on the scission of C—O bond during benzofuran HDO was also done (Bunch & Ozkan, 2002; Romero et al., 2009). Bunch and Ozkan (2002) concluded that benzofuran HDO contained multiple steps of hydrogenation and hydrogenolysis which occurred through  $\beta$  hydrogen elimination ( $E_2$  elimination) or nucleophilic substitution ( $S_N2$ ). During the transformation of 2,3-dihydrobenzofuran to 2-ethylphenol, the  $C(sp^3)$ —O bond cleavage occurs at the furan ring through the nucleophilic substitution of  $SH^-$ , leading to the eventual opening of furan ring (Figure 2.9). The 2-ethylphenol intermediate which is a phenolic compound will then undergo HDO through either DDO or HYD pathway for the elimination of hydroxyl group (—OH), having ethylbenzene or ethylcyclohexane as the respective major product. This form of transformation was reported when using a sulfided catalyst (Romero et al., 2009).

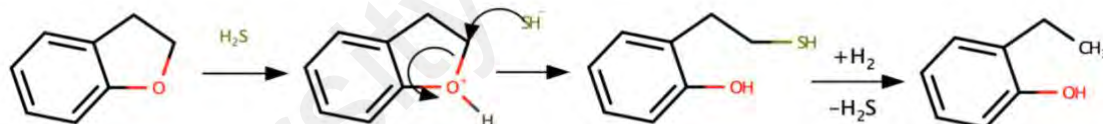


**Figure 2.9: Mechanism of  $C(sp^3)$ —O bond cleavage in benzofuran HDO starting from 2,3-dihydrobenzofuran (Romero et al., 2009)**

The kinetic models of benzofuran HDO were also proposed based on Langmuir-Hinshelwood model (Furimsky, 2000). Lee and Ollis (1984) obtained the first-order model equation (Equation 2.11) for benzofuran HDO over a sulfided CoMo/Al<sub>2</sub>O<sub>3</sub> catalyst at 6.9 MPa and below 623 K with the assumption of competitive reactant adsorption, independent H<sub>2</sub> adsorption site and constant H<sub>2</sub> pressure. Likewise, Edelman et al. (1988) also proposed another kinetic model (Equation 2.12) for benzofuran HDO with similar assumptions and also negligible water concentration when HYD pathway

predominates. The model proposed by Edelman et al. (1988) does not follow the first order kinetics. With the increase of  $k_{HDO}$ ,  $P_{ox}$  decreases which indicates the presence of self-inhibiting effect of the oxygenated compounds.

$$-\ln(1 - X_{HDO}) = kC_R^0 \left(\frac{W}{F}\right) \quad (2.11)$$

$$-\ln\left(\frac{P_{ox}}{P_{R,o}}\right) = k_{HDO} \left(\frac{W}{F}\right) \quad (2.12)$$

where  $X_{HDO}$  is conversion of benzofuran,  $k$  and  $k_{HDO}$  are rate constants,  $w$  is catalyst weight,  $F$  is flow rate of reactants,  $C_R^0$  is initial reactant concentration,  $P_{R,o}$  is initial partial pressure of reactants,  $P_{ox}$  is partial pressure of oxygenate intermediates.

The HDO of dibenzofuran over supported NiCu (Ambursa et al., 2016), Ni<sub>2</sub>P/SiO<sub>2</sub> (Cecilia et al., 2013), Pd/COK-12 (Wang et al., 2013) and supported Pt catalysts (Wang et al., 2015b) were also studied. COK-12 is an ordered mesoporous silica support and its synthesis procedure was reported by Jammaer et al. (2009; 2011) and Martens et al. (2011). The HDO of dibenzofuran consists of multiple steps of hydrogenation of benzene ring before the opening of furan ring and scission of C—O bond. The HDO of dibenzofuran mainly yields bicyclohexane as main product (Ambursa et al., 2016; Cecilia et al., 2013; Wang et al., 2015b). The HDO of dibenzofuran is more difficult than that of benzofuran and furan due to the high bond energy C<sub>AR</sub>—C<sub>AR</sub> bond between two benzene rings. Furthermore, the established order of resonance energy: dibenzofuran > benzofuran > furan, indicates dibenzofuran being the most stable and unlikely to be deoxygenated as compared with benzofuran and furan (Furimsky, 2000).

The deoxygenation processes of maleic anhydride over several metal catalysts such as Pd-Sn/SiO<sub>2</sub> (Jung et al., 2003), Cu/ZnO/TiO<sub>2</sub> (Hu et al., 2007; Zhang et al., 2008), Pd/Al<sub>2</sub>O<sub>3</sub> (Pillai et al., 2003) and Cu-Zn-Zr (Zhang et al., 2009) were also studied.

Despite of the variations in the reaction conditions and the type of metal catalysts used, the maleic anhydride deoxygenation mainly involves the hydrogenolysis of C=O bond of the oxo group of furan ring to produce tetrahydrofuran and the ring opening step to produce aliphatic alcohols (Jeong et al., 2006). The products obtained from the maleic anhydride deoxygenation such as tetrahydrofuran, 1,4-butanediol, *n*-propanol and *n*-butanol may have to be further deoxygenated in an additional deoxygenation process in order to obtain deoxygenated products.

Catalyst variation also has major effects in affecting the reaction mechanisms of furanic deoxygenation. Furanic deoxygenation mechanisms are dependent on furan adsorption modes. The effect of metal catalyst on the furanic adsorption modes were reported by Sitthisa et al. (2011) as reviewed in the earlier part of this section. Transition metals such as Pt, Ni and Pd which tend to saturate aromatic rings also have strong interaction with furanic rings, leading to preferential hydrogenation of furanic rings. The greater electron delocalization effect of benzene would cause itself to have greater aromaticity and stability than furan. Thus, it can be inferred that hydrogenation and C—C cleavage of furanic ring would generally be easier as compared with benzene ring. Copper which catalyzed the hydrogenation of maleic anhydride into  $\gamma$ -butyrolactone and tetrahydrofuran also experienced an increase in hydrogenation activity in the presence of ZnO, ZrO<sub>2</sub> and TiO<sub>2</sub>. The synergistic effect was attributed to the formation of metallic copper (Cu<sup>0</sup>) in the presence of ZnO, ZrO<sub>2</sub> and TiO<sub>2</sub> which would result in the increased metallic behavior of Cu for hydrogenation (Hu et al., 2007; Zhang et al., 2009). Likewise, a direct scission of C=O bond in furanic ring is generally not easily accomplished and often requires a ring opening step. Ring opening steps in furans are usually made feasible by metals which have high C—C hydrogenolysis activity such as Ni (Chen et al., 2015a; Tran et al., 2016) and Ru (Maris & Davis, 2007). Hence, with the use of a good C—C cleavage metal catalyst,

deoxygenated aliphatic hydrocarbons were often the major products of furanic ring deoxygenation.

The use of solid basic catalysts such as MgO/NaY (Huang et al., 2012), MgO/USY (Puértolas et al., 2016) and MgO-ZrO<sub>2</sub> (Shen et al., 2011) were also reported to catalyze the aldol condensation of furanic compounds such as furfural. Unlike ring opening reactions, aldol condensation is a C—C coupling step in furanic deoxygenation which increases the carbon chain length of the deoxygenated hydrocarbons (Serrano-Ruiz et al., 2012). Catalysts such as Pt/C (Dickinson et al., 2012), Mo<sub>2</sub>C (Dhandapani et al., 1998), Ni<sub>2</sub>P (Cecilia et al., 2013) and sulfided NiMoP/Al<sub>2</sub>O<sub>3</sub> (Romero et al., 2009) were also studied for benzofuran deoxygenation. These catalysts were reported to catalyze the mechanism of C(*sp*<sup>3</sup>)—O bond cleavage of benzofuran (Figure 2.9) to form 2-ethylphenol which can be further deoxygenated into 2-ethylbenzene. Table 2.5 gives an overview of the major deoxygenated products formed from furanic compounds which are commonly found in bio-oil samples. The information on the reaction pathway observed and the metal based catalysts used for furanic deoxygenation will be necessary for the appropriate catalyst selection in bio-oil upgrading and the effective valorization of desired deoxygenated products.

**Table 2.5: Deoxygenation process for furanic compounds commonly found in bio-oil**

Furans	Deoxygenated products	Metal-based catalysts	Reaction pathway	Ref.
Benzofuran	Ethylbenzene, Ethylcyclohexane	Pt, Ni-Mo, Ni <sub>2</sub> P	Hydrodeoxygenation	(Bunch & Ozkan, 2002; Dickinson et al., 2012; Romero et al., 2009; Song et al., 2015)
MTHF	Pentane, butane	Ni <sub>2</sub> P	Hydrogenation-dehydration, decarbonylation	(Iino et al., 2014)
Dibenzofuran	Bicyclohexyl	Ni, Ni <sub>2</sub> P, Ni-Cu, Pd, Pt	Hydrodeoxygenation	(Ambursa et al., 2016; Cecilia et al., 2013; Wang et al., 2015b)
Furfural	2-methylfuran, tetrahydrofuran	Cu, Fe, Ni, Pd	Hydrogenolysis, dehydroxylation, decarbonylation	(Sitthisa et al., 2011a; Sitthisa & Resasco, 2011)
Furfuryl alcohol	2-methylfuran	Cu, Fe, Ni, Pd	Hydrogenolysis, dehydroxylation	(Sitthisa et al., 2011a; Sitthisa & Resasco, 2011)

### 2.2.3 Ethers

Ether is a chemical compound which contains an oxygen atom being singly bonded to alkyl or aryl groups on both sides. It is commonly found in bio-oils as one of the oxygenate compounds due to the fragmentation of lignin-based compounds in biomass (Jin et al., 2014). Aliphatic ether has alkyl groups on both sides of the oxygen atom while aromatic ether has aryl groups on both sides of the oxygen atom. Aromatic ethers are generally more difficult to be deoxygenated than aliphatic ethers due to the greater bond energy of C<sub>Aromatic</sub>—O ether bond (422 kJ/mol) compared to C<sub>Aliphatic</sub>—O ether bond (339 kJ/mol) (Furimsky, 2000). Figure 2.10 shows some of aromatic ether model compounds found in bio-oil samples derived from lignocellulosic biomass.

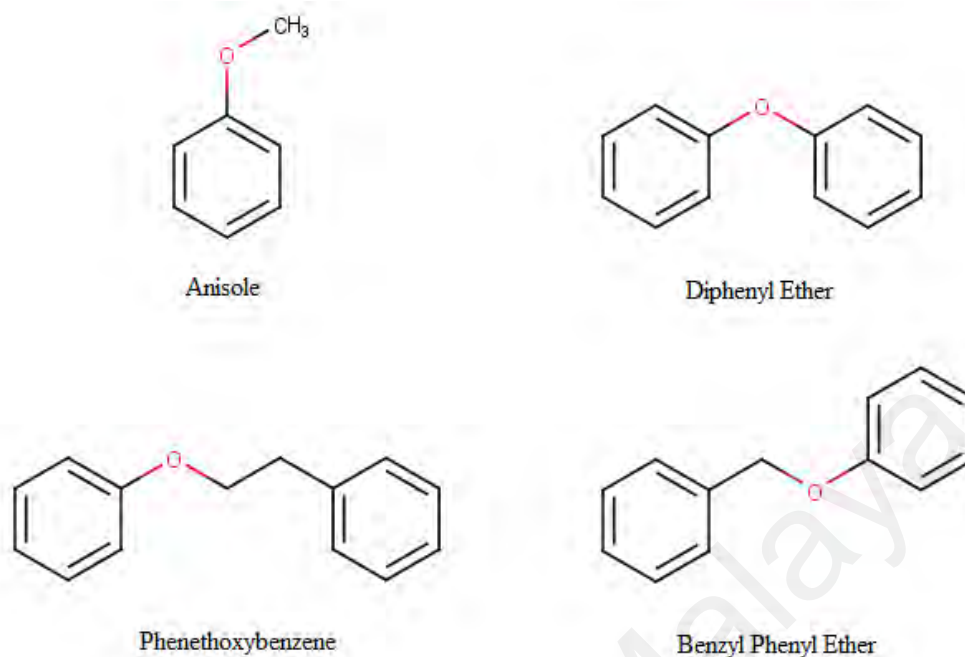
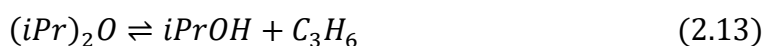


**Figure 2.10: Molecular structures of aromatic ether model compounds**

Diisopropyl ether is one of the aliphatic ethers which had been studied for its vapor phase deoxygenation over a bifunctional Pt-heteropoly acid catalyst (Pt-CsPW catalyst) (Alharbi et al., 2016). The diisopropyl ether was observed to undergo E1 elimination (Figure 2.11) in which the diisopropyl ether decomposed into propane and isopropyl alcohol (Equation 2.13) which further dehydrated and hydrogenated into propane (Equation 2.14 and 2.15). The decomposition of diisopropyl ether and dehydration of isopropyl alcohol were acid-catalyzed reactions which required Brønsted acid sites whereas the hydrogenation of propene was catalyzed by Pt metals (Alharbi et al., 2016).



where *iPr* is isopropyl group and *iPrOH* is isopropyl alcohol.



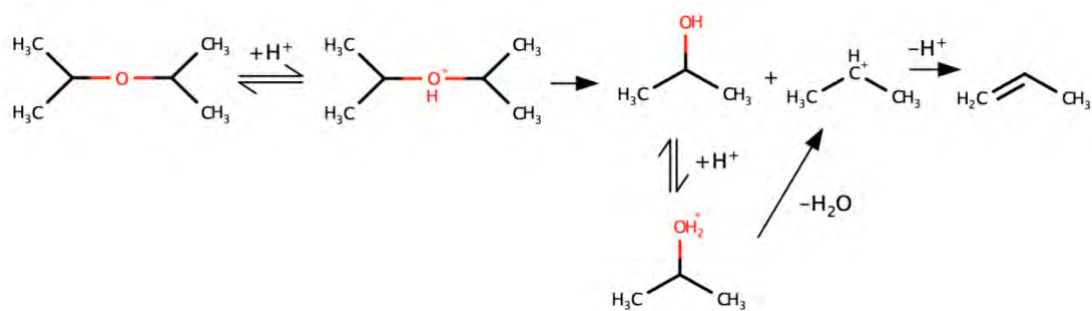


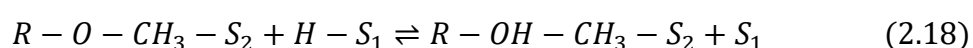
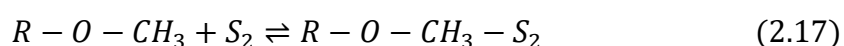
**Figure 2.11: Mechanism of E1 elimination of diisopropyl ether (Alharbi et al., 2016)**

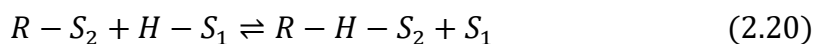
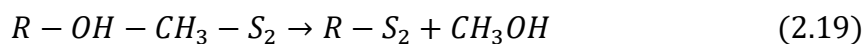
The deoxygenation of aromatic ethers in bio-oil samples such as benzyl phenyl ether (Kim et al., 2015), diphenyl ether (Prasomsri et al., 2014), phenethoxybenzene (Luo et al., 2016; Luo & Zhao, 2016) and anisole (Zhu et al., 2011) were also being investigated in past studies. Deoxygenation of aromatic ether is more difficult than aliphatic ether due to the higher ether bond energy by aromatic ring (Furimsky, 2000). Upon the scission of ether linkages, aromatics and oxygenated aromatics would be formed as intermediates in which the oxygenated aromatics would be further deoxygenated into aromatics. For instance, aromatic products such as toluene, phenol, ethylbenzene and cyclic products such as methylcyclohexane and ethylcyclohexane were the products obtained from the deoxygenation of benzyl phenyl ether over Pd-Fe catalyst supported on ordered mesoporous carbon (Kim et al., 2015). Kim et al. (2015) reported that the use of Pd/OMC instead of Pd-Fe/OMC showed a higher selectivity for cyclic products (47.1% and 4.6%) as Pd has better hydrogen adsorption ability compared to Fe.

Unlike the aforementioned ethers, anisole (methoxybenzene) is asymmetrical ether which consists of a phenyl group and a methoxy group. The deoxygenation of anisole over supported Ni (Jin et al., 2014; Li et al., 2011; Yang et al., 2014), Pt/ $\text{Al}_2\text{O}_3$  (Saidi et al., 2015), Pt/HBeta (Zhu et al., 2011), Pt-Sn (González-Borja & Resasco, 2011), molybdenum carbide (Lee et al., 2014) and Ru-Mn catalysts (Ishikawa et al., 2016)

were also being investigated in past studies. For deoxygenation of anisole, there are three major reaction pathways: demethylation, demethoxylation and transalkylation (Jin et al., 2014; Yang et al., 2014). The demethylation of anisole produces phenol intermediate which will then be hydrodeoxygenated into benzene or cyclohexane (Li et al., 2011). Likewise, demethoxylation of anisole directly produces benzene while transalkylation of anisole produces cresol intermediates which will then be hydrodeoxygenated into benzene (Ishikawa et al., 2016). Methane and methanol are also seen as by-products of anisole deoxygenation owing to the removal of methyl (—CH<sub>3</sub>) and methoxy (—OCH<sub>3</sub>) groups through demethylation and demethoxylation respectively (Lee et al., 2014).

Lee et al. (2014) have also proposed the reaction mechanism for vapor phase HDO of anisole to benzene over molybdenum carbide catalyst. The reaction mechanism is insightful as it was able to account for the experimentally observed reaction data to establish quantitative understanding on the kinetics of anisole deoxygenation. Lee et al. (2014) noted that the mechanism involved the adsorption of H<sub>2</sub> and anisole on catalytic site 1 and 2 respectively (Equation 2.16 and 2.17) and the subsequent formation of anisole-hydrogen intermediate (Equation 2.18) which enabled the cleavage of phenolic C—O bond to form methanol (Equation 2.19) and benzene (Equation 2.20) which would then be desorbed from catalytic site (Equation 2.21). The benzene formation rate would have reaction orders of zero order for anisole and ½ order for hydrogen if cleavage of phenolic C—O bond as rate determining step (Equation 2.19) and anisole as the most abundant reactive intermediate on S<sub>2</sub> were assumed.





where  $R$  is phenyl group.

The reaction mechanism of ether deoxygenation generally involves the scission of ether bond as the rate determining step and is dependent on the type of ether and the physicochemical properties of metal catalyst. For aliphatic ether deoxygenation, catalysts such as bifunctional acidic catalyst and transition metal carbides will tend to catalyze the conversion of ether to alcohol and the dehydration of alcohol. Transition metals which have high hydrogenating ability would hydrogenolyze the C—O ether bond and the hydrogenation of its intermediate into an alcohol which would then be dehydrated over the acid sites of catalyst. For aryl ether deoxygenation, the structural symmetry of ether is an important factor which affects its reaction mechanism. Generally, the C—O bond of asymmetrical ether which has the lower bond energy will be favored for hydrogenolysis. Thus, it would be expected to have demethylation being more favored than demethoxylation during anisole deoxygenation, owing to the lower bond energy of CH<sub>3</sub>—O bond than C<sub>AR</sub>—O bond.

Nevertheless, several studies have shown the capability of several metal catalysts to catalyze demethoxylation, owing to their high C—O hydrogenolysis ability. Catalysts such as Co-based (Mochizuki et al., 2014); Re sulfide and oxide based (Leiva et al., 2015b); Rh, Ru and Mo carbide based (Ishikawa et al., 2016; Lee et al., 2014; Mu et al., 2014) were noted to catalyze demethoxylation as the main reaction pathway. On the other hand, demethylation pathway was often noted to be catalyzed by Pt-based catalysts (Zanuttini et al., 2013; Zhu et al., 2011) or transition metal phosphides such as

Ni<sub>2</sub>P, MoP, NiMoP catalysts (Li et al., 2011). Other reaction pathway such as debenzilation was also reported to be catalyzed by Fe-based catalyst during the deoxygenation of benzyl phenyl ether (Kim et al., 2015). Transalkylation was also noted to be a side reaction pathway when acidic catalysts such as Pt/HBeta (Zhu et al., 2011) and Pt/Al<sub>2</sub>O<sub>3</sub> (Nimmanwudipong et al., 2011a; Saidi et al., 2015) were used. The alkylated phenolic intermediates will then be hydrodeoxygenated to form deoxygenated aromatics. Table 2.6 summarized on the major deoxygenated products formed from ethers which are commonly found in bio-oil samples. The information on the reaction pathway observed and the metal based catalysts used for ether deoxygenation will be necessary for the appropriate catalyst selection in bio-oil upgrading and the effective valorization of desired deoxygenated products.

**Table 2.6: Deoxygenation process for ethers commonly found in bio-oil**

Ethers	Deoxygenated products	Metal-based catalysts	Reaction pathway	Ref.
Anisole	Benzene, cyclohexane	Ni, Mn, Mo, Pt, Ru, Sn	Hydrodeoxygenation	(González-Borja & Resasco, 2011; Jin et al., 2014; Lee et al., 2014; Smirnov et al., 2016; Yang et al., 2014; Zhu et al., 2011)
Benzyl phenyl ether	Toluene, ethylbenzene	Fe, Pd	Hydrodeoxygenation	(Kim et al., 2015)
Diisopropyl ether	Propane	Pt	Dehydration	(Alharbi et al., 2016)

#### 2.2.4 Carboxylic acids

The reaction pathway of carboxylic acid deoxygenation has three distinct pathways (He & Wang, 2012):

- 1) Ketonization to form ketone by cleavage of C—OH bond and subsequent C=O hydrogenation to form secondary alcohol;

- 2) Hydrogenolysis to form aldehyde by cleavage of C—OH bond and subsequent C=O hydrogenation to form primary alcohol. The primary alcohol may dehydrate and hydrogenate into alkane or react with acid to form ester by esterification;
- 3) Direct decarboxylation or decarbonylation by cleavage of C—C bond to form alkane with one less carbon. The dissociated carboxyl or carbonyl group may further react into CO<sub>2</sub> and CO respectively.

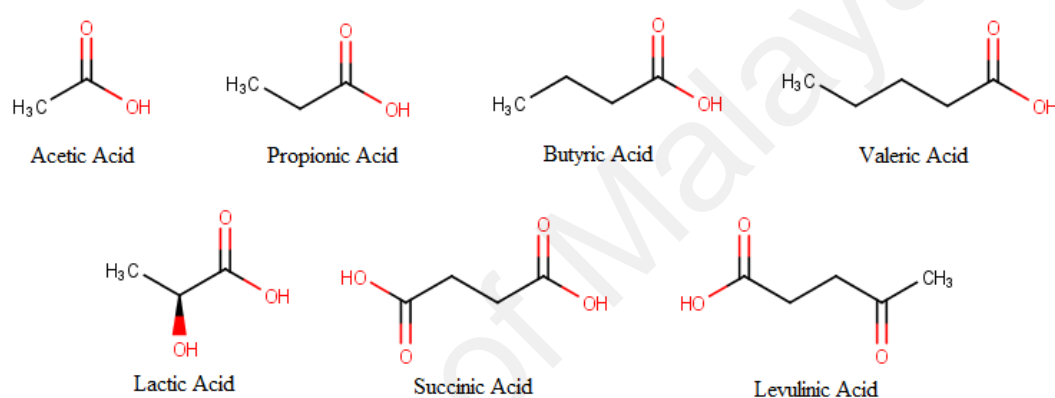


**Figure 2.12: Molecular structures of acid model compounds**

Simakova and Murzin (2016) explained that the ketonization of carboxylic acid involves the carboxylate adsorption on metal cationic sites and the stabilization of the adsorbed carboxylate ion for the abstraction of proton from another carboxyl group (—COOH) and  $\alpha$ -hydrogen. Upon the interaction of the carboxylate ions through the proton abstraction, an intermediate called  $\beta$ -ketoacid is formed which will subsequently decarboxylate into a ketone. The ketone can be deoxygenated into alkane or alkene through C=O hydrogenation and dehydration. For instance, valeric acid (pentanoic acid) was found to undergo ketonization into 5-nonanone which then formed nonane or nonenes during the deoxygenation of valeric acid over ZrO<sub>2</sub> catalyst in H<sub>2</sub> atmosphere (Panchenko et al., 2014). The reaction pathway of carboxylic acid deoxygenation

involving ketonization is favorable as the formation of  $\beta$ -ketoacid intermediate will result in an increase of carbon chain length ( $C_n \rightarrow C_{2n-1}$ ) to produce deoxygenated hydrocarbon in gasoline ( $C_7$ - $C_9$ ) or jet fuel ( $>C_8$ ) range (Serrano-Ruiz et al., 2010).

Past studies on the deoxygenation of other short-chained aliphatic carboxylic acids such as acetic acid, propionic acid, butyric acid, succinic acid and lactic acid were also conducted (Figure 2.12). Lactic acid (2-hydroxypropanoic acid) is a common intermediate obtained from hydrogenolysis of glycerol or polyols (Chaudhari et al., 2013) which can be converted to propylene glycol through hydrogenation over Ru/C catalyst (Jang et al., 2013). Succinic acid (butanedioic acid) can be subjected to hydrogenation over catalysts such as Pd/ $\gamma$ -AlOOH (Zhang et al., 2016), carbon supported Re-Ru (Kang et al., 2015) or Re-Cu (Kang et al., 2014) to produce  $\gamma$ -butyrolactone and 1,4-butanediol. The  $\gamma$ -butyrolactone and 1,4-butanediol products can then be further deoxygenated through dehydration in which  $\gamma$ -butyrolactone has to undergo decyclization as a prior step.

The ketonization of acetic acid into acetone was reported during its deoxygenation over catalysts such as alkali-metals promoted zirconia (Parida & Mishra, 1999), Zn-Cr oxide (Bayahia et al., 2015), Ru/TiO<sub>2</sub> (Pham et al., 2012) and sulfided NiMo/MoO<sub>3</sub>/Al<sub>2</sub>O<sub>3</sub> (Joshi & Lawal, 2012). In the ketonization pathway, the C—C coupling step for formation of  $\beta$ -ketoacid intermediate was known to be the rate limiting step (Bayahia et al., 2015). However, some metal catalysts were also reported to suppress ketonization and instead favor the hydrogenation of acetic acid into acetaldehyde or ethanol such as InNi/Al<sub>2</sub>O<sub>3</sub> (Onyestyák et al., 2012), Ir-MoO<sub>x</sub>/SiO<sub>2</sub> (Wang et al., 2014b), Pt-Sn/CNT (Zhang et al., 2013a) and Pt-based catalysts (Pestman et al., 1997). Likewise, Alotaibi et al. (2012a) reported the ketonization of propionic

acid over bifunctional metal-loaded heteropoly acid catalyst ( $\text{Cs}_{2.5}\text{H}_{0.5}\text{PW}_{12}\text{O}_{40}$ ) and the hydrogenolysis of propionic acid over Pt-based catalysts.

Deoxygenation of acids which are commonly found in bio-oil is summarized in Table 2.7. Pestman et al. (1997) noted that the metal-oxygen bond strength in the adsorbed carboxylic acid affects the reaction pathway and that noble metals such as Pt, Pd, Ru and Rh are good hydrogen activators which preferentially catalyze hydrogenolysis, decarboxylation and decarbonylation instead. The deoxygenation of propionic acid over Pd, Pt, Rh, Ru and Ni catalysts mainly proceeds through decarbonylation or decarboxylation with the order of catalytic activity: Pd > Ru > Pt > Rh > Ni (Lugo-José et al., 2014). Ru-based catalyst was also reported to catalyze the cleavage of C—C bond, decarbonylation and hydrogenolysis during the deoxygenation of acetic, propionic, butyric and isobutyric acids (Chen et al., 2011; Li et al., 2015a). In addition, the effects of supports ( $\text{ZrO}_2$ ,  $\text{SiO}_2$ ,  $\text{TiO}_2$ ,  $\gamma\text{-Al}_2\text{O}_3$  and  $\text{SiO}_2\text{-Al}_2\text{O}_3$ ) on propionic acid deoxygenation over Ru catalysts were also investigated (Chen et al., 2014). Supports with more Lewis acid sites ( $\gamma\text{-Al}_2\text{O}_3$ ,  $\text{SiO}_2\text{-Al}_2\text{O}_3$ ) were found to favor C=O hydrogenation while supports with weaker metal-support interaction and lesser Lewis acid sites ( $\text{ZrO}_2$ ,  $\text{SiO}_2$ ,  $\text{TiO}_2$ ) favored decarbonylation pathway (Chen et al., 2014).

**Table 2.7: Deoxygenation process for acids commonly found in bio-oil**

Acids	Deoxygenated products	Metal-based catalysts	Reaction pathway	Ref.
Acetic acid	Ethane	Ni-Mo, Ru, Zr, Zn-Cr	Ketonization, decarboxylation	(Bayahia et al., 2015; Joshi & Lawal, 2012; Parida & Mishra, 1999; Pham et al., 2012)
Propionic acid	Propane, ethane	Pd, Pt, Rh, Ru and Ni	Hydrogenolysis, decarboxylation	(Alotaibi et al., 2012a; Chen et al., 2012b; Lugo-José et al., 2014)
Succinic acid	Butane	Pd, Re, Ru, Cu	Hydrogenation, dehydration	(Kang et al., 2015; Kang et al., 2014; Zhang et al., 2016)
Levulinic acid	Nonane	$\text{Fe}_2\text{O}_3$	Ketonization, deoxygenation	(Karimi et al., 2012)

### 2.2.5 Aldehydes and ketones

Deoxygenation of carbonyl compounds (Figure 2.13) were also commonly studied during the catalytic upgrading of bio-oils derived from lignocellulosic biomass. The reaction pathway of carbonyls deoxygenation has four distinct pathways (He & Wang, 2012):

- 1) Direct hydrogenolysis of C=O bond to form alkane;
- 2) Hydrogenation of C=O bond to form alcohol which form alkane by hydrogenolysis of C—OH bond;
- 3) Hydrogenation of C=O bond to form alcohol which dehydrates into alkene. Alkene further hydrogenates into alkane;
- 4) Decarbonylation to form alkane with one less carbon atom.

Zaccheria et al. (2005) have studied the deoxygenation of aromatic ketones over Cu/SiO<sub>2</sub> catalysts at 90 °C and 1 atm of H<sub>2</sub>. The aromatic ketones studied were 9-fluorenone, 11-oxo-dibenzocycloheptane, benzophenone, benzyhydrol, 4-alkylated acetophenone, 2-acetonaphthone, 6-methoxy-2-acetonaphthone,  $\alpha$ -tetralone,  $\beta$ -tetralone and 9,10-anthroquinone which had conversions ranging from 84%-100%. Their respective deoxygenated products were fluorene, dibenzocycloheptane, benzylbenzene, benzylbenzene, 4-alkylated ethylbenzene, 2-ethylnaphthalene, 2-ethyl-6-methoxynaphthalene, tetralin, 2-hydroxytetralin and 9,10-dihydroanthracene which had selectivities ranging from 87%-100%. It was noted that aromatic ketones with carbonyl group (C=O) at  $\alpha$  position of benzyl group were deoxygenated through the direct hydrogenolysis of C=O bond except for  $\beta$ -tetralone (Zaccheria et al., 2005). For  $\beta$ -tetralone, the carbonyl group was located at the  $\beta$  position of benzyl group causing it to be only reduced to alcohol instead of methylene.



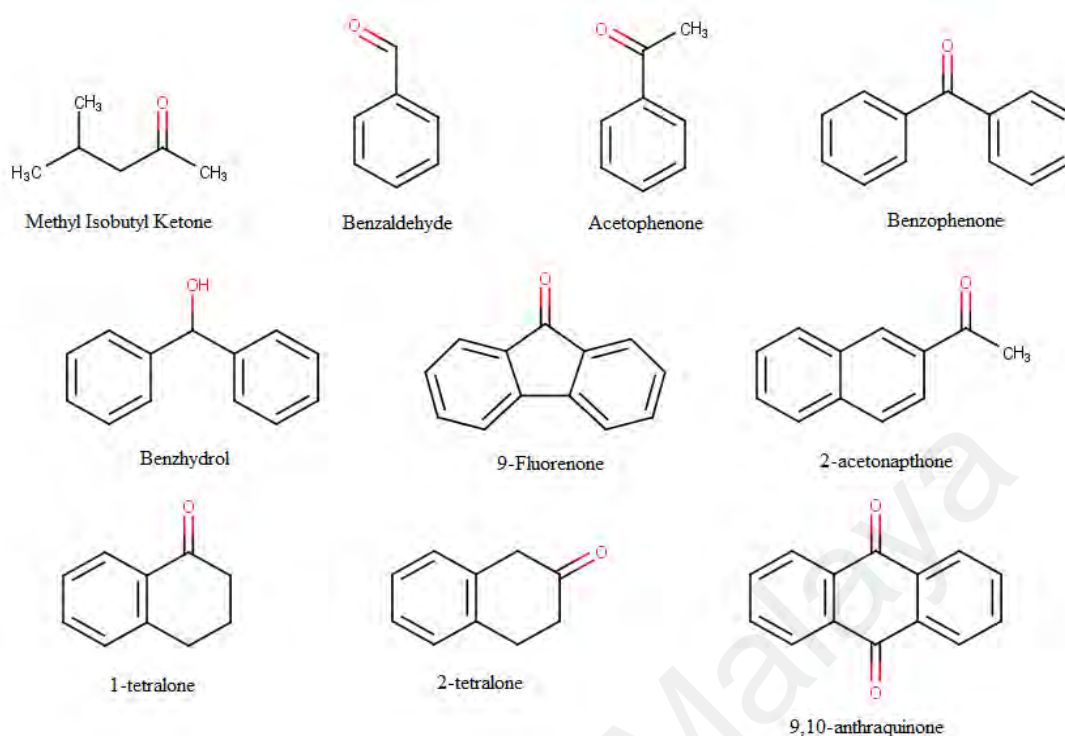


**Figure 2.13: Molecular structures of carbonyl model compounds**

Likewise, the gaseous phase deoxygenation of acetophenone was also studied in a fixed bed down-flow reactor over Pt-heteropoly acid catalyst (Pt/CsPW) at 100 °C and 1 bar (Alharbi et al., 2015). With the use of 0.5 wt% Pt/CsPW catalyst, ethylcyclohexane was the major product with a selectivity of 98 mol% and an acetophenone conversion of 74 mol%. Based on Figure 2.14, the deoxygenation of acetophenone in the presence of bifunctional metal-acid catalyst proceeds through the hydrogenation of C=O bond to form 1-phenylethanol which then undergoes dehydration-hydrogenation to form ethylcyclohexane.

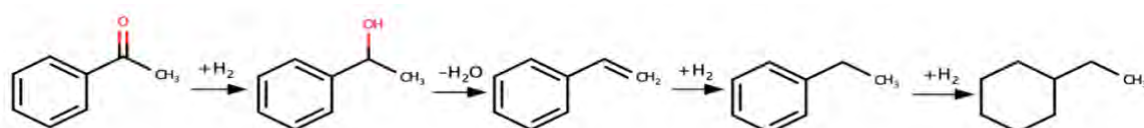


**Figure 2.14: Deoxygenation of acetophenone into ethylcyclohexane (Alharbi et al., 2015)**

In addition, the study of aromatic aldehyde deoxygenation was also studied by Procházková et al. (2007) through the hydrodeoxygenation of benzaldehyde over Pd/Beta (70 Si/Al ratio) and Pd/ZSM-5 (15 Si/Al ratio) catalysts with hexane solvent in autoclave at 130 °C and 6 MPa. Toluene was the major product of benzaldehyde hydrodeoxygenation over both catalysts with Pd/Beta (70) catalyst showing a higher toluene selectivity (94 mol%) than Pd/ZSM-5 (15) catalyst (56.5 mol%). Based on Figure 2.15, the HDO of benzaldehyde into toluene was proposed to proceed through either direct scission of C=O bond ( $r_3$ ); hydrogenation of C=O bond and dehydroxylation ( $r_1$  and  $r_2$ ); hydrogenation of C=O bond, methylation of hydroxyl group and demethoxylation ( $r_1$ ,  $r_6$  and  $r_7$ ); formation of dimethylacetal benzaldehyde (D) and phenyl methyl ether (E) which then demethoxylates into toluene ( $r_4$ ,  $r_5$  and  $r_7$ ).

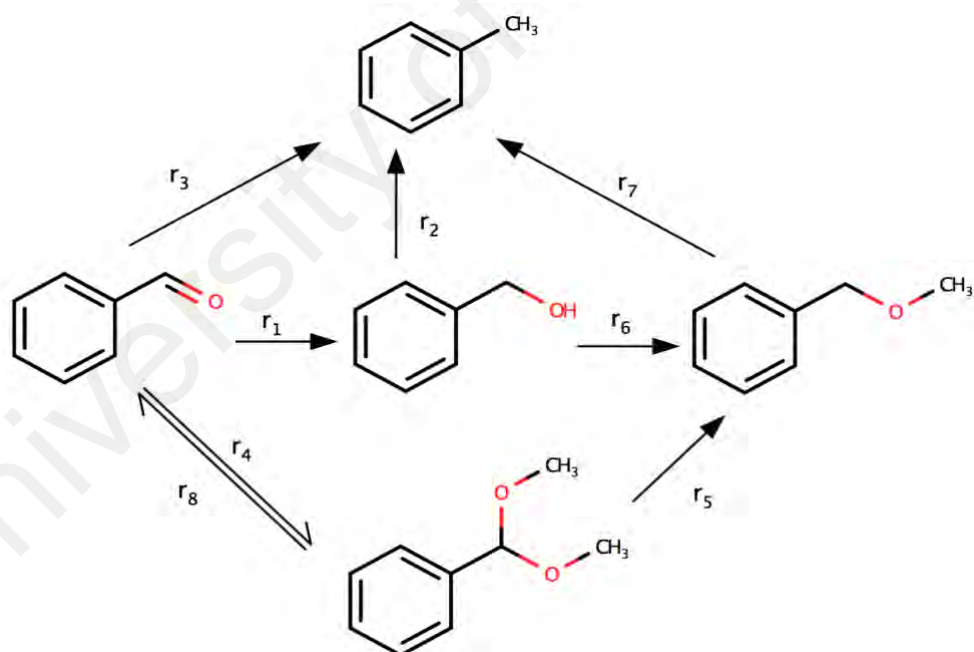


**Figure 2.15: Reaction network of benzaldehyde HDO (Procházková et al., 2007)**

In this study, the reaction rate equations ( $r_1$ ,  $r_2$ ,  $r_3$ ,  $r_4$ ,  $r_5$ ,  $r_6$ ,  $r_7$  and  $r_8$ ) were derived based on Langmuir-Hinshelwood model with the assumption that surface reaction is the rate determining step (Procházková et al., 2007):

$$r_i = w \frac{k_i K_X C_X}{1 + K_A C_A + K_B C_B + K_C C_C + K_D C_D + K_E C_E} \quad (2.22)$$

where  $r_i$  is rate of  $i$ -th reaction,  $w$  is catalyst weight,  $k_i$  is rate constant of  $i$ -th reaction,  $K$  is adsorption constant,  $C_i$  is concentration of reactant of  $i$ ,  $A$  is benzaldehyde,  $B$  is benzylalcohol,  $C$  is toluene,  $D$  is dimethylacetal benzaldehyde,  $E$  is benzyl methyl ether and  $X$  is reactant of the  $i$ -th reaction. Table 2.8 shows the kinetic terms ( $k_i K_X w$ ) for the benzaldehyde HDO at 130 °C and 6 MPa. With the use of hexane solvent, the kinetic terms for pathways of 4, 5, 6, 7 and 8 were reported to be negligible and thus not reported (Procházková et al., 2007). The larger  $k_1 K_{AW}$  and  $k_2 K_{BW}$  values as compared with  $k_3 K_{AW}$  value also indicated that hydrogenation and dehydroxylation of benzaldehyde to toluene were the major reaction pathways with the latter as the rate determining step. As for the catalyst type, the larger value of kinetic terms for Pd/beta (70) would also result in higher benzaldehyde HDO activity and yield as reported in the results of catalyst testing by Procházková et al. (2007)

**Table 2.8: Kinetic terms of benzaldehyde HDO on different catalysts in hexane. Data obtained from (Procházková et al., 2007)**

Kinetic term (s <sup>-1</sup> )	Pd/beta (70)	Pd/HZSM-5 (15)
$k_1 K_{AW}$	2.4400	0.3150
$k_2 K_{BW}$	1.1400	0.0467
$k_3 K_{AW}$	0.5700	0.1000

The deoxygenation of aliphatic carbonyl compounds was also studied. Xiong et al. (2014) have investigated on the deoxygenation of aliphatic aldehyde over Mo<sub>2</sub>C catalyst. The results of temperature programmed desorption (TPD) analysis and Auger electron spectroscopy (AES) showed propene as the major product through the selective scission of C=O bond of the propoxide intermediate (Xiong et al., 2014). Likewise,

Alotaibi et al. (2012b) have studied on the deoxygenation of methyl isobutyl ketone (MIBK) over zeolite supported Pt catalyst in a fixed bed down-flow reactor at 200 °C. With the use of 0.3 wt% Pt/H-ZSM-5 catalyst, MIBK conversion was at 100 mol% with a 2-methylpentane (2MP) selectivity of 83 mol%, indicating 2-methylpentane as the major product of MIBK deoxygenation (Alotaibi et al., 2012b). The deoxygenation of MIBK in bifunctional metal-acid catalyst also showed the same reaction pathway as the deoxygenation of acetophenone in bifunctional metal-acid catalyst (Alharbi et al., 2015). The deoxygenation of MIBK proceeded through the hydrogenation of C=O bond to form 4-methylpentan-2-ol (MP-ol) and the subsequent dehydration-hydrogenation to form 2-methylpentane.

Deoxygenation of aldehydes and ketones which are commonly found in bio-oil is summarized in Table 2.9. The reaction mechanism of carbonyl deoxygenation generally occurs through hydrogenation and dehydration when bifunctional metal-acid catalysts were used. Metals such as Pt (Alotaibi et al., 2012b), Ru (Alharbi et al., 2015) and Pd (Bejblova et al., 2005) which have excellent hydrogenation ability were often observed to catalyze the hydrogenation of C=O bond in carbonyls into C—OH bond. Likewise, the acid sites of bifunctional catalysts such as carbide (Bejblova et al., 2005), zeolites (Alotaibi et al., 2012b) and heteropoly acid CsPW support (Alharbi et al., 2015) would then catalyze the dehydration of C—OH bond to form alkenes. However, with the use of Cs (Peralta et al., 2009), Cu (Zaccheria et al., 2005) and Pd based catalysts (Ding et al., 2015; Dragu et al., 2015; Simakova et al., 2009), decarbonylation was reported to be the alternative reaction pathway instead, causing the deoxygenated product to have one lesser carbon atom. The direct C=O hydrogenolysis of carbonyls was also made possible when oxophilic metal catalysts such as Fe, Ti, Sn, V and W which have high affinity for C=O and C—O bonds were used. In addition, the use of Sn-based catalyst was also reported by Zhang et al. (2013a) in which Sn inhibits C—C bond cleavage.

Hence, the use of Sn in carbonyl deoxygenation will tend to minimize decarbonylation and favor the direct scission of oxygen.

**Table 2.9: Deoxygenation process for carbonyl compounds commonly found in bio-oil**

Carbonyls	Deoxygenated products	Metal-based catalysts	Reaction pathway	Ref.
Acetophenone	Ethylcyclohexane	Pt	Hydrogenation-dehydration	(Alharbi et al., 2015)
Methyl isobutyl ketone	2-methylpentane	Pt, Ru	Hydrogenation-dehydration	(Alharbi et al., 2015; Alotaibi et al., 2012b)
Benzophenone	Diphenylmethane	Pd, Cu	Hydrogenation, hydrogenolysis	(Bejblova et al., 2005; Zaccheria et al., 2005)
Benzaldehyde	Toluene, benzene	Pd, Ga, Cs	Hydrodeoxygenation	(Ausavasukhi et al., 2009; Peralta et al., 2009; Procházková et al., 2007)

### 2.2.6 Alcohols

The deoxygenation of alcohol model compounds (Figure 2.16) can proceed through several reaction pathways depending on the reaction environment. Dehydration of alcohol is one of the common reaction pathways over metal catalyst (Chaudhari et al., 2013). For dehydration pathway, the scission of C—O bond of alcohol occurs and leads to the elimination of a mole of water and the formation of alkene which may be hydrogenated into alkane in the presence of metal catalyst. The dehydration rate increases when the number of hydroxyl group within the alcohol increases, causing the C—O bond strength to decrease (Peng et al., 2012).

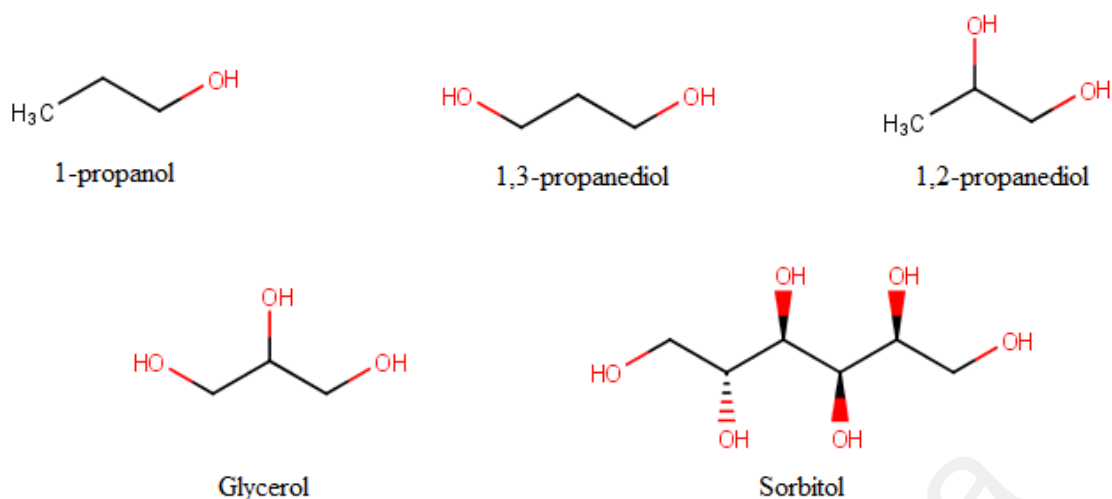
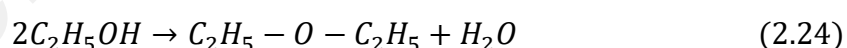


**Figure 2.16: Molecular structures of alcohol model compounds**

Pan et al. (2014) have studied on the kinetics of ethanol dehydration over a Lewis acidic Zr-KIT-6 catalyst which is a zirconium incorporated ultra large pore mesoporous silicate (Pan et al., 2013; Ramanathan et al., 2013). The dehydration of ethanol proceeded through two parallel reactions to respectively form ethylene and diethyl ether.



However, it has also been noted that the aqueous phase deoxygenation of alcohol does not proceed mainly through dehydration pathway. It has been proposed that the presence of water in abundant amount tends to block the Lewis acid site of catalyst, causing a drastic decrease in the dehydration rate of alcohol (Peng et al., 2012). Another proposed deoxygenation pathway of alcohol is also known as the dehydrogenation-disproportionation-decarboxylation mechanism. The terminal alcohol will firstly dehydrogenate into an aldehyde which undergoes decarbonylation to form an alkane. Disproportionation will also occur between two aldehydes through the Tishchenko or

Cannizzaro mechanism to form carboxylic acid which undergoes decarboxylation to form an alkane while the alcohol will be recycled for the reaction (Peng et al., 2012; Vilcoq et al., 2014). Since this mechanism involves decarboxylation or decarbonylation steps, the alkane formed will have one carbon lesser as compared with the alkane formed through dehydration of alcohol.

The deoxygenation of alcohol with multiple hydroxyl groups (polyol) was also studied and generally consists of dehydration, hydrogenation, hydrogenolysis, isomerization and aldol condensation as part of the deoxygenation reaction pathways (Chaudhari et al., 2013). Due to the complexity of the reaction pathways, the deoxygenation of polyols produce a wider distribution of deoxygenated products compared to the deoxygenation of alcohol with single hydroxyl group. Sad et al. (2011) have studied on the deoxygenation of 1,3-propanediol on Cu/ZnO/Al<sub>2</sub>O<sub>3</sub> catalyst in packed bed reactor at 503 K. The study showed that propanal was the major product of 1,3-propanediol with a 100 mol% 1,3-propanediol conversion and a propanal selectivity of 86 mol%. However, when the 1,3-propanediol was co-fed with hydrogen (80 kPa), 1-propanol was the major product of 1,3-propanediol with a 100 mol% 1,3-propanediol conversion and a 1-propanol selectivity of 83 mol%. Sad et al. (2011) proposed that 1,3-propanediol undergoes a series of unimolecular reactions such as hydrogenation and dehydration over the Cu/ZnO/Al<sub>2</sub>O<sub>3</sub> catalyst to form a mixture of 3-hydroxypropanal, allyl alcohol, acrolein and propanal. The presence of hydrogen will enable the propanal intermediate to further hydrogenate into 1-propanol. The 1-propanol can also undergo dehydration-hydrogenation steps to form propane.

In the analysis of polyols deoxygenation, the deoxygenation of glycerol (Maris & Davis, 2007; Soares et al., 2016) and sorbitol (Guo et al., 2015; Liu et al., 2016; Vilcoq et al., 2014) were studied. For the deoxygenation of glycerol (1,2,3-propanetriol) in the

presence of Ru-Cu bimetallic catalysts, the direct hydrogenolysis of C—O bond of glycerol without any C—C bond breaking was shown to be the main reaction pathway to produce 1,2-propanediol as the major product (Soares et al., 2016). With the usage of Ru/C and Pt/C catalysts, 1,2-propanediol was also one of the major products formed from direct hydrogenolysis of glycerol. However, the occurrence of C—C bond breaking was identified through the detection of ethylene glycol as one of the major products. The other major product detected was lactic acid. Maris and Davis (2007) proposed that the C—C bond scission is a metal-catalyzed reaction on Ru whereas on Pt, it is a base-catalyzed reaction.

Sorbitol is one of the sugar alcohols found in carbohydrates of plant crops. The study on sorbitol deoxygenation is of high relevance because its reaction pathway also involves glycerol and propanediols. The hydrogenolysis of sorbitol yields several major products such as glycerol, lactic acid, 1,2-propanediol, 2-propanol, ethylene glycol, ethanol, glycolic acid and 1,2-butanediol (Chaudhari et al., 2013). Further deoxygenation reactions are required in order to fully deoxygenate these partial deoxygenated products. Liu et al. (2016) have also investigated the deoxygenation of sorbitol without external hydrogen over Pt-Ir-ReO<sub>x</sub>/SiO<sub>2</sub> catalyst. It was noted that the synergistic interactions between Pt-Ir alloy and ReO<sub>x</sub> species enabled the efficient in-situ H<sub>2</sub> generation for sorbitol hydrogenolysis through catalyzed aqueous phase reforming reaction which occurred simultaneously (Liu et al., 2016).

Deoxygenation of alcohols which are commonly found in bio-oil is summarized in Table 2.10. The use of transition metal carbides for alcohol deoxygenation was also discussed by Stottlemeyer et al. (2012). Surface reaction studies such as TPD and HREELS techniques were extensively used to study the reaction of methanol, ethanol, propanol and polyol over Mo, Ti, V, W, Zr carbide catalysts. Stottlemeyer et al. (2012)



noted that the major reaction pathway of polyols and short chain alcohols generally involves the selective cleavage of C—O bond when transition metal carbides are used. The ability of transition metal carbides to form oxycarbide surface under the exposure of an oxygen source was also attributed to the oxygen abstraction from alcohol. This characteristic is in corroboration with the results by Stellwagen & Bitter (2015) on the hydrodeoxygenation of stearic acid over W<sub>2</sub>C/CNF and Mo<sub>2</sub>C/CNF catalysts. For ethanol reaction studies over vanadium carbide (VC) catalyst, Guenard et al. (2002) reported that the conversion of ethanol into ethylene involves the  $\gamma$ -hydride elimination of adsorbed ethoxy group to form an oxametallacycle intermediate which subsequently undergoes C—O bond scission to form ethylene.

**Table 2.10: Deoxygenation process for alcohols commonly found in bio-oil**

Alcohols	Deoxygenated products	Metal-based catalysts	Reaction pathway	Ref.
Propanol	Propane, propene	Ir, Re, W	Hydrogenolysis	(Nakagawa et al., 2010; Ren et al., 2014)
Propanediols*	Propanol	Cu, Ir, Re	Hydrogenolysis	(Nakagawa et al., 2010; Sad et al., 2011)
Glycerol*	Propylene glycol, propanediols	Pt, Ru, Cu, Ir, Re, Rh	Dehydration, hydrogenolysis	(Auneau et al., 2011; Durán-Martín et al., 2013; Maris & Davis, 2007; Nakagawa et al., 2010)
Sorbitol*	Lactic acid, propanol, propanediols, ethylene glycol	Ru, Ni, Cu	Hydrogenolysis	(Chaudhari et al., 2013)

\* Partial deoxygenation

### 2.3 Deoxygenation reactivity of model compounds

An in-depth study on the reactivity of model compounds is instrumental for a better understanding of their reaction mechanisms and kinetics. Table 2.11 shows C—O bond dissociation energies (BDE) for some of the model compounds of phenolics, ethers, acids and alcohols (Luo, 2007). Model compounds which have similar BDE due to similar C—O bond configuration were not shown such as guaiacol, since it has both the

C—O bond configuration of both phenol and anisole collectively. Based on the values of BDE shown in Table 2.11, a model compound with higher C—O BDE would generally result in a more energy intensive oxygen removal process, indicating its lower deoxygenation reactivity. The BDE values among the functional groups could also be noted to increase in the order of: alcohols < acids < ethers < phenols. The order of BDE values can be the primary factor in determining the deoxygenation reactivity. Nevertheless, compounds such as ethers will experience more steric effects than other compounds which ought to be taken into consideration. Thus, with the account of geometric effects of ether and BDE values, aromatic ethers were noted to be less reactive than phenolics while aliphatic ethers were more reactive than phenolics for deoxygenation (Furimsky, 2000). The deoxygenation reactivity order of O-containing compounds can be generally summarized as: alcohols > ketones > dialkyl ethers > carboxylic acids > phenols > diaryl ethers > alkylfurans > benzofuran > dibenzofuran (Furimsky, 2000). In addition, within the same class, the BDE values also tend to marginally increase with the number of carbon atoms, indicating the presence of inductive effect in affecting deoxygenation reactivity of model compound.

There are several factors which affect the deoxygenation reactivity of model compounds. A preliminary analysis of the bond energies and configurations of a compound will give a quantitative result on its reactivity. For instance, a targeted chemical bond for scission which has higher bond energy will tend to require more external energy for bond dissociation, resulting in a higher reaction temperature. Likewise, the determination of activation energy through experimental analyses is also one of the main technical insights used to determine the reactivity of model compounds. Activation energy which is the energy level threshold required for the occurrence of chemical reaction, will indicate that a model compound is of high deoxygenation reactivity if it has a low activation energy. Arrhenius' equation (Equation 2.25) or

Bells-Evans-Polanyi principle (Evans & Polanyi, 1936) (Equation 2.26) are some of the quintessential equations which can be used for the determination of activation energy of deoxygenation.

$$k = Ae^{\left(\frac{-E_a}{RT}\right)} \quad (2.25)$$

$$E_a = E_o + \alpha\Delta H \quad (2.26)$$

where  $k$  is rate constant,  $A$  is pre-exponential factor,  $E_a$  is activation energy,  $R$  is ideal gas constant,  $T$  is absolute temperature,  $E_o$  is reference activation energy,  $\alpha$  is characterization coefficient of transition state position in reaction coordinate and  $\Delta H$  is enthalpy of reaction. By varying the reaction temperature and constructing a linear plot of Arrhenius' equation using  $\ln k$  versus  $1/T$ , the activation energy for a model compound deoxygenation can be determined.

The reactivity of HDO model compounds is also dependent on inductive effect within the chemical structures. Inductive effect arises due to the difference in electronegativity of bonded atoms. The electronegativity difference will result in a non-uniform electron cloud within the bond which is a state known as bond polarization. Thus, the polarized bond will be more susceptible or resistant to bond scission, depending on the type of chemical species and reaction. It has been noted that proton transfer to the oxygen of C—O and C=O bonds commonly occurs in deoxygenation mechanism (Crevier & Mayer, 1997; Qin et al., 2010; To & Resasco, 2015). Hence, electron withdrawing substituents such as —CHO, —CO and —COOH will tend to reduce the availability of lone pair electron of oxygen at C—O and C=O bonds through inductive effect. With the reduced availability of lone pair electron of oxygen for proton transfer, the model compound would be of lower reactivity for deoxygenation. However, electron donating substituents such as alkyl and alcohol groups will have an

opposite inductive effect which promotes proton transfer to oxygen, making the compound to be of higher deoxygenation reactivity.

The lower deoxygenation reactivity of O-containing aromatic compounds as compared with O-containing aliphatic compounds could also be attributed to the mesomeric effect within aromatic compounds. O-containing aromatic compounds which have benzene or furanic rings obey Hückel's rule and usually have enhanced stability due to the delocalization of electron ring. The electron ring delocalization within these conjugated systems will form a set of resonance structures in which through resonance stabilization, the overall energy of the actual molecular structure of the conjugated system will be lower. Thus, structures which exhibit resonance stabilization through mesomerism are generally more stable. Likewise, a more stable aromatic structure which experiences mesomerism will also be less susceptible to deoxygenation. Furimsky (2000) has also concluded that the stability of O-containing aromatic compound increases with its number of aromatic rings. This is because an increase in aromatic rings will result in a stronger resonance stabilization or higher resonance energy with such order: dibenzofuran > benzofuran > alkylfuran, indicating dibenzofuran to have the lowest deoxygenation reactivity among these groups.

**Table 2.11: C—O bond dissociation energies (BDE) of O-containing model compounds at 298 K (Luo, 2007)**

Compound	Dissociated Bond ( <b>in boldface</b> )	BDE (kJ/mol)
<u>Phenolics</u>		
Phenol	<b>HO—C<sub>6</sub>H<sub>5</sub></b>	463.6 ± 4.2
1-Naphthol	<b>1-C<sub>10</sub>H<sub>7</sub>—OH</b>	468.6 ± 6.3
<u>Ethers</u>		
Dimethyl ether	<b>CH<sub>3</sub>—OCH<sub>3</sub></b>	351.9 ± 4.2
Diethyl ether	<b>C<sub>2</sub>H<sub>5</sub>—OC<sub>2</sub>H<sub>5</sub></b>	357.3 ± 6.3
Dipropyl ether	<b>C<sub>3</sub>H<sub>7</sub>—OC<sub>3</sub>H<sub>7</sub></b>	361.9 ± 9.2
Diisopropyl ether	<b><i>iso</i>-C<sub>3</sub>H<sub>7</sub>—O—<i>iso</i>-C<sub>3</sub>H<sub>7</sub></b>	356.9 ± 8.4
Dibutyl ether	<b>C<sub>4</sub>H<sub>9</sub>—OC<sub>4</sub>H<sub>9</sub></b>	348.5 ± 8.4
Anisole	<b>C<sub>6</sub>H<sub>5</sub>—O—CH<sub>3</sub></b>	418.8 ± 5.9
	<b>C<sub>6</sub>H<sub>5</sub>—O—CH<sub>3</sub></b>	263.2 ± 4.2
Ethyl phenyl ether	<b>C<sub>6</sub>H<sub>5</sub>—O—CH<sub>2</sub>CH<sub>3</sub></b>	416.7 ± 5.4
	<b>C<sub>6</sub>H<sub>5</sub>—O—CH<sub>2</sub>CH<sub>3</sub></b>	269.0 ± 4.8
Diphenyl ether	<b>C<sub>6</sub>H<sub>5</sub>—OC<sub>6</sub>H<sub>5</sub></b>	326.8 ± 4.2
Phenyl benzyl ether	<b>C<sub>6</sub>H<sub>5</sub>CH<sub>2</sub>—O—C<sub>6</sub>H<sub>5</sub></b>	218.0
Phenethoxybenzene	<b>C<sub>6</sub>H<sub>5</sub>—OCH<sub>2</sub>CH<sub>2</sub>C<sub>6</sub>H<sub>5</sub></b>	314
	<b>C<sub>6</sub>H<sub>5</sub>O—CH<sub>2</sub>CH<sub>2</sub>C<sub>6</sub>H<sub>5</sub></b>	289
<u>Acids</u>		
Acetic acid	<b>CH<sub>3</sub>C(O)—OH</b>	459.4 ± 4.2
Propionic acid	<b>C<sub>2</sub>H<sub>5</sub>C(O)—OH</b>	460.8 ± 8.4
Butyric acid	<b>C<sub>3</sub>H<sub>7</sub>C(O)—OH</b>	457.5
Valeric acid	<b>C<sub>4</sub>H<sub>9</sub>C(O)—OH</b>	458.8
Benzoic acid	<b>C<sub>6</sub>H<sub>5</sub>C(O)—OH</b>	447.7 ± 10.5
<u>Alcohols</u>		
Methanol	<b>HO—CH<sub>3</sub></b>	385.8 ± 0.8
Ethanol	<b>HO—CH<sub>2</sub>CH<sub>3</sub></b>	391.2 ± 2.9
1-Propanol	<b>HO—CH<sub>2</sub>CH<sub>2</sub>CH<sub>3</sub></b>	392.0 ± 2.9
2-Propanol	<b>HO—CH<sub>2</sub>(CH<sub>3</sub>)<sub>2</sub></b>	397.9 ± 4.2
1-Butanol	<b>HO—CH<sub>2</sub>CH<sub>2</sub>CH<sub>2</sub>CH<sub>3</sub></b>	389.9 ± 4.2
2-Butanol	<b>HO—CH<sub>2</sub>(CH<sub>3</sub>)(CH<sub>2</sub>CH<sub>3</sub>)</b>	396.1 ± 4.2
1-Pentanol	<b>HO—CH<sub>2</sub>CH<sub>2</sub>CH<sub>2</sub>CH<sub>2</sub>CH<sub>3</sub></b>	386.2 ± 6.3
2-Pentanol	<b>HO—CH<sub>2</sub>(CH<sub>3</sub>)(CH<sub>2</sub>CH<sub>2</sub>CH<sub>3</sub>)</b>	398.3 ± 4.2
3-Pentanol	<b>HO—CH<sub>2</sub>(CH<sub>2</sub>CH<sub>3</sub>)<sub>2</sub></b>	399.2 ± 4.2
1-Hexanol	<b>HO—CH<sub>2</sub>CH<sub>2</sub>CH<sub>2</sub>CH<sub>2</sub>CH<sub>2</sub>CH<sub>3</sub></b>	386.6 ± 8.4
2-Hexanol	<b>HO—CH<sub>2</sub>(CH<sub>3</sub>)(CH<sub>2</sub>CH<sub>2</sub>CH<sub>2</sub>CH<sub>3</sub>)</b>	400.0 ± 6.3
Cyclohexanol	<b><i>Cyclo</i>-C<sub>6</sub>H<sub>11</sub>—OH</b>	398.7 ± 6.3
Glycerol	<b>(HOCH<sub>2</sub>)<sub>2</sub>CH—OH</b>	335.6
	<b>HOCH<sub>2</sub>CH(OH)CH<sub>2</sub>—OH</b>	333.0
Ethenediol	<b>CH<sub>3</sub>CH(OH)—OH</b>	413.0
	<b>HOCH<sub>2</sub>CH<sub>2</sub>—OH</b>	338.9

## **Part B: A Review on Reactivity of Heterogeneous Metal Catalysts for Deoxygenation of Bio-Oil Model Compounds**

### **2.4 Introduction**

The use of metal catalysts in deoxygenation process has always been highly sought after due to their desired properties such as high catalytic activity, high turnover frequency, high chemical stability and small amount of catalysts required for catalysis. These catalytic properties would lead to a higher yield of desired deoxygenated products in a shorter reaction time as compared with a non-catalyzed deoxygenated process. In deoxygenation process, metal catalysts of various forms have been used to increase the rate of deoxygenation and to increase the yield of desired deoxygenated products. The metal catalyst can exist in the form of pure metals, metallic mixtures (bimetallic, trimetallic or metallic admixture), metal oxides, metal phosphides, metal nitrides or metal carbides (Boullosa-Eiras et al., 2014; He & Wang, 2012). The metal catalysts are commonly used in the form of solid for heterogeneous deoxygenation whereas the model compounds are in gas or liquid phase. In deoxygenation process, the metal catalyst has the following essential catalytic functions (Tanaka, 2010):

- Decreases the overall activation energy of deoxygenation through the formation of intermediates which are more readily to be deoxygenated.
- Acts as the active phase for the reactant to be adsorbed onto for oxygen abstraction or hydrogen insertion.
- Forms a temporary metal-reactant bond to weaken the C—O or C=O bonds for deoxygenation process.

The study of metal catalyst used in deoxygenation process is instrumental for the optimization of bio-oil deoxygenation process. This is because numerous works have shown the significant effects of physicochemical properties, electronic interactions and

chemical structures of various metal catalysts on the performance of deoxygenation processes. In this section, the discussion on the advances of existing heterogeneous metal-catalyzed deoxygenation processes to produce liquid fuel was provided. Reaction conditions and properties of metal catalysts such as metal type, metal loading, support type and preparation method were also discussed in order to give a better insight on metallic interactions in deoxygenation and also to establish several important selection criteria for an excellent deoxygenation metal catalyst.

## **2.5 Metal catalysts in deoxygenation processes**

In this section, a discussion on the role of heterogeneous supported metal catalysts in deoxygenation processes is presented. Several aspects of such catalysts to be reviewed would include the functions and mechanisms of respective metals as active sites, promoters or supports due to their respective physicochemical properties and electronic interactions. Effects of metal loading, supports and preparation methods of catalyst on deoxygenation process were also discussed in this section. This section covers only metal catalysts which were used in model compound studies, with the order of discussion ranging from the most commonly used to the scarcely used metal catalysts. The metals are usually of transition metals and some of the metals from alkali metal, alkaline earth metal (Mg), post-transition metal (Ga, Sn) categories. Several outlooks would also be given based on the tabulated trends of reaction parameters and their effects on the catalytic performances of metal catalysts in deoxygenation processes.

## 2.5.1 Effect of metal element

### 2.5.1.1 Pt-based catalyst

Platinum is a transition metal which is often classified as noble metals due to their high resistance to corrosion and oxidation. As a noble metal, the excellent hydrogenation activity was also observed in a Pt-based catalyst. The use of Pt-based catalysts has been reported in the deoxygenation of oxygenated compounds such as acetophenone (Alharbi et al., 2015), anisole (Zhu et al., 2011), benzofuran (Dickinson et al., 2012), *m*-cresol (Chen et al., 2015a; Zanuttini et al., 2013), difurfurylidene acetone (Li et al., 2015b), glycerol (Maris & Davis, 2007), guaiacol (Lee et al., 2016a; Nimmanwudipong et al., 2011a), methyl isobutyl ketone (Alotaibi et al., 2012b), methyl palmitate (Chen et al., 2016b), 4-propylphenol (Ohta et al., 2014), propanol (Peng et al., 2012) and propanoic acid (Lugo-José et al., 2014). The use of Pt-based catalysts in deoxygenation would often result in a saturation of aromatic rings or C=C bonds prior to the removal of oxygen containing functional group due to its high hydrogenation activity (Zanuttini et al., 2013). Nevertheless, the synergy of platinum metal with an acid support such as  $\gamma$ -Al<sub>2</sub>O<sub>3</sub> or zeolites was concluded to be capable of significantly enhancing the deoxygenation performance of Pt-based catalyst (Foster et al., 2012; Nimmanwudipong et al., 2011a). The bifunctional Pt catalyst with acidic support would have the H<sub>2</sub> activation at Pt site which has high H<sub>2</sub> sticking probability (Hong et al., 2014b) and the activation of oxygenated compound at the electrophilic acidic centers of acidic supports (Li et al., 2015b). Subsequently, H<sub>2</sub> spillover from Pt site to acidic support would enable a facile dehydration of the oxygenated compound. The use of acidic supported Pt-based catalyst does show a good deoxygenation performance but an extensive optimization of the metal to acid sites ratio and the acidic site strength is still required to minimize the severe coking of such metal-acid catalysts (Zanuttini et al., 2015).



The chemoselective hydrogenation of C=O bond or partial saturation of aromatic ring has also been reported when platinum was supported with an oxophilic support such as ZrO<sub>2</sub> or TiO<sub>2</sub> (Nie & Resasco, 2014). With an oxophilic support, the Pt-catalyzed deoxygenation mainly proceeded through the tautomerization pathway instead of the hydrogenation-dehydration pathway. Likewise, Hellinger et al. (2015) have also studied the effects of support on HDO activity of platinum catalyst and noted the reactivity order as: Pt/SiO<sub>2</sub> > Pt/Al<sub>2</sub>O<sub>3</sub> ≈ Pt/ZrO<sub>2</sub> > Pt/TiO<sub>2</sub> ≈ Pt/CeO<sub>2</sub>. In addition, Pt-based catalysts have also been noted to promote decarbonylation and decarboxylation pathways during the deoxygenation of alcohols, aldehydes, ketones and carboxylic acids as platinum catalyzes C—C bond cleavage to an extent (Lugo-José et al., 2014; Peng et al., 2012). However, the effectiveness of C—C bond cleavage by Pt is still low if it is compared with Ru (Maris & Davis, 2007) and Ni (Chen et al., 2015a). In terms of hydrogenation activity, the order proceeds as: Pt > Ru > Pd > Ni > Cu, indicating the preferential catalyzing effect of Pt on hydrogenation instead of C—C bond cleavage (Alharbi et al., 2015; Chen et al., 2015a). On an overall basis, Pt-based catalyst does provide excellent deoxygenation performance but owing to its exorbitant price, a cheaper non-noble metal may be suggested as an alternative instead for the reduction of process cost (Chen et al., 2013).

Based on Table 2.12, deoxygenation processes over Pt-based catalysts were carried out in liquid-solid or gas-solid phases with temperature range of 373 K to 673 K and pressure range of 1 bar to 220 bar. Hydrodeoxygenation, dehydration and hydrogenation were the major reaction pathways catalyzed by Pt-based catalysts during deoxygenation process. For vapor phase Pt-catalyzed deoxygenation processes, model compounds such as acetophenone, anisole, 2-propanol, methyl isobutyl ketone and *m*-cresol were able to be deoxygenated to their respective deoxygenated products at a high conversion ranging from 44% to 100% and a high selectivity ranging from 40% to

100%. The exceptional case would be the HDO of *m*-cresol to toluene over Pt/SiO<sub>2</sub> which only achieved 22% conversion and 40.9% selectivity. This is attributable to its catalytic deactivation by coking and fouling over prolonged reaction.

The effect of zeolite support was also studied by Alotaibi et al. (2012b) in which H-ZSM-5 zeolite supported Pt catalyst achieved the highest conversion of methyl isobutyl ketone (100%) and selectivity for 2-methylpentane (83%). H-ZSM-5 zeolite, being the best zeolite support in this case, has the optimal number of acid sites and molecular sieve size for the particular reaction. The effect of Pt loading was also noted in the HDO of *m*-cresol to toluene over Pt/ $\gamma$ -Al<sub>2</sub>O<sub>3</sub> by Zanuttini et al. (2013) whereby an increase in Pt loading from 0.05 wt% to 1.70 wt% was capable of increasing the selectivity for toluene from 46.4% to 86.11%. Likewise, the synergistic effects of various metals with Pt were also studied in the liquid phase HDO of 4-propylphenol to propylbenzene by Ohta et al. (2014) All the bimetallic zirconia supported Pt catalyst had a fixed metal ratio of 3 between Pt and a secondary metal. Metals such as Re, W, Ir and Au were found to increase the catalytic performances of Pt/ZrO<sub>2</sub> while Sn, Pd, Ga, Fe, In, Mo and Bi were found to decrease the catalytic performances of Pt/ZrO<sub>2</sub>.

**Table 2.12: Deoxygenation processes using Pt-based catalysts**

Entry	Metal Catalyst	Preparation Method	S <sub>BET</sub> (m <sup>2</sup> /g)	Type of Compound		Major Reaction Pathways	Reaction Parameters						Ref.
				Reactant	Product		Phase	Type	T (K)	P (bar)	X (%)	S (%)	
1	Pt/CsPW (0.5 wt% Pt)	Wet impregnation	128	Acetophenone	Ethylcyclohexane	Hydrogenation Dehydration	G-S	Continuous	373	1	74	98	(Alharbi et al., 2015)
2	Pt/Al <sub>2</sub> O <sub>3</sub> (3.0 wt% Pt)	Dry impregnation	88	2-Propanol	Propane	Hydrodeoxygenation	G-S	Continuous	523	1.01	99	98	(Peng et al., 2012)
3	Pt/CsPW (0.5 wt% Pt)	Wet impregnation	128	Methyl isobutyl ketone	2-Methylpentane	Hydrogenation Dehydration	G-S	Continuous	373	1	100	100	(Alharbi et al., 2015)
4	Pt/SiO <sub>2</sub> (0.5 wt% Pt)	Wet impregnation	287	Methyl isobutyl ketone	2-Methylpentane	Hydrogenation Dehydration	G-S	Continuous	473	1.01	46	47	(Alotaibi et al., 2012b)
5	Pt/C (10 wt% Pt)	-	801	Methyl isobutyl ketone	2-Methylpentane	Hydrogenation Dehydration	G-S	Continuous	473	1.01	47	40	(Alotaibi et al., 2012b)
6	Pt/H-ZSM-5 (0.30 wt% Pt)	Ion exchange	362	Methyl isobutyl ketone	2-Methylpentane	Hydrogenation Dehydration	G-S	Continuous	373	1.01	94	65	(Alotaibi et al., 2012b)
7	Pt/H-ZSM-5 (0.30 wt% Pt)	Ion exchange	362	Methyl isobutyl ketone	2-Methylpentane	Hydrogenation Dehydration	G-S	Continuous	473	1.01	100	83	(Alotaibi et al., 2012b)
8	Pt/H-Beta (0.39 wt% Pt)	Ion exchange	491	Methyl isobutyl ketone	2-Methylpentane	Hydrogenation Dehydration	G-S	Continuous	473	1.01	44	70	(Alotaibi et al., 2012b)
9	Pt/HY (0.45 wt% Pt)	Ion exchange	690	Methyl isobutyl ketone	2-Methylpentane	Hydrogenation Dehydration	G-S	Continuous	473	1.01	81	55	(Alotaibi et al., 2012b)
10	Pt/γ-Al <sub>2</sub> O <sub>3</sub> (0.05 wt% Pt)	Wet impregnation	193.1	<i>m</i> -Cresol	Toluene	Hydrodeoxygenation	G-S	Continuous	573	1.01	100	46.4	(Zanuttini et al., 2013)
11	Pt/γ-Al <sub>2</sub> O <sub>3</sub> (0.50 wt% Pt)	Wet impregnation	195	<i>m</i> -Cresol	Toluene	Hydrodeoxygenation	G-S	Continuous	573	1.01	100	56.8	(Zanuttini et al., 2013)
12	Pt/γ-Al <sub>2</sub> O <sub>3</sub> (1.70 wt% Pt)	Wet impregnation	214	<i>m</i> -Cresol	Toluene	Hydrodeoxygenation	G-S	Continuous	573	1.01	100	86.1	(Zanuttini et al., 2013)
13	Pt/SiO <sub>2</sub> (1.0 wt% Pt)	Dry impregnation	200	<i>m</i> -Cresol	Toluene	Hydrodeoxygenation	G-S	Continuous	523	1.01	97.5	49.8	(Chen et al., 2015a)
14	Pt/SiO <sub>2</sub> (1.0 wt% Pt)	Dry impregnation	135	<i>m</i> -Cresol	Toluene	Hydrodeoxygenation	G-S	Continuous	573	1.01	22	40.9	(Nie & Resasco, 2014)
15	Pt/SiO <sub>2</sub> (1.0 wt% Pt)	Dry impregnation	-	Anisole	Benzene	Hydrodeoxygenation	G-S	Continuous	673	1.01	100	69.2	(Zhu et al., 2011)
16	Pt/C (5 wt% Pt)	-	-	Benzofuran	Ethylbenzene	Hydrodeoxygenation	L-S	Batch	653	220	100	50	(Dickinson et al., 2012)
17	Pt/SAPO-11 (0.33 wt% Pt)	Dry impregnation	113	Methyl palmitate	<i>n</i> -C <sub>15,16</sub> alkanes	Decarbonylation Decarboxylation	L-S	Continuous	648	30	81.3	50.4	(Chen et al., 2016b)
18	Pt/H-MFI-90 (1.0 wt% Pt)	Dry impregnation	414	Guaiacol	Cyclohexane	Hydrodeoxygenation	L-S	Batch	453	50	100	93	(Hellinger et al., 2015)

‘Table 2.12, continued’

Entry	Metal Catalyst	Preparation Method	S <sub>BET</sub> (m <sup>2</sup> /g)	Type of Compound		Major Reaction Pathways	Reaction Parameters						Ref.
				Reactant	Product		Phase	Type	T (K)	P (bar)	X (%)	S (%)	
19	Pt/Al <sub>2</sub> O <sub>3</sub> (0.5 wt% Pt)	-	116	Furfurylidene acetone	Octane	Hydrodeoxygenation	L-S	Batch	473	55	95	38	(Faba et al., 2014)
20	Pt/C (3.0 wt% Pt)	-	-	Glycerol	Propylene glycol	Dehydration	L-S	Batch	473	40	13	79	(Maris & Davis, 2007)
21	Pt/C with 0.8 M NaOH (3.0 wt% Pt)	-	-	Glycerol	Propylene glycol	Dehydration	L-S	Batch	473	40	92	46	(Maris & Davis, 2007)
22	Pt/C with 0.8 M CaO (3.0 wt% Pt)	-	-	Glycerol	Propylene glycol	Dehydration	L-S	Batch	473	40	100	36	(Maris & Davis, 2007)
23	Pt-Re/ZrO <sub>2</sub> (2.0 wt% Pt)	Coprecipitation	-	4-Propylphenol	Propylbenzene	Hydrodeoxygenation	L-S	Batch	573	20	67	85	(Ohta et al., 2014)
24	Pt-W/ZrO <sub>2</sub> (2.0 wt% Pt)	Coprecipitation	-	4-Propylphenol	Propylbenzene	Hydrodeoxygenation	L-S	Batch	573	20	66	50	(Ohta et al., 2014)
25	Pt-Ir/ZrO <sub>2</sub> (2.0 wt% Pt)	Coprecipitation	-	4-Propylphenol	Propylbenzene	Hydrodeoxygenation	L-S	Batch	573	20	65	66	(Ohta et al., 2014)
26	Pt-Au/ZrO <sub>2</sub> (2.0 wt% Pt)	Coprecipitation	-	4-Propylphenol	Propylbenzene	Hydrodeoxygenation	L-S	Batch	573	20	63	59	(Ohta et al., 2014)
27	Pt/ZrO <sub>2</sub> (2.0 wt% Pt)	Coprecipitation	72	4-Propylphenol	Propylbenzene	Hydrodeoxygenation	L-S	Batch	573	20	62	65	(Ohta et al., 2014)
28	Pt-Sn/ZrO <sub>2</sub> (2.0 wt% Pt)	Coprecipitation	-	4-Propylphenol	Propylbenzene	Hydrodeoxygenation	L-S	Batch	573	20	61	72	(Ohta et al., 2014)
29	Pt-Pd/ZrO <sub>2</sub> (2.0 wt% Pt)	Coprecipitation	-	4-Propylphenol	Propylbenzene	Hydrodeoxygenation	L-S	Batch	573	20	59	56	(Ohta et al., 2014)
30	Pt-Ga/ZrO <sub>2</sub> (2.0 wt% Pt)	Coprecipitation	-	4-Propylphenol	Propylbenzene	Hydrodeoxygenation	L-S	Batch	573	20	58	67	(Ohta et al., 2014)
31	Pt-Fe/ZrO <sub>2</sub> (2.0 wt% Pt)	Coprecipitation	-	4-Propylphenol	Propylbenzene	Hydrodeoxygenation	L-S	Batch	573	20	54	63	(Ohta et al., 2014)
32	Pt-In/ZrO <sub>2</sub> (2.0 wt% Pt)	Coprecipitation	-	4-Propylphenol	Propylbenzene	Hydrodeoxygenation	L-S	Batch	573	20	51	47	(Ohta et al., 2014)
33	Pt-Mo/ZrO <sub>2</sub> (2.0 wt% Pt)	Coprecipitation	-	4-Propylphenol	Propylbenzene	Hydrodeoxygenation	L-S	Batch	573	20	8.8	56	(Ohta et al., 2014)
34	Pt-Bi/ZrO <sub>2</sub> (2.0 wt% Pt)	Coprecipitation	-	4-Propylphenol	Propylbenzene	Hydrodeoxygenation	L-S	Batch	573	20	4.4	50	(Ohta et al., 2014)

### 2.5.1.2 Ni-based catalyst

Nickel is also one of the transition metals which had been commonly studied for deoxygenation processes. The Ni-based catalysts for deoxygenation processes could exist as monometallic nickel or bimetallic nickel-based catalysts in supported or unsupported form, in which bimetallic nickel-based catalysts were noted to have better deoxygenation performances due to various synergistic metallic effects. For deoxygenation of phenolic compounds, Ni-based catalysts are also highly active for the hydrogenation of aromatic rings due to the high hydrogenation activity of nickel (Jin et al., 2014). The high hydrogenation activity of nickel was also reported in the hydrogenation of levulinic acid to  $\gamma$ -valerolactone (Hengst et al., 2015); *m*-cresol to 3-methylcyclohexanol (Chen et al., 2015a; Nie et al., 2014); dimethyl oxalate to methyl glycolate (Chen et al., 2016a) and 1,5-dinitronaphthalene to 1,5-diaminonaphthalene (Xiong et al., 2016). In addition, nickel was also reported to favor successive hydrogenolysis of C—C bond (Tran et al., 2016), leading to ring opening of furans or formation of shorter chained hydrocarbons such as methane at high temperature (Chen et al., 2015a).

The deoxygenation of compounds such as anisole (Jin et al., 2014; Yang et al., 2014), dibenzofuran (Ambursa et al., 2016), difurfurylidene acetone (Li et al., 2015b), guaiacol (Bykova et al., 2012), *m*-cresol (Nie et al., 2014), methyl laurate (Shi et al., 2014), methyl stearate (Qian et al., 2014), oleic acid (Ayodele et al., 2014), palmitic acid (Miao et al., 2016), phenol (Zhao et al., 2012b), triglyceride (Morgan et al., 2012; Santillan-Jimenez et al., 2014), stearic acid (Kumar et al., 2014) over Ni-based catalysts have been investigated. Over Ni-based catalysts, the direct scission of C—O bond was minimal while hydrogenation, decarbonylation and decarboxylation reactions were often observed instead (Kubička & Kaluža, 2010; Srifa et al., 2015). Nickel metal has a lower electrophilicity as compared with other metals such as molybdenum, making it to

be less favorable for the activation and direct scission of C=O and C—O bonds (Shi et al., 2014). Nevertheless, this can be circumvented by synergizing nickel with another electrophilic metal such as molybdenum in order to improve its deoxygenation activity (Pan et al., 2015). With the synergistic metal effects, several desired properties of Ni-based catalysts have also been acquired such as higher Ni dispersion (Morgan et al., 2012); lower gasification activity (Dickinson & Savage, 2014) and higher direct deoxygenation selectivity (Shafaghat et al., 2016; Wang et al., 2009).

Based on Table 2.13, deoxygenation processes over Ni-based catalysts were carried out in liquid-solid or gas-solid phases with temperature range of 483 K to 623 K and pressure range of 1.01 bar to 170 bar. Hydrodeoxygenation, decarboxylation, decarbonylation, dehydrogenation and hydrogenation were the major reaction pathways catalyzed by Ni-based catalysts during deoxygenation processes. With the use of Ni-based catalysts, model compounds such as anisole, phenol, guaiacol, *m*-cresol, dibenzofuran, 2-methyltetrahydrofuran, stearic acid, palmitic acid, ethyl heptanoate and methyl laurate were able to be fully deoxygenated to their respective deoxygenated products with conversion ranging from 21.7% to 100% and selectivity ranging from 27.9% to 99%. There were many Ni-based catalysts which have excellent deoxygenation activity for anisole. If cyclohexane was the desired product, then Ni/SiO<sub>2</sub> catalyst would be preferred for the deoxygenation of anisole in liquid phase at 483 K and 30 bar due to its highest specific yield of cyclohexane. If aromatics such as benzene, toluene and xylene were the desired products, then Ni/CeO<sub>2</sub> catalyst would be preferred for the deoxygenation of anisole in vapor phase at 563 K and 3 bar due to its highest specific yield of aromatics. For the deoxygenation of methyl laurate to *n*-undecane and *n*-dodecane, Ni<sub>2</sub>P/SiO<sub>2</sub> catalyst would be preferred as it had the highest conversion (99%) and selectivity (99%) among the Ni-based catalysts.

**Table 2.13: Deoxygenation processes using Ni-based catalysts**

Entry	Metal Catalyst	Preparation Method	S <sub>BET</sub> (m <sup>2</sup> /g)	Pore Size (nm)	Acidity (mmol/g)	Type of Compound		Major Reaction Pathways	Reaction Parameters					Ref.	
						Reactant	Product		Phase	Type	T (K)	P (bar)	X (%)		S (%)
1	Ni/Al-SBA-15 (20 wt% Ni)	Wet impregnation	563	8.0	0.212	Anisole	Cyclohexane	Hydrodeoxygenation Hydrogenation	G-S	Continuous	563	3	100	60	(Yang et al., 2014)
2	Ni/CeO <sub>2</sub> (20 wt% Ni)	Wet impregnation	57	14.9	0.151	Anisole	Aromatics	Hydrodeoxygenation	G-S	Continuous	563	3	90	55	(Yang et al., 2014)
3	Ni/C (20 wt% Ni)	Wet impregnation	1410	-	0.099	Anisole	Aromatics	Hydrodeoxygenation	G-S	Continuous	563	3	98	50	(Yang et al., 2014)
4	Ni/SBA-15 (20 wt% Ni)	Wet impregnation	513	8.1	0.099	Anisole	Cyclohexane	Hydrodeoxygenation Hydrogenation	G-S	Continuous	563	3	100	70	(Yang et al., 2014)
5	Ni/Al <sub>2</sub> O <sub>3</sub> (20 wt% Ni)	Wet impregnation	153	9.3	0.213	Anisole	Cyclohexane	Hydrodeoxygenation Hydrogenation	G-S	Continuous	563	3	100	56	(Yang et al., 2014)
6	Ni/TiO <sub>2</sub> (20 wt% Ni)	Wet impregnation	46	26.8	0.064	Anisole	Aromatics	Hydrodeoxygenation	G-S	Continuous	563	3	50	75	(Yang et al., 2014)
7	Ni/SiO <sub>2</sub> (5.0 wt% Ni)	Dry impregnation	186	-	-	<i>m</i> -Cresol	Toluene	Hydrodeoxygenation	G-S	Continuous	523	1.01	100	71.5	(Chen et al., 2015a)
8	Ni-Mo-S (0.43 Ni/Mo molar ratio)	Thermal decomposition	29	-	-	Ethyl Heptanoate	Hexane	Decarboxylation	G-S	Continuous	523	15	21.7	27.9	(Ruinart de Brimont et al., 2012)
9	Ni/γ-Al <sub>2</sub> O <sub>3</sub> -HZSM- 5 (9.3 wt% Ni)	Wet impregnation	-	-	0.091	Phenol	Cyclohexane	Hydrodeoxygenation	L-S	Batch	493	50	84	53	(Zhao et al., 2012b)
10	Ni-Mo-S (0.43 Ni/Mo molar ratio)	Hydrothermal	268	-	-	Phenol	Cyclohexane	Hydrodeoxygenation	L-S	Batch	623	28	96.2	61.8	(Yoosuk et al., 2012)
11	NiCu/SiO <sub>2</sub> -ZrO <sub>2</sub> (52 wt% Ni, 5.6 wt% Cu)	Sol-gel	188	-	-	Guaiacol	Cyclohexane	Hydrodeoxygenation	L-S	Batch	593	170	95	70.5	(Bykova et al., 2014)
12	Ni <sub>2</sub> P/SiO <sub>2</sub> (7.9 wt% Ni)	Dry impregnation	214	-	0.055	2-methyl tetrahydrofuran	Pentane	Hydrodeoxygenation	L-S	Continuous	623	5	99.5	85	(Iino et al., 2014)
13	Ni <sub>2</sub> P/SiO <sub>2</sub> (5.0 wt% Ni)	Dry impregnation	162	-	-	Dibenzofuran	Bicyclohexane	Hydrodeoxygenation	L-S	Continuous	573	30	90	80	(Cecilia et al., 2013)
14	Ni/HBeta (4.94 wt% Ni)	Dry impregnation	463	-	0.53	50 wt% Phenol, 25 wt% <i>o</i> -Cresol, 25 wt% Guaiacol	Cycloalkanes	Hydrodeoxygenation	L-S	Batch	573	16	-	21.39	(Shafaghat et al., 2016)
15	NiFe/HBeta (4.95 wt% Ni, 4.98 wt% Fe)	Dry impregnation	417	-	0.38	50 wt% Phenol, 25 wt% <i>o</i> -Cresol, 25 wt% Guaiacol	Aromatics	Hydrodeoxygenation	L-S	Batch	573	16	-	29.48	(Shafaghat et al., 2016)
16	Ni/SiO <sub>2</sub> (10.4 wt% Ni)	Dry impregnation	191	-	0.01	Stearic acid	Heptadecane	Dehydrogenation Decarbonylation	L-S	Batch	543	13.5	80	76.6 (X=40%)	(Kumar et al., 2014)

‘Table 2.13, continued’

Entry	Metal Catalyst	Preparation Method	S <sub>BET</sub> (m <sup>2</sup> /g)	Pore Size (nm)	Acidity (mmol/g)	Type of Compound		Major Reaction Pathways	Reaction Parameters					Ref.	
						Reactant	Product		Phase	Type	T (K)	P (bar)	X (%)		S (%)
17	Ni/Al <sub>2</sub> O <sub>3</sub> (8.1 wt% Ni)	Dry impregnation	201	-	0.26	Stearic acid	Heptadecane	Dehydrogenation Decarbonylation	L-S	Batch	543	13.5	40	90.7	(Kumar et al., 2014)
18	Ni/HZSM (10.2 wt% Ni)	Dry impregnation	353	-	0.60	Stearic acid	Heptadecane	Dehydrogenation Decarbonylation	L-S	Batch	543	13.5	40	39	(Kumar et al., 2014)
19	Ni/γ-Al <sub>2</sub> O <sub>3</sub> (9.3 wt% Ni)	Dry impregnation	229	7.0	0.163	Anisole	Cyclohexyl methyl ether	Hydrogenation	L-S	Batch	483	30	100	57	(Jin et al., 2014)
20	Ni/SBA-15 (10.3 wt% Ni)	Dry impregnation	662	6.0	0.190	Anisole	Cyclohexane	Hydrodeoxygenation	L-S	Batch	483	30	100	70	(Jin et al., 2014)
21	Ni/AC (10.2 wt% Ni)	Dry impregnation	1293	1.9	0.292	Anisole	Cyclohexyl methyl ether	Hydrogenation	L-S	Batch	483	30	100	74	(Jin et al., 2014)
22	Ni/SiO <sub>2</sub> (9.0 wt% Ni)	Dry impregnation	549	2.2	0.205	Anisole	Cyclohexane	Hydrodeoxygenation	L-S	Batch	483	30	100	95	(Jin et al., 2014)
23	Ni/ZrO <sub>2</sub> (10 wt% Ni)	Dry impregnation	-	-	-	Palmitic acid	Pentadecane	Decarbonylation Decarboxylation	L-S	Batch	573	55.2	100	30.2	(Miao et al., 2016)
24	Ni <sub>2</sub> P/CeO <sub>2</sub>	Dry impregnation	53	7.8	0.044	Methyl laurate	<i>n</i> -C <sub>11,12</sub> alkanes	Hydrodeoxygenation Decarbonylation	L-S	Continuous	613	20	70	84	(Shi et al., 2014)
25	Ni <sub>2</sub> P/SAPO-11	Dry impregnation	58	11.6	0.384	Methyl laurate	<i>n</i> -C <sub>11,12</sub> alkanes	Hydrodeoxygenation Decarbonylation	L-S	Continuous	613	20	76	93	(Shi et al., 2014)
26	Ni <sub>2</sub> P/TiO <sub>2</sub>	Dry impregnation	21	2.1	0.070	Methyl laurate	<i>n</i> -C <sub>11,12</sub> alkanes	Hydrodeoxygenation Decarbonylation	L-S	Continuous	613	20	95	96	(Shi et al., 2014)
27	Ni <sub>2</sub> P/SiO <sub>2</sub>	Dry impregnation	411	5.6	0.420	Methyl laurate	<i>n</i> -C <sub>11,12</sub> alkanes	Hydrodeoxygenation Decarbonylation	L-S	Continuous	613	20	99	99	(Shi et al., 2014)



### 2.5.1.3 Pd-based catalyst

Palladium is a transition metal which is also known as noble metal and it exhibits high hydrogenation activity for many chemical processes. Its excellent hydrogenation activity has been observed in numerous conventional hydrogenation process and in some of the processes currently being studied such as the hydrogenation of maleic anhydride to  $\gamma$ -butyrolactone (Jung et al., 2003; Pillai et al., 2003); nitrobenzyl ethers to aminobenzyl ethers (Chen et al., 2015b); 4-carboxybenzaldehyde to *p*-toluic acid (Zhu et al., 2015); *p*-chloronitrobenzene (Cárdenas-Lizana et al., 2014) and nitrobenzene (Turáková et al., 2015) to aniline. Likewise, Pd-based catalysts have also been commonly studied in the deoxygenation processes of several model compounds such as benzophenone (Bejblová et al., 2005), furfurylideneacetone (Faba et al., 2014), benzyl phenyl ether (Kim et al., 2015), *m*-cresol (Hong et al., 2014b), guaiacol (Gutierrez et al., 2009; Hong et al., 2014a), phenol (Echeandia et al., 2014), lauric acid (Bernas et al., 2010; Mäki-Arvela et al., 2008), oleic acid (Dragu et al., 2015), palmitic acid and stearic acid (Sapunov et al., 2017; Simakova et al., 2009).

The direct removal of oxygen is not readily favored by Pd-based catalysts, owing to the hydrogenation nature of palladium. Rather, the saturation of aromatic or furanic rings often occurs prior to the scission of C—O bond since Pd surface shows a stronger surface-adsorbate interaction with aromatic ring than with C—O or C=O bonds (Hensley et al., 2014b). The preferential hydrogenation of aromatic rings by Pd-based catalyst was also further been corroborated in the deoxygenation of benzyl phenyl ether (Kim et al., 2015) and phenol (Zhao et al., 2011). Similarly, Pd-based catalysts often hydrogenate carbonyl group into alcohol for further hydrogenolysis during the deoxygenation of carbonyl compounds. This mechanism is often known as the hydrogenation-hydrogenolytic mechanism (Bejblová et al., 2005; Procházková et al., 2007). As for the deoxygenation of esters, Pd-based catalysts often favor

decarboxylation and decarbonylation pathways (Bernas et al., 2010; Mäki-Arvela et al., 2008). Similar reaction pathways have also been proposed by several raw feed deoxygenation studies using woody tar (Mochizuki et al., 2014), *Jatropha* residue (Kaewpengkrow et al., 2014), castor oil (Meller et al., 2014) and macauba oil (Silva et al., 2016).

Nevertheless, Pd-based catalysts also have certain desirable properties for deoxygenation. Hensley et al. (2014a) stated that palladium has an excellent H<sub>2</sub> sticking coefficient over catalyst surface and synergistic electronic interaction. An excellent H<sub>2</sub> sticking coefficient would enable a facile H<sub>2</sub> activation at palladium surface and H<sub>2</sub> spillover to active sites. Thus, Pd-based catalysts which have acidic support sites are often bifunctionalized due to the facile hydrogenation by palladium and dehydration by acidic sites (Dragu et al., 2015) to exhibit higher HDO activity (Echeandia et al., 2014). In addition, palladium is also efficient in debenzylolation in which the methylbenzene formed can be retrieved as deoxygenated product (Chen et al., 2015b).

Based on Table 2.14, deoxygenation processes over Pd-based catalysts were carried out in liquid-solid or gas-solid phases with temperature range of 403 K to 573 K and pressure range of 1.01 bar to 60 bar. Hydrodeoxygenation, decarbonylation, decarboxylation and hydrogenation were the major reaction pathways catalyzed by Pd-based catalysts during deoxygenation processes. With the use of Pd-based catalysts, model compounds such as phenol, *m*-cresol, guaiacol, benzophenone, furfurylidene acetone, benzaldehyde, benzyl phenyl ether, lauric acid, oleic acid and palmitic acid were able to be fully deoxygenated to their respective deoxygenated products with conversion ranging from 20% to 100% and selectivity ranging from 22.2% to 100%. For the deoxygenation of palmitic acid to pentadecane, Pd/C and Pd/CNT catalysts of different preparation methods were used by Simakova et al. (2009) and Ding et al.

(2015) respectively. It can be inferred from the results that the increase of pressure from 17.5 bar (Simakova et al., 2009) to 40 bar (Ding et al., 2015) had negligible improvement on the conversion and selectivity of the process. However, the doping of Fe in Pd-Fe/OMC catalyst in the study of benzyl phenyl ether HDO by Kim et al. (2015) did help to improve the selectivity of toluene from 17.3% to 45.1%. Since Pd is an excellent hydrogenating metal, additional doping metal such as Fe is necessary to minimize the excessive hydrogenation of aromatic deoxygenated products. Likewise, a combination of 20% of HY zeolite and 80% of  $\gamma$ -Al<sub>2</sub>O<sub>3</sub> support was also found to have the optimal pore size and number of acid site for the HDO of phenol (Echeandia et al., 2014), thus having the best conversion of phenol (57%) and overall selectivity for cyclohexane and cyclohexene (93%) as compared with the use of HY zeolite and  $\gamma$ -Al<sub>2</sub>O<sub>3</sub> support separately.

**Table 2.14: Deoxygenation processes using Pd-based catalysts**

Entry	Metal Catalyst	Preparation Method	S <sub>BET</sub> (m <sup>2</sup> /g)	Pore Size (nm)	Acidity (mmol/g)	Type of Compound		Major Reaction Pathways	Reaction Parameters					Ref.	
						Reactant	Product		Phase	Type	T (K)	P (bar)	X (%)		S (%)
1	Pd/Fe <sub>2</sub> O <sub>3</sub> (5.0 wt% Pd)	Dry impregnation	40	-	-	<i>m</i> -Cresol	Benzene-Toluene-Xylene	Hydrodeoxygenation	G-S	Continuous	573	-	56	92	(Hong et al., 2014b)
2	Pd/SiO <sub>2</sub> (1.0 wt% Pd)	Dry impregnation	197	-	-	<i>m</i> -Cresol	Toluene	Hydrodeoxygenation	G-S	Continuous	523	1.01	99.8	68.4	(Chen et al., 2015a)
3	Pd/ZrO <sub>2</sub> (2.24 wt% Pd)	Dry impregnation	84	-	0.101	Phenol	Benzene	Hydrodeoxygenation	G-S	Continuous	573	1.01	75	54	(de Souza et al., 2015)
4	Pd/C (5.0 wt% Pd)	Impregnation	-	-	-	Benzophenone	Diphenylmethane	Hydrogenation-hydrogenolytic mechanism	L-S	Batch	403	60	100	98.8	(Bejblová et al., 2005)
5	Pd/C (1.0 wt% Pd)	Deposition	379	-	-	Palmitic acid	Pentadecane	Decarbonylation Decarboxylation	L-S	Semibatch	573	17.5	95	80	(Simakova et al., 2009)
6	Pd/CNT (5.0 wt% Pd)	Dry impregnation	234.5	2.7	-	Palmitic acid	Pentadecane	Decarbonylation Decarboxylation	L-S	Batch	553	40	95.8	78.3	(Ding et al., 2015)
7	Pd/MB (14.2 wt% Pd)	Impregnation	274	-	-	Oleic acid	Heptadecane	Decarbonylation Decarboxylation	L-S	Batch	573	20.3	100	70.5	(Dragu et al., 2015)
8	Pd/OMC (9.8 wt% Pd)	Dry impregnation	732	3.93	-	Benzyl phenyl ether	Toluene	Hydrodeoxygenation	L-S	Batch	523	10	93	17.3	(Kim et al., 2015)
9	Pd-Fe/OMC (4.9 wt% Pd, 4.5 wt% Fe)	Dry impregnation	778	3.99	-	Benzyl phenyl ether	Toluene	Hydrodeoxygenation	L-S	Batch	523	10	88.5	45.1	(Kim et al., 2015)
10	Pd/C (5.0 wt% Pd)	Dry impregnation	845	3.6	-	Phenol	Cyclohexane	Hydrodeoxygenation	L-S	Batch	473	50	99	85	(Zhao et al., 2011)
11	Pd/WO <sub>3</sub> /γ-Al <sub>2</sub> O <sub>3</sub> (2.0 wt% Pd, 32 wt% W)	Dry impregnation	157.3	-	0.440	Guaiacol	Cyclohexane	Hydrodeoxygenation	L-S	Batch	573	70	100	88.4	(Hong et al., 2014a)
12	Pd/Al <sub>2</sub> O <sub>3</sub> (0.5 wt% Pd)	-	92	18.2	1.491	Furfurylidene acetone	Octane	Hydrodeoxygenation	L-S	Batch	473	55	95	25	(Faba et al., 2014)
13	Pd/C (5 wt% Pd)	Impregnation	976 (Support)	-	-	Benzaldehyde	Toluene	Hydrodeoxygenation	L-S	Batch	403	60	99	28	(Procházková et al., 2007)
14	Pd/Beta (35) (5 wt% Pd)	Impregnation	510 (Support)	-	-	Benzaldehyde	Toluene	Hydrodeoxygenation	L-S	Batch	403	60	99	93	(Procházková et al., 2007)
15	Pd/ZSM-5 (140) (5 wt% Pd)	Impregnation	325 (Support)	-	-	Benzaldehyde	Toluene	Hydrodeoxygenation	L-S	Batch	403	60	99	22.2	(Procházková et al., 2007)
16	Pd/C (5 wt% Pd)	-	1214	-	-	Lauric acid	Undecane	Decarboxylation	L-S	Continuous	543	10	100	100	(Mäki-Arvela et al., 2008)
17	Pd/γ-Al <sub>2</sub> O <sub>3</sub> (0.81 wt% Pd)	Wet impregnation	154	12.7	1.3	Phenol	Cyclohexene Cyclohexane	Hydrodeoxygenation Hydrogenation	L-S	Continuous	573	15	35	98	(Echeandia et al., 2014)
18	Pd/10%HY-γ-Al <sub>2</sub> O <sub>3</sub> (0.77 wt% Pd)	Wet impregnation	179	11.0	1.7	Phenol	Cyclohexene Cyclohexane	Hydrodeoxygenation Hydrogenation	L-S	Continuous	573	15	22	97	(Echeandia et al., 2014)
19	Pd/20%HY-γ-Al <sub>2</sub> O <sub>3</sub> (0.80 wt% Pd)	Wet impregnation	194	10.2	2.5	Phenol	Cyclohexene Cyclohexane	Hydrodeoxygenation Hydrogenation	L-S	Continuous	573	15	57	93	(Echeandia et al., 2014)
20	Pd/HY (0.77 wt% Pd)	Wet impregnation	476	8.9	4.8	Phenol	Cyclohexene Cyclohexane	Hydrodeoxygenation Hydrogenation	L-S	Continuous	573	15	20	58	(Echeandia et al., 2014)

#### 2.5.1.4 Cu-based catalyst

Numerous Cu-based catalysts have been reported in the deoxygenation studies of various model compounds. For instance, Cu-based catalysts which were used in the hydrogenolysis of glycerol were Cu-ZrO<sub>2</sub> (Durán-Martín et al., 2013), Ru-Cu/Al<sub>2</sub>O<sub>3</sub> and Ru-Cu/ZrO<sub>2</sub> (Soares et al., 2016). Cu crystallites were reported to be the active sites in catalyzing the hydrogenolysis of glycerol for the selective 1,2-propanediol formation as ZrO<sub>2</sub> exhibited a higher glycerol conversion but negligible yield of 1,2-propanediol in the absence of Cu (Durán-Martín et al., 2013). The synergy of Cu with other metal elements was also noticed in bimetallic catalyst for glycerol hydrogenolysis. The formation of smaller Cu crystallites is desirable for the increase in hydrogenolysis activity and is favored in the presence of ZrO<sub>2</sub>. Likewise, Cu is a transition metal which has a completely filled and narrow *d*-orbital that can function as a stabilizer for the reduced metallic particles in Ru-Cu catalysts (Soares et al., 2016). The stabilization of the reduced metallic particles is required for the selective formation of 1,2-propanediol from glycerol without the cleavage of C—C bonds.

Cu-based catalysts such as Cu/ZnO/ZrO<sub>2</sub> (Zhang et al., 2009) and Cu/ZnO/TiO (Hu et al., 2007; Zhang et al., 2008) were also studied for the catalytic conversion of maleic anhydride into  $\gamma$ -butyrolactone and tetrahydrofuran. The ZnO was noted to favor the selective hydrogenation of maleic anhydride to  $\gamma$ -butyrolactone whereas Cu and ZrO<sub>2</sub> species were noted to favor the deep hydrogenation of  $\gamma$ -butyrolactone to tetrahydrofuran (Zhang et al., 2009). The loadings of foreign phases such as ZnO, ZrO<sub>2</sub> and TiO in the Cu-based catalysts were also beneficial as they enable the formation of small crystallite sized metallic copper (Hu et al., 2007). Peng et al. (2010) also asserted that ZnO species helps in achieving a high dispersion of Cu phase in Cu-Zn/Al<sub>2</sub>O<sub>3</sub> catalyst for the hydrogenation of esters to alcohols. Similarly, the addition of cerium

also improves the Cu dispersion, minimizes Cu aggregation and enables surface enrichment of  $\text{Cu}^+$  species for hydrogenation of methyl acetate to alcohol (Ye et al., 2016).

The aforementioned synergistic effects are essential as the hydrogenation activity of Cu increases with the decrease of copper crystallite size and the increase of lattice distortion degree of CuO structure (Zhang et al., 2008). Generally,  $\text{Cu}^+$  and  $\text{Cu}^0$  species are the important phases for the hydrogenation activity of Cu-based catalysts (Di et al., 2016; Qin et al., 2015). In addition, the hydrogenation activity of Cu species can also be enhanced by having a synergistic metal such as Fe to electronically interact with Cu (He et al., 2014). Additional interactions of Cu with other non-transitional metals were also reported. Copper doping was also reported to promote micropores formation in  $\beta$ -zeolite while an excess of doped copper ( $>1.0$  wt% Cu) will lead to formation of Cu aggregates on surface zeolite which blocks the pores of zeolite (Widayatno et al., 2016). Likewise, copper which has complete filling of  $d$  orbitals tends to repel phenyl groups, causing aromatics such as acetophenone to preferentially adsorb on copper surface through the C=O bond instead of the aromatic ring.

Several Cu-based catalysts have also been reported with favorable results for their usage in the deoxygenation processes. Ambursa et al. (2016) have evaluated the hydrodeoxygenation of dibenzofuran to bicyclohexyl-1-ene over  $\text{NiCu/ZrO}_2$ ,  $\text{NiCu/CeO}_2$  and  $\text{NiCu/TiO}_2$  catalysts and listed the bicyclohexyl-1-ene selectivity in this order:  $\text{NiCu/ZrO}_2$  (95%),  $\text{NiCu/CeO}_2$  (83%) and  $\text{NiCu/TiO}_2$  (61%). Likewise, several aromatic ketones such as benzhydrol, tetralone, 9-fluorenone, benzophenone and 9,10-anthraquinone were also reported to be readily deoxygenated ( $>84\%$  conversion) in the presence of  $\text{Cu/SiO}_2$  catalyst and toluene at  $90^\circ\text{C}$  and 1 atm  $\text{H}_2$  into deoxygenated polyaromatics. The deoxygenation of 1,3-propanediol on  $\text{Cu/ZnO/Al}_2\text{O}_3$  was also found

to preferentially occur through hydrogenolysis, decarboxylation and decarbonylation of propanol-propanal equilibrium mixture by copper (Sad et al., 2011).

Based on Table 2.15, deoxygenation processes over Cu-based catalysts were carried out in liquid-solid or gas-solid phases with temperature range of 363 K to 563 K and pressure range of 0.8 bar to 100 bar. Hydrodeoxygenation, hydrogenolysis, decarbonylation, decarboxylation, dehydrogenation and hydrogenation were the major reaction pathways catalyzed by Cu-based catalysts during deoxygenation processes. With the use of Cu-based catalysts, model compounds such as glycerol, 1,3-propanediol, furfural, dibenzofuran, maleic anhydride, aromatic ketones and methyl esters were able to be deoxygenated to their respective deoxygenated products with conversion ranging from 11.5% to 100% and selectivity ranging from 10% to 100%. Based on the study of Cu/SiO<sub>2</sub> catalyst by Zaccheria et al. (2005), one can infer that it is a potent deoxygenation catalyst for the deoxygenation of aromatic ketones, having achieved conversion and selectivity of more than 80% at 363 K and 1.01 bar.

**Table 2.15: Deoxygenation processes using Cu-based catalysts**

Entry	Metal Catalyst	Preparation Method	S <sub>BET</sub> (m <sup>2</sup> /g)	Type of Compound		Major Reaction Pathways	Reaction Parameters						Ref.
				Reactant	Product		Phase	Type	T (K)	P (bar)	X (%)	S (%)	
1	Cu/SiO <sub>2</sub> (10.3 wt% Cu)	Dry impregnation	110	Furfural	2-methyl Furan	Hydrodeoxygenation Hydrogenation	G-S	Continuous	563	1.01	70	14.2	(Sitthisa et al., 2011c)
2	Cu/ZnO/Al <sub>2</sub> O <sub>3</sub> (5:3:2 Cu/Zn/Al molar ratio)	Coprecipitation	-	1,3-Propanediol	Propanol	Decarbonylation Decarboxylation	G-S	Continuous	503	0.8	100	83	(Sad et al., 2011)
3	Cu-Zn-Ti (1:2:1 Cu/Zn/Ti atomic ratio)	Coprecipitation	173	Maleic anhydride	γ-Butyrolactone	Partial deoxygenation	L-S	Continuous	518	1.01	100	90.89	(Hu et al., 2007)
4	Cu-Zn/Al <sub>2</sub> O <sub>3</sub> (28.25 wt% CuO, 35.42 wt% ZnO)	Coprecipitation	-	Methylesters	Alcohols	Hydrogenolysis Hydrogenation	L-S	Batch	513	100	84% (yield)		(Peng et al., 2010)
5	CuPd/rGO (2.0 wt% Cu)	In-situ reduction	-	Glycerol	Lactic acid	Dehydrogenation	L-S	Batch	413	14	56.2	88.1	(Jin et al., 2013)
6	Cu-ZrO <sub>2</sub> (2.6 Cu/Zr atomic ratio)	Coprecipitation	-	Glycerol	1,2-Propanediol	Hydrogenolysis	L-S	Batch	473	40	11.5	95.7	(Durán-Martín et al., 2013)
7	NiCu/CeO <sub>2</sub> (15 wt% Ni, 5 wt% Cu)	Wet impregnation	-	Dibenzofuran	Bicyclohexyl	Hydrodeoxygenation	L-S	Batch	523	100	90	14	(Ambursa et al., 2016)
8	NiCu/TiO <sub>2</sub> (15 wt% Ni, 5 wt% Cu)	Wet impregnation	-	Dibenzofuran	Bicyclohexyl	Hydrodeoxygenation	L-S	Batch	523	100	96	38	(Ambursa et al., 2016)
9	NiCu/ZrO <sub>2</sub> (15 wt% Ni, 5 wt% Cu)	Wet impregnation	-	Dibenzofuran	Bicyclohexyl	Hydrodeoxygenation	L-S	Batch	523	100	65	10	(Ambursa et al., 2016)
10	Cu/SiO <sub>2</sub> (8 wt% Cu)	Deposition	320 (SiO <sub>2</sub> )	9-Fluorenone	Fluorene	Deoxygenation	L-S	Batch	363	1.01	100	100	(Zaccheria et al., 2005)
11	Cu/SiO <sub>2</sub> (8 wt% Cu)	Deposition	320 (SiO <sub>2</sub> )	11-oxo-dibenzocycloheptane	Dibenzocycloheptane	Deoxygenation	L-S	Batch	363	1.01	100	100	(Zaccheria et al., 2005)
12	Cu/SiO <sub>2</sub> (8 wt% Cu)	Deposition	320 (SiO <sub>2</sub> )	Benzophenone	Benzylbenzene	Deoxygenation	L-S	Batch	363	1.01	100	98	(Zaccheria et al., 2005)
13	Cu/SiO <sub>2</sub> (8 wt% Cu)	Deposition	320 (SiO <sub>2</sub> )	Benzhydrol	Benzylbenzene	Deoxygenation	L-S	Batch	363	1.01	100	90	(Zaccheria et al., 2005)
14	Cu/SiO <sub>2</sub> (8 wt% Cu)	Deposition	320 (SiO <sub>2</sub> )	4-isobutyl acetophenone	4-isobutyl ethylbenzene	Deoxygenation	L-S	Batch	363	1.01	92	89	(Zaccheria et al., 2005)
15	Cu/SiO <sub>2</sub> (8 wt% Cu)	Deposition	320 (SiO <sub>2</sub> )	2-acetonaphthone	2-ethyl naphthalene	Deoxygenation	L-S	Batch	363	1.01	100	100	(Zaccheria et al., 2005)
16	Cu/SiO <sub>2</sub> (8 wt% Cu)	Deposition	320 (SiO <sub>2</sub> )	6-methoxy-2-acetonaphthone	2-ethyl-6-methoxynaphthalene	Deoxygenation	L-S	Batch	363	1.01	100	90	(Zaccheria et al., 2005)
17	Cu/SiO <sub>2</sub> (8 wt% Cu)	Deposition	320 (SiO <sub>2</sub> )	1-tetralone	Tetralin	Deoxygenation	L-S	Batch	363	1.01	93	87	(Zaccheria et al., 2005)
18	Cu/SiO <sub>2</sub> (8 wt% Cu)	Deposition	320 (SiO <sub>2</sub> )	2-tetralone	2-hydroxy Tetralin	Deoxygenation	L-S	Batch	363	1.01	84	97	(Zaccheria et al., 2005)
19	Cu/SiO <sub>2</sub> (8 wt% Cu)	Deposition	320 (SiO <sub>2</sub> )	9,10-anthraquinone	9,10-dihydroanthracene	Deoxygenation	L-S	Batch	363	1.01	100	100	(Zaccheria et al., 2005)



### 2.5.1.5 Mo-based catalyst

Mo-based catalysts are not uncommon to be used in fuel processing and production. Many studies on Mo-based catalysts such as Mo<sub>2</sub>C, MoS<sub>2</sub>, MoO<sub>3</sub>, Ni-Mo-S, Co-Mo-S have reported of their high selective deoxygenation activity, making them to be a desirable deoxygenation catalyst. The studies of Mo<sub>2</sub>C catalyst have been conducted on the deoxygenation of numerous model compounds such as anisole (Lee et al., 2014), phenol (Boullosa-Eiras et al., 2014), propanal, propanol (Xiong et al., 2014), 1-octanol (Mortensen et al., 2015), glycolaldehyde, furfural (McManus & Vohs, 2014), ethyl formate (Chen et al., 2016c) and solvolyzed lignocellulosic biomass (Grilc et al., 2015). The Mo<sub>2</sub>C catalyst is known for its selective deoxygenation without the hydrogenation of furanic or aromatic rings as it specifically facilitates the  $\eta_2(\text{C},\text{O})$  adsorption of oxygenated compounds, leading to a direct scission of C=O or C—O bond of the intermediate (McManus & Vohs, 2014; Xiong et al., 2014). Pan et al. (2015) noted that the preferential adsorption of electronegative oxygen and activation of C=O bond were due to the low electron density and high electrophilicity of molybdenum. In addition, this ability has also enabled the facile hydrogenolysis of esters such as ethyl formate (Chen et al., 2016c). The absence of acidic sites within Mo<sub>2</sub>C catalyst also renders the C—C bond cleavage to be unfavorable, making decarboxylation and decarbonylation as the minor pathways (Lee et al., 2014). However, molybdenum carbide catalyst can be deactivated in the presence of water as water tends to oxidize Mo<sub>2</sub>C to MoO<sub>2</sub> which is of lower activity (Mortensen et al., 2015).

The MoS<sub>2</sub>, Ni-Mo-S and Co-Mo-S catalysts were known for the role of MoS<sub>2</sub> active phase and sulfur vacancy sites (CUS) in the direct scission of C—O bond through the direct deoxygenation pathway. Model compounds such as phenol (Yoosuk et al., 2012), 2-ethylphenol (Badawi et al., 2013), ethyl heptanoate (Ruinart de Brimont et al., 2012), methyl heptanoate (Şenol et al., 2005) and methyl stearate (Qian et al., 2014) have been

deoxygenated over sulfided Mo-based catalysts in which high yield of deoxygenated products were reported. Nickel and cobalt are promoters which increase the HDO activity by improving the quality of the active sites (Badawi et al., 2013; Yoosuk et al., 2012). Sulfided NiMo bimetallic catalyst has a higher overall deoxygenation activity due to the Ni-Mo synergy. However, a sulfided Mo monometallic catalyst has a higher selectivity towards hydrodeoxygenation instead of decarboxylation and decarbonylation (Kubička & Kaluža, 2010). Sulfided Mo-based catalysts were also noted for the continuous replenishment of sulfur through external sulfiding agents such as H<sub>2</sub>S or CS<sub>2</sub> in maintaining the catalytic activity due to the absence of sulfur in bio-oils (Mochizuki et al., 2014).

Molybdenum oxide catalysts have also been studied in the deoxygenation of model compounds such as acrolein (Moberg et al., 2010), anisole (Smirnov et al., 2016), palmitic acid (Ding et al., 2015), phenol (Boullosa-Eiras et al., 2014) and tetrahydrofurfuryl alcohol (Wang et al., 2014c). They were also found to be promoting hydrogenolysis (Wang et al., 2014c) and direct scission of C—O bond such as the HDO of phenol to benzene (Boullosa-Eiras et al., 2014). Molybdenum oxide catalysts usually exist in MoO<sub>3</sub> phase which can be over-reduced into MoO<sub>2</sub> phase which is said to be of lower activity (Prasomsri et al., 2014). However, the use of carbon nanotubes supported MoO<sub>2</sub> for the HDO of palmitic acid into hexadecane (92.2% selectivity) at 220 °C has also been reported (Ding et al., 2015). The deoxygenation mechanism over molybdenum oxide (Figure 2.17) mainly involves the interaction of oxygenated compound with oxygen vacant site to form Mo—O bond and the direct cleavage of the C—O bond from the adsorbed intermediate (Prasomsri et al., 2013). Thus, the concentration of oxygen vacant site has a significant effect on the catalytic performance of molybdenum oxide. The strength of metal-oxygen bond within the metal oxide also affects the deoxygenation performance in which metals with weak metal-oxygen bond

are unable to effectively abstract oxygen from the oxygenated compounds whereas metals with strong metal-oxygen bond may strongly bind the oxygen on the catalyst surface, inhibiting the formation of oxygen vacant sites (Moberg et al., 2010).

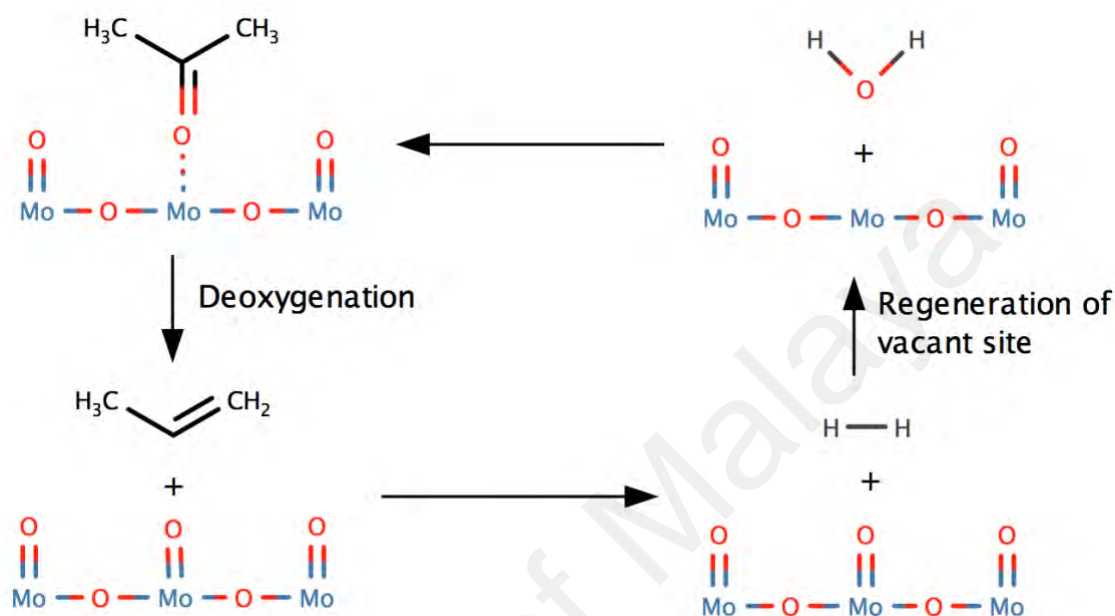


**Figure 2.17: Regeneration of oxygen vacant site in molybdenum oxide catalyst during acetone deoxygenation (Prasomsri et al., 2013)**

Based on Table 2.16, deoxygenation processes over Mo-based catalysts were carried out in liquid-solid or gas-solid phases with temperature range of 408 K to 673 K and pressure range of 25 bar to 100 bar. Hydrodeoxygenation, hydrogenolysis, demethoxylation, dehydration and hydrogenation were the major reaction pathways catalyzed by Mo-based catalysts during deoxygenation processes. With the use of Mo-based catalysts, model compounds such as anisole, phenol, octanol, palmitic acid and methyl stearate were able to be fully deoxygenated to their respective deoxygenated products with conversion ranging from 42% to 100% and selectivity ranging from 45.2% to 93%. Certain Mo-based catalysts such as  $\text{Mo}_2\text{C}$  and  $\text{Mo}_2\text{N}$  which were prepared using temperature programmed reaction method also had decent reaction selectivity (49% and 51%) for partial deoxygenated product such as ethanol. Based on

the studies of phenol HDO to benzene by Boulloussa-Eiras et al. (2014) and Mortensen et al. (2015), one can infer that the effects of support and temperature on the conversion and selectivity of the process were more prominent as compared with the effect of pressure. From these studies, the use of titania support and the increase of reaction temperature to 673 K were both effective enough to increase the conversion of phenol and the benzene selectivity to 90%. For the HDO of methyl stearate to *n*-octadecane, Al-SAPO-11 support would be the preferred support as it enabled the catalyst to have optimal specific surface area and number of acid sites which resulted in the highest selectivity for *n*-octadecane (71.75%).

University of Malaysia

**Table 2.16: Deoxygenation processes using Mo-based catalysts**

Entry	Metal Catalyst	Preparation Method	S <sub>BET</sub> (m <sup>2</sup> /g)	Pore Size (nm)	Acidity (mmol/g)	Type of Compound		Major Reaction Pathways	Reaction Parameters					Ref.	
						Reactant	Product		Phase	Type	T (K)	P (bar)	X (%)		S (%)
1	MoS/Al <sub>2</sub> O <sub>3</sub> (9.9 wt% Mo)	Dry impregnation	251	-	-	2-ethylphenol	2-ethyl Cyclohexane	Hydrodeoxygenation	G-S	Continuous	613	70	7.9 mmol/h.g (HDO activity)	(Badawi et al., 2013)	
2	Mo <sub>2</sub> C/TiO <sub>2</sub> (6.8 wt% Mo)	Dry impregnation	74	-	-	Phenol	Benzene	Hydrodeoxygenation	L-S	Continuous	673	25	90	90	(Boullousa-Eiras et al., 2014)
3	Mo <sub>2</sub> C/ZrO <sub>2</sub> (15 wt% MoO <sub>3</sub> )	Dry impregnation, Carburization	-	-	-	Phenol	Benzene	Hydrodeoxygenation	L-S	Continuous	633	100	42	45.2	(Mortensen et al., 2015)
4	Mo <sub>2</sub> C/ZrO <sub>2</sub> (15 wt% MoO <sub>3</sub> )	Dry impregnation, Carburization	-	-	-	Octanol	Octane	Dehydration Hydrogenation	L-S	Continuous	633	100	100	93	(Mortensen et al., 2015)
5	MoO <sub>2</sub> /CNTs (5.0 wt% MoO <sub>2</sub> )	Dry impregnation	130	2.4	-	Palmitic Acid	Hexadecane	Hydrodeoxygenation	L-S	Batch	493	40	100	92.2	(Ding et al., 2015)
6	Mo <sub>2</sub> C	Temperature programmed reaction	151	-	-	Ethyl formate	Ethanol	Hydrogenolysis	L-S	Batch	408	30	-	49	(Chen et al., 2016c)
7	Mo <sub>2</sub> N	Temperature programmed reaction	153	-	-	Ethyl formate	Ethanol	Hydrogenolysis	L-S	Batch	408	30	-	51	(Chen et al., 2016c)
8	NiMoO <sub>x</sub> -SiO <sub>2</sub> (28 wt% Ni, 43 wt% Mo)	Sol-gel	-	-	-	Anisole	Cyclohexane	Demethoxylation Hydrogenation	L-S	Batch	573	60	100	90	(Smirnov et al., 2016)
9	NiMo/Al <sub>2</sub> O <sub>3</sub> (3.6 wt% NiO, 19.3 wt% MoO <sub>3</sub> )	Impregnation	254	12.12	0.389	Methyl stearate	<i>n</i> -Octadecane	Hydrodeoxygenation	L-S	Continuous	573	30	100	70.37	(Qian et al., 2014)
10	NiMo/Al-SAPO-11 (3.5 wt% NiO, 19.0 wt% MoO <sub>3</sub> )	Impregnation	125	0.70	0.417	Methyl stearate	<i>n</i> -Octadecane	Hydrodeoxygenation	L-S	Continuous	573	30	100	71.75	(Qian et al., 2014)
11	NiMo/SAPO-11 (3.5 wt% NiO, 19.8 wt% MoO <sub>3</sub> )	Impregnation	65	0.70	0.587	Methyl stearate	<i>n</i> -Octadecane	Hydrodeoxygenation	L-S	Continuous	573	30	100	55.25	(Qian et al., 2014)
12	NiMo/SBA-15 (3.2 wt% NiO, 17.6 wt% MoO <sub>3</sub> )	Impregnation	845	3.71	-	Methyl stearate	<i>n</i> -Octadecane	Hydrodeoxygenation	L-S	Continuous	573	30	100	70.08	(Qian et al., 2014)

### 2.5.1.6 Co-based catalyst

One of the most common Co-based catalysts is the CoMoS catalyst which is known for its good catalytic activity for the hydrodesulfurization of sulfur-containing compounds and the hydrodeoxygenation of oxygen-containing compounds (Furimsky, 2000). The use of CoMoS catalyst had been studied in the hydrodeoxygenation of phenol (Platanitis et al., 2014; Yang et al., 2009), 2-ethylphenol (Badawi et al., 2013), *p*-cresol (Wang et al., 2014a), guaiacol (Mochizuki et al., 2014), pyrolysis fuel oil (Upare et al., 2017) and canola oil (Zhang et al., 2014). Numerous studies have reported the promoting effects of Co on MoS<sub>2</sub> catalyst. For instance, Badawi et al. (2013) reported that the doping of 4.2 wt% of Co on MoS<sub>2</sub> catalyst increased the total HDO activity of phenol and 2-ethylphenol from 10.3 mmol.h<sup>-1</sup>.g<sup>-1</sup> to 29.1 mmol.h<sup>-1</sup>.g<sup>-1</sup> and 7.6 mmol.h<sup>-1</sup>.g<sup>-1</sup> to 22.0 mmol.h<sup>-1</sup>.g<sup>-1</sup> respectively. During HDO process, the DDO to HYD ratio was also noted to increase in the presence of Co, indicating a higher selectivity for aromatics by Co metal (Badawi et al., 2013). The results of the HDO of *p*-cresol by Wang et al. (2014a) also showed enhanced DDO activity and increased toluene selectivity when Co was added, thus in corroboration with other studies.

The promoting effect of Co on MoS<sub>2</sub> catalyst was noted to be the decrease in metal-sulfur bonds which allows the facile formation of sulfur vacancies (CUS) (Badawi et al., 2013). Based on Rim-Edge model for the active sites of MoS<sub>2</sub> catalyst, the increase in Co content was also seen to increase the number of layers in the stack and decrease the slab length of MoS<sub>2</sub> phase which will enhance DDO activity (Wang et al., 2015d). Likewise, cobalt also activates the saturated sulfur sites in CoMoS catalyst to facilitate hydrogen adsorption and C—C scission for the decarbonylation of stearic acid into *n*-heptadecane, *n*-heptadecene and formic acid (Zhang et al., 2014). However, the addition of excessive Co will also cause aggregation of CoS<sub>2</sub> species on MoS<sub>2</sub> active sites, leading to a reduced activity (Wang et al., 2014a).

Besides CoMoS catalyst, monometallic Co catalysts such as Co/Al-MCM-41 (Tran et al., 2016), Co/ $\gamma$ -Al<sub>2</sub>O<sub>3</sub> (Srifal et al., 2015), Co/SiO<sub>2</sub> (Mochizuki et al., 2014) were also found to enhance deoxygenation activity. The deoxygenation of C<sub>18</sub> fatty acids over Co/ $\gamma$ -Al<sub>2</sub>O<sub>3</sub> was reported to mainly proceed through decarbonylation and hydrodeoxygenation with a respective contribution of 43.0% and 45.8% to form *n*-C<sub>15</sub> to *n*-C<sub>18</sub> hydrocarbons as main products (Srifal et al., 2015). Likewise, the deoxygenation of guaiacol over Co/SiO<sub>2</sub> was noted to perform better than CoMo/Al<sub>2</sub>O<sub>3</sub> in terms of their respective guaiacol conversion (100% and 77.8%) and HDO selectivity (96.4% and 48.1%) (Mochizuki et al., 2014). The HDO mechanism on Co/SiO<sub>2</sub> surface (Figure 2.18) was seen to proceed through H<sub>2</sub> activation on Co and the hydrogen spillover effects to guaiacol in which hydrogenolysis of C<sub>AR</sub>—O—CH<sub>3</sub> bond took precedence over hydrogenolysis of C<sub>AR</sub>—O—H bond (Tran et al., 2016).

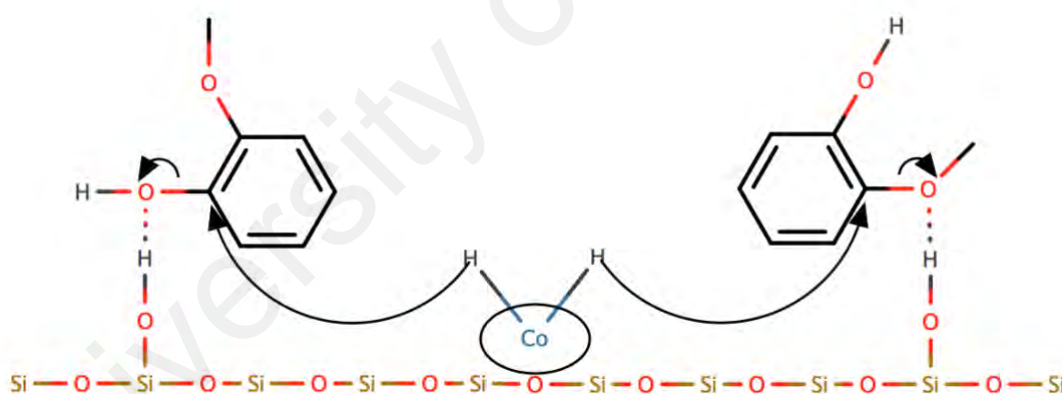


**Figure 2.18: HDO mechanism of guaiacol over Co/SiO<sub>2</sub> catalyst (Mochizuki et al., 2014)**

Based on Table 2.17, deoxygenation processes over Co-based catalysts were carried out in liquid-solid or gas-solid phases with temperature range of 548 K to 723 K and pressure range of 1.01 bar to 70 bar. Hydrodeoxygenation, decarboxylation and transalkylation were the major reaction pathways catalyzed by Co-based catalysts during deoxygenation processes. The table also shows that Co-based catalysts are

suitable for the deoxygenation of phenolic compounds such as phenol, guaiacol, *p*-cresol and 2-ethylphenol with conversion ranging from 84% to 100% and selectivity ranging from 20% to 92.2%. Cobalt was often used as a promoter for sulfided molybdenum catalysts in deoxygenation process. Nevertheless, monometallic Co catalysts such as Co/ $\gamma$ -Al<sub>2</sub>O<sub>3</sub> (Srifa et al., 2015) and Co/SiO<sub>2</sub> (Mochizuki et al., 2014) were also able to achieve high yield of deoxygenation products.

University of Malaya



**Table 2.17: Deoxygenation processes using Co-based catalysts**

Entry	Metal Catalyst	Preparation Method	S <sub>BET</sub> (m <sup>2</sup> /g)	Pore Size (nm)	Acidity (mmol/g)	Type of Compound		Major Reaction Pathways	Reaction Parameters					Ref.	
						Reactant	Product		Phase	Type	T (K)	P (bar)	X (%)		S (%)
1	Co/Al-MCM-41 (10 wt% Co)	Wet impregnation	583.0	3.33	-	Guaiacol	Benzene	Hydrodeoxygenation Transalkylation	G-S	Continuous	673	1.01	100	20	(Tran et al., 2016)
2	CoMoS/Al <sub>2</sub> O <sub>3</sub> (4.2 wt% Co, 9.2 wt% Mo)	Dry impregnation	255	-	-	2-ethylphenol	2-ethyl cyclohexane	Hydrodeoxygenation	G-S	Continuous	613	70	22.0 mmol/h.g (HDO activity)	(Badawi et al., 2013)	
3	Co-Mo-S (0.5 Co/Mo molar ratio)	Hydrothermal	4.8	2.20	-	<i>p</i> -Cresol	Toluene	Hydrodeoxygenation	L-S	Batch	548	40	100	92.2	(Wang et al., 2014a)
4	Co/ $\gamma$ -Al <sub>2</sub> O <sub>3</sub> (9.05 wt% Co)	Dry impregnation	181.2	7.51	-	Palm oil (palmitic, oleic acids)	C <sub>15</sub> -C <sub>18</sub> alkanes	Hydrodeoxygenation Decarboxylation	L-S	Continuous	573	50	92.2	45.8 (HDO) 43.0 (DCO)	(Srifá et al., 2015)
5	Co/SiO <sub>2</sub> (20 wt% Co)	Dry impregnation	160.0	-	0.039	Guaiacol	Benzene	Hydrodeoxygenation	L-S	Batch	573	10	100	53.1	(Mochizuki et al., 2014)
6	CoMo/TiO <sub>2</sub> (1.95 wt% Co)	Equilibrium-deposition-filtration	122.0	9.18	-	Phenol	Cyclohexane	Hydrodeoxygenation	L-S	Continuous	623	15	84	-	(Platanitis et al., 2014)
7	CoMoP/MgO (1.8 wt% Co, 7.6 wt% Mo, 1.4 wt% P)	Dry impregnation	51.1	-	-	Phenol	Benzene	Hydrodeoxygenation	L-S	Batch	723	50	89.4	74.8	(Yang et al., 2009)

### 2.5.1.7 Zn-based catalyst

Zinc is one of the catalysts commonly used in various applications as it is inexpensive and abundant as compared with other precious metals. Some of the common Zn-based catalysts were zinc dust and zinc-mercury amalgam which were respectively used in various homogeneous organic syntheses and Clemmensen reduction as reductants (Nakabayashi, 1960; Poutsma & Wolthuis, 1959; Schabel et al., 2013). Several past studies have shown the excellent reducing power of Zn-based catalysts in homogeneous organic syntheses to achieve desired products (Everson et al., 2010; Krasovskiy et al., 2009; Wei et al., 2005). Nevertheless, the use of such Zn-based catalysts may pose a challenge in the design of a heterogeneous Zn-based catalyst owing to the non-porosity of zinc dust and toxicity of mercury.

In several studies of bio-oil processing, Zn-based catalysts have been used for catalytic cracking (Zhao et al., 2015) and pyrolysis of bio-oil (Fanchiang & Lin, 2012). As for the deoxygenation of bio-oil, studies on Zn-based catalysts are sparse. Some of the Zn-catalyzed deoxygenation processes which have been studied were partial deoxygenation of maleic anhydride to  $\gamma$ -butyrolactone (Hu et al., 2007; Jeong et al., 2006; Zhang et al., 2009), hydrogenolysis of glycerol (Feng et al., 2011), deoxygenation of acetaldehyde and glycolaldehyde (McManus et al., 2013). McManus et al. (2013) observed the role of Zn atoms in increasing the activation energy of C—C or C—H bond and selectively interacting with carbonyl oxygen during the deoxygenation of aldehydes. With such results, it was suggested that Zn could help in suppressing C—C bond cleavage of hydrocarbons and favoring C—O bond cleavage.

Based on Table 2.18, the deoxygenation of maleic anhydride over Zn-based catalysts was carried out in liquid-solid or gas-solid phases with temperature range of 493 K to 553 K. The liquid phase deoxygenation of maleic anhydride was at higher pressure

range of 10 bar to 70.9 bar while the vapor phase process was at atmospheric pressure. Majority of the Zn-based catalysts were prepared using co-precipitation method except for Pd-Zn-Ni/SiO<sub>2</sub> catalyst which was prepared using impregnation method. Both preparation methods showed similar range of catalytic performances, indicating that preparation method was not the major factor in affecting the catalytic performances. The addition of Zr and Ti metals into Cu-Zn was reported to increase the selectivity of partial deoxygenated product which is tetrahydrofuran. However, Ti metal showed a greater metal synergy than Zr metal in Cu-Zn catalyst which resulted in a greater increase in the selectivity of tetrahydrofuran. The increase in reaction temperature had also caused an increase in the process selectivity and a slight decrease in the conversion of maleic anhydride in which the latter can be attributed to the higher tendency of sintering at elevated temperature.

**Table 2.18: Deoxygenation processes using Zn-based catalysts**

Entry	Metal Catalyst	Preparation Method	$S_{BET}$ (m <sup>2</sup> /g)	Pore Size (nm)	Type of Compound		Major Reaction Pathways	Reaction Parameters					Ref.	
					Reactant	Product		Phase	Type	T (K)	P (bar)	X (%)		S (%)
1	Pd-Zn-Ni/SiO <sub>2</sub> (2.3 wt% Pd, 4 wt% Zn, 25 wt% Ni)	Impregnation	-	-	Maleic anhydride	$\gamma$ -Butyrolactone	Partial deoxygenation	L-S	Batch	513	70.9	96.8	81.2	(Jeong et al., 2006)
2	Cu-Zn (2:2 atomic ratio)	Coprecipitation	28.6	17.1	Maleic anhydride	Tetrahydrofuran	Partial deoxygenation	L-S	Continuous	493	10	98	10	(Zhang et al., 2009)
3	Cu-Zn (2:2 atomic ratio)	Coprecipitation	28.6	17.1	Maleic anhydride	Tetrahydrofuran	Partial deoxygenation	L-S	Continuous	533	10	97	19	(Zhang et al., 2009)
4	Cu-Zn (2:2 atomic ratio)	Coprecipitation	28.6	17.1	Maleic anhydride	Tetrahydrofuran	Partial deoxygenation	L-S	Continuous	553	10	95	25	(Zhang et al., 2009)
5	Cu-Zn-Zr (2:2:1 atomic ratio)	Coprecipitation	77.9	16.4	Maleic anhydride	Tetrahydrofuran	Partial deoxygenation	L-S	Continuous	493	10	98	8	(Zhang et al., 2009)
6	Cu-Zn-Zr (2:2:1 atomic ratio)	Coprecipitation	77.9	16.4	Maleic anhydride	Tetrahydrofuran	Partial deoxygenation	L-S	Continuous	533	10	97	40	(Zhang et al., 2009)
7	Cu-Zn-Zr (2:2:1 atomic ratio)	Coprecipitation	77.9	16.4	Maleic anhydride	Tetrahydrofuran	Partial deoxygenation	L-S	Continuous	553	10	95	80	(Zhang et al., 2009)
8	Cu-Zn-Ti (2:2:1 atomic ratio)	Coprecipitation	148.9	3.4	Maleic anhydride	$\gamma$ -Butyrolactone	Partial deoxygenation	G-S	Continuous	498	1.01	91.8	49	(Hu et al., 2007)
9	Cu-Zn-Ti (2:2:1 atomic ratio)	Coprecipitation	148.9	3.4	Maleic anhydride	$\gamma$ -Butyrolactone	Partial deoxygenation	G-S	Continuous	538	1.01	100	99	(Hu et al., 2007)
10	Cu-Zn-Ti (2:2:2 atomic ratio)	Coprecipitation	186.3	3.41	Maleic anhydride	$\gamma$ -Butyrolactone	Partial deoxygenation	G-S	Continuous	498	1.01	100	65.1	(Hu et al., 2007)
11	Cu-Zn-Ti (2:2:2 atomic ratio)	Coprecipitation	186.3	3.41	Maleic anhydride	$\gamma$ -Butyrolactone	Partial deoxygenation	G-S	Continuous	538	1.01	97.4	100	(Hu et al., 2007)

### 2.5.1.8 Ru-based catalyst

Ruthenium, like other transition metals is also commonly known for its hydrogenation activity (Bond & Webb, 1962). The significantly lower price of ruthenium as compared with other transition metals such as rhodium also makes it more economical to be implemented in large scale processes. The Ru-catalyzed hydrogenation may be used as a precursor step in reducing complex oxygenated compounds from biomass into simpler form for facile deoxygenation. Several Ru-catalyzed hydrogenation of compounds such as glucose (Guo et al., 2014; Romero et al., 2016), lactic acid (Jang et al., 2013), levulinic acid (Kuwahara et al., 2015; Upare et al., 2016), methyl laurate (Taniguchi et al., 2011), methyl oleate (Corradini et al., 2008; Echeverri et al., 2009) and succinic acid (Kang et al., 2015) have been studied and they showed Ru-catalyzed hydrogenation performances which are above average and having high selectivity towards desired products. Romero et al. (2016) studied the hydrogenation of glucose into sorbitol between 80 °C to 120 °C in which 100% sorbitol selectivity and a minimum 70% glucose conversion over Ru/C were achieved. Likewise, Kuwahara et al. (2015) have also reported 88.3% levulinic acid conversion and 84.8%  $\gamma$ -valerolactone yield during the hydrogenation of levulinic acid over Ru/SiO<sub>2</sub> catalyst at 70 °C and 0.5 MPa of H<sub>2</sub>. The hydrogenation activity of Ru can also be further enhanced by graphene oxide support to achieve deep hydrogenation products from levulinic acid such as tetrahydrofuran and methyltetrahydrofuran (Upare et al., 2016).

Ru-catalyzed hydrogenation is often observed alongside with hydrogenolysis (Feng et al., 2008). Both of these Ru-catalyzed reactions are often required for the deoxygenation of sugar compounds such as glycerol. Lazaradis et al. (2015) stated that Ru-based catalysts consist of crystalline Ru<sup>0</sup> nanoparticles and amorphous Ru(O)<sub>x</sub><sup>H+</sup> phase which are required for the formation of protonic acidic sites to catalyze

hydrogenolysis. However, ruthenium is also an effective C—C bond cleavage catalyst (Maris & Davis, 2007) which may cause a significant reduction of carbon length of hydrocarbons during deoxygenation process. Thus, metals which suppress C—C bond cleavage such as Cu were doped into Ru-based catalysts to improve its selectivity for deoxygenated products which are of longer carbon chain length (Soares et al., 2016). Other deoxygenation pathways such as decarbonylation and dehydroxylation have also been reported in the Ru-catalyzed hydrodeoxygenation of phenolics (Lu & Heyden, 2015). Based on the DFT study, Lu and Heyden (2015) further added that Ru-catalyzed direct scission of C—O bond is very unlikely owing to the high  $C_{AR}$ —O bond energy. However, Nelson et al. (2015) noted that the addition of Ru onto amphoteric  $TiO_2$  support is able to reduce the activation energy of C—O bond, making DDO pathway to be more favorable than HYD pathway over Ru/ $TiO_2$  catalyst.

Based on Table 2.19, deoxygenation processes over Ru-based catalysts were carried out in liquid-solid or gas-solid phases with temperature range of 373 K to 473 K and pressure range of 1 bar to 64 bar. Dehydration, decarbonylation, dehydrogenation and hydrogenolysis were the major reaction pathways catalyzed by Ru-based catalysts during deoxygenation process. For the vapor phase deoxygenation of methyl isobutyl ketone over Ru/CsPW-I catalyst, high conversion of methyl isobutyl ketone (96%) and selectivity for 2-methylpentane (100%) were achieved at 373 K and 1 bar, indicating a facile deoxygenation process at mild conditions. For the hydrogenolysis of glycerol to 1,2-propanediol, Ru/ $TiO_2$  catalyst had the highest conversion of glycerol (90.1%) while Ru/ $ZrO_2$  catalyst had the highest selectivity for 1,2-propanediol (69.8%). The doping of copper metal in Ru-Cu/ $ZrO_2$  catalyst had further increased the selectivity for 1,2-propanediol from 69.8% to 100% but the conversion of glycerol decreased from 30.1% to 13.7%. The effect of alkaline solvent had also been noted in the study of the dehydration of glycerol to propylene glycol. With the addition of 0.8 M of NaOH or

CaO solvent, the conversion of glycerol increased from 40% to 100% or 85% respectively.

University of Malaya

**Table 2.19: Deoxygenation processes using Ru-based catalysts**

Entry	Metal Catalyst	Preparation Method	S <sub>BET</sub> (m <sup>2</sup> /g)	Type of Compound		Major Reaction Pathways	Reaction Parameters					Ref.	
				Reactant	Product		Phase	Type	T (K)	P (bar)	X (%)		S (%)
1	Ru/CsPW-I (5 wt% Ru)	Wet impregnation	103	Methyl isobutyl ketone	2-Methylpentane	Dehydrogenation Dehydration	G-S	Continuous	373	1	96	100	(Alharbi et al., 2015)
2	Ru/ZrO <sub>2</sub> (1.0 wt% Ru)	Wet impregnation	58	Propanoic acid	Ethane	Dehydrogenation Decarbonylation	L-S	Continuous	463	64	80.3	44.2	(Chen et al., 2012b)
3	Ru/TiO <sub>2</sub>	Wet impregnation	52	Glycerol	1,2-Propanediol	Hydrogenolysis	L-S	Batch	453	50	90.1	20.6	(Feng et al., 2008)
4	Ru/Al <sub>2</sub> O <sub>3</sub>	Dry impregnation	178	Glycerol	1,2-Propanediol	Hydrogenolysis	L-S	Batch	473	25	32.8	41.7	(Soares et al., 2016)
5	Ru/ZrO <sub>2</sub>	Dry impregnation	18	Glycerol	1,2-Propanediol	Hydrogenolysis	L-S	Batch	473	25	30.1	69.8	(Soares et al., 2016)
6	Ru-Cu/Al <sub>2</sub> O <sub>3</sub>	Dry impregnation	177	Glycerol	1,2-Propanediol	Hydrogenolysis	L-S	Batch	473	25	20.6	91.9	(Soares et al., 2016)
7	Ru-Cu/ZrO <sub>2</sub>	Dry impregnation	9	Glycerol	1,2-Propanediol	Hydrogenolysis	L-S	Batch	473	25	13.7	100	(Soares et al., 2016)
8	Ru/C (5.0 wt% Ru)	-	-	Glycerol	Propylene glycol	Dehydration	L-S	Batch	473	40	40	26	(Maris & Davis, 2007)
9	Ru/C with 0.8 M NaOH (5.0 wt% Ru)	-	-	Glycerol	Propylene glycol	Dehydration	L-S	Batch	473	40	100	19	(Maris & Davis, 2007)
10	Ru/C with 0.8 M CaO (5.0 wt% Ru)	-	-	Glycerol	Propylene glycol	Dehydration	L-S	Batch	473	40	85	36	(Maris & Davis, 2007)



### 2.5.1.9 Re-based catalyst

Rhenium is one of the few transition metals which is expensive in price and receives little interest for the study of deoxygenation process, making it less favored for industrial scale processes (Chen et al., 2016c). However, some beneficial effects of rhenium usage in Re-based bimetallic catalyst such as metal crystallite size reduction (Ohta et al., 2014) and isomerization of intermediates for facile conversion (Duan et al., 2014) were reported. Its hydrogenation activity has also been tested and observed in its synergistic use with other metals such as copper or ruthenium for the hydrogenation of succinic acid to 1,4-butanediol (Kang et al., 2015; Kang et al., 2014).

Several studies have shown that Re-catalyzed deoxygenation usually promotes hydrogenolysis of oxygenated compounds such as glycerol (Nakagawa et al., 2010), tetrahydrofurfuryl alcohol (Chen et al., 2012a) and tetrahydropyran-2-methanol (Chen et al., 2010). Leiva et al. (2015b) proposed that Re-based catalysts mainly consist of  $\text{ReO}_x$  or  $\text{ReS}_2$  as the active sites for deoxygenation. The  $\text{ReS}_2$  sites mainly catalyze demethoxylation pathway which is required for the deoxygenation of methoxy group containing compound such as guaiacol (Sepulveda et al., 2012). As for the  $\text{ReO}_x$  sites, they catalyze the hydrogenolysis of C—O bond of adsorbed substrate such as 1-glyceride species through hydride species. The addition of acids in Re-based catalysts has also been reported to enhance the activation of glycerol on  $\text{ReO}_x$  surface cluster (Nakagawa et al., 2012). This is because the protonating effect of acid helps to increase the amount of hydroxorhenium sites which are needed for the activation of glycerol. Similarly,  $\text{ReO}_x$  species is often synergized with other hydrogenating metals such as Ir to improve the effectiveness of such hydride attacks (Amada et al., 2011).

Based on Table 2.20, deoxygenation processes over Re-based catalysts were carried out in liquid-solid phases with temperature range of 393 K to 573 K and pressure range

of 50 bar to 80 bar. Hydrodeoxygenation, hydrogenolysis, demethoxylation and hydrogenation were the major reaction pathways catalyzed by Re-based catalysts during deoxygenation process. For the hydrodeoxygenation of guaiacol,  $\text{ReO}_x$  based catalyst is more preferred than  $\text{ReS}_2$  based catalyst as it is able to produce fully deoxygenation product which is cyclohexane. For Ir modified  $\text{ReO}_x$  catalysts, high selectivity for partial deoxygenation product was attainable through hydrogenolysis. However, they exhibited low conversions of 1,3-propanediol (22.6%), 2,3-butanediol (18.2%), 1-propanol (14.9%) and 2-propanol (20.9%).

University of Malaysia

**Table 2.20: Deoxygenation processes using Re-based catalysts**

Entry	Metal Catalyst	Preparation Method	S <sub>BET</sub> (m <sup>2</sup> /g)	Type of Compound		Major Reaction Pathways	Reaction Parameters					Ref.	
				Reactant	Product		Phase	Type	T (K)	P (bar)	X (%)		S (%)
1	ReO <sub>x</sub> /SiO <sub>2</sub>	Dry impregnation	-	Guaiacol	Cyclohexane	Hydrodeoxygenation Hydrogenation	L-S	Batch	573	50	81	54.3	(Leiva et al., 2015b)
2	ReS <sub>2</sub> /C (10 wt% Re)	Dry impregnation	664	Guaiacol	Phenol	Demethoxylation	L-S	Batch	573	50	75	86.7	(Sepulveda et al., 2012)
3	Ir- ReO <sub>x</sub> /SiO <sub>2</sub> (4 wt% Ir) (Ir/Re molar ratio = 1)	Impregnation	-	Glycerol	1,3-Propanediol	Hydrogenolysis	L-S	Batch	393	80	62.8	49	(Nakagawa et al., 2010)
4	Ir- ReO <sub>x</sub> /SiO <sub>2</sub> (4 wt% Ir) (Ir/Re molar ratio = 1)	Impregnation	-	1,2-Propanediol	1-Propanol	Hydrogenolysis	L-S	Batch	393	80	71.7	85	(Nakagawa et al., 2010)
5	Ir- ReO <sub>x</sub> /SiO <sub>2</sub> (4 wt% Ir) (Ir/Re molar ratio = 1)	Impregnation	-	1,3-Propanediol	1-Propanol	Hydrogenolysis	L-S	Batch	393	80	22.6	99	(Nakagawa et al., 2010)
6	Ir- ReO <sub>x</sub> /SiO <sub>2</sub> (4 wt% Ir) (Ir/Re molar ratio = 1)	Impregnation	-	2,3-Butanediol	2-Butanol	Hydrogenolysis	L-S	Batch	393	80	18.2	81	(Nakagawa et al., 2010)
7	Ir- ReO <sub>x</sub> /SiO <sub>2</sub> (4 wt% Ir) (Ir/Re molar ratio = 1)	Impregnation	-	1-Propanol	Propane	Hydrogenolysis	L-S	Batch	393	80	14.9	99	(Nakagawa et al., 2010)
8	Ir- ReO <sub>x</sub> /SiO <sub>2</sub> (4 wt% Ir) (Ir/Re molar ratio = 1)	Impregnation	-	2-Propanol	Propane	Hydrogenolysis	L-S	Batch	393	80	20.9	99	(Nakagawa et al., 2010)

#### 2.5.1.10 Ir-based catalyst

Iridium is a transition metal which is highly resistant to corrosion, making it favorable to be used as a HDO metal catalyst under severe conditions. Similarly, iridium metal catalyst also has exhibited good hydrogenation activity like other transition metals. Ir-based catalysts such as supported Ir nanoparticles and mesoporous silica nanoparticle (MSN) supported PdIr catalysts have been respectively studied for the chemoselective hydrogenation of chloronitrobenzene and nitrobenzene to aniline (Dongil et al., 2015; Yang et al., 2015). Both cases showed high selectivity for aniline but the hydrogenation of nitrobenzene to aniline using monometallic Ir/MSN suffers a lower conversion and requires the synergy of Pd to have excellent catalytic activity (Yang et al., 2015). It has been proposed that chlorine as an electron withdrawing group activates the nitro group, making chloronitrobenzene to be more active for hydrogenation (Dongil et al., 2015).

Iridium-based catalysts were also reported to catalyze the hydrogenolysis of glycerol and tetrahydrofurfuryl alcohol. The Ir-catalyzed hydrogenolysis of glycerol mainly forms propanediols and lactic acid as major products (Auneau et al., 2011). Nakagawa et al. (2010) noted that the attack of metal-activated hydrogen species to the adsorbed glycerol is fundamental to its hydrogenolysis. Likewise, Auneau et al. (2011) also observed the Ir-catalyzed hydrogenolysis of glycerol to propanediol in hydrogen atmosphere while lactic acid was formed through Cannizzaro reaction in helium atmosphere. As for the Ir-catalyzed hydrogenolysis of tetrahydrofurfuryl alcohol to 1,5-pentanediol, it has been reported to proceed through the direct hydride attack onto the carbon atom of neighboring C—OH group of tetrahydrofurfuryl alcohol and subsequent ring opening to form 1,5-pentanediol (Chen et al., 2012a). The monometallic Ir-catalyzed hydrogenolysis of tetrahydrofurfuryl alcohol showed a high selectivity for 1,5-pentanediol (98.6%) despite its very low conversion (1.6%). Thus, additional metals

had been used to improve its conversion for which Re (33.3%) and Mo (14.0%) metals were observed to be effective while W (1.0%) metal was not effective.

Based on Table 2.21, deoxygenation processes over Ir-based catalysts were carried out in liquid-solid phases with temperature range of 373 K to 453 K and pressure range of 30 bar to 80 bar. Hydrogenolysis and Cannizzaro rearrangement were the major reaction pathways catalyzed by Ir-based catalysts during deoxygenation process. With the use of Ir-based catalysts, model compounds such as glycerol and tetrahydrofurfuryl alcohol were able to partially deoxygenate to their respective deoxygenated products with conversion ranging from 14% to 76% and selectivity ranging from 48% to 96.3%. The exceptional case would be Ir/SiO<sub>2</sub> and Ir-WO<sub>x</sub>/SiO<sub>2</sub> catalysts which had only about 1% conversion of tetrahydrofurfuryl alcohol despite having 98% selectivity for 1,5-pentanediol, rendering them to be ineffective for Ir-based deoxygenation processes. In addition, the study on the conversion of glycerol by Auneau et al. (2011) also showed the Ir/C catalyst to have better catalytic performance as compared with the Ir/CaCO<sub>3</sub> catalyst. The use of different carrier gases during conversion of glycerol over Ir/C catalyst also had a role in affecting the major reaction pathway of deoxygenation. For instance, the formation of 1,2-propanediol from glycerol through hydrogenolysis was promoted in H<sub>2</sub> environment while the formation of lactic acid from glycerol through Cannizzaro rearrangement was promoted in helium environment.

**Table 2.21: Deoxygenation processes using Ir-based catalysts**

Entry	Metal Catalyst	Preparation Method	S <sub>BET</sub> (m <sup>2</sup> /g)	Type of Compound		Major Reaction Pathways	Reaction Parameters						Ref.
				Reactant	Product		Phase	Type	T (K)	P (bar)	X (%)	S (%)	
1	Ir/C (0.6 wt% Ir) (H <sub>2</sub> atmosphere)	Cationic exchange	-	Glycerol	1,2-propanediol	Hydrogenolysis	L-S	Batch	453	50	51	72.5	(Auneau et al., 2011)
2	Ir/C (0.6 wt% Ir) (Helium atmosphere)	Cationic exchange	-	Glycerol	Lactic acid	Cannizzaro rearrangement	L-S	Batch	453	30	76	48.7	(Auneau et al., 2011)
3	Ir/CaCO <sub>3</sub> (5 wt% Ir) (H <sub>2</sub> atmosphere)	Cationic exchange	8 (CaCO <sub>3</sub> )	Glycerol	Lactic acid	Cannizzaro rearrangement	L-S	Batch	453	50	23	48	(Auneau et al., 2011)
4	Ir/CaCO <sub>3</sub> (5 wt% Ir) (Helium atmosphere)	Cationic exchange	8 (CaCO <sub>3</sub> )	Glycerol	Lactic acid	Cannizzaro rearrangement	L-S	Batch	453	30	21	86	(Auneau et al., 2011)
5	Ir/SiO <sub>2</sub> (4 wt% Ir)	Impregnation	535 (SiO <sub>2</sub> )	Tetrahydrofurfuryl alcohol	1,5-Pentanediol	Hydrogenolysis	L-S	Batch	413	80	1.6	98.6	(Chen et al., 2012a)
6	Ir-WO <sub>3</sub> /SiO <sub>2</sub> (4 wt% Ir) (0.5 W/Ir molar ratio)	Impregnation	535 (SiO <sub>2</sub> )	Tetrahydrofurfuryl alcohol	1,5-Pentanediol	Hydrogenolysis	L-S	Batch	393	80	1.0	98.6	(Chen et al., 2012a)
7	Ir-MoO <sub>3</sub> /SiO <sub>2</sub> (4 wt% Ir) (0.5 Mo/Ir molar ratio)	Impregnation	535 (SiO <sub>2</sub> )	Tetrahydrofurfuryl alcohol	1,5-Pentanediol	Hydrogenolysis	L-S	Batch	393	80	14.0	95.0	(Chen et al., 2012a)
8	Ir-ReO <sub>3</sub> /SiO <sub>2</sub> (4 wt% Ir) (0.5 Re/Ir molar ratio)	Impregnation	535 (SiO <sub>2</sub> )	Tetrahydrofurfuryl alcohol	1,5-Pentanediol	Hydrogenolysis	L-S	Batch	373	80	33.3	96.3	(Chen et al., 2012a)

### 2.5.1.11 Zr-based catalyst

Zirconium is also one of the transition metals reasonably studied for deoxygenation processes. Several Zr-based catalysts used for process such as epoxides deoxygenation over  $ZrCl_4/NaI$  (Firouzabadi et al., 2005), oleic acid deoxygenation over  $CeO_2-ZrO_2$  (Shim et al., 2014), guaiacol hydrodeoxygenation over Ce-Zr catalyst (Schimming et al., 2015), sorbitol hydrodeoxygenation over Pt/Zr phosphate (Kim et al., 2013) and partial deoxygenation of maleic anhydride over Cu-Zn-Zr catalyst (Zhang et al., 2009) have been studied. These studies have shown the role of zirconium as the active site ( $Zr^{4+}$  cation) in effectively catalyzing such deoxygenation processes owing to its nature of Lewis acidity and its high charge-to-size ratio. Likewise, zirconia can also be supported on an acidic support to form a bifunctional metallic catalyst which is an effective deoxygenation catalyst.

When  $ZrO_2$ , a common Zr-based material, is doped with another metal to form bimetallic catalyst, promotional effects such as enhanced metal dispersion, smaller metal crystallite size have been reported (Durán-Martín et al., 2013; Wang et al., 2015b). The amphoteric and oxophilic natures of  $ZrO_2$  were also proven to be useful in its use as a support for deoxygenation processes (Mortensen et al., 2015; Qin et al., 2010; Zhang et al., 2013c). The amphoteric nature of  $ZrO_2$  provides it with the sufficient acidity in catalyzing deoxygenation and also its basicity in minimizing the coke formation. The oxophilic nature of  $ZrO_2$  also enables a facile C—O or C=O bond activation, improving the direct deoxygenation activity (de Souza et al., 2015).

Based on Table 2.22, deoxygenation processes over Zr-based catalysts were carried out in liquid-solid phases with temperature range of 513 K to 573 K and pressure range of 1.01 bar to 70.9 bar. Decarboxylation, cracking and partial deoxygenation were the major reaction pathways catalyzed by Zr-based catalysts during deoxygenation process.

For the deoxygenation of oleic acid, the decrease in Ce/Zr ratio resulted in an increase of surface area but a decrease in conversion and selectivity of the process. This indicated that Ce and Zr were both active in catalyzing oleic acid deoxygenation in which Ce/Zr ratio of 0.6:0.4 was found to yield the best conversion and selectivity. The deoxygenation of maleic anhydride at high pressures (10, 70.9 bar) showed higher conversion and selectivity which were more than 90% and 40% respectively. In addition, the selectivity of partial deoxygenated products such as tetrahydrofuran and  $\gamma$ -butyrolactone had respectively increased from 44% to 80% and 41.4% to 78.7% when Zr content of Cu-Zn-Zr catalyst was increased and 25 wt% of Ni was doped into Pd-Zr-Ni/SiO<sub>2</sub> catalyst.



**Table 2.22: Deoxygenation processes using Zr-based catalysts**

Entry	Metal Catalyst	Preparation Method	S <sub>BET</sub> (m <sup>2</sup> /g)	Pore Size (nm)	Type of Compound		Major Reaction Pathways	Reaction Parameters				Ref.		
					Reactant	Product		Phase	Type	T (K)	P (bar)		X (%)	S (%)
1	CeO <sub>2</sub> -ZrO <sub>2</sub> (0.6:0.4 Ce/Zr)	Coprecipitation	171	-	Oleic acid	C <sub>9</sub> -C <sub>17</sub> alkanes	Decarboxylation Cracking	L-S	Batch	573	1.01	73.8	18.1	(Shim et al., 2014)
2	CeO <sub>2</sub> -ZrO <sub>2</sub> (0.4:0.6 Ce/Zr)	Coprecipitation	209	-	Oleic acid	C <sub>9</sub> -C <sub>17</sub> alkanes	Decarboxylation Cracking	L-S	Batch	573	1.01	53.1	14.5	(Shim et al., 2014)
3	CeO <sub>2</sub> -ZrO <sub>2</sub> (0.2:0.8 Ce/Zr)	Coprecipitation	244	-	Oleic acid	C <sub>9</sub> -C <sub>17</sub> alkanes	Decarboxylation Cracking	L-S	Batch	573	1.01	45.7	13.8	(Shim et al., 2014)
4	Cu-Zn-Zr (1:2:1 atomic ratio)	Coprecipitation	69.6	11.1	Maleic anhydride	Tetrahydrofuran	Partial deoxygenation	L-S	Continuous	553	10	97	44	(Zhang et al., 2009)
5	Cu-Zn-Zr (1:2:2 atomic ratio)	Coprecipitation	80.8	9.6	Maleic anhydride	Tetrahydrofuran	Partial deoxygenation	L-S	Continuous	553	10	97	80	(Zhang et al., 2009)
6	Pd-Zr/SiO <sub>2</sub> (8 wt% Pd, 4 wt% Zr)	Impregnation	-	-	Maleic anhydride	γ-Butyrolactone	Partial deoxygenation	L-S	Batch	513	70.9	94.4	41.4	(Jeong et al., 2006)
7	Pd-Zr-Ni/SiO <sub>2</sub> (2 wt% Pd, 2 wt% Zr, 25 wt% Ni)	Impregnation	-	-	Maleic anhydride	γ-Butyrolactone	Partial deoxygenation	L-S	Batch	513	70.9	97.5	78.7	(Jeong et al., 2006)

### 2.5.1.12 Fe-based catalyst

Numerous Fe-based catalysts were studied and reported to favor HDO reaction and the formation of deoxygenated aromatics (Hensley et al., 2014a; Olcese et al., 2013b). Unlike other transition metals such as Ni, Pd, Pt, Co or Cu, Fe was noted to be inactive for the total hydrogenation of aromatics such as benzene (Emmett & Skau, 1943; Yoon & Albert Vannice, 1983). Thus, Fe-based catalysts are useful for the hydrodeoxygenation of phenolics in selectively producing deoxygenated aromatics which are of higher octane rating (Zanuttini et al., 2013). Several studies also corroborated with the high deoxygenation activity of Fe-based catalyst but with different deoxygenation pathways. In the HDO of *m*-cresol to toluene over SiO<sub>2</sub> supported Fe and Ni-Fe catalysts, the formation of toluene as major product was proposed to proceed through the Fe-catalyzed tautomerization-deoxygenation pathway since dehydration of *m*-cresol is not feasible in the absence of acidic support (Nie et al., 2014). The high deoxygenation activity of Fe-based catalysts was explained by Nie et al. (2014) that Fe is an oxophilic transition metal which favors the interaction with carbonyl group rather than aromatic ring hydrogenation. However, it was also reported that the HDO of guaiacol over Fe/SiO<sub>2</sub> catalyst mainly proceeds through the hydrogenolysis of C<sub>AR</sub>—O bond instead (Olcese et al., 2012). A thorough mechanistic study of phenol deoxygenation was also done on Fe(110) surface through DFT study which showed the direct scission of C<sub>AR</sub>—O bond being the most kinetically favored reaction pathway (Hensley et al., 2015).

Monometallic Fe is a very active and selective deoxygenation catalyst but it has been noted to be very susceptible to poisoning due to its oxidation by surface oxygen species (Olcese et al., 2013a). Thus, Fe is doped with another metal in bimetallic catalyst to improve the overall catalytic activity, selectivity and resistance to deactivation. For bimetallic Cu/Fe catalyst, iron exist as Fe<sub>3</sub>O<sub>4</sub> species which electronically promotes the

hydrogenation activity of  $\text{Cu}^0$  and  $\text{Cu}^+$  species for the selective hydrogenation of ethyl stearate to stearyl alcohol. The electron transferring from Fe to Cu was confirmed by XPS results showing a shift to a lower Cu  $2p$  binding energy in the presence of Fe (He et al., 2014). Metals such as Pd and Ni were also added with Fe to improve their selective deoxygenation activity. Shafaghat et al. (2016) have demonstrated that the doping of Fe (4.98 wt%) to 4.94 wt% Ni/HBeta was able to increase the aromatics selectivity from 7.12 wt% to 29.48 wt% while retaining the cycloalkanes selectivity (21.39 and 21.66 wt%) during the deoxygenation of phenolic bio-oil. Likewise, Nie et al. (2014) have also shown that the doping of 5 wt% Fe to 5 wt% Ni/SiO<sub>2</sub> was able to increase the toluene selectivity from 14.2% to 52.6% and decrease the selectivity for cyclic compounds to zero during the deoxygenation of *m*-cresol.

The synergy of Pd and Fe in Pd-Fe catalysts was also investigated. In the deoxygenation of benzyl phenyl ether, Kim et al. (2015) stated that Pd/OMC catalyst tends to saturate the aromatic rings due to the abundant activated hydrogen species while Fe/OMC catalyst shows a lower conversion of benzyl phenyl ether due to its poor hydrogen adsorption ability. The synergy of Pd and Fe would have to be considered to form a bimetallic Pd-Fe/OMC catalyst which is able to selectively produced deoxygenated aromatics without the saturation of benzene ring (Kim et al., 2015). Similarly, Pd/Fe<sub>2</sub>O<sub>3</sub> catalyst was also studied in the HDO of *m*-cresol and was found to have enhanced toluene selectivity (Hong et al., 2014b). Pd was observed to partially donate electrons to Fe and delocalize the oxide surface electrons in forming a more stabilized and reduced Fe species which is more resistant to oxidation by surface oxygen species (Hensley et al., 2014a). Palladium which has better hydrogen adsorption ability than Fe also induces hydrogen spillover effects onto Fe surface for more efficient hydrodeoxygenation. In addition, the strong interaction between Pd and Fe also leads to

a weaker adsorption of products, enabling a facile product desorption (Hong et al., 2014b).

Based on Table 2.23, deoxygenation processes over Fe-based catalysts were carried out in liquid-solid or gas-solid phases with temperature range of 523 K to 673 K and pressure range of 1.01 bar to 16 bar. Hydrodeoxygenation was the major reaction pathway catalyzed by Fe-based catalysts. With the use of Fe-based catalysts, model compounds such as phenol, guaiacol, cresols and benzyl phenyl ether were able to be fully deoxygenated to their respective deoxygenated products with conversion ranging from 8.8% to 74% and selectivity ranging from 49.3% to 60.2%. The best performing Fe-based catalyst would be Fe/SiO<sub>2</sub> catalyst for the HDO of guaiacol into BTX mixture by Olcese et al. (2012) in which conversion of 74% and selectivity of 51.4% were achieved.

**Table 2.23: Deoxygenation processes using Fe-based catalysts**

Entry	Metal Catalyst	Preparation Method	S <sub>BET</sub> (m <sup>2</sup> /g)	Type of Compound		Major Reaction Pathways	Reaction Parameters				Ref.		
				Reactant	Product		Phase	Type	T (K)	P (bar)		X (%)	S (%)
1	Fe/SiO <sub>2</sub> (5 wt% Fe)	Dry impregnation	128	<i>m</i> -Cresol	Toluene	Hydrodeoxygenation	G-S	Continuous	573	1.01	8.8	60.2	(Nie et al., 2014)
2	NiFe/SiO <sub>2</sub> (5 wt% Ni, 5 wt% Fe)	Dry impregnation	115	<i>m</i> -Cresol	Toluene	Hydrodeoxygenation	G-S	Continuous	573	1.01	13.7	52.6	(Nie et al., 2014)
3	Fe/SiO <sub>2</sub> (17 wt% Fe)	Impregnation	116	Guaiacol	Benzene-Toluene-Xylene	Hydrodeoxygenation	G-S	Continuous	673	1.01	74.0	51.4	(Olcese et al., 2012)
4	Fe/OMC (9.5 wt% Fe)	Dry impregnation	784	Benzyl phenyl ether	Toluene	Hydrodeoxygenation	L-S	Batch	523	10	50.1	49.3	(Kim et al., 2015)
5	Fe/HBeta (4.97 wt% Fe)	Dry impregnation	445	50 wt% Phenol, 25 wt% <i>o</i> -Cresol, 25 wt% Guaiacol	Aromatics	Hydrodeoxygenation	L-S	Batch	573	16	-	20.21	(Shafaghat et al., 2016)

### 2.5.1.13 W-based catalyst

Tungsten, like other transition metals such as titanium, vanadium and iron has high affinity for oxygen besides having multiple oxidation states (Arun et al., 2015). Despite of the scarcity of the applications of tungsten-based catalysts in deoxygenation process, several studies have reported of W-based catalysts being active for such process (Ren et al., 2014). Tungsten carbides and oxides were some of the common W-based catalysts being studied while tungsten sulfide catalyst ( $WS_2$ ) was also studied by Grilc et al. (2015) for the HDO of solvolyzed lignocellulosic biomass. Tungsten carbides and oxides are more versatile as they were shown to catalyze various reactions such as hydrogenation, hydrogenolysis, isomerization, hydrodeoxygenation and dehydration (Sullivan et al., 2016; Zhao & Yang, 2015). However, the reactivity and the electronic structure of W-based catalysts are easily influenced by minor phase changes, making the proper control of phase transition to be necessary (Gosselink et al., 2013).

Tungsten oxides are solid acid catalysts which have Lewis and Brønsted acid sites. Tungsten oxides can be paired with other transition metals such as Pd or Pt which have high  $H_2$  sticking probability (Hong et al., 2014a). The synergy is seen through the hydrogen spillover from transition metal and the activation of oxygenated compound over the acid sites of tungsten oxides. For tungsten oxides, the determination of W loading has to be carefully determined as  $WO_x$  species has different crystallographic phase at different surface coverage (Horsley et al., 1987; Vuurman & Wachs, 1992; Wachs, 1996). An evolution of crystallographic phase of active site may result in a change of reactivity of catalyst. Monotungstate species are prominent at low W surface coverage ( $<2$  W atoms/ $nm^2$ ) while polytungstate species are prominent when W surface coverage is more than 2 W atoms/ $nm^2$ . In addition, crystalline  $WO_3$  particulates will form on the top layer of polytungstate species ( $>5$  W atoms/ $nm^2$ ).

Tungsten carbides were shown to be highly selective for the scission of C—O or C=O bonds due to their oxophilicity, making them a potential deoxygenation catalyst (Ren et al., 2014; Sullivan et al., 2016). This is because a direct and selective removal of oxygen from oxygenated compound will minimize H<sub>2</sub> consumption, improve selectivity of desired product and maintain the carbon chain length of product. The oxygen modification of tungsten carbides is also one of the issues to be addressed due to its oxophilicity. Upon oxygen exposure, surface oxidation readily occurs as tungsten carbides tend to form bifunctional oxo-carbide type species (WO<sub>x</sub>) which are of acid sites (Stellwagen & Bitter, 2015). The evolution of such catalytic functionality may be advantageous due to the increase in acidic character or disadvantageous due to the decrease of metallic character. For instance, with WC<sub>x</sub> oxidation, dehydration rate of octadecanol was observed to increase (Sullivan et al., 2016) while decomposition of formaldehyde and methanol was suppressed (Stottlemyer et al., 2012). Thus, proper evaluation of the process may have to be done to ensure such modification is favorable for the process.

Based on Table 2.24, deoxygenation processes over W-based catalysts were carried out in liquid-solid or gas-solid phases with temperature range of 573 K to 653 K. The liquid phase deoxygenation was at 30 bar while the vapor phase deoxygenation was at atmospheric pressure. Hydrodeoxygenation was the major reaction pathway catalyzed by W-based catalysts which can be of oxide or carbide form. For the hydrodeoxygenation of octadecanol, both forms had equivalent catalytic performances. For the hydrodeoxygenation of stearic acid, W<sub>2</sub>C/CNF catalyst showed a higher stearic acid conversion than WO<sub>3</sub>/CNF catalyst. However, the higher stearic acid conversion by W<sub>2</sub>C/CNF catalyst (100%) as compared with WO<sub>3</sub>/CNF catalyst (90.4%) would also be caused by the higher reaction temperature used for W<sub>2</sub>C/CNF catalyst. Likewise,

W<sub>2</sub>C/CNF catalyst showed a higher selectivity for alkane product while WO<sub>3</sub>/CNF catalyst showed a higher selectivity for alkene product.

University of Malaya



**Table 2.24: Deoxygenation processes using W-based catalysts**

Entry	Metal Catalyst	Preparation Method	$S_{\text{BET}}$ (m <sup>2</sup> /g)	Type of Compound		Major Reaction Pathways	Reaction Parameters						Ref.
				Reactant	Product		Phase	Type	T (K)	P (bar)	X (%)	S (%)	
1	W/C (54.2 wt% W)	Deposition	-	Propanol	Propene	Deoxygenation	G-S	-	653	1.01	80	98	(Ren et al., 2014)
2	W <sub>2</sub> C/CNF (14.6 wt% W)	Impregnation	118	Stearic acid	Octadecane	Hydrodeoxygenation	L-S	Batch	623	30	100	85	(Stellwagen & Bitter, 2015)
3	W <sub>2</sub> C/CNF (14.6 wt% W)	Impregnation	118	Octadecanol	Octadecene	Hydrodeoxygenation	L-S	Batch	573	30	99	81	(Stellwagen & Bitter, 2015)
4	WO <sub>3</sub> /CNF (15 wt% W)	Impregnation	-	Stearic acid	Octadecene	Hydrodeoxygenation	L-S	Batch	573	30	90.4	53.1	(Stellwagen & Bitter, 2015)
5	WO <sub>3</sub> /CNF (15 wt% W)	Impregnation	-	Octadecanol	Octadecene	Hydrodeoxygenation	L-S	Batch	573	30	99	81	(Stellwagen & Bitter, 2015)

#### 2.5.1.14 Sn-based catalyst

Sn-based catalysts may offer some new prospects in deoxygenation studies due to the unique properties of tin. In the past studies, several homogeneous Sn-based catalysts were found to be effective in catalyzing Barton-McCombie deoxygenation and Meerwein-Ponndorf-Verley reaction. Barton-McCombie deoxygenation involves the replacement of a hydroxyl group with an alkyl group in the presence of hydrogen donor such as tributylstannane,  $\text{Bu}_3\text{SnH}$  catalyst (Lopez et al., 1997) whereas Meerwein-Ponndorf-Verley (MPV) reaction involves the reduction of carbonyl compounds into alcohols in the presence of another secondary alcohol (Shiner & Whittaker, 1969). Further studies on MPV reduction have also shown that it can be catalyzed by heterogeneous Sn-based catalysts such as Sn-beta zeolite catalyst (Boronat et al., 2006; Corma et al., 2002).

Sn-beta zeolite catalysts were noted to have high Lewis acidity (Boronat et al., 2006) and high affinity for C=O bond activation (Tahara et al., 1997), making them the effective catalysts for Lewis acid catalyzed reactions such as MPV reduction. In addition, Sn also has higher electronegativity than Ti, better reactant coordination factor than Al and is hydrophobic in nature (Corma et al., 2003). These unique properties of Sn-based catalysts are also fundamental for an effective and stable deoxygenation process. With its high affinity for carbonyl groups, Sn-based catalysts may be an excellent choice for processing biomass containing furanic or carbonyl compounds (Assary et al., 2013).

Several hydrogenation studies on compounds such as acetic acid (Zhang et al., 2013a), fatty acid methyl esters (Miyake et al., 2009), levulinic acid (Wettstein et al., 2012), maleic anhydride (Jung et al., 2003), methyl laurate (Taniguchi et al., 2011) and methyl oleate (Echeverri et al., 2009) have also shown the facile C=O bond activation

leading to an effective conversion. The aforementioned studies which involve bimetallic Sn-based catalysts have also shown the ability of Sn in suppressing C—C bond cleavage and forming bimetallic alloys which minimize sintering and leaching of metal species. In addition, the hydrodeoxygenation study on methyl palmitate over PtSn/SAPO-11 catalyst also corroborates with the increased Lewis acidity upon Sn addition due to the presence of partial reduced tin oxides, SnO<sub>x</sub> (Chen et al., 2016b). However, the ineffectiveness of H<sub>2</sub> dissociation by monometallic Sn necessitates the use of bimetallic Sn-based catalysts for deoxygenation processes (González-Borja & Resasco, 2011).

Based on Table 2.25, deoxygenation processes over Sn-based catalysts were carried out in liquid-solid or gas-solid phases at temperature above 600 K. Demethoxylation, hydrodeoxygenation, isomerization were the major reaction pathways catalyzed by Sn-based catalysts during deoxygenation process. It has been noted that monometallic Sn catalyst such as Sn/Inconel monolith has high deoxygenation selectivity (90%) but also has poor conversion (10%) for deoxygenation processes, owing to the fact that Sn has low H<sub>2</sub> dissociation capability. When Sn catalyst was doped with other hydrogenating metals such as Pt, the conversion of guaiacol over Pt-Sn/Inconel monolith was higher (90%) than Sn/Inconel monolith (10%). The optimal synergy between Pt and Sn metals was also observed in the deoxygenation of methyl palmitate over PtSn/SAPO-11 catalyst with varying Pt/Sn ratios. PtSn/SAPO-11 catalyst which had 0.34 wt% Pt and 0.37 wt% Sn was noted to have the highest conversion of methyl palmitate (86.6%) and highest total selectivity for isomerized pentadecane and hexadecane (57.8%), indicating an optimal synergy between the catalytic functions of Pt and Sn metals.

**Table 2.25: Deoxygenation processes using Sn-based catalysts**

Entry	Metal Catalyst	Preparation Method	S <sub>BET</sub> (m <sup>2</sup> /g)	Acidity (mmol/g)	Type of Compound		Major Reaction Pathways	Reaction Parameters					Ref.	
					Reactant	Product		Phase	Type	T (K)	P (bar)	X (%)		S (%)
1	Sn/Inconel monolith (8.01 wt% Sn)	Impregnation	-	-	Guaiacol	Phenol	Demethoxylation	G-S	Continuous	673	1.01	10	90	(González-Borja & Resasco, 2011)
2	Pt-Sn/Inconel monolith (3.67 wt% Pt, 3.58 wt% Sn)	Coimpregnation	-	-	Guaiacol	Phenol	Demethoxylation	G-S	Continuous	673	1.01	85	82.3	(González-Borja & Resasco, 2011)
3	PtSn/SAPO-11 (0.26 wt% Pt, 0.18 wt% Sn)	Dry coimpregnation	99	0.632	Methyl palmitate	<i>i</i> -C <sub>15,16</sub> alkanes	Hydrodeoxygenation Isomerization	L-S	Continuous	648	30	72.7	43.2	(Chen et al., 2016b)
4	PtSn/SAPO-11 (0.34 wt% Pt, 0.37 wt% Sn)	Dry coimpregnation	76	0.662	Methyl palmitate	<i>i</i> -C <sub>15,16</sub> alkanes	Hydrodeoxygenation Isomerization	L-S	Continuous	648	30	86.6	57.8	(Chen et al., 2016b)
5	PtSn/SAPO-11 (0.31 wt% Pt, 0.58 wt% Sn)	Dry coimpregnation	68	0.692	Methyl palmitate	<i>i</i> -C <sub>15,16</sub> alkanes	Hydrodeoxygenation Isomerization	L-S	Continuous	648	30	42.9	17.3	(Chen et al., 2016b)

### 2.5.1.15 Ga-based catalyst

Gallium is a post-transition metal in Group 13 in which its usage for deoxygenation processes is limited. Gallium metal has been used in modifying HBeta and HZSM-5 zeolite catalysts for the deoxygenation of benzaldehyde (Ausavasukhi et al., 2009) and *m*-cresol (Ausavasukhi et al., 2012). Unlike other transition metals which are highly active HDO metal catalyst under high H<sub>2</sub> pressure, gallium-doped zeolites are known for its aromatization of short-chain alkanes which may be used as HDO catalysts under milder conditions (Biscardi & Iglesia, 1996; Buckles & Hutchings, 1996; Montes & Giannetto, 2000). In addition, gallium may exist in Ga-doped zeolites as three general forms: (a) gallium oxide which appears as aggregate on external surface of zeolite, (b) small particles in zeolite micropores and (c) cationic forms such as reduced Ga<sup>+</sup>, GaH<sub>2</sub><sup>+</sup> or oxidic GaO<sup>+</sup> species (Kazansky et al., 2004).

For the deoxygenation of *m*-cresol and benzaldehyde over Ga-based zeolites, benzene and toluene were reported as the major products (Ausavasukhi et al., 2012; Ausavasukhi et al., 2009). Benzene was formed through direct decarbonylation at Brønsted acid sites of zeolites while toluene was formed through hydrogenolysis of condensation products by GaH<sub>2</sub><sup>+</sup> species (Ausavasukhi et al., 2009). The GaH<sub>2</sub><sup>+</sup> species has been reported to be promoting hydride transfer and functioning as active sites for hydrogenolysis (Nowak et al., 2003; Pokrovski et al., 2002). Since hydride transfer is fundamental to the formation of light aromatics from phenolics (Prasomsri et al., 2011), the reduced GaH<sub>2</sub><sup>+</sup> species have to be constantly replenished with H<sub>2</sub> for hydrogenolysis activity (Figure 2.19).

Based on Table 2.26, deoxygenation processes over Ga-based catalysts were carried out in gas-solid phases at atmospheric pressure with temperature range of 723 K to 823 K. Hydrodeoxygenation was the major reaction pathway catalyzed by Ga-based

catalysts. The deoxygenation of benzaldehyde and *m*-cresol over Ga-based catalysts to toluene were able to achieve conversion ranging from 20.22% to 97.5% and selectivity ranging from 22.06% to 69.83%. The exceptional case would be the low conversion (4.49%) and selectivity (7.19%) achieved by Ga/SiO<sub>2</sub> catalyst due to its lack of acidity, in which an acidic support was often seen to effectively promote deoxygenation processes instead (Ausavasukhi et al., 2012). Likewise, the effect of catalyst support on the catalytic performance of Ir-based catalyst was noted to be very prominent. With the use of an acidic support such as HZSM-5 zeolite, the conversions of benzaldehyde and *m*-cresol had respectively increased up to 97.50% and 40.32%. The HZSM-5 support was also favored as it produced supported Ir catalysts which are of higher specific surface area. The use of HBeta zeolite in Ga/HBeta would be even better due to its larger molecular sieve size than HZSM-5 zeolite which enabled larger phenolic molecules to easily bind on the active sites.

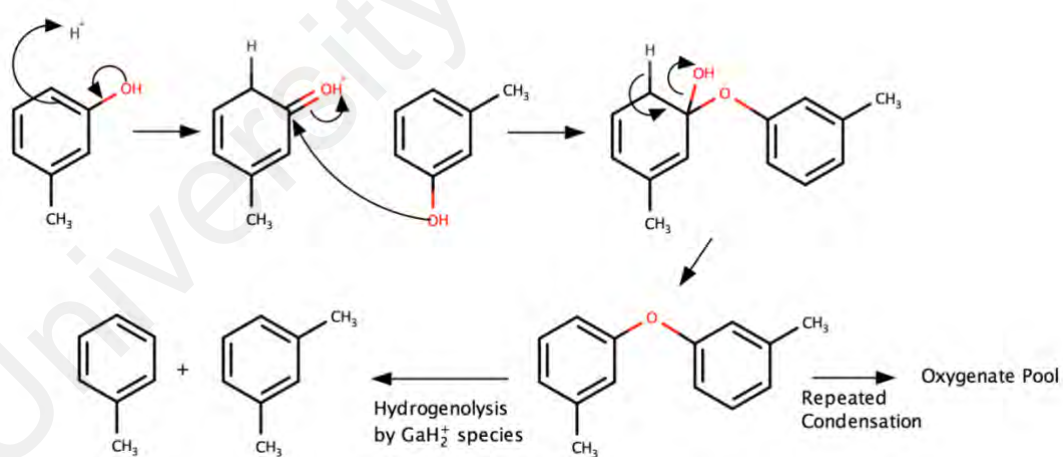


**Figure 2.19: HDO of *m*-cresol over Ga-based zeolite catalyst (Ausavasukhi et al., 2012)**

**Table 2.26: Deoxygenation processes using Ga-based catalysts**

Entry	Metal Catalyst	Preparation Method	S <sub>BET</sub> (m <sup>2</sup> /g)	Acidity (mmol/g)	Type of Compound		Major Reaction Pathways	Reaction Parameters				Ref.		
					Reactant	Product		Phase	Type	T (K)	P (bar)		X (%)	S (%)
1	Ga/SiO <sub>2</sub> (2.9 wt% Ga)	Impregnation	370	-	Benzaldehyde	Toluene	Hydrodeoxygenation	G-S	Continuous	823	1.01	20.22	69.83	(Ausavasukhi et al., 2009)
2	Ga/HZSM-5 (2.8 wt% Ga)	Impregnation	510	0.305	Benzaldehyde	Toluene	Hydrodeoxygenation	G-S	Continuous	823	1.01	97.50	66.03	(Ausavasukhi et al., 2009)
3	Ga/SiO <sub>2</sub> (2.9 wt% Ga)	Impregnation	370	-	<i>m</i> -Cresol	Toluene	Hydrodeoxygenation	G-S	Continuous	723	1.01	4.49	7.19	(Ausavasukhi et al., 2012)
4	Ga/HZSM-5 (2.8 wt% Ga)	Impregnation	510	0.305	<i>m</i> -Cresol	Toluene	Hydrodeoxygenation	G-S	Continuous	723	1.01	40.32	22.06	(Ausavasukhi et al., 2012)
5	Ga/HBeta (2.9 wt% Ga)	Impregnation	580	0.66	<i>m</i> -Cresol	Toluene	Hydrodeoxygenation	G-S	Continuous	723	1.01	82.78	27.85	(Ausavasukhi et al., 2012)

#### 2.5.1.16 Rh-based catalyst

Rhodium is a well-known transition metal for its application in catalytic converter for the reduction of NO<sub>x</sub> in exhaust fumes. Several studies involving the hydrogenation of acetophenone (Lee et al., 2016b), nitroacetophenone (Abdul-Wahab & Jackson, 2013; Currall & Jackson, 2014), nerol (Mäki-Arvela et al., 2005) and phenol (Kuklin et al., 2016) have also noted rhodium as one of the excellent hydrogenating catalysts. Rhodium can be used as one of the deoxygenating catalysts while being supported with acidic supports if hydrogenation-dehydration pathway is preferred. However, there are very few studies on Rh-based catalyst for deoxygenation processes owing to the fact that rhodium is one of the rarest and expensive metals.

The hydrodeoxygenation of nerol to 3,7-dimethyloctane has been studied using Rh/Al<sub>2</sub>O<sub>3</sub> catalyst (Mäki-Arvela et al., 2005). The study revealed that hydrogenation, isomerization and hydrodeoxygenation reactions were competitive in which the HDO selectivity only increase with the decrease of H<sub>2</sub> pressure. The maximum yield of HDO product which was 3,7-dimethyloctane was only 4% at 90 °C and 30% nerol conversion (Mäki-Arvela et al., 2005). Rh-based catalyst has also been used in the deoxygenation of guaiacol. Mu et al. (2014) have used Rh/C catalyst and reported that demethoxylation is dominant, forming phenol (36% selectivity) as the main product and other hydrogenated oxygen containing compounds such as cyclohexanone and cyclohexanol. Gutierrez et al. (2009) have also used Rh/ZrO<sub>2</sub> catalyst to achieve a high conversion of guaiacol (98.9%). However, hydrogenated oxygen containing compounds such as 1-methyl-1,2-cyclohexanediol were the major products at low temperature (100 °C) and similar O/C ratios between reactant and product were observed, indicating negligible deoxygenation of guaiacol. Thus, with its poor deoxygenation activity and its exorbitant price, it is very unlikely to use it on a large-scale deoxygenation process.



Based on Table 2.27, deoxygenation processes over Rh-based catalysts were carried out in liquid-solid or gas-solid phases with temperature range of 363 K to 573 K and pressure range of 10 bar to 50 bar. Hydrodeoxygenation, demethoxylation and hydrogenolysis were the major reaction pathways catalyzed by Rh-based catalysts during deoxygenation process. For the hydrogenolysis of glycerol, Rh/C catalyst exhibited low selectivity for 1,2-propanediol in H<sub>2</sub> (9%) and He (4%) environments. However, Rh-based catalyst showed an excellent deoxygenation activity for *m*-cresol hydrodeoxygenation (89% conversion and 98% selectivity) when it is supported with Fe<sub>2</sub>O<sub>3</sub>. This was due to the enhanced metal stability by the synergy between Pt and Fe metals which was reported by Hong et al. (2014b).

**Table 2.27: Deoxygenation processes using Rh-based catalysts**

Entry	Metal Catalyst	Type of Compound		Major Reaction Pathways	Reaction Parameters					Ref.	
		Reactant	Product		Phase	Type	T (K)	P (bar)	X (%)		S (%)
1	Rh/Fe <sub>2</sub> O <sub>3</sub> (1.0 wt% Rh)	<i>m</i> -Cresol	Benzene-Toluene-Xylene	Hydrodeoxygenation	G-S	Continuous	573	-	89	98	(Hong et al., 2014b)
2	Rh/Al <sub>2</sub> O <sub>3</sub> (5.0 wt% Rh)	Nerol	3,7-dimethyl octane	Hydrodeoxygenation	L-S	Batch	363	10	30	13.3	(Mäki-Arvela et al., 2005)
3	Rh/C (5.0 wt% Rh)	Guaiacol	Phenol	Demethoxylation	L-S	Batch	523	40	65	36	(Mu et al., 2014)
4	Rh/C (0.7 wt% Rh) (1 M NaOH, H <sub>2</sub> gas)	Glycerol	1,2-Propanediol	Hydrogenolysis	L-S	Batch	453	50	22	9	(Auneau et al., 2011)
5	Rh/C (0.7 wt% Rh) (1 M NaOH, He gas)	Glycerol	1,2-Propanediol	Hydrogenolysis	L-S	Batch	453	30	55	4	(Auneau et al., 2011)

### 2.5.1.17 Cs-based catalyst

The use of cesium-based catalyst for deoxygenation is limited. Cesium is an alkali metal which is soft in nature and does not readily exist in a stable elemental form. Thus, monometallic Cs catalyst is unlikely to be used in deoxygenation process. However, Cs-containing zeolite catalyst (CsNaX) has been reported for the deoxygenation of benzaldehyde (Peralta et al., 2009) and methyl octanoate (Sooknoi et al., 2008). The Cs-containing NaX zeolite was prepared through cation exchange between NaX zeolite and CsNO<sub>3</sub> solution (Danuthai et al., 2011). The presence of Cs species was reported to function as the active sites for both benzaldehyde and methyl octanoate deoxygenation and also to increase the basic character of the catalyst (Peralta et al., 2009; Sooknoi et al., 2008). When NaX zeolite was used in the absence of Cs element, the yield of desired products significantly decreased and coking effect becomes more severe.

For the deoxygenation of benzaldehyde to benzene, Cs cation was noted to interact with the electrons of aromatic ring to weaken the benzylic C—C bond of adsorbed benzoate intermediate (Peralta et al., 2009). Hence, the weakening of benzylic C—C bond would lead to a direct decarbonylation to form benzene and CO. Coupling reaction between benzoate intermediates was also observed to be a side reaction which becomes dominant in the absence of Cs to produce condensation products. As for the deoxygenation of methyl octanoate, *n*-hept-1-ene was formed through the  $\beta$ -hydrogen elimination and decarbonylation whereas *n*-hex-1-ene was formed through the rearrangement and deacetalation (Figure 2.20). Both decarbonylation and deacetalation activities have been reported to increase in the presence of Cs, indicating the role of Cs species in catalyzing the reactions (Danuthai et al., 2011; Sooknoi et al., 2008).

Based on Table 2.28, deoxygenation processes over Cs-based catalysts were carried out in gas-solid phases at atmospheric pressure with temperature range of 698 K to 748

K. Decarbonylation and deacetalation were the major reaction pathways catalyzed by Cs-based catalysts during deoxygenation process. CsNaX zeolite is the Cs-based catalyst prepared through ion exchange method and is capable of fully deoxygenating model compounds such as benzaldehyde and methyl octanoate to their respective deoxygenated products with conversion ranging from 62.3% to 100% and selectivity ranging from 41.9% to 80%.

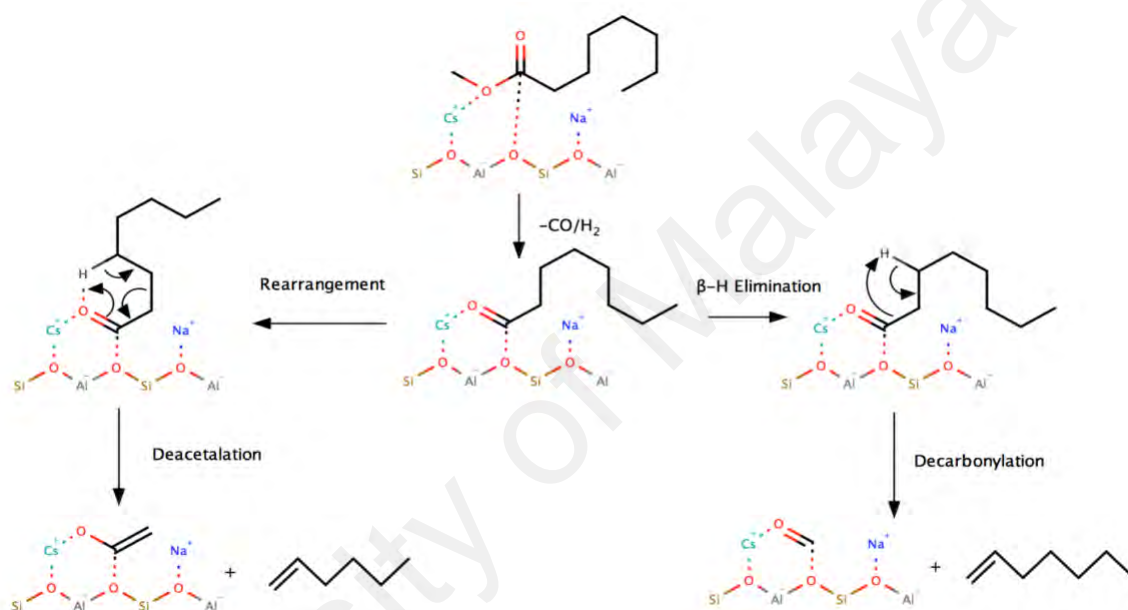


**Figure 2.20: Deoxygenation of methyl octanoate over CsNaX zeolite catalyst (Sooknoi et al., 2008)**

**Table 2.28: Deoxygenation processes using Cs-based catalysts**

Entry	Metal Catalyst	Preparation Method	S <sub>BET</sub> (m <sup>2</sup> /g)	Type of Compound		Major Reaction Pathways	Reaction Parameters						Ref.
				Reactant	Product		Phase	Type	T (K)	P (bar)	X (%)	S (%)	
1	CsNaX zeolite (17.5 mol% Cs)	Ion exchange	460	Benzaldehyde	Benzene	Decarbonylation	G-S	Continuous	748	1.01	100	80	(Peralta et al., 2009)
2	CsNaX zeolite	Ion exchange	468	Methyl octanoate	Heptene	Decarbonylation Deacetalation	G-S	Continuous	698	1.01	62.3	41.9	(Sooknoi et al., 2008)

University of Malaya

### 2.5.1.18 Mg-based catalyst

Magnesium is an alkaline earth metal which often forms basic oxide such as magnesium oxide. Mg-based catalysts are often used as solid basic catalyst for heterogeneous catalytic processes. Mg-based catalysts such as MgO (Chouhan & Sarma, 2011) and Mg-Al hydrotalcite (Zabeti et al., 2009) catalysts were reviewed to be an effective solid basic catalyst for biodiesel production through transesterification. In addition, several studies were also done in assessing the catalytic performances of Mg-based catalysts for deoxygenation processes. Since acidic supported catalysts were reported to have higher propensity to coking (Echeandia et al., 2014), solid basic catalysts were attempted to be used as deoxygenation catalysts which are more resistant to coking. However, the absence of acidic sites may also affect the dehydration of hydroxyl groups during deoxygenation (Alharbi et al., 2015). Sooknoi et al. (2008) compared the performances of CsNaX, NaX and MgO catalysts for the deoxygenation of methyl octanoate. The MgO-catalyzed decarbonylation of methyl octanoate was reported to show a conversion of 8% for methyl octanoate and a selectivity of 8% to hexene. The poor performance of MgO was attributed to its low specific surface area ( $<40 \text{ m}^2/\text{g}$ ) and its absence of highly polarized environment as compared with CsNaX catalyst. The absence of highly polarized environment in MgO rendered it to be not readily capable for the adsorption and the decomposition of methyl octanoate (Sooknoi et al., 2008).

However, MgO catalyst was also noted to be able to activate coupling reactions such as aldol condensation (Resasco & Crossley, 2015; Sooknoi et al., 2008). For instance, several studies reported the base-catalyzed aldol condensation of furfural with acetone over MgO/NaY (Huang et al., 2012), MgO/USY (Puértolas et al., 2016) and MgO-ZrO<sub>2</sub> (Shen et al., 2011) during deoxygenation processes. Aldol condensation is one of the viable C—C coupling steps in the deoxygenation of furanic compounds which helps to

increase the carbon chain length of the deoxygenated hydrocarbons (Serrano-Ruiz et al., 2012). Similarly, MgO was also noted for the activation of C=O group, rendering the facile hydrogenation of carbonyl group by metals such as Cu (Qin et al., 2015) and Pd (Li et al., 2016). Lastly, MgO supported CoMo catalysts for hydrodeoxygenation process was also reported to be more resistant to coking (Yang et al., 2009).

#### 2.5.1.19 Overview

The use of various metal-based catalysts for deoxygenation process is indeed numerous as discussed in the preceding section. Based on the discussion on the existing work, the electronic and physicochemical properties of metal elements certainly do have unique catalytic effects on the deoxygenation of various model compounds. In fact, it has been commonly established that the pyrolysis of lignocellulosic biomass would result in the fragmentation and depolymerization of its lignin, hemicellulose and cellulose components into various O-containing compounds such as phenolics, furans, ethers, acids, ketones, aldehydes and alcohols (Figure 2.21). The upgrading of bio-oil generally involves the deoxygenation of O-containing compounds but owing to their different functional groups, their deoxygenation mechanisms would also occur via different reaction pathways. Thus, the variation in the deoxygenation mechanism is an important factor which ought to be considered during the selection of an appropriate metal-based catalyst.

Based on the numerous deoxygenation studies done by others, Table 2.29 shows a summary of the suitable metal-based catalysts which can catalyze the particular reaction pathway for the deoxygenation of the particular model compounds. For deoxygenation of phenolic compounds, metal elements with excellent hydrogenation ability (Pt, Ni, Pd, Rh) and oxophilicity (Fe, Mo) are suitable in ensuring a facile direct scission of C<sub>AR</sub>—

OH bonds. For the deoxygenation of O-containing cyclic compounds such as furan, metal catalysts such as Pd, Ni, Cu that catalyze ring opening steps are also suitable in producing deoxygenated aliphatic products from furans. For the deoxygenation of acids and carbonyls, metal catalysts such as Pt, Pd, Cu, Ga and Cs that catalyze decarboxylation and decarbonylation would be preferred. For the deoxygenation of alcohols, metal catalysts such as Ru, Re, Ir, W and Rh that catalyze dehydration would be preferred instead.

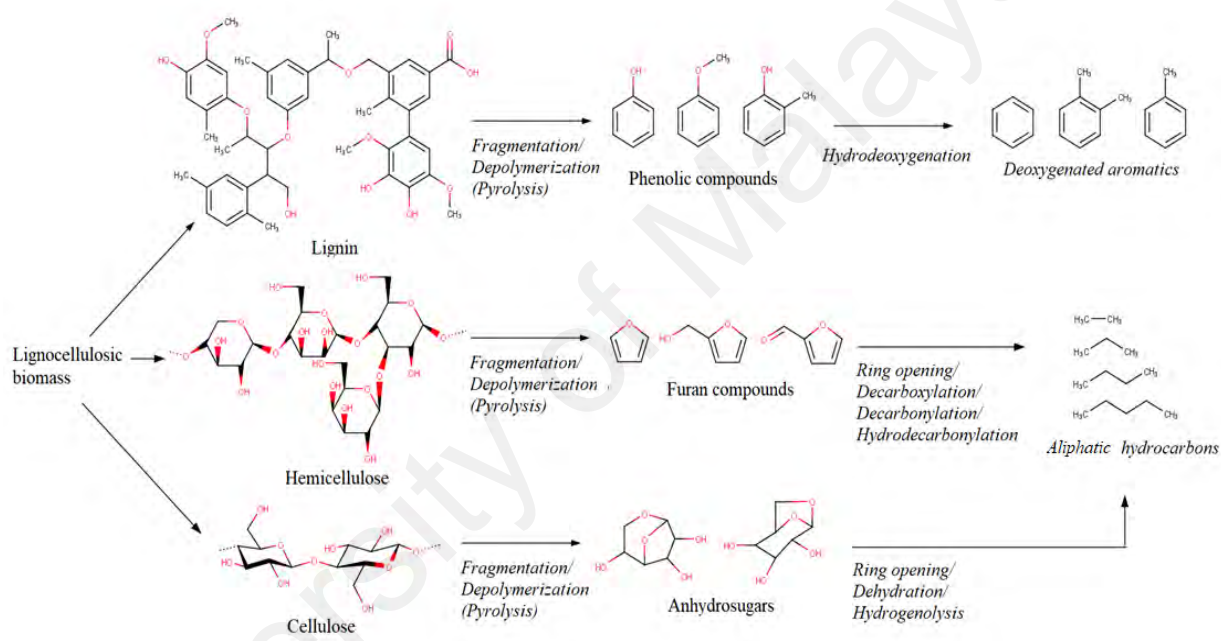


**Figure 2.21: Conversion of lignocellulosic biomass into valorized deoxygenated products (Yildiz et al., 2014)**

**Table 2.29: Deoxygenation process of bio-oil model compounds over metal-based catalysts**

Model Compound	Deoxygenation mechanism	Metal-based catalyst	Deoxygenated product
Phenolics	Hydrodeoxygenation	Pt, Ni, Pd, Mo, Co, Re, Fe, Ga, Rh	Benzene, toluene, xylene, ethylbenzene, cyclohexane
Furans	Ring opening, dehydroxylation, decarbonylation	Pd, Ni, Cu, Fe, Zn, Zr	Tetrahydrofuran, alkanes, alkenes
Ethers	Demethoxylation, Hydrogenolysis	Ni, Fe, Sn	Alkanes, alkenes
Carboxylic acids	Decarboxylation	Co, Zr, W	Alkanes, alkenes
Aldehydes and ketone	Decarbonylation	Pt, Pd, Cu, Ga, Cs	Alkanes, alkenes
Alcohols	Dehydration, hydrogenolysis	Ru, Re, Ir, W, Rh	Alkanes, alkenes



### 2.5.2 Effect of metal loading and dispersion

The metal content and dispersion within a catalyst will also affect its catalytic performance in deoxygenation process. One of the direct observations of higher metal loading would be the increase in active site amount for the catalysis of deoxygenation process. The effect of Ga loading on benzaldehyde and *m*-cresol HDO over Ga/HZSM-5 catalyst was studied by Ausavasukhi et al. (2012; 2009). With the increase of Ga loading from 0 wt% to 3 wt%, toluene yields from benzaldehyde and *m*-cresol HDO were noted to increase from 0 wt% to 36.4 wt% and 2 wt% to 8.9 wt% respectively. The higher yields of toluene from benzaldehyde and *m*-cresol HDO were attributed to the enhanced C—O hydrogenolysis activity by the incorporation of higher Ga loading, in which Ga was known to effectively catalyze C—O hydrogenolysis (Ausavasukhi et al., 2009). Similar effect of enhanced hydrogenolysis activity with the increase of Ni loading was also reported in which Ni was also known to catalyze C—O hydrogenolysis (De et al., 2015; Kumar et al., 2014). For a bifunctional metal catalyst, HDO products such as benzene and toluene were also noted to increase in their yields with the increase of metal loadings because a higher ratio of metal/acid ratio results in the enhanced C<sub>aromatic</sub>—OH bond hydrogenolysis (Zanuttini et al., 2014). Likewise, the HDO conversion of dibenzofuran over Pd-based catalyst was also noted to increase from 11 wt% to 84 wt% when Pd loading increased from 0.5 wt% to 2.0 wt%, indicating more active metal sites for HDO of dibenzofuran at higher Pd loading (Wang et al., 2013). Copper which catalyzes maleic anhydride hydrogenation also increased in its maleic anhydride conversion (95.6 wt% to 96.2 wt%) and  $\gamma$ -butyrolactone selectivity (89.37 wt% to 100 wt%) when copper loading increases from 25 at% to 40 at% (Hu et al., 2007). Thus, the increase in metal loading of catalyst generally would result in higher conversion of reactant due to the higher abundance of active metal sites for the catalysis of such reaction.

Nevertheless, metal loading effect may not be a direct correlation for the yield and selectivity of the desired product. It must also be realized that different metals catalyze different reaction pathways which would result in the formation of different products. For instance, Ru metal is known to catalyze hydrogenolysis and C—C bond cleavage (Maris & Davis, 2007). Chen et al. (2011) investigated on the Ru loadings for propanoic acid deoxygenation and reported the higher selectivity of ethane than propane when Ru loading increases. This was attributed to the increasing C—C bond scission by the higher Ru loading while it also catalyzed C—O hydrogenolysis simultaneously. For bimetallic catalysts, the difference in metal compositions will also result in different product formation when the metals catalyzed different reaction pathways. Bimetallic catalysts such as NiFe/HBeta (Shafaghat et al., 2016), NiFe/SiO<sub>2</sub> (Nie et al., 2014) and Pd-Fe ordered mesoporous carbon catalysts (Kim et al., 2015) were noted to exhibit different product selectivity at different spectrum of metal loadings. Deoxygenated cyclic products such as cyclohexane, methylcyclohexane and ethylcyclohexane were seen to increase in their yields when Ni and Pd metal loadings increased, owing to the enhanced phenyl ring hydrogenation by Ni and Pd (Nie et al., 2014). Likewise, deoxygenated aromatics such as benzene, toluene and ethylbenzene were seen to increase in their yields when Fe loading increased, owing to the enhanced tautomerization pathway by oxophilic Fe (de Souza et al., 2015; Shafaghat et al., 2016). Over loading of Ga (3 wt% to 6 wt%) within Ga/HZSM-5 catalyst was also noted to increase coking products as Ga also catalyzed condensation as secondary reactions (Ausavasukhi et al., 2009).

The physicochemical properties of catalysts are also affected by metal loadings. For instance, Pt metal dispersion decreased with the increase of Pt loading which would affect the turnover frequency of Pt metal sites (Chen et al., 2013). A higher metal loading may also result in larger particle size due to metal aggregation, as seen in Ni

metal (Santillan-Jimenez et al., 2014). Higher Co loading in sulfided CoMoS catalyst for cresol HDO was also reported to cause CoS<sub>2</sub> aggregation which is of lower dispersion (Wang et al., 2014a). Formation of metal aggregates is often undesired as it would result in lower catalytic surface area and metal dispersion, thus lower catalytic activity. Nevertheless, the extent of metal aggregation due to high metal loading was also reported to be minimal and negligibly affects the deoxygenation activity in cases such as cresol deoxygenation over Pt/Al<sub>2</sub>O<sub>3</sub> (Zanuttini et al., 2013). This is because metal aggregation is not mainly affected by metal loading but also affected by other factors such as preparation method and thermodynamic conditions of reaction. A lower catalytic surface area due to high metal loading may also be attributed to pore filling effect during metal deposition at higher loadings (Arun et al., 2015). Acidity of catalyst may also be affected by metal loading. For instance, bimetallic catalysts containing Sn were noted to have higher Lewis acid sites due to presence of partially reduced tin oxides, SnO<sub>x</sub> (Chen et al., 2016b). Likewise, the change in Sn loading has also resulted in formation of various metal phases in RuSn catalyst such as Ru, Ru<sub>2</sub>Sn<sub>3</sub>, Ru<sub>3</sub>Sn<sub>7</sub> and β-Sn which would affect catalyst activity (Wettstein et al., 2012). Thus, an optimization of metal loading of catalyst is instrumental to ensure its physicochemical properties are favorable for high catalytic activity and at the same time without compromising the active metal sites for reaction.

### **2.5.3 Effect of support and its metal-support interaction**

The act of depositing active metal sites on surfaces or pores of support has been well recognized in its ability to achieve higher catalytic surface area, higher metal dispersion and higher attrition resistance for active metal phase and also to reduce metal agglomeration. In deoxygenation processes, various supports such as carbon, metal

oxides ( $\text{Al}_2\text{O}_3$ ,  $\text{TiO}_2$ ,  $\text{SiO}_2$ ,  $\text{CeO}_2$ ,  $\text{ZrO}_2$ ), mesoporous silica (SBA-15, MCM-41, Al-SBA-15, Al-MCM-41) and zeolites (HY, HBeta, HZSM-5) were studied and found to have various effects on the deoxygenation performance (Arun et al., 2015). Acidic supports such as  $\text{Al}_2\text{O}_3$  and zeolites were common supports for deoxygenation catalysts as many studies have shown the importance of acid sites in catalyzing hydrogenolysis of C—O bond (Furimsky, 2000; He & Wang, 2012; Zanuttini et al., 2013). The acidities of several supports were also well documented in the following order: H-ZSM-5 > H-Beta > HY >  $\text{Al}_2\text{O}_3$  >  $\text{TiO}_2$  >  $\text{ZrO}_2$  >  $\text{CeO}_2$  >  $\text{SiO}_2$  with zeolites supports commonly having higher acidity than metal oxide supports (Alotaibi et al., 2012b; He & Wang, 2012; Mortensen et al., 2013). Supports with high acidity were noted to enhance C—O hydrogenolysis activity and increase selectivity of HDO products such as benzene, toluene and xylene. Ausavasukhi et al. (2012) compared supported Ga catalysts of increasing acid strengths (Ga/ $\text{SiO}_2$ , Ga/HBeta, Ga/HZSM-5) for *m*-cresol HDO and noted that toluene yield has the following order: Ga/ $\text{SiO}_2$  (0.32 wt%) < Ga/HZSM-5 (8.9 wt%) < Ga/HBeta (23.06 wt%). The lower toluene yield by HZSM-5 support in spite of its higher acid strength than HBeta was attributed to the diffusion limitation of bulkier molecule in the restricted pores of HZSM-5 zeolite. Besides the acidity of the support, pore size and porosity of supports also significantly affect the deoxygenation of bulkier molecules such as phenolics through diffusion limitations. The variations in support pore size and porosity were also noted to alter the certain reaction pathways such as isomerization. Isomerization which occurs as a secondary reaction during deoxygenation requires more space within pore channels to form multi-branched isomers. For instance, the isomerization of methyl stearate was reported with the use of Al-SBA-15 but not with the use of SAPO-11 support owing to the smaller pore size of the latter (0.6 nm) than the former (3.3 nm) (Qian et al., 2014).

Supports with high acid strength were also noted to experience severe coking as the acid sites also promote condensation of products which are coke precursors (Echeandia et al., 2014). For instance, zeolites are supports of high acidity which were commonly reported to experience deactivation due to coking (To & Resasco, 2014; To & Resasco, 2015; Zanuttini et al., 2013). Echeandia et al. (2014) noted that the amount of coke deposition on zeolite supported Pd catalysts increases with the acidity of zeolites, with acidity and coke content having the same order of: Pd/Al < Pd/10%HY-Al < Pd/20%HY-Al < Pd/HY. In addition, supports with high acidity also caused cracking of alkanes which may affect the selectivity of long chained hydrocarbons from deoxygenation process (Galadima & Muraza, 2015). Basic support such as MgO was also used for phenol HDO over sulfided CoMo/MgO catalyst and was noted to be more resistant to sintering and coking but offers significantly lower HDO activity as compared with acidic supports. Therefore, mild to moderate acidic supports such as C, TiO<sub>2</sub>, ZrO<sub>2</sub>, Al<sub>2</sub>O<sub>3</sub> and CeO<sub>2</sub> were often recommended for HDO process due to their ability to catalyze C—O bond hydrogenolysis with minimal coking effect. The use of C, TiO<sub>2</sub> and ZrO<sub>2</sub> supports was also recommended due to their oxophilicity which was noted to increase selectivity of aromatics during HDO. Several studies on the use of TiO<sub>2</sub> and ZrO<sub>2</sub> oxophilic supports have shown that products such as benzene, toluene were favored through tautomerization of phenolics (de Souza et al., 2014; de Souza et al., 2015; Nie & Resasco, 2014).

The use of supports for catalysts was also known to exhibit metal-support interactions and physicochemical properties which were not present when metals were merely physically mixed with support materials. Metal-support interactions generally arise due to the electronic perturbation of metallic atoms by surrounding foreign atoms by supports which would result in the change of electronic properties of the metal catalyst (Tauster, 1987). The interaction of TiO<sub>2</sub> support with Ni<sub>2</sub>P metal for methyl

laurate deoxygenation was studied by Shi et al. (2014). Such interaction was reported to be synergistic as the oxygen vacancies of  $\text{TiO}_x$  species readily polarized  $\text{Ni}_2\text{P}$  to result in a facile activation of hydrogen at Ni and C=O bond at  $\text{TiO}_x$ . Likewise, the strong metal-support interaction in  $\text{Ru}/\text{Al}_2\text{O}_3$  also showed a synergism to produce electron deficient ruthenium species which readily catalyze C=O hydrogenation for acid deoxygenation (Chen et al., 2011). However, certain metal-support interactions may not be favored such as the high bond strength between metal and the oxide of supports. Pestman et al. (1997) have summarized the metal-oxygen bond strength in the order of:  $\text{Mg} > \text{Al} > \text{Zr} > \text{Ti} > \text{W} > \text{Cr} > \text{Zn} > \text{V} > \text{Sn} > \text{Fe} > \text{Ge} > \text{Mn} > \text{Ni} > \text{Bi} > \text{Cu} > \text{Pb}$ . The strength of metal-support interactions is a factor which ought to be considered during the selection of an appropriate supported metal catalyst. Based on Sabatier rule, an oxide support with moderate metal-oxygen bond strength is the optimal support of choice (He & Wang, 2012). This is because high metal-oxygen bond strength would inhibit formation of oxygen vacancy for O-containing compound adsorption while low metal-oxygen bond strength would cause the catalyst unable to abstract oxygen effectively (Arun et al., 2015). Thus, the choice of support for deoxygenation catalyst is fundamental to ensure the supported metal catalyst has a good combination of metal dispersion, acid sites and metal-support interactions for achieving excellent deoxygenation activity with minimal deactivation effects.

#### **2.5.4 Effect of preparation method and condition**




Similarly to other catalytic reactions, catalyst preparation is a fundamental process which would significantly affect deoxygenation process. This is because the change in method and conditions of catalyst preparation would result in the synthesis of catalyst with altered physicochemical properties. Based on previous section, there are indeed many preparation methods employed to synthesize various deoxygenation metal support

catalysts such as impregnation, precipitation, sol-gel, hydrothermal, ion exchange and temperature programmed reaction. The first two preparation methods were more established and commonly used as compared to others. Impregnation method generally involves the contacting of metal precursor solution with porous support for the deposition of metal in support pore (Lee & Yoo, 2014; Marceau et al., 2010). It can be classified as wet impregnation and dry impregnation whereby the former uses excess volume of metal solution and the latter uses metal solution volume which is equivalent to total pore volume of support. The latter is also known as incipient wetness impregnation or pore volume impregnation and tends to result in better metal deposition in support pores as the uptake of metal solution into the pore is driven by capillary action while wet impregnation relies on diffusion for the deposition of metal within pores. Drying process has to be coupled with impregnation method for the removal of solvent and the effective metal deposition within support pores. The conditions of drying such as drying rate and temperature are also important in affecting the metal redistribution within the pores. By varying such conditions, several metal distributions in pores could be achieved (Table 2.30). In addition, it has also been reported that high drying rate may cause weakly adsorbing metal species to be transported with the solvent to external surface, causing metal deposition on support surface instead of the pores (Munnik et al., 2015). Likewise, coimpregnation is also an impregnation technique for bimetallic catalyst preparation. Coimpregnation tends to be more difficult than impregnation as the different metal solubilities and diffusivities would result in different extents of precipitation within the pores (Marceau et al., 2010).

Precipitation method is also commonly employed in supported metal catalyst synthesis due to its formation of highly dispersed supported metal catalyst at high metal loading (De Jong, 2010). There are two methods of precipitation which are coprecipitation and deposition-precipitation. In coprecipitation, salts of metal and

support were dissolved and mixed together to enable nucleation and growth of combined precursor particles of active metal and support. The combined precursor salts are usually insoluble metal carbonates or hydroxides which would readily precipitate upon their formation. Coprecipitation is favored when synthesis of high metal weight to volume ratio catalyst is required as it has been reported to achieve high metal loadings of 80 wt% while maintaining the small particle size (Lok, 2010). In deposition-precipitation method, precipitation of active metal from metal precursor solution was done in the presence of a preformed support material. Formation of metal hydroxide during deposition-precipitation could also be done through the addition of precipitant such as urea droplets into the mixture for hydroxide ions addition (De Jong, 2010). Precipitation method is often more difficult to be done than impregnation method due to the extra cautions in controlling the precipitation conditions. Poorly controlled precipitation conditions such as poor mixing rate, sudden addition of excess precipitant would result in localized precipitation of metal salts which leads to agglomeration issues for catalyst (Munnik et al., 2015). Proper mixing and slow addition of precipitant in droplet basis have to be done to minimize localized concentration gradient which is required for a homogeneous nucleation of metal salt precipitate within the mixture.

**Table 2.30: Effect of impregnation and drying conditions on metal distribution within pore (Marceau et al., 2010; Munnik et al., 2015)**

Metal Distribution	Impregnation and drying conditions
 Homogeneous	<ul style="list-style-type: none"> <li>- Weakly adsorbing metal precursors with room temperature drying</li> <li>- Precursor solution is concentrated and viscous</li> </ul>
 Egg-yolk	<ul style="list-style-type: none"> <li>- Fast drying with back-diffusion effect</li> </ul>
 Egg-shell	<ul style="list-style-type: none"> <li>- Precursor has strong adsorption on pores</li> <li>- Slow drying</li> </ul>



Sol-gel processing is also one of the emerging techniques for the preparation of supported deoxygenation catalysts. Sol-gel processing is a wet chemistry process for the fabrication of metal oxides which is characterized by the condensation of colloidal particles (miscelles) in the stable colloidal solution (sol) into an integrated network of polymers or discrete particles (gel) (Landau, 2010; Lee & Yoo, 2014). Sol-gel method has been used to synthesize Ni-based catalysts for guaiacol HDO (Bykova et al., 2012). The prepared catalyst was reported to show high HDO activity and high specific surface area due to the formation of nickel oxide-silicate species in thin layered flakes with thickness of 1-2 nm. Hydrothermal synthesis is another catalyst preparation involving crystallization within metal salt solution at elevated temperature and pressure. The crystal size growth from nanoparticles to aggregates could be controlled in this method to achieve the desired particle size. With this, issue of aggregation and hard agglomeration associated with sol-gel and precipitation methods could be avoided (Lee & Yoo, 2014). This method is very well established in the preparation of Mo-based sulfided catalyst for hydrodeoxygenation as this method was reported to produce highly active nano-sized Mo-based sulfided particles (Wang et al., 2014a; Yoosuk et al., 2012). Ion exchange is commonly used in zeolite catalyst which requires metal doping for the formation of active metal sites (Alotaibi et al., 2012b). Temperature programmed reaction is a technique which converts active elemental metals into metal compounds such as metal carbides, sulfides, nitrides, phosphides and oxides which may exhibit the necessary catalytic properties (Chen et al., 2016c).

These studies have reported of the various benefits and effects of such preparation methods on the physicochemical properties of catalysts. There were also other studies reporting treatments such as ultraviolet irradiation which altered the electronic properties of catalyst through excitation (Wang et al., 2015c) and sonication which resulted in smaller particle size for better deoxygenation selectivity (Wang et al., 2009).

A study to determine the best preparation method may not be as straightforward as it seems because the optimal physicochemical properties for a particular deoxygenation reaction have to be determined beforehand, in order to ensure the appropriate preparation method is able to yield the desired physicochemical properties of catalyst. Hellinger et al. (2015) did study on the HDO of guaiacol over Pt/SiO<sub>2</sub> catalysts with different preparation methods such as incipient wetness impregnation (IWI), wetness impregnation (W), flame-spray method (FSP) and sol-gel (SG) method. The conversion of guaiacol was noted to decrease with the order of: IWI (86%) > W (35%) > FSP (10%) > SG (7%). Pt/SiO<sub>2</sub> catalysts were noted to have higher acidity when prepared using FSP method and higher surface area when prepared using SG method but large Pt particles of low dispersion were also observed which leads to the lower conversion of guaiacol (Hellinger et al., 2015). Nevertheless, such study on the catalytic performance of a deoxygenation catalyst prepared using various preparation methods for the same deoxygenation reaction at same reaction conditions is still scarce.

## **2.6 Catalyst selection criteria for deoxygenation**

This review has shown numerous deoxygenation studies done by other researchers using various metal catalysts. Their results generally showed the effectiveness and the feasibility of such metal catalysts in catalyzing the deoxygenation of various O-containing compounds. The selection of an effective metal catalyst for deoxygenation process is necessary to ensure high turnover frequency of desired product is achieved economically, safely and environmentally friendly. Indeed, general properties of good catalyst such as high activity and selectivity, high mechanical strength, high abrasion and erosion resistances, high thermal and chemical stabilities, low cost and low

deactivation susceptibility are highly sought after during the selection of effective deoxygenation catalyst.

Nevertheless, an effective deoxygenation catalyst must also have the following properties to ensure its catalytic role in deoxygenation: oxophilic, bifunctional with acidic support, moderate metal-oxygen bond strength and high H<sub>2</sub> sticking coefficient. Oxophilicity is important for the metals to have high C=O and C—O bond affinities for their facile bond scissions. Thus, the use of oxophilic support such as carbon, TiO<sub>2</sub> and ZrO<sub>2</sub> would enhance the direct scission of C—O bonds from O-containing compounds. Acidic support is needed for the activation of O-containing compound while high H<sub>2</sub> sticking coefficient of metal site is needed for the effective adsorption and activation of hydrogen molecules. Based on Sabatier's principle, moderate metal-oxygen bond strength is also important to ensure the adsorption strength of metal is optimum for reactant adsorption and product desorption. The selection of suitable metal catalyst is important as different metals catalyze different reaction pathways which are required for the deoxygenation of different model compounds. As for support, its selection must also be done based on the required physicochemical properties and metal-support interaction strength for a particular deoxygenation process. Thus, Table 2.31 is an overall outlook done based on the review in previous section on metal-based deoxygenation catalysts while Table 2.32 summarized on the traits of support concerning deoxygenation process. These data will be beneficial for decision making during the optimization of deoxygenation processes as they show the suitable reaction condition ranges and model compounds to be used for the metal-based catalyst with the expected reaction pathways and performances and the suitable supports with desired physicochemical properties for deoxygenation process.

**Table 2.31: Deoxygenation processes over metal-based catalysts**

Metal-based Catalyst	Model Compounds	Reaction Pathways	Reaction Parameters			
			T (K)	P (bar)	X (%)	S (%)
Pt	Phenols, Ketones	Hydrodeoxygenation, Hydrogenation	373 – 673	1.00 – 220.0	4.4 – 100.0	36.0 – 100.0
Ni	Phenols, Ethers, Esters, Furans	Hydrodeoxygenation, Decarboxylation, Decarbonylation	483 – 623	1.01 – 170.0	21.7 – 100.0	21.4 – 99.0
Pd	Phenols, Ketones, Aldehydes	Hydrodeoxygenation, Decarbonylation	403 – 573	1.01 – 60.0	20.0 – 100.0	22.2 – 100.0
Cu	Furans, Ketones	Decarbonylation	363 – 563	0.80 – 100.0	11.5 – 100.0	10.0 – 100.0
Mo	Phenols, Esters	Hydrodeoxygenation	408 – 673	25.0 – 100.0	42.0 – 100.0	49.0 – 93.0
Co	Phenols, Acids	Hydrodeoxygenation, Decarboxylation	548 – 723	1.01 – 70.0	84.0 – 100.0	20.0 – 92.2
Zn	Furans	Partial deoxygenation	493 – 553	1.01 – 70.9	91.8 – 100.0	8.0 – 100.0
Ru	Alcohols	Dehydration, Hydrogenolysis	373 – 473	1.00 – 64.0	13.7 – 100.0	19.0 – 100.0
Re	Phenols, Alcohols	Hydrodeoxygenation, Hydrogenolysis	393 – 573	50.0 – 80.0	14.9 – 81.0	49.0 – 99.0
Ir	Alcohol	Hydrogenolysis	373 – 453	30.0 – 80.0	1.0 – 76.0	48.0 – 98.6
Zr	Acids, Furans	Decarboxylation, Partial deoxygenation	513 – 573	1.01 – 70.9	45.7 – 97.5	13.8 – 80.0
Fe	Phenols, Ethers	Hydrodeoxygenation	523 – 673	1.01 – 16.0	8.8 – 74.0	20.2 – 60.2
W	Acids, Alcohols	Hydrodeoxygenation	573 – 653	1.01 – 30.0	80.0 – 100.0	53.1 – 98.0
Sn	Ethers, Esters	Demethoxylation, Hydrodeoxygenation	648 – 673	1.01 – 30.0	10.0 – 86.6	17.3 – 90.0
Ga	Phenols, Aldehydes	Hydrodeoxygenation	723 – 823	1.01	4.5 – 97.5	7.19 – 69.8
Rh	Phenols, Alcohols	Hydrodeoxygenation, Hydrogenolysis	363 – 573	10.0 – 50.0	22.0 – 89.0	4.0 – 98.0
Cs	Aldehydes, Esters	Decarbonylation, Deacetalation	698 – 748	1.01	62.3 – 100.0	41.9 – 80.0

**Table 2.32: Catalyst supports for deoxygenation process**

<b>Support type</b>	<b>Acidity</b>	<b>Oxophilicity</b>	<b>Properties</b>
Carbon-based material - Activated carbon	Mild to weak	Yes	<ul style="list-style-type: none"> <li>- High porosity and surface area (&gt; 500 m<sup>2</sup>/g)</li> <li>- Carbon is oxophilic which enhances direct scission of C—O bond.</li> </ul>
Metal oxides - Al <sub>2</sub> O <sub>3</sub> , TiO <sub>2</sub> , SiO <sub>2</sub> , CeO <sub>2</sub> , ZrO <sub>2</sub>	Mild to weak	Only for TiO <sub>2</sub> and ZrO <sub>2</sub>	<ul style="list-style-type: none"> <li>- Acidity order of: Al<sub>2</sub>O<sub>3</sub> &gt; TiO<sub>2</sub> &gt; ZrO<sub>2</sub> &gt; CeO<sub>2</sub> &gt; SiO<sub>2</sub></li> <li>- Introduces suitable metal-support interaction for the activation of O-containing compounds</li> <li>- Oxophilic supports such as TiO<sub>2</sub> and ZrO<sub>2</sub> enhance direct scission of C—O bond.</li> </ul>
Mesoporous silica - SBA-15, MCM-41, Al-SBA-15, Al-MCM-41	Mild to weak	No	<ul style="list-style-type: none"> <li>- Uniform pore channels and low tortuosity which enhance mass transfer</li> <li>- Large pore size</li> <li>- High thermal stability</li> </ul>
Zeolites - HY, H-Beta, H-ZSM-5	High	No	<ul style="list-style-type: none"> <li>- Acidity order of: H-ZSM-5 &gt; H-Beta &gt; HY</li> <li>- High porosity with uniform pore channels</li> <li>- Catalyzes C—O hydrogenolysis</li> <li>- Catalyzes condensation, cracking and isomerization of hydrocarbons as secondary reaction</li> <li>- Higher tendency of coking</li> </ul>
Basic MgO support	No	No	<ul style="list-style-type: none"> <li>- More resistant to coking and sintering than acidic supports</li> <li>- Poor deoxygenation activity</li> <li>- Low surface area (&lt; 40 m<sup>2</sup>/g)</li> </ul>

## **2.7 Discussion on hydrodeoxygenation scenarios**

These reviews showed that many researchers have studied on the potency of bio-oil upgrading via deoxygenation process of various types of model compounds and supported metal catalysts, and that the results are certainly very insightful and encouraging. Numerous investigations were done to obtain high yield of deoxygenated products while optimizing the reaction conditions. Apart from these, there are a few facets of catalytic deoxygenation process which would be further emphasized as the main work in this thesis to establish new findings and validate existing findings of bio-oil upgrading via catalytic deoxygenation process.

### **2.7.1 Titania supported silver catalyst for phenol hydrodeoxygenation**

The use of silver metal catalyst for deoxygenation processes is still a vastly unexplored area of research. Therefore, investigations on its catalytic ability and performance for oxygen removal in bio-oil upgrading would certainly provide numerous insights in the discovery of excellent heterogeneous deoxygenation metal catalyst with high deoxygenation yield for a necessary breakthrough for an optimized bio-oil catalytic deoxygenation. As mentioned in previous sections, for an effective deoxygenation supported metal catalyst, fundamental properties such as high H<sub>2</sub> sticking coefficient, optimal metal-oxygen bond strength, high metal reducibility and suitable acid strength from support are needed to ensure facile scission of C—O bonds and activation of H<sub>2</sub> and O-containing compounds. Even though the application of silver catalyst for deoxygenation is still fairly scarce and not well established, preliminary review on its metal property and other similar catalytic applications may give insights on the potential of silver catalyst in catalyzing deoxygenation.

Firstly, silver is a transition metal like Pt, Ni, Pd, Cu, Mo, etc. Silver has been noted to have strong proton and hydride ion donor properties and good chemisorption affinity for oxygen (Pearson, 1985; Seyedmonir et al., 1985). Thus, it may function as hydrogen adsorption and activation site to a different extent as compared with other transition metals. Secondly, excellent catalytic role of silver in reductive organic syntheses were also reported in literature. For instance, silver-based catalysts were reported to have excellent activity and selectivity for chemoselective reduction of styrene oxides, stilbene oxide, carbonyls, alcohols, nitro-aromatics and epoxides (Dong et al., 2015; Du et al., 2012; Mikami et al., 2010; Mitsudome et al., 2010). Mitsudome et al. (2012) have also further reported the heterolytic cleavage of H<sub>2</sub> on silver nanoparticle surface which aided in the reductive transformation. Reductive transformation could be classified as a general process involving reduction through oxygen removal or hydrogen addition. Likewise, reduction of organic compounds may also differ with the use of same catalyst due to the different targeted bond to be reduced. Unlike nitroaromatics and epoxides which respectively require reduction of nitro group ( $\text{—NO}_2$ ) and cyclic ether group, phenolic deoxygenation requires the scission of C<sub>AR</sub>—OH bond via hydrogenolysis. Thus, hydrogenolysis activity of silver-based catalysts for phenolic deoxygenation remains a subject to be focused upon.

Nevertheless, there are also computational studies which reported of silver catalyst having low HDO activity. For instance, Jalid et al. (2017) reported of the transition metal activity for ethanol conversion to ethane with the order: Co > Ru > Ir > Rh > Ni > Fe > Pt > Pd > Cu > Re > Ag > Au. Likewise, Lausche et al. (2014) also reported of high C—O bond breaking energy over Ag(211) surface. The stark differences within these Ag-catalyzed HDO may very likely due to the use of different model compounds. Furthermore, the HDO activity of silver catalyst may very much depends on the type of model compound as different model compounds may require different HDO

mechanisms. Thus the physicochemical properties of Ag/TiO<sub>2</sub> have to be prior investigated without the influence of model compound to determine whether it exhibits suitable physicochemical properties for generic HDO. Subsequently, a model compound approach phenol hydrodeoxygenation has to be done to experimentally verify whether silver catalyst can catalyze phenolic hydrodeoxygenation. Phenol was chosen as the model compound as the hydrogenolysis of its C<sub>AR</sub>—OH bond is representative of other phenolics besides being one of the main constituents of bio-oil. The choice of supporting silver on titania was also an apt scenario for further insights on hydrogen spillover and oxophilicity of titania in affecting phenol hydrodeoxygenation.

### **2.7.2 Phenol hydrodeoxygenation as catalytic gas-solid reaction**

Reaction studies of phenol HDO have mainly been done as catalytic liquid-solid reaction at an elevated pressure due to the high H<sub>2</sub> requirement to achieve good HDO yield. However, this requirement may result in HDO processes utilizing highly pressurized reactor, high H<sub>2</sub> consumption which would pose several concerns regarding the safety, cost and sustainability of liquid-phase phenolic HDO and eventually affecting its commerciality. Gas-phase phenolic HDO, on the other hand, is able to operate at atmospheric pressure, lower H<sub>2</sub> consumption and has better handling with gas-phase phenolic flows. Nevertheless, studies on gas-phase phenolic HDO are required to investigate whether HDO at low H<sub>2</sub> pressure is feasible. The choice of suitable catalyst must also be made to ensure the process has high selectivity for the desired deoxygenated product, thus further maximizing HDO efficiency while minimizing H<sub>2</sub> consumption.

For lab scale kinetic studies, catalytic solid-gas reactions were investigated using various kinds of reactors such as batch, packed bed, plug flow, fluidized bed, trickle



bed, etc. (Fogler, 2006). The aforementioned reactors certainly do provide various advantageous features for reaction studies. However, one of the major limitations in such reactors is the requirement for an additional spectroscopic instrument for the accurate determination of reaction intermediates in kinetic modeling. On the other hand, a TGA-FTIR (Thermogravimetric analysis—Fourier transform infrared spectroscopy) based reactor may offer better feature in this aspect for kinetic modeling as compared with the former. Table 2.33 shows the comparison between TGA-FTIR based reactor and conventional lab scale reactors. The choice of reactor is certainly not rigid; rather, it should be made by choosing reactor which has features that are applicable for the requirements of a particular reaction study. For an effective kinetic modeling, TGA-FTIR based reactor may be a viable choice through its simpler reactor setup, lesser reactants requirement, negligible mass transfer limitations and higher accuracy for determination of reaction intermediates.

**Table 2.33: Reactor features**

	TGA-FTIR based reactor	Conventional lab scale reactor
1. Reaction intermediates identification and quantification	Detection is in-situ and more sensitive	Detection requires additional spectroscopic instrument and more samples for better detection.
2. Mass transfer limitations	Negligible	Variable, depending on reactor setup
3. Process setup	Simple and ready to be used with built-in accessories	Complexity depends on design and requires fabrication of parts
4. Residence time	Short (Order of seconds)	Variable, depending on reactor size
5. Reaction phase	Solid-gas	Solid-gas or solid-liquid
6. Temperature	Built-in furnace for temperature control	Requires external furnace for temperature control
7. Pressure	Atmospheric	Variable
8. Reaction scale	$\mu\text{g}$ — $\text{mg}$ or $\mu\text{L}$ — $\text{mL}$	$\text{mg}$ — $\text{kg}$ or $\text{mL}$ — $\text{L}$

# CHAPTER 3: SYNERGISTIC INTERACTION OF METAL-ACID SITES FOR PHENOL HYDRODEOXYGENATION OVER BIFUNCTIONAL Ag/TiO<sub>2</sub> NANOCATALYST

## 3.1 Introduction

The use of bifunctional metal-acid catalyst has been known to be effective for hydrodeoxygenation (HDO) of phenolic compounds in bio-oil (Kay Lup et al., 2017a; Mortensen et al., 2011). These catalysts contain metal and acid sites which are instrumental in catalyzing several reactions occurring in hydrodeoxygenation. For instance, metal sites catalyze hydrogenation and hydrogenolysis reactions while acid sites catalyze dehydration, transalkylation, isomerization, alkylation and condensation reactions (Echeandia et al., 2014; Procházková et al., 2007). Likewise, metal sites promote hydrogen adsorption and activation whereas acid sites promote adsorption and activation of O-containing model compounds through formation of oxygen vacancies (He & Wang, 2012; Zhang et al., 2017). For phenolic HDO, removal of hydroxyl group (—OH) from phenolics could occur through: (i) direct hydrogenolysis of C<sub>aromatic</sub>—OH bond to form deoxygenated aromatics; (ii) phenyl ring hydrogenation to form cycloalcohol intermediate which dehydrates and hydrogenates to form cycloalkane; (iii) phenolics tautomerization to form keto intermediates that undergoes C=O hydrogenation and dehydration to form deoxygenated aromatics (Kay Lup et al., 2017a).

The catalytic roles of acid and metal sites of HDO catalyst were well established in past studies. For HDO catalyst to exhibit excellent HDO activity, validation of the existence and nature of acid and metal sites in catalyst is not suffice. In fact, the synergistic interactions of both sites had to be analyzed in order to further understand the HDO mechanism occurring at both sites within the catalyst. Synergy of acid and

metal sites is also important for the surface migration of activated hydrogen species from metal site to acid site which is known as hydrogen spillover (Hong et al., 2014b). Hydrogen spillover is commonly made more possible by having both sides existing in close proximity. Nevertheless, physicochemical properties of the selected metal and support are also important in influencing chemisorption and activation of phenolics in the presence of hydrogen. Therefore, proper designing of a bifunctional catalyst model for HDO is necessary to ensure efficient hydrogen spillover and optimal surface acidity for excellent hydrogenolysis of C—OH bond in phenolics.

Metal-promoted zeolite is one of the bifunctional metal-acid catalysts reported to have good HDO activity owing to the presence of metal sites and high surface acidity (Rezaei et al., 2015). However, high surface acidity has also been known to favor secondary condensation reactions which would lead to severe catalytic coking (To & Resasco, 2015). Thus, mild acid supports such as Al<sub>2</sub>O<sub>3</sub>, TiO<sub>2</sub>, ZrO<sub>2</sub> and CeO<sub>2</sub> may offer better coking resistance while having optimal acid sites for hydrogenolysis in HDO. Among these, TiO<sub>2</sub> has been increasingly studied on due to its support reducibility, metal-support interaction and higher oxophilicity for C—O bond scission (de Souza et al., 2015; Kay Lup et al., 2017b; Tauster, 1987; Tauster et al., 1978). Besides using acidic metal oxides as HDO catalyst supports, they have also been used as promoters (Chia et al., 2011) and ligands (Zhang et al., 2018) which were respectively reported to improve hydrogenolysis activity and to tune the Brønsted acid strength of catalyst. Likewise, many transition metals were used in past HDO studies such as Co, Cu, Fe, Ga, Ir, Mo, Ni, Pd, Pt, Re, Rh, Ru, Sn, W, Zn and Zr (Kay Lup et al., 2017b). The use of transition metals in HDO was also favored as they contained metal sites which effectively promote hydrogen adsorption and activation. However, one of their limitations is their high material cost which would be a major challenge to

their applications at commercial scale. Silver, on the other hand, is categorized with Cu, Fe, Ni, Ti and Zn as low cost transition metals (Sá & Śrębowata, 2016; Su et al., 2006).

In several studies, silver-based catalysts were reported to have excellent activity and selectivity for chemoselective reduction of styrene oxides, stilbene oxide, carbonyls, alcohols, nitro-aromatics and epoxides (Dong et al., 2015; Du et al., 2012; Mikami et al., 2010; Mitsudome et al., 2010). Mitsudome et al. have also further reported that heterolytic H<sub>2</sub> cleavage by silver and basic oxide interface favored chemoselective reduction of nitro compounds containing C=C (Mitsudome et al., 2012). However, there were also several HDO studies that reported of the low HDO activity of Ag. For instance, Jalid et al. (2017) reported of the transition metal activity for ethanol conversion to ethane with the order: Co > Ru > Ir > Rh > Ni > Fe > Pt > Pd > Cu > Re > Ag > Au. Likewise, Lausche et al. (2014) also reported of high C—O bond breaking energy over Ag(211) surface. The stark differences within these Ag-catalyzed HDO may very likely be due to the use of different model compounds. Thus, the physicochemical properties of Ag/TiO<sub>2</sub> have to be prior investigated without the influence of model compound to determine whether it exhibits suitable physicochemical properties for HDO process. In this work, synergistic interaction of metal-acid sites and catalytic performance of Ag/TiO<sub>2</sub> catalyst for phenol HDO were experimentally assessed.

## **3.2 Experimental**

### **3.2.1 Materials**

Silver nitrate (ACS reagent) and titanium (IV) dioxide (technical, ≥97%) were purchased from Sigma-Aldrich. All chemicals were used as received without any

purification. Purified argon, helium and gas mixtures of 10% NH<sub>3</sub> in He and 5% H<sub>2</sub> in N<sub>2</sub> were purchased from Linde Malaysia Sdn. Bhd.

### 3.2.2 Synthesis of Ag/TiO<sub>2</sub> catalysts

Titania supported silver metal of various silver loadings (1 wt%, 3 wt%, 5 wt% and 10 wt%) were used as catalysts. They were synthesized via incipient wetness impregnation method (Kay Lup et al., 2017b; Marceau et al., 2010; Munnik et al., 2015; Shafaghat et al., 2016). In each production batch, 100 g of pure anatase TiO<sub>2</sub> was impregnated with 10 mL silver nitrate aqueous solution of different concentrations to produce catalyst precursor of varying silver loadings. Impregnation suspension was stirred at room temperature for 1 h to achieve complete homogenization. Samples were then oven dried at 120 °C for 24 h and calcined in air at 400 °C for 24 h in a furnace. The catalyst samples were denoted as Ag/TiO<sub>2</sub>-1, Ag/TiO<sub>2</sub>-3, Ag/TiO<sub>2</sub>-5 and Ag/TiO<sub>2</sub>-10 respectively. A sample of titania support was also calcined in air at 400 °C for 24 h and characterized to investigate the effect of support on catalyst.

### 3.2.3 Characterization of Ag/TiO<sub>2</sub> catalysts

Textural properties of catalysts and bare TiO<sub>2</sub> support were determined by N<sub>2</sub> isothermal adsorption-desorption using Micromeritics ASAP 2020 surface area and porosity analyzer. Samples were outgassed under vacuum at 90 °C for 1 h and subsequently at 250 °C for 2 h before textural analysis.

X-ray diffraction (XRD) patterns of catalysts were obtained using PANalytical X'Pert diffractometer with Cu K $\alpha$  ( $\lambda = 1.540598 \text{ \AA}$ ) radiation. The working voltage and current of X-ray tube were 40 kV and 40 mA respectively. Scanning range was from 10°

to 90° with step size of 0.026° and scan rate of 3°/min. JCPDS card number 04-0783, 42-0874 and 21-1272 for Ag, Ag<sub>2</sub>O and TiO<sub>2</sub> were used.

Surface morphology and topography of catalysts were examined using field emission scanning electron microscope (FESEM), ZEISS GeminiSEM 300 equipment. Elemental composition and mapping of catalyst surfaces were done using energy dispersive X-ray spectroscopy (EDX) and elemental mapping features of ZEISS GeminiSEM 300. Morphology and size of catalyst particles were analyzed using transmission electron microscope (TEM), TEM LEO 912 Omega equipment. Inductively coupled plasma optical emission spectroscopy (ICP-OES) was done to determine the actual silver loading of catalyst samples (Alloncle et al., 2009).

Ammonia temperature programmed desorption (NH<sub>3</sub>-TPD) was done to study catalyst acidity using Micromeritics Chemisorb 2720 instrument in a 10 vol% NH<sub>3</sub>/He gas flow. Samples (50 mg) were loaded in quartz U-tube reactor and heated from 298 K to 573 K at 20 K/min and held at 573 K for 30 min under 20 mL/min helium flow for sample outgassing. Outgassed samples were subsequently cooled down to 298 K and used for ammonia chemisorption by changing gas flow from pure He to 10 vol% NH<sub>3</sub>/He for 30 min. Samples were then purged with He for 30 min at 373 K for physisorbed molecules removal. Next, samples were heated from 373 K to 1173 K at 40 K/min using He carrier gas (20 mL/min) for ammonia desorption measurement. For Ag/TiO<sub>2</sub>-10 sample, NH<sub>3</sub>-TPD was conducted using different heating rates (30, 40, 50, 60 K/min) for determination of NH<sub>3</sub> desorption activation energy. Procedures for baseline correction and stabilization of thermal conductivity detector (TCD) signal were also done to enhance signal-to-noise ratio of NH<sub>3</sub>-TPD spectra.

The nature of surface Brønsted and Lewis acid sites was determined by FTIR analyses of pyridine adsorbed on samples (Py-FTIR) using Bruker TENSOR 27 FTIR

spectrometer. Similar Py-FTIR procedures were employed with reference to other works (Xing et al., 2017; Zanuttini et al., 2014). IR spectra were collected after pyridine desorption at different outgassing temperatures (770, 860, 950 K).

H<sub>2</sub>-TPD analysis was done to study desorption properties of adsorbed hydrogen species on Ag/TiO<sub>2</sub> catalysts using Micromeritics Chemisorb 2720 instrument. Samples were reduced under 5 vol% H<sub>2</sub>/N<sub>2</sub> flow (20 mL/min) at 573 K for 0.5 h and were allowed to cool down to 298 K for hydrogen adsorption. After hydrogen adsorption for 0.5 h, gas flow was changed to 20 mL/min helium flow for physisorbed molecules removal. When TCD signal was stabilized, hydrogen desorption tests were then carried out by heating samples from 298 K to 1000 K at 40 K/min under 20 mL/min helium flow. For Ag/TiO<sub>2</sub>-10 sample, H<sub>2</sub>-TPD was done at several heating rates (30, 40, 50, 60 K/min) for determination of H<sub>2</sub> desorption activation energy.

#### **3.2.4 Catalytic reactivity test**

HDO activity of Ag/TiO<sub>2</sub> catalyst was examined by conducting gas-phase hydrodeoxygenation of phenol over Ag/TiO<sub>2</sub> catalysts in a continuous-flow microreactor. Before reaction, catalyst (230 mg) was pretreated with hydrogen at 400 °C under a 20 mL/min of 5% H<sub>2</sub>/N<sub>2</sub> flow for 2 h in the microreactor. Reactions were then performed at 460, 480, 500 and 520 K with similar catalyst weight and hydrogen flow rate. All experiments were done at atmospheric pressure and with 3.5 μmol/s average phenol flow rate. Reaction product mixtures were collected and analyzed via GC-MS. Phenol conversion was calculated as percentage ratio of the number of moles of reacted phenol to the number of moles of initial phenol. Product selectivity was calculated as percentage ratio of the number of moles of a certain product to the number of moles of total products (Kay Lup et al., 2018b). Effect of internal mass transfer on reaction was

also determined using Weisz-Prater criterion and reaction was validated to have negligible internal mass transfer limitations (Appendix A). All experiments were repeated twice and result deviations were less than  $\pm 5\%$ . The mass balance in each experiment was within  $\pm 2\%$  deviation.

### **3.3 Results and discussion**

#### **3.3.1 Physical properties of Ag/TiO<sub>2</sub> catalysts**

##### **3.3.1.1 Textural properties**

Based on N<sub>2</sub> adsorption-desorption isotherms (Figure 3.1A), type IV isotherms with H1 hysteresis loop type were obtained which indicate mesoporous character of Ag/TiO<sub>2</sub> samples (Shi et al., 2015; Wang et al., 2013; Wu et al., 2016). At  $P/P_0 < 0.04$ , the initial sharp increase in N<sub>2</sub> adsorbed quantity was attributed to monolayer N<sub>2</sub> adsorption on sample. For relative pressure of 0.04 to 0.8, the steady increase in N<sub>2</sub> adsorbed quantity was attributed to multilayer N<sub>2</sub> adsorption on sample. At  $P/P_0 > 0.8$ , the sharp adsorption volume increase was due to Kelvin type condensation which occurs in mesoporous pore structures. The H1 hysteresis loops as exhibited by the adsorption-desorption isotherms of TiO<sub>2</sub> and Ag/TiO<sub>2</sub> samples also indicate the characteristics of mesoporous cylindrical channels with uniform size and shape (Leofanti et al., 1998). Figure 3.1B shows the BJH pore size distributions of the samples. All samples exhibited two distinct mesopore size ranges: 2 – 4 nm and 4 – 30 nm with respective modes of 3 nm and 10 nm. With the increase in Ag loading, average pore size, pore volume and specific surface area of sample were noted to decrease which are due to Ag deposition within the pores (Table 3.1). Specific surface areas of stock and calcined TiO<sub>2</sub> (400 °C) samples were  $10.5312 \pm 0.0562$  and  $10.2421 \pm 0.0776$  m<sup>2</sup>/g respectively which indicated negligible sintering effect by calcination.



**Table 3.1: Physicochemical properties of TiO<sub>2</sub> and Ag/TiO<sub>2</sub> samples**

Sample	$S_{\text{BET}}^{\text{a}}$ (m <sup>2</sup> /g)	$S_{\text{micro}}^{\text{b}}$ (m <sup>2</sup> /g)	$V_{\text{micro}}^{\text{b}}$ (cm <sup>3</sup> /g)	$V_{\text{meso}}^{\text{c}}$ (cm <sup>3</sup> /g)	$V_{\text{total}}^{\text{d}}$ (cm <sup>3</sup> /g)	$\bar{D}_p^{\text{e}}$ (nm)	$\bar{D}^{\text{f}}$ (nm)	$\bar{D}_{\text{Ag}}$ (nm)		Ag (wt%)	
								XRD <sup>g</sup>	TEM <sup>h</sup>	ICP-OES	EDX
TiO <sub>2</sub> <sup>i</sup>	10.242	4.259	0.00183	0.04349	0.04532	10.86	89.74	-	-	-	-
Ag/TiO <sub>2</sub> -1	9.745	4.120	0.00186	0.04133	0.04319	10.77	97.45	19.33	16.86	0.78	0.41
Ag/TiO <sub>2</sub> -3	9.105	3.767	0.00167	0.03409	0.03576	10.13	106.28	16.98	12.27	2.43	1.65
Ag/TiO <sub>2</sub> -5	8.791	3.483	0.00154	0.02829	0.02983	10.07	110.03	14.94	10.53	3.98	3.47
Ag/TiO <sub>2</sub> -10	8.689	3.455	0.00155	0.02805	0.02960	9.53	113.13	13.34	7.45	9.13	8.64

<sup>a</sup> Total specific surface area obtained by multi-point BET method

<sup>b</sup> Total surface area and volume of micropores evaluated by *t*-plot method

<sup>c</sup> Mesopore volume, calculated as  $V_{\text{meso}} = V_{\text{total}} - V_{\text{micro}}$

<sup>d</sup> Total pore volume evaluated at  $P/P_0 = 0.99$

<sup>e</sup> Average pore size based on BJH pore size distribution curve

<sup>f</sup> Average TiO<sub>2</sub> particle size

<sup>g</sup> Ag (200) crystallite size via Debye-Scherrer equation

<sup>h</sup> Ag particle size via TEM particle size distribution

<sup>i</sup> Calcined at 400 °C

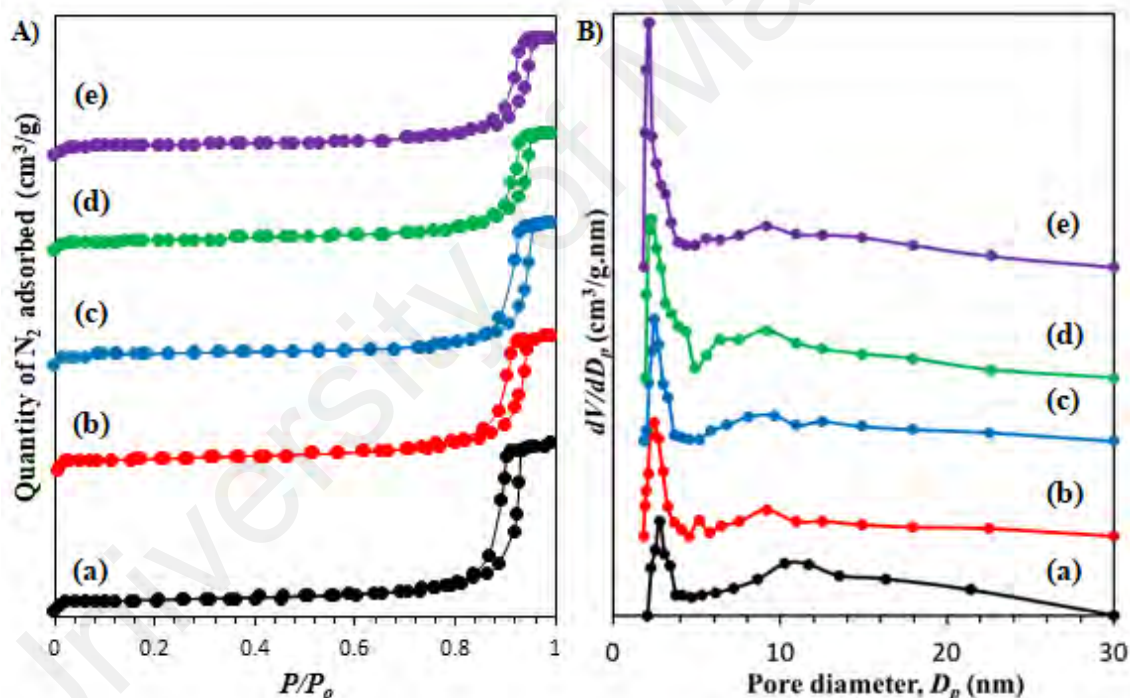


**Figure 3.1: A) N<sub>2</sub> adsorption-desorption isotherms and B) respective pore size distributions of samples with different Ag loadings: (a) TiO<sub>2</sub> (calcined at 400 °C), (b) Ag/TiO<sub>2</sub>-1, (c) Ag/TiO<sub>2</sub>-3, (d) Ag/TiO<sub>2</sub>-5 and (e) Ag/TiO<sub>2</sub>-10**

### 3.3.1.2 XRD analysis

XRD diffractograms (Figure 3.2) confirmed the presence of anatase TiO<sub>2</sub> and metallic silver in samples (b) – (e). Diffraction peaks of anatase at  $2\theta = 25.46^\circ, 37.11^\circ,$

37.96°, 38.71°, 48.20°, 54.04°, 55.21°, 62.25°, 62.82°, 68.89°, 70.42°, 75.17°, 76.15°, 82.79° and 83.15° with their corresponding crystallographic planes (101), (103), (004), (112), (200), (105), (211), (213), (204), (116), (220), (215), (301), (224) and (312) were observed in all of the titania-supported samples (Swanson et al., 1969). Ag<sub>2</sub>O small crystallites were also well dispersed as the diffraction peaks of Ag<sub>2</sub>O for (111), (200), (220) and (311) planes were not significantly detected by XRD.

Diffraction peaks at  $2\theta = 38.11^\circ$ ,  $44.79^\circ$ ,  $65.01^\circ$  and  $78.17^\circ$  were attributed to metallic silver with the corresponding crystallographic planes of (111), (200), (220) and (311) (Morris et al., 1981). For Ag (200) crystallites, their average crystallite sizes decreased with the increase in Ag loading (Table 3.1). The Ag diffraction peak at  $44.79^\circ$  for Ag (200) crystal plane was noted to experience a slight peak shifting effect since the actual diffraction peak for pure Ag was noted to be  $44.295^\circ$  instead (Morris et al., 1981). Based on Bragg's law, the XRD peak shifting of Ag (200) peak to a higher  $2\theta$  from  $44.295^\circ$  to  $44.79^\circ$  would cause the lattice spacing of Ag (200),  $d_{200}$  to decrease from  $2.0433 \text{ \AA}$  to  $2.0218 \text{ \AA}$ . This may indicate the presence of compressive stress on Ag crystal in this particular crystallographic direction during its addition onto TiO<sub>2</sub> support. The compressive stress was also observed to be anisotropic as the peak shifting effect was not observed in other diffraction peaks of silver crystal planes. The absence of silver nitrate peaks in XRD patterns would indicate that all of the silver nitrate precursors in TiO<sub>2</sub> support were thermally decomposed into Ag<sub>2</sub>O or metallic Ag during calcination at 400 °C.

All XRD patterns of samples exhibited similar degree of crystallinity and minimal peak broadening effect which indicated that the addition of silver from 1 wt% to 10 wt% marginally affected the crystallinity of sample. XRD peaks of silver crystallites (Figure 3.2) were not as prominent as compared with TiO<sub>2</sub> XRD peaks. This would be

mainly attributed to the low Ag proportion and also the good dispersion of Ag nanoparticles in TiO<sub>2</sub> support. However, several tiny Ag crystallites were also detected by XRD to give the characteristic Ag diffraction peaks at higher Ag loadings (Figure 3.2). The absence of 81.53° diffraction peak which corresponds to (311) crystal plane of Ag in Fig. 3 may thus be due to the well dispersion of Ag nanoparticles in TiO<sub>2</sub> support and its nature of being a minor characteristic peak of Ag metal. The existence of Ag in TiO<sub>2</sub> support was also confirmed by ICP-OES and EDX analyses (Section 3.3.2.1).

University of Malaya

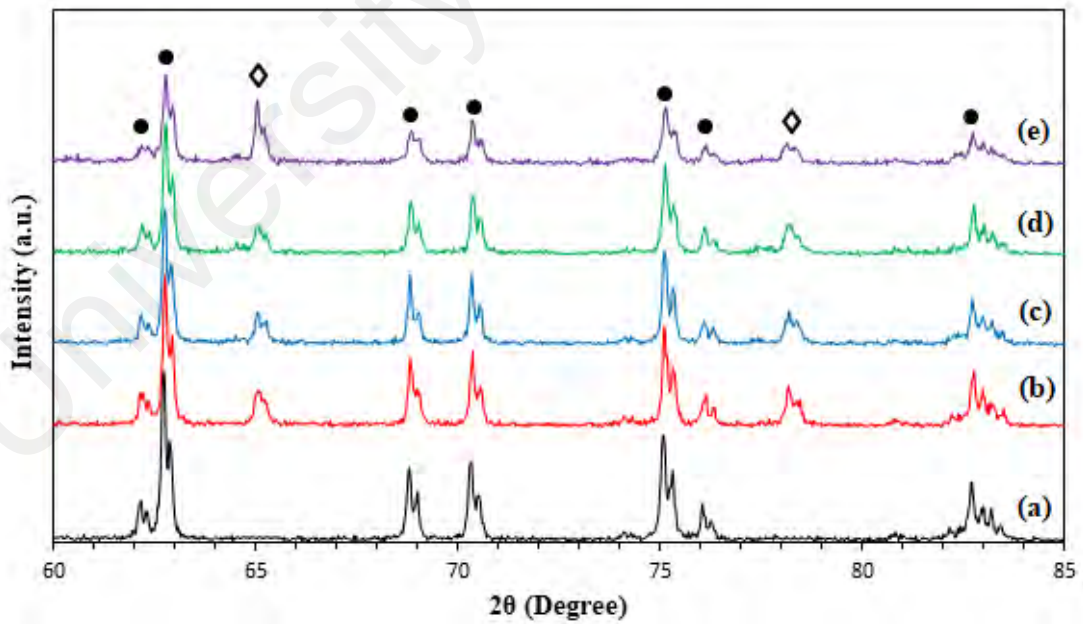
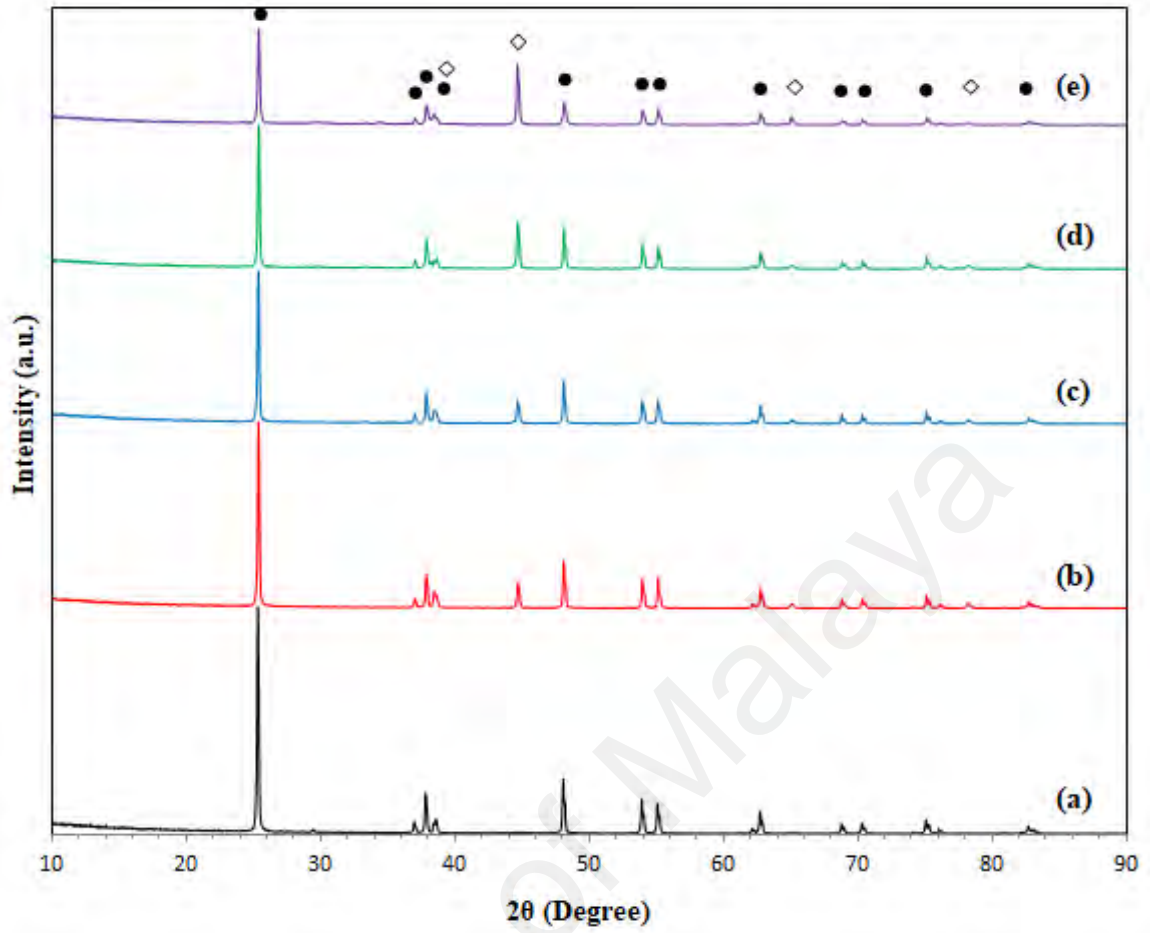
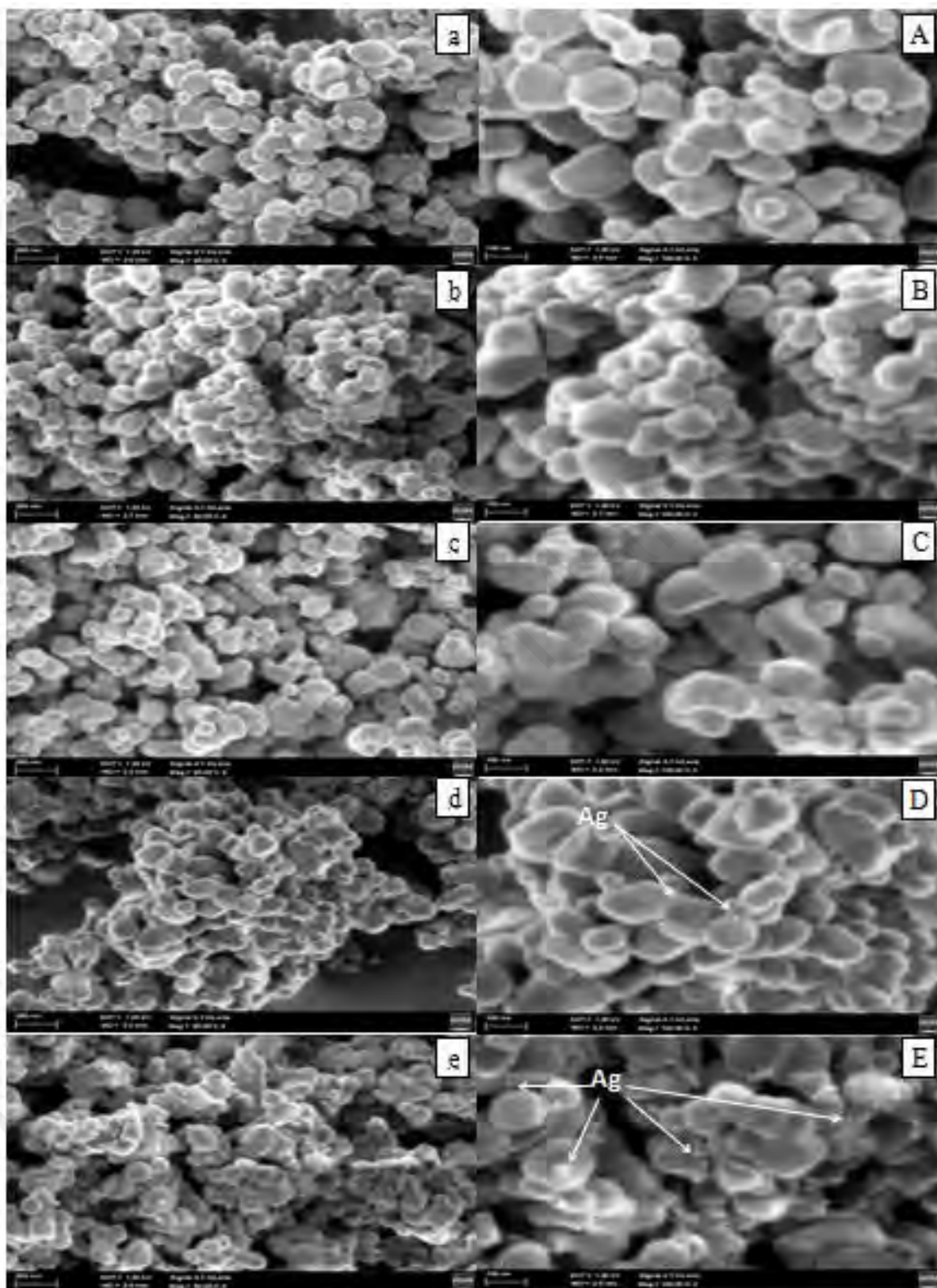


Figure 3.2: XRD patterns of (a)  $\text{TiO}_2$  (calcined at  $400\text{ }^\circ\text{C}$ ), (b)  $\text{Ag/TiO}_2\text{-1}$ , (c)  $\text{Ag/TiO}_2\text{-3}$ , (d)  $\text{Ag/TiO}_2\text{-5}$  and (e)  $\text{Ag/TiO}_2\text{-10}$  where: (●)  $\text{TiO}_2$ ; (◇) metallic Ag

### 3.3.1.3 Morphology and topography

Based on the FESEM micrographs (Figure 3.3), all Ag/TiO<sub>2</sub> samples were observed to have circular slab-like particles. The particles were arranged in numerous stacking layers in various orientations to form aggregates of Ag/TiO<sub>2</sub>. The addition of silver had no effects on the particle shape of catalyst since similar particle shape was also seen in the calcined TiO<sub>2</sub> support. The FESEM micrographs of Ag/TiO<sub>2</sub>-1 and Ag/TiO<sub>2</sub>-3 showed no visible silver deposition on catalyst surface. However, Ag/TiO<sub>2</sub>-5 micrograph (Figure 3.3D) showed little silver nanoparticles deposited on the surface while this phenomenon was more obvious in Ag/TiO<sub>2</sub>-10 sample (Figure 3.3E). These were due to the dominant pore filling effect by Ag at low loadings and the onset of Ag deposition on catalyst surface at higher loadings which were in corroboration with BET results.

Identification of these fine particles as silver nanoparticles on catalyst surface was also further analyzed using TEM. TEM micrographs of samples (Figure 3.4) also showed similar circular slab-like particles which were attributed to titania. Extremely fine particles surrounding and within TiO<sub>2</sub> particles were also observed in TEM micrographs upon the addition of silver. These Ag nanoparticles were observed to decrease in particle size with the increase of metal loading (Table 3.1). Their particle sizes were also noted to be slightly smaller than their crystallite sizes, indicating Ag nanoparticles are anisotropic and not entirely spherical. Particle sizes of TiO<sub>2</sub> support were also analyzed from the micrographs based on more than 100 sampled particles for each sample. Average particle size of sample was observed to increase with the increase in Ag loading (Table 3.1). The increase in particle size with Ag loading could be due to the Ag deposition on the catalyst particles which corroborates with the decreasing trend of specific surface area of samples in textural analysis.



**Figure 3.3: FESEM micrographs of calcined  $\text{TiO}_2$ ,  $\text{Ag}/\text{TiO}_2$ -1,  $\text{Ag}/\text{TiO}_2$ -3,  $\text{Ag}/\text{TiO}_2$ -5 and  $\text{Ag}/\text{TiO}_2$ -10 at 50 kX (a, b, c, d, e) and 100 kX (A, B, C, D, E) magnifications**

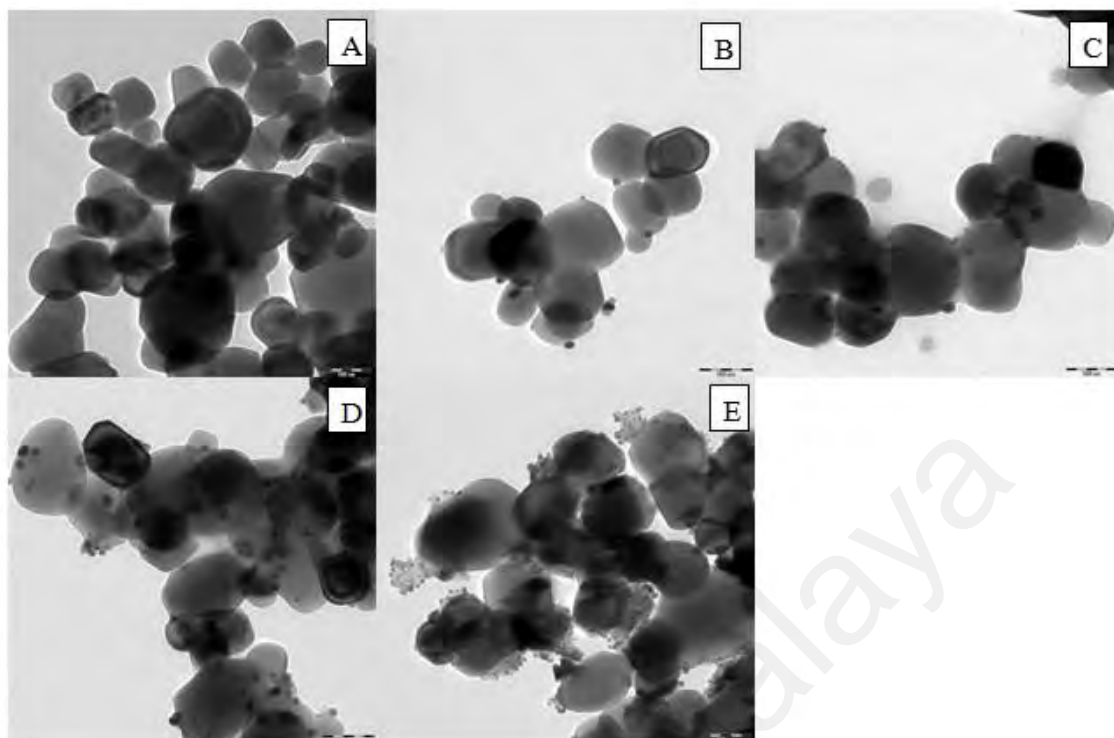


**Figure 3.4: TEM micrographs of (A) calcined TiO<sub>2</sub>, (B) Ag/TiO<sub>2</sub>-1, (C) Ag/TiO<sub>2</sub>-3, (D) Ag/TiO<sub>2</sub>-5 and (E) Ag/TiO<sub>2</sub>-10 at 200 kX magnification**

### 3.3.2 Chemical properties of Ag/TiO<sub>2</sub> catalysts

#### 3.3.2.1 Elemental analysis and mapping

Elemental analyses via ICP-OES and EDX showed that all of the Ag/TiO<sub>2</sub> catalysts consisted only of Ag, Ti and O elements with increasing Ag loadings (Table 3.1). Based on the elemental mapping analysis (Figure 3.5), all Ag/TiO<sub>2</sub> catalysts were reported to have similar and uniform spatial dispersion of Ag and Ti on catalyst surfaces and pores. The uniform distribution of Ag and Ti would also indicate that good dispersion of metal and acid sites within catalyst was achieved. Thus, this would significantly enhance the accessibility of catalytic sites by phenolics for hydrodeoxygenation.

The slight discrepancies between the stoichiometric silver loadings and the actual silver loadings reported using ICP-OES were attributable to the slight sample loss during catalyst synthesis or calcination of catalysts with thermally decomposable

compounds such as nitrates (Leofanti et al., 1997). The silver compositions of catalysts reported by EDX analysis were slightly lower than that of ICP-OES analysis. The detection of characteristic X-ray peaks during EDX analysis would require sufficient excitation of elements within samples by primary electrons and sufficient generation of characteristic X-ray by excited elements which are primarily affected by the depth of the samples. The generation of characteristic X-ray by excited elements is isotropic in nature and may be reabsorbed by other atoms in samples before reaching to the surface for detection (Goldstein et al., 2003). Thus, the detection of silver deposited in pores by EDX may not be as effective as ICP analysis. However, it should also be noted that silver composition values reported by EDX were determined based on a particular region of catalysts, making them to be localized in nature.

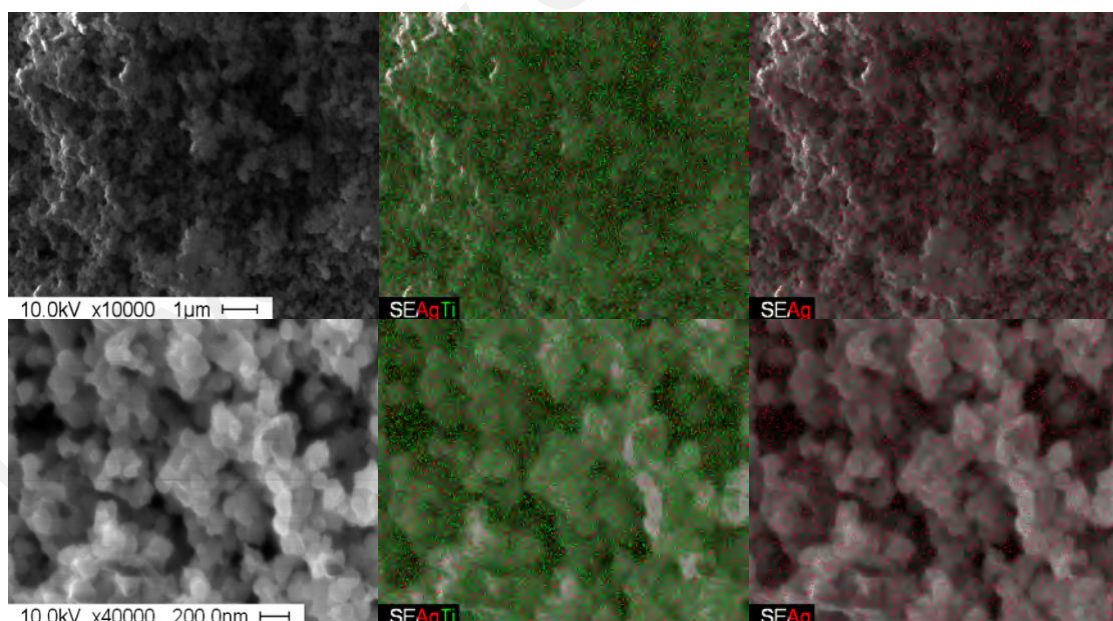


**Figure 3.5: Elemental mapping of Ti (green) and Ag (red) for Ag/TiO<sub>2</sub>-10 catalyst with FESEM micrographs of 10 kX and 40 kX magnifications**



### 3.3.2.2 NH<sub>3</sub>-TPD and Py-FTIR analysis

Figure 3.6 and Table 3.2 show the strength distribution of acid sites of bare TiO<sub>2</sub> support and Ag/TiO<sub>2</sub> catalysts as determined by NH<sub>3</sub>-TPD analysis. Based on NH<sub>3</sub>-TPD spectra, the area under curve represents the amount of NH<sub>3</sub> desorbed from catalysts which correlates to the acid site density of catalysts. For calcined TiO<sub>2</sub> support, mild surface acidity was observed with the existence of a broad desorption peak ranging from 670 K to 800 K. The mild surface acidity of TiO<sub>2</sub> was attributed mainly to Ti<sup>4+</sup> ions as the Lewis acid sites and marginally to the bridging hydroxyl groups within TiO<sub>2</sub> as Brønsted acid sites (Chu et al., 2011; Dines et al., 1991; Galan-Fereres et al., 1995).

The addition of Ag has resulted in the increase in acid site density which is attributed to the increase in surface hydroxyl formation during Ag deposition on TiO<sub>2</sub> (Rismanchian et al., 2016; Seyedmonir et al., 1985; Xin et al., 2005) and its strong proton and hydride ion donor properties (Pearson, 1985). Acid site density of TiO<sub>2</sub> support was significantly lower than that of Ag/TiO<sub>2</sub> catalysts in which addition of silver was observed to produce synergistic effects on the acid sites of catalysts. The first desorption peak which had almost similar desorption temperature range as TiO<sub>2</sub> sample may involve the alteration of acid sites upon silver addition. The alteration of nature and abundance of acid sites may be due to the metal-support interaction between Ag and TiO<sub>2</sub> in which silver metal was involved in the additional bridging hydroxyl groups between the Ti and Ag metals. For instance, in the IR studies of 2,6-lutidine adsorption on titania supported Nb and W based catalysts, Onfroy et al. (2006) showed the progressive increase of Brønsted acidity and decrease of TiO<sub>2</sub> Lewis acidity in the catalysts with the increase of metal loadings. Similar observations were also reported in other metal combinations such as Mo-Ti (Martin et al., 1994), polytungstate (Baertsch et al., 2002), Pd-Fe (Hensley et al., 2014a), Ru-Ti (Nelson et al., 2015), Zr-Zr (Föttinger

et al., 2006), Pd-Al (Zhang et al., 2016), Al-Si (Chu et al., 2011) and Re-Al (Sautet & Delbecq, 2010).

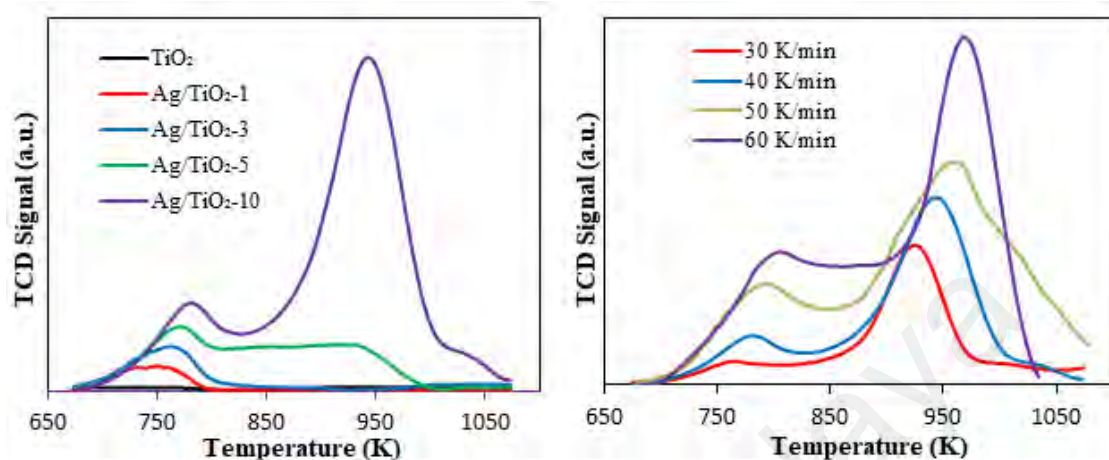


**Figure 3.6: NH<sub>3</sub>-TPD spectra of catalyst samples at 40 K/min (left) and Ag/TiO<sub>2</sub>-10 at different heating rates (right)**

The nature of surface Lewis and Brønsted acid sites in Ag/TiO<sub>2</sub> was further validated via Py-FTIR analysis. Based on Figure 3.7, adsorbed pyridine on Ag/TiO<sub>2</sub> resulted in observed IR bands at 1641 and 1540 cm<sup>-1</sup> that are characteristic of pyridinium ions at surface Brønsted acid sites (PyH<sup>+</sup>) while at 1619 and 1445 cm<sup>-1</sup> that are characteristic of pyridinium ions at surface Lewis acid sites (PyL) (Wachs, 1996; Xing et al., 2017; Zanuttini et al., 2014). The 1490 cm<sup>-1</sup> band is attributed to adsorbed pyridine on both surface Brønsted and Lewis acid sites. Figure 3.7(A) shows that the increase in Ag loading resulted in higher amount of surface Brønsted and Lewis acid sites as observed from the increase in PyH<sup>+</sup> and PyL band intensities. Based on Figure 3.7(B), significant portion of PyH<sup>+</sup> bands were detected at 770 K while PyL bands were notably detected at 950 K. This observation is consistent with NH<sub>3</sub>-TPD result on the higher NH<sub>3</sub> desorption temperature at Lewis acid site, indicating the greater acid strength of Lewis acid site as compared with Brønsted acid sites in Ag/TiO<sub>2</sub> catalyst.

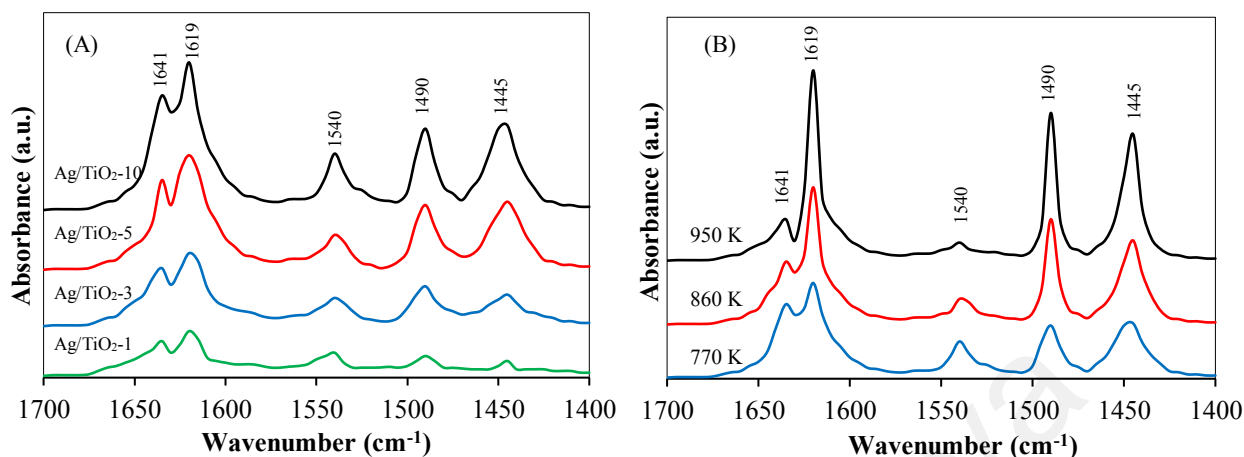


**Figure 3.7: Pyridine-FTIR spectra after desorption for: (A) Ag/TiO<sub>2</sub> with different Ag loadings at 770 K, (B) Ag/TiO<sub>2</sub>-10 at different outgassing temperatures.**

**Table 3.2: NH<sub>3</sub>-TPD analysis of Ag/TiO<sub>2</sub> catalysts**

Catalysts	Peak temperature (K)		Acid site density (μmol/g)		
	Peak 1	Peak 2	Peak 1	Peak 2	Total
Ag/TiO <sub>2</sub> -1	749.0	-	12.5	-	12.5
Ag/TiO <sub>2</sub> -3	762.7	-	25.2	-	25.2
Ag/TiO <sub>2</sub> -5	770.8	915	31.9	46.2	78.1
Ag/TiO <sub>2</sub> -10	779.1	940	49.2	208.4	257.6

Desorption kinetics at Ag/TiO<sub>2</sub> acid sites were also investigated via NH<sub>3</sub>-TPD spectra of Ag/TiO<sub>2</sub>-10 catalyst at various heating rates (Figure 3.6). Desorption rate equation was assumed to be of first order Polanyi-Wigner desorption model in this case:

$$r_d = -\beta \frac{d\theta}{dT} = A\theta^m \exp\left(\frac{-E_d}{RT}\right) \quad (3.1)$$

where  $r_d$  is desorption rate,  $\beta$  is heating rate,  $\theta$  is coverage,  $A$  is pre-exponential factor,  $m$  is kinetic order of desorption ( $m = 1$ ),  $E_d$  is desorption activation energy,  $R$  is ideal gas constant,  $T$  is absolute temperature. By correlating peak temperature ( $T_p$ ) and surface coverage at peak temperature ( $\theta_p$ ) with heating rate (Figure 3.8), desorption

activation energies and pre-exponential factors were determined via Redhead equations (Equation 3.2 and 3.3) (Kay Lup et al., 2018a; Redhead, 1962).

$$\frac{E_d}{RT_p^2} = \frac{A}{\beta} m \theta_p^{m-1} \exp\left(\frac{-E_d}{RT_p}\right) \quad (3.2)$$

$$\ln\left(\frac{\beta}{T_p^2}\right) = -\frac{E_d}{R}\left(\frac{1}{T_p}\right) + \ln\left(\frac{AR}{E_d}\right) \quad (3.3)$$

The activation energies of NH<sub>3</sub> desorption from Ag/TiO<sub>2</sub>-10 were reported to be 77.84 kJ/mol for Brønsted acid site and 96.24 kJ/mol for Lewis acid site. Both desorption phenomena showed similar range of pre-exponential factors which are 1.75 x 10<sup>3</sup> s<sup>-1</sup> and 1.94 x 10<sup>3</sup> s<sup>-1</sup> respectively. The presence of Brønsted and Lewis acid sites in Ag/TiO<sub>2</sub> catalysts is instrumental in catalyzing hydrodeoxygenation. In fact, hydrogenolysis of phenolic compounds during HDO is made possible through the respective roles of Lewis acid site as adsorption sites of phenolic compounds and Brønsted acid site as proton donor to adsorbed phenolic intermediates (He & Wang, 2012). The significant desorption activation energies at both acid sites of Ag/TiO<sub>2</sub> would indicate its excellent adsorption capability to adsorb and activate phenolic compounds for subsequent C—OH bond scission via hydrogenolysis. In previous studies, bifunctional metal-acid catalysts with high surface acidity were noted to achieve high hydrogenolysis activity. Nevertheless, high surface acidity has also been reported to cause secondary condensation reactions to form excess phenolic pool which is a coking precursor (To & Resasco, 2015). Thus, metal oxide supports may serve as alternatives due to their better coking resistances and optimal acidities for HDO. The acidities of metal oxide supported HDO catalysts which achieved more than 70% HDO conversion and selectivity were compared in Table 3.4. The similar range of acidities of Ag/TiO<sub>2</sub> catalyst as compared with these excellent HDO catalysts would also further

support the capability of Ag/TiO<sub>2</sub> in catalyzing hydrogenolysis via its synergistic Brønsted and Lewis acid sites.

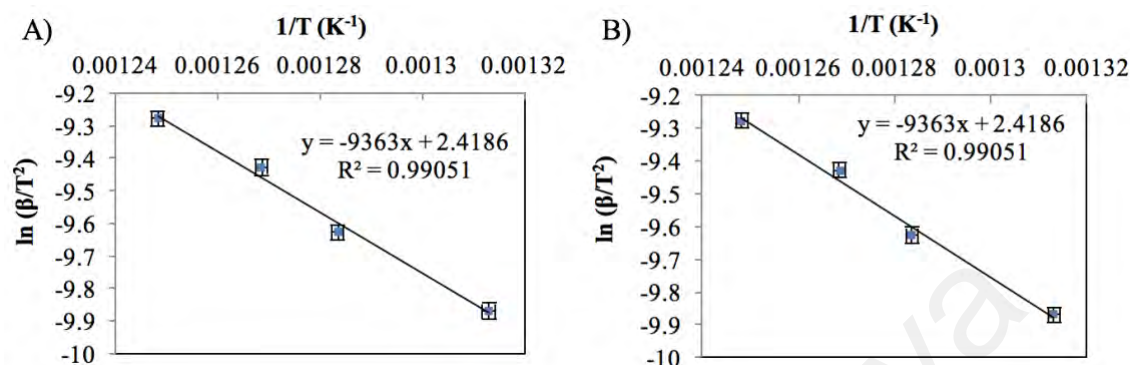


**Figure 3.8: Linear plot of  $\ln (\beta/T_p^2)$  versus  $1/T_p$  for (A) peak 1 and (B) peak 2 of Ag/TiO<sub>2</sub>-10 catalyst**

### 3.3.2.3 H<sub>2</sub>-TPD analysis

H<sub>2</sub>-TPD analysis of Ag/TiO<sub>2</sub> catalysts was done to investigate their relative catalytic activities. Based on Figure 3.9, the area under curve represents the amount of hydrogen desorbed from catalyst. A catalyst with higher amount of hydrogen desorbed would be correlated with its higher amount of metal active site which is an important parameter for its catalytic activity (Liu et al., 2007; Zhang et al., 2017). With the increase of Ag loading, the total H<sub>2</sub> desorption amount was noted to increase which indicated the role of silver in functioning as the main metal active sites. Smaller H<sub>2</sub> desorption peak was also observed in TiO<sub>2</sub> support which indicated the ability of TiO<sub>2</sub> as a reducible support for H<sub>2</sub> desorption and activation (Karim et al., 2017). Investigation of the nature and the quantity of desorbed hydrogen species via H<sub>2</sub>-TPD analysis was done to assess the propensity of hydrogen dissociation over Ag metal site and hydrogen spillover from metal to support sites which are the crucial elements for the catalysis of HDO by Ag/TiO<sub>2</sub> (Furimsky, 2000; Hong et al., 2014b; Nelson et al., 2015). Likewise, these would also draw further insights on the nature of the adsorption and activation

mechanisms of hydrogen over Ag/TiO<sub>2</sub> catalyst during HDO process. Peak deconvolution was done to resolve overlapping peaks. It was found that the first broad peak consisted of two overlapping desorption peaks and the second peak as the only peak by itself (Figure 3.10). For Ag/TiO<sub>2</sub>-1 catalyst (Figure 3.10b), peak deconvolution was done only on the first broad peak while the second peak was analyzed separately as a single desorption peak. The first two deconvoluted peaks which were below 673 K would be attributed to H<sub>2</sub> desorption from metal sites whereas the third deconvoluted peak which was above 673 K would be due to hydrogen spillover species (Chen et al., 2009; Li et al., 2011; Shafaghat et al., 2016).

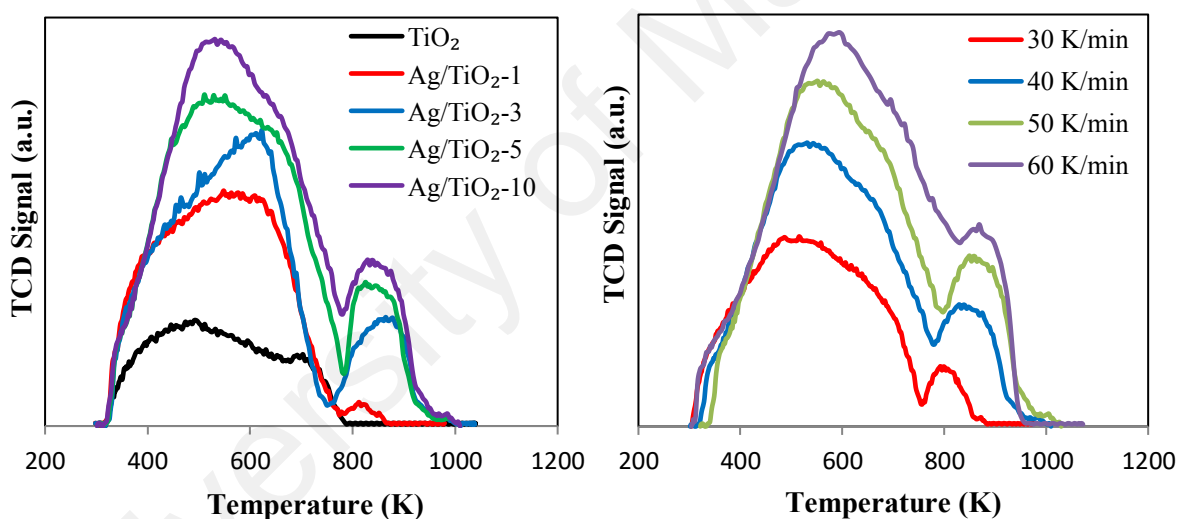


**Figure 3.9: H<sub>2</sub>-TPD spectra of catalyst samples at 40 K/min (left) and Ag/TiO<sub>2</sub>-10 at different heating rates (right)**

Existence of two distinct deconvoluted peaks below 673 K would indicate the occurrence of H<sub>2</sub> chemisorption on metal active sites in two dissimilar manners: molecular and dissociative chemisorption. Molecular H<sub>2</sub> chemisorption generally involves lesser energy than dissociative H<sub>2</sub> chemisorption since the latter requires additional dissociation energy to dissociate H<sub>2</sub> molecule into atomic hydrogen prior to its adsorption. Thus, from H<sub>2</sub>-TPD perspective, the first deconvoluted peak accounts for

the molecular H<sub>2</sub> desorption from metal sites whereas the second deconvoluted peak accounts for the atomic H desorption from metal sites (Gupta et al., 1988). Based on Table 3.3, it can be noted that the ratio of molecular H<sub>2</sub> desorption to atomic H desorption decreased significantly during initial addition of Ag but subsequently increased when more Ag was added. Adsorption of atomic hydrogen on metal active sites may be preferred as they are more readily accessible for reactions, causing the aforementioned parameter as one of the factors in considering its optimal catalytic activity. Nevertheless, it should also be realized that the increase of Ag loading may have greater compensating effects for catalytic activity due to the higher abundance of catalytic sites for reaction.

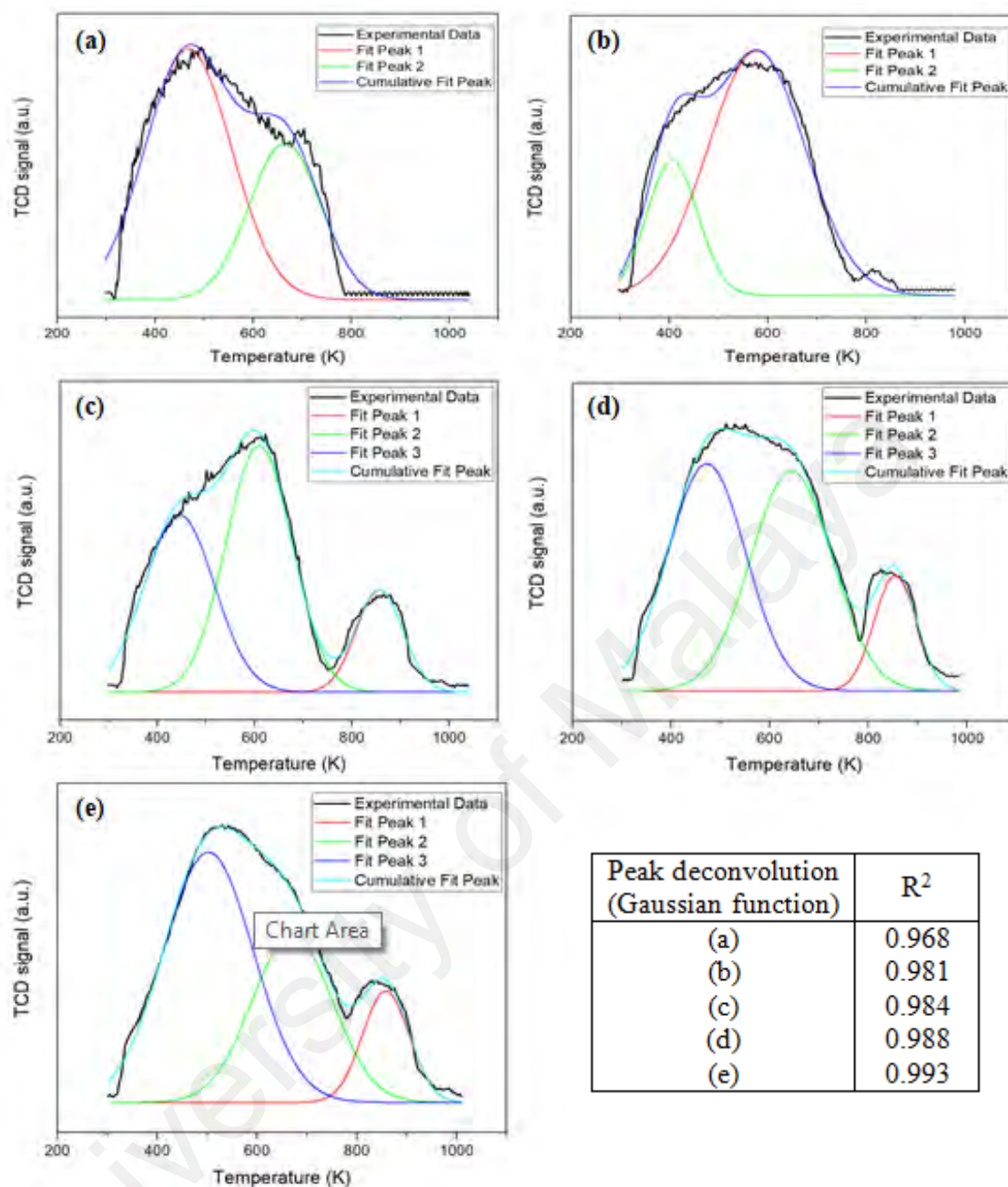


**Figure 3.10: Deconvoluted H<sub>2</sub>-TPD spectra of (a) TiO<sub>2</sub>, (b) Ag/TiO<sub>2</sub>-1, (c) Ag/TiO<sub>2</sub>-3, (d) Ag/TiO<sub>2</sub>-5 and (e) Ag/TiO<sub>2</sub>-10**

Hydrogen spillover which involves surface migration of activated H atoms from metal sites to catalyst support was also observed in Ag/TiO<sub>2</sub> catalysts. The silver metal functioned as the metal active sites which readily adsorb and activate hydrogen. The activated hydrogen subsequently diffused to the support surface which is thermodynamically more favored as compared with the direct generation of adsorbed H



atoms on support surface. This phenomenon is instrumental for the facile activation and reaction of model compounds by hydrogen (Conner & Falconer, 1995; Karim et al., 2017; Kay Lup et al., 2017a; Miller et al., 1993). The hydrogen spillover ratio was noted to increase from 0.018 to 0.144 during the initial increase of Ag loading from 1 wt% to 3 wt%. At higher loadings, hydrogen spillover ratio remained almost similar. Nevertheless, the extent of hydrogen spillover would increase due to the increase in total amount of metal active site, making the higher loading catalyst being more effective instead. Kinetic parameters of H<sub>2</sub> desorption from Ag/TiO<sub>2</sub>-10 catalyst were also determined using Redhead analysis at different heating rates. With the increase in heating rate, similar desorption modes were observed while desorption peak temperatures were shown to increase (Figure 3.9). By using Equation 3.2, Equation 3.3 and 3.4 can be used to correlate desorption peak temperature with heating rate for first ( $m = 1$ ) and second ( $m = 2$ ) order H<sub>2</sub> desorption respectively (Figure 3.11). For instance, molecular H<sub>2</sub> desorption has first order of desorption while atomic H and hydrogen spillover species desorption have second order of desorption to account for their recombination of two hydrogen atoms into molecular hydrogen.

$$\ln\left(\frac{\beta}{T_p^2}\right) = -\frac{E_d}{R}\left(\frac{1}{T_p}\right) + \ln\left(\frac{AR\theta_0}{E_d}\right) \quad (3.4)$$

**Table 3.3: H<sub>2</sub>-TPD analysis of TiO<sub>2</sub> support and Ag/TiO<sub>2</sub> catalysts**

Catalysts	Peak temperature (K)			H <sub>2</sub> desorption amount (μmol/g)				Molecular to atomic H ratio	Hydrogen spillover ratio
	Peak 1 <sup>a</sup>	Peak 2 <sup>b</sup>	Peak 3 <sup>c</sup>	Peak 1	Peak 2	Peak 3	Total		
TiO <sub>2</sub>	467.4	665.0	-	70.0	37.1	-	107.1	1.89	-
Ag/TiO <sub>2</sub> -1	407.9	577.1	811	53.9	188.7	4.4	247.0	0.29	0.018
Ag/TiO <sub>2</sub> -3	444.8	609.3	856.9	113.3	151.5	44.7	309.5	0.75	0.144
Ag/TiO <sub>2</sub> -5	472.7	644.2	854.6	176.1	180.4	48.9	405.4	0.98	0.121
Ag/TiO <sub>2</sub> -10	501.9	669.9	859.2	245.0	149.0	57.6	451.6	1.64	0.128

<sup>a</sup> Deconvoluted peak (furthest to the left of TPD spectra) which accounts for molecular H<sub>2</sub> desorption

<sup>b</sup> Deconvoluted peak (middle of TPD spectra) which accounts for atomic H desorption

<sup>c</sup> Deconvoluted peak (furthest to the right of TPD spectra) which accounts for hydrogen spillover species

For molecular H<sub>2</sub> desorption mode from Ag/TiO<sub>2</sub>-10 catalyst, desorption activation energy and pre-exponential factor were respectively determined to be 15.09 kJ/mol and 0.17 s<sup>-1</sup>. For atomic hydrogen desorption mode from Ag/TiO<sub>2</sub>-10 catalyst, desorption activation energy and pre-exponential factor were respectively determined to be 47.66 kJ/mol and 40.83 s<sup>-1</sup>. Likewise, desorption activation energy and pre-exponential factor for hydrogen spillover species desorption were 49.91 kJ/mol and 6.28 s<sup>-1</sup> respectively. The higher desorption activation energies of the atomic hydrogen and hydrogen spillover species desorption would indicate the stronger interaction of such hydrogen species with the metal active sites and support surface respectively. The presence of metal sites in Ag/TiO<sub>2</sub> is necessary to create a synergy with the acid sites for C—OH bond hydrogenolysis of phenolics because activated hydrogen species is an important precursor for such bond scission. Likewise, the formation of activated hydrogen species on metal sites is highly dependent on the hydrogen sticking probability and the electronic interaction of hydrogen with the metal species. Silver which is a transition metal was also compared with other transition metals such as Ni, Pd, Pt and Ru which have high sticking probabilities (Table 3.4). Silver was noted to have similar range of hydrogen sorption and activation which would indicate its role in producing sufficient activated hydrogen species for the hydrogenolysis of adsorbed phenolic intermediates at acid sites. The acid site with activated hydrogen ratio of Ag/TiO<sub>2</sub> also indicated the abundance of activated hydrogen for hydrogen spillover to TiO<sub>2</sub> support. Elemental mapping has shown the uniform spatial distribution of metal and acid sites with both of them existing in close proximity. Thus, with these advantages, about 12.8 mol% to 14.4 mol% of adsorbed hydrogen was observed to have undergone surface migration to TiO<sub>2</sub> support. The hydrogen spillover occurring within Ag/TiO<sub>2</sub> catalyst was also noted to be facile as TiO<sub>2</sub> is a reducible support. By observing the synergistic role of acid and metal sites and the efficient hydrogen spillover over TiO<sub>2</sub> support, Ag/TiO<sub>2</sub> catalyst could be a

potential HDO catalyst for phenolics in which rigorous kinetic studies have to be done in future studies for the elucidation of its catalytic interaction.

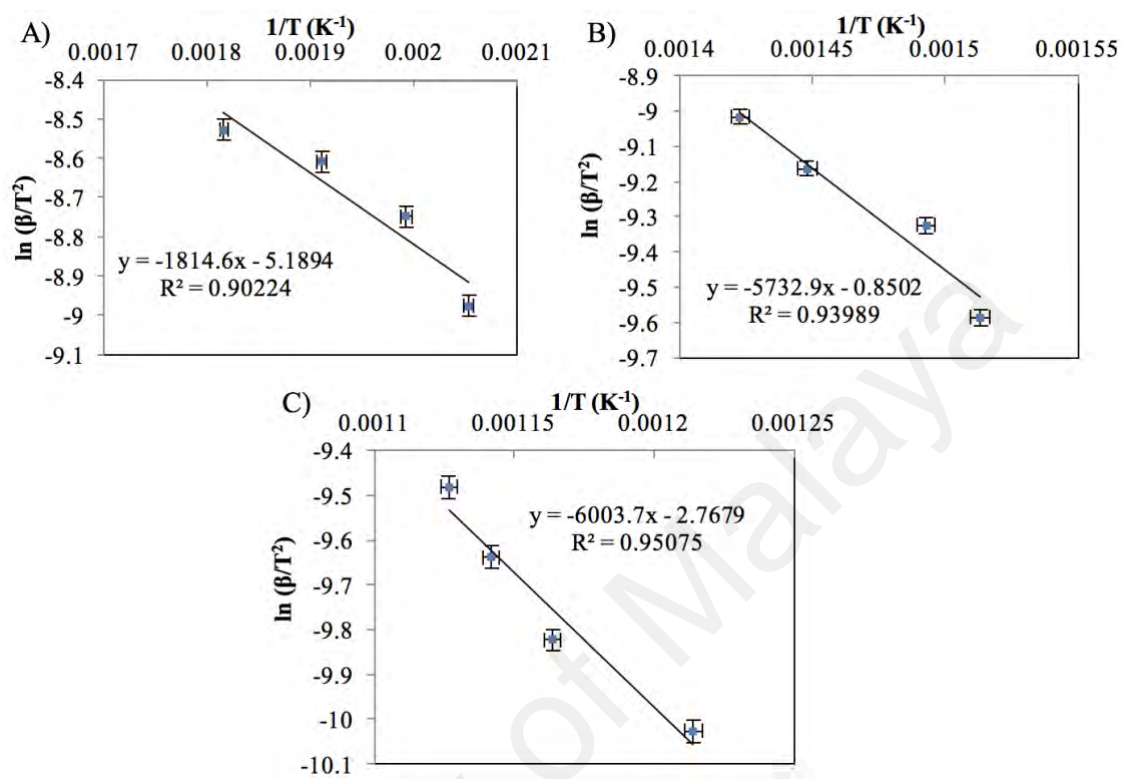


**Figure 3.11: Linear plot of  $\ln(\beta/T_p^2)$  versus  $1/T_p$  for A) peak 1, B) peak 2 and C) peak 3 of Ag/TiO<sub>2</sub>-10 catalyst**

**Table 3.4: Comparison of various HDO catalysts in terms of acid and metal site densities**

Catalyst	Preparation method	Surface area (m <sup>2</sup> /g)	Acidity (mmol NH <sub>3</sub> /g)	H/metal atomic ratio	Acid site/H ratio	Ref.
Ag/TiO <sub>2</sub> (9.13 wt% Ag)	Dry impregnation	8.689	0.2576	1.067	0.285	this work
Ni <sub>2</sub> P/Al <sub>2</sub> O <sub>3</sub> (11.2 wt% Ni <sub>2</sub> P)	Dry impregnation	90	0.2110	1.336	0.105	(Wu et al., 2013)
Ni <sub>2</sub> P/ZrO <sub>2</sub> (11.2 wt% Ni <sub>2</sub> P)	Dry impregnation	47	0.2050	1.453	0.093	(Wu et al., 2013)
Ni <sub>2</sub> P/SiO <sub>2</sub> (11.2 wt% Ni <sub>2</sub> P)	Dry impregnation	127	0.2000	1.690	0.078	(Wu et al., 2013)
Pd/WO <sub>x</sub> /Al <sub>2</sub> O <sub>3</sub> (2 wt% Pd, 31.6 wt% W)	Dry impregnation	157.3	0.4400	0.075	31.22	(Hong et al., 2014a)
Pd/SiO <sub>2</sub> -Al <sub>2</sub> O <sub>3</sub> (2.03 wt% Pd, 1.88 Si/Al)	Sol-gel	505.2	0.4430	0.587	3.956	(Hong et al., 2014a)
Pd/Al <sub>2</sub> O <sub>3</sub> (2.1 wt% Pd)	Dry impregnation	238.6	0.0787	0.588	0.678	(Hong et al., 2014a)
Pt/Al <sub>2</sub> O <sub>3</sub> (2.93 wt% Pt)	Dry impregnation	88	0.1600	0.900	1.184	(Peng et al., 2012)
Pt-ReO <sub>x</sub> /C <sup>a</sup> (5 wt% Pt, 4.9 wt% Re)	Dry impregnation	621	0.1675	0.256	2.553	(Kim et al., 2013)
Ru/C <sup>a</sup> (1 wt% Ru)	Dry impregnation	1021	0.3063	0.604	5.125	(Chen et al., 2011)

<sup>a</sup> Activated carbon

### 3.3.3 HDO activity of Ag/TiO<sub>2</sub> catalysts

Benzene yield and phenol conversion over Ag/TiO<sub>2</sub>-10 catalyst in phenol HDO at different reaction temperatures are shown in Table 3.5. Ag/TiO<sub>2</sub> catalyst was noted to have mediocre phenol conversion but high benzene selectivity. Other minor HDO products formed were cyclohexanol, cyclohexene, cyclohexane, cyclohexanone and benzenediols which indicated side reactions of phenyl ring hydrogenation and trans-hydroxylation over Ag/TiO<sub>2</sub>. With the increase in Ag loading, phenol conversion increased proportionally while benzene selectivity remained relatively constant. Higher phenol conversion at higher Ag loading was due to the increase in available Ag metal sites for HDO process (Kay Lup et al., 2017b; Mortensen et al., 2011). Likewise, the smaller Ag particle size at higher loading has also resulted in better Ag dispersion which in turn improved phenol conversion.

Benzene turnover frequency ( $\text{TOF}_{\text{benzene}}$ ) was calculated in order to quantify the specific deoxygenation rates of the catalyst. Based on Table 3.5 and 3.6, TOFs of Ag/TiO<sub>2</sub> catalyst increased with the increase in reaction temperature and metal loading which suggests that higher number of Ag sites enhances phenol deoxygenation activity. The deoxygenation TOF of Ag/TiO<sub>2</sub> (0.78 wt% Ag,  $\text{TOF}_{500\text{K}} = 0.0055 \text{ s}^{-1}$ ) was reported to be lower than TOFs of Pd and Pt-based catalysts such as Pd/ZrO<sub>2</sub> (0.89 wt% Pd,  $\text{TOF}_{573\text{K}} = 0.09 \text{ s}^{-1}$ ), Pd/SiO<sub>2</sub> (1 wt% Pd,  $\text{TOF}_{523\text{K}} = 0.14 \text{ s}^{-1}$ ) and Pt/SiO<sub>2</sub> (1 wt% Pd,  $\text{TOF}_{523\text{K}} = 0.17 \text{ s}^{-1}$ ) (Chen et al., 2015a; de Souza et al., 2015) which indicates Ag has lower phenol deoxygenation activity than Pd and Pt-based HDO catalysts. Likewise, this is also in corroboration with computational findings that associated the low HDO activity of Ag to its high C—O bond breaking energy barrier (Jalid et al., 2017; Lausche et al., 2014). Decent HDO activity by Ag was able to be achieved in spite of its high C—O bond breaking energy barrier which is attributed to the good dispersion of Ag nanoparticles, proper distribution of metal-acid sites for efficient diffusion of adsorbed intermediates across metal-support interfaces. Among other supported metal catalysts such as Pd, Pt, Ni and Mo-based catalysts, the phenol conversion of Ag/TiO<sub>2</sub> catalyst is certainly inferior to theirs which could reach up to about 90% conversion (Kay Lup et al., 2017b). One of the considerations is that this particular work was done at atmospheric pressure while many studies involved HDO processes with high H<sub>2</sub> pressure.

**Table 3.5: Catalytic performance of Ag/TiO<sub>2</sub>-10 catalyst for phenol HDO. Reaction conditions: Pressure = 1 atm, W<sub>cat</sub> = 230 mg, 100 mL/min 5% H<sub>2</sub>/N<sub>2</sub> flow, WHSV = 5.09 h<sup>-1</sup>.**

Parameter (mol%)	Temperature (K)		
	450	500	550
$X_{phenol}^a$ (mol%)	23.1	32.3	34.2
$S_{benzene}^b$ (mol%)	93.1	95.2	98.9
$S_{cyclohexanol}$ (mol%)	4.3	2.7	0.6
$S_{cyclohexene}$ (mol%)	1.6	1.2	0.3
$S_{cyclohexane}$ (mol%)	1.0	0.9	0.2
$S_{cyclohexanone}$ (mol%)	< 0.01 (trace)	< 0.02 (trace)	< 0.01 (trace)
$S_{benzenediols}$ (mol%)	< 0.01 (trace)	< 0.01 (trace)	< 0.01 (trace)
$TOF_{benzene}^c$ (s <sup>-1</sup> )	0.0190	0.0272	0.0299

<sup>a</sup> Conversion of phenol

<sup>b</sup> Selectivity of benzene

<sup>c</sup>  $TOF_{benzene} = r_{benzene}/N_{Ag}^*$  where  $r_{benzene}$  ( $\mu\text{mol}/g_{cat}\cdot\text{s}$ ) is benzene formation rate and  $N_{Ag}^*$  ( $\mu\text{mol}/g_{cat}$ ) is number of exposed Ag surface atoms determined by H<sub>2</sub> chemisorption (Spivey et al., 2004).

**Table 3.6: Effect of Ag loading on catalyst performance. Reaction conditions: Pressure = 1 atm, T = 500 K, W<sub>cat</sub> = 230 mg, 100 mL/min 5% H<sub>2</sub>/N<sub>2</sub> flow, WHSV = 5.09 h<sup>-1</sup>.**

Parameter	Ag/TiO <sub>2</sub> -1	Ag/TiO <sub>2</sub> -3	Ag/TiO <sub>2</sub> -5	Ag/TiO <sub>2</sub> -10
$X_{phenol}$ (mol%)	2.7	9.2	15.9	32.3
$S_{benzene}$ (mol%)	93.6	95.0	94.8	95.2
$TOF_{benzene}$ at 500 K <sup>a</sup> (s <sup>-1</sup> )	0.0055	0.0132	0.0154	0.0272

<sup>a</sup> Number of exposed Ag surface atoms determined by H<sub>2</sub> chemisorption = 69.9, 101.1, 149.1 and 172.3  $\mu\text{mol}/g_{cat}$  for Ag/TiO<sub>2</sub>-1, Ag/TiO<sub>2</sub>-3, Ag/TiO<sub>2</sub>-5 and Ag/TiO<sub>2</sub>-10 catalysts.

### 3.4 Conclusion

Effect of silver loading on titania supported silver catalyst and its physicochemical properties were examined in detail in this study. The incorporation of silver as metal active site onto titania support mainly involved the filling of pores with silver at low silver loadings and subsequently the deposition of silver aggregates on catalyst surface at high silver loadings. Addition of silver onto catalyst has also resulted in the increase of acid site density with silver metal sites as Lewis acid sites and the bridging hydroxyl

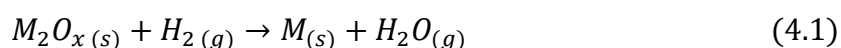
groups between Ti and Ag metals as Brønsted acid sites. The Brønsted and Lewis acid sites were noted to have  $\text{NH}_3$  desorption activation energies of 77.84 kJ/mol and 96.24 kJ/mol respectively. Addition of silver onto catalyst has also resulted in the increase of  $\text{H}_2$  uptake due to the increase in metal active sites as shown in  $\text{H}_2$ -TPD analysis. Molecular and dissociative  $\text{H}_2$  chemisorption and hydrogen spillover species were noted to be the main chemisorption modes of hydrogen on Ag metal sites. Hydrogen spillover was observed due to the close proximity of acid and metal sites as indicated by elemental mapping. The synergy between acid and metal sites in Ag/TiO<sub>2</sub> catalyst would indicate its catalytic activity for hydrogenolysis of adsorbed phenolic intermediates at acid site by activated hydrogen species that undergone surface migration from metal sites. These initial findings have thus formed the basis for more detailed studies on the kinetics and mechanism of HDO over Ag/TiO<sub>2</sub> catalyst which would be the focus of future reports.

**CHAPTER 4: TEMPERATURE-PROGRAMMED REDUCTION OF SILVER(I)  
OXIDE IN TITANIA SUPPORTED SILVER CATALYST UNDER H<sub>2</sub>  
ATMOSPHERE**

**4.1 Introduction**

Metal oxides have various applications in different fields of science and technology owing to their unique magnetic, optical, electrical, dielectric, acid-base and redox properties. In catalysis, redox property of transition metal oxides is one of the major aspects in understanding their catalytic interactions with reactants. This is because transition metals or metal oxides are often capable of having multiple stable oxidation states which are required in catalyzing reactions involving electron transfers or exchanges such as oxidation, reduction, dehydrogenation, deoxygenation, etc. There are many examples of metal oxides being studied for their uses as heterogeneous catalysts such as oxides of Al, Ce, Co, Cu, Ga, Mg, Mn, Mo, Nb, Ni, Ti, V, Zr, etc. (Gervasini, 2013) Some metal oxides were known to be highly stable and thus remain as irreducible oxides. Likewise, metal oxides such as Co, Cu, Ni and Mo were known to be reducible oxides while oxides of Ga and Nb were known to be quasi-irreducible oxides which require higher temperature (>1000 °C) for observable reduction.

The reduction properties of metal oxides can be quantitatively studied via their reduction reactions and its associated thermodynamic parameter,  $\Delta G$ , which is the Gibbs free energy change of reduction:



$$\Delta G = \Delta G^* + RT \ln \left[ \frac{p_{H_2O}}{p_{H_2}} \right] \quad (4.2)$$



where  $M$  represents metal element,  $x$  is oxidation state of metal,  $\Delta G^*$  is standard Gibbs free energy change of reduction,  $p_{H_2O}$  and  $p_{H_2}$  are partial pressures of water vapor and hydrogen gas respectively. Based on previous work,  $\Delta G^*$  values of several metal oxides were comprehensively reported as followed:  $Ag_2O \ll PdO < RhO < IrO_2 < CuO < Sb_2O_5 < PbO < NiO \approx CoO \approx CdO \approx MnO_2 < Fe_2O_3 < SnO_2 < V_2O_5 < ZnO < Cr_2O_3 \ll SiO_2 < TiO_2 \ll Al_2O_3 < La_2O_3 < CaO$ ; in which metal oxides of Ag, Pd, Rh, Ir, Cu, Sb, Pb, Ni, Co, Cd and Mn had negative  $\Delta G^*$  values (Hurst et al., 1982). Gibbs free energy change of reduction is a thermodynamic parameter that indicates spontaneity of reduction in which a larger negative  $\Delta G^*$  value means that reduction is more spontaneous and thermodynamically favored. By performing reduction in an experimental setup that constantly removes water vapor from reaction zone at higher temperature; the second term on the right hand side of Equation 4.2 becomes a larger negative value. Thus,  $\Delta G$  value of a particular metal reduction would also become a larger negative value, indicating its reduction being thermodynamically favored at higher temperature and lower water vapor concentration.

Reduction process of metal oxide powdered samples is a form of solid state transformation which generally involves i.) diffusion of hydrogen and oxygen from gas phase to solid sample or vice versa; ii.) nucleation of metal nuclei from metal oxides; iii.) rearrangement of metal oxide lattice into reduced metal lattice. Therefore, kinetic study on the reduction of metal oxide samples would elucidate more on the role and dominance of such elementary steps involved in reduction process. For instance, several TPR kinetic analyses on reduction of metal oxides such as cobalt oxide, chromium oxide, iron oxide, vanadium oxide and silver(I) oxide were reported in literature (Jelić et al., 2011; Juarez & Morales, 2008; Kanervo et al., 2003; Kanervo & Krause, 2002; Lin & Chen, 2004; Lin et al., 2003). Tiernan et al. (2001) reported that reduction

mechanism of metal oxide is influenced by particle size in which larger metal oxide particles were noted to be reduced via phase boundary mechanism while smaller metal oxide particles were noted to be reduced via uniform internal reduction mechanism. Various kinetic results on metal oxide reduction such as  $\text{Fe}_2\text{O}_3$  were also reviewed by Pineau et al. (2006) in which the numerous variations in reduction behavior were also noted to be affected by powdered sample preparation, its physicochemical properties and TPR procedures (Heidebrecht et al., 2008; Jozwiak et al., 2007). As for silver(I) oxide, its current scholarship is more established in its thermal decomposition as compared with  $\text{H}_2$ -based reduction. Majority of the works on  $\text{Ag}_2\text{O}$  thermal decomposition (Garner & Reeves, 1954; Herley & Prout, 1960; L'vov, 1999; Shahcheraghi & Khayati, 2014a; Shahcheraghi & Khayati, 2014b; Waterhouse et al., 2001) reported on its autocatalytic nature and nucleation mechanism while  $\text{H}_2$ -based  $\text{Ag}_2\text{O}$  reduction experiments by Jelić et al. (2011), Juarez and Morales (2008) also reported likewise.

When metal oxides catalyze oxidative or reductive reactions, it is possible for them to undergo a series of reduction and oxidation due to exchange of hydrogen and various oxygen species such as surface or lattice oxygen between catalyst active sites and gas phase. Hydrodeoxygenation would be one of the reactions which would be classified under this category since it involves the cleavage of C—O bond from O-containing compounds by hydrogen which is also termed as hydrogenolysis (Kay Lup et al., 2017a). Hydrogenolysis is often catalyzed by various transition metals supported on transition metal oxides (Mortensen et al., 2011). Several fundamental properties such as surface acidity, oxophilicity, hydrogen sticking probability and reducibility of metals were noted to have significant impacts on hydrodeoxygenation activity of such catalysts (de Souza et al., 2015; Hong et al., 2014b; Kay Lup et al., 2017b). For transition metal-based HDO catalysts such as Co, Ir, Pd, Pt, Re, Rh and Ru, reducibility was noted to aid

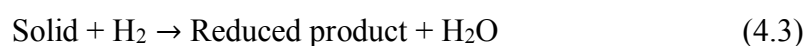
in their oxygen abstraction activity. However, high material costs of transition metals may adversely affect their commerciality for HDO process. Silver, however, is categorized with Cu, Fe, Ni, Ti and Zn as low cost transition metals which would improve the catalyst commerciality, thus serving as the motivation of such selection in this study.

Herein this study, Ag<sub>2</sub>O reduction in Ag/TiO<sub>2</sub> catalyst was analyzed via TPR technique. This study was done with the motivation to determine the reduction model that accurately describes reduction of Ag<sub>2</sub>O to Ag in Ag/TiO<sub>2</sub> catalyst. Studies on Ag<sub>2</sub>O reduction model were also done in previous studies at lower heating rates such as 5—11 K/min (Juarez & Morales, 2008) and 2.5—30 K/min (Jelić et al., 2011). Thus, this study provides further insight on Ag<sub>2</sub>O reduction model over higher heating rates (20—50 K/min). Kinetic parameters for the reduction model are also presented in this study based on the generalized Kissinger approach and other supplementary techniques reported in several studies (Gervasini, 2013; Heidebrecht et al., 2008; Kissinger, 1957; Wimmers et al., 1986). Thus, by determining the accurate reduction model and its kinetic parameters for Ag/TiO<sub>2</sub> catalyst, further development on its redox interaction with hydrogen and O-containing compounds can then be established.

## **4.2 Theory**

### **4.2.1 Determination of reduction rate equation**

Consider a gas-solid reaction involving reduction of solid by a stream of reducing gas such as hydrogen:



The reduction rate equation can be modeled as an overall function (Equation 4.4) which is the product of a temperature-dependent function:  $k'(T)$  and two concentration-dependent functions:  $f(\alpha)$  and  $\varphi(p_{H_2}, p_{H_2O})$ . With high H<sub>2</sub> flow rate and small amount of solid sample conditions, reduction can be assumed to occur at quasi-steady state which enables the concentration-dependent function,  $\varphi(p_{H_2}, p_{H_2O})$  to be approximated as a constant (Equation 4.5).

$$r = \frac{d\alpha}{dt} = k'(T)f(\alpha)\varphi(p_{H_2}, p_{H_2O}) \quad (4.4)$$

$$r = \frac{d\alpha}{dt} = k(T)f(\alpha) \quad (4.5)$$

where  $r$  is reduction rate,  $\alpha$  is conversion of solid reactant,  $t$  is reaction time,  $T$  is temperature,  $p_{H_2}$  and  $p_{H_2O}$  are partial pressures of hydrogen and water,  $k'(T)$  and  $k(T)$  are reduction rate constants with  $k(T) = k'(T)\varphi(p_{H_2}, p_{H_2O})$ . The  $f(\alpha)$  function which is the reduction model can be mathematically described by several gas-solid reaction models given in Table 4.1. For H<sub>2</sub>-TPR processes, linear heating rate is commonly used where  $\beta = \frac{dT}{dt} = \text{constant}$  and  $\beta$  represents the heating rate. Likewise,  $k(T)$  function which correlates the reduction rate constant with temperature could also be modeled using Arrhenius' equation. With these information, Equation 4.5 can be rewritten as Equation 4.6 and hence Equation 4.7.

$$\frac{d\alpha}{dT} = \frac{k(T)}{\beta} f(\alpha) \quad (4.6)$$

$$\frac{d\alpha}{dT} = \frac{A}{\beta} e^{-E/RT} f(\alpha) \quad (4.7)$$

where  $E$  is the reduction activation energy,  $R$  is ideal gas constant and  $A$  is product of  $\varphi(p_{H_2}, p_{H_2O})$  constant and pre-exponential factor.

#### 4.2.2 Calculation of TPR patterns

To compute TPR pattern as a mathematical function relating  $d\alpha/dT$  with  $T$ , Equation 4.7 which is a separable first order differential equation can be integrated via separation of variables (Equation 4.8) to yield  $\alpha$  as a function of  $T$ . The integral which contains the exponential term requires substitution of  $x = E/RT$  and  $dx = -\frac{E}{RT^2} dT = -\frac{Rx^2}{E} dT$  to form Equation 4.9.

$$\int_0^\alpha \frac{d\alpha}{f(\alpha)} = g(\alpha) = \frac{A}{\beta} \int_0^T e^{-E/RT} dT \quad (4.8)$$

$$g(\alpha) = \frac{A}{\beta} \int_{x=\infty}^{x=E/RT} -\frac{Ee^{-x}}{Rx^2} dx = \frac{AE}{R\beta} P(x) \quad (4.9)$$

where:

$$P(x) = \int_x^\infty \frac{e^{-x}}{x^2} dx \quad (4.10)$$

Equation 4.10 can be further solved using integration by parts and be rewritten as:

$$P(x) = \left[ -\frac{e^{-x}}{x} \right]_x^\infty - \int_x^\infty \frac{e^{-x}}{x} dx = \frac{e^{-x}}{x} - \int_x^\infty \frac{e^{-x}}{x} dx \quad (4.11)$$

The exponential integral of  $P(x)$ ,  $Ei(-x)$ , is not an elementary function. Thus, the following simplification was used to compute the values of  $P(x)$  (Doyle, 1961; Šesták & Berggren, 1971).

$$P(x) = \frac{e^{-x}}{x} \left( \frac{674.567 + 57.421x - 6.055x^2 - x^3}{1699.066 + 841.655x + 49.313x^2 - 8.02x^3 - x^4} \right) \quad (4.12)$$

Computation of  $P(x)$  value via this postulated simplification is valid only for  $x$  values between 9 and 174 which are generally applicable to TPR conditions. By substituting Equation 4.12 into Equation 4.9, one can get:

$$g(\alpha) = \frac{AEe^{-x}}{R\beta} \left( \frac{674.567 + 57.421x - 6.055x^2 - x^3}{1699.066x + 841.655x^2 + 49.313x^3 - 8.02x^4 - x^5} \right) \quad (4.13)$$

The  $g(\alpha)$  function can be derived from  $f(\alpha)$  as given in Table 4.1. By substituting the appropriate  $g(\alpha)$  function into Equation 4.13 based on the correct reduction mechanism and with the use of  $x = E/RT$  substitution,  $\alpha$  can be derived as an explicit function of  $T$ . The derivative of  $\alpha$  with respect to  $T$ ,  $d\alpha/dT$ , would then be the mathematical function of TPR pattern.

**Table 4.1:  $f(\alpha)$  and  $g(\alpha)$  of reduction models (Heidebrecht et al., 2008; Lin & Chen, 2004; Wimmers et al., 1986)**

Reduction models	$f(\alpha)$	$g(\alpha)^a$
1. Unimolecular decay (Random nucleation)	$(1 - \alpha)$	$-\ln(1 - \alpha)$
2. Power law ( $n = 1, 2, 3, 4$ )	$n\alpha^{(n-1)/n}$	$\alpha^{1/n}$
3. Two-dimensional growth of nuclei (Avrami-Erofeev equation)	$2(1 - \alpha)[- \ln(1 - \alpha)]^{1/2}$	$[- \ln(1 - \alpha)]^{1/2}$
4. Three-dimensional growth of nuclei (Avrami-Erofeev equation)	$3(1 - \alpha)[- \ln(1 - \alpha)]^{2/3}$	$[- \ln(1 - \alpha)]^{1/3}$
5. Phase boundary controlled reaction (Contracting cylinder) <sup>b</sup>	$(1 - \alpha)^{1/2}$	$2[1 - (1 - \alpha)^{1/2}]$
6. Phase boundary controlled reaction (Contracting sphere) <sup>b,c</sup>	$(1 - \alpha)^{2/3}$	$3[1 - (1 - \alpha)^{1/3}]$
7. One-dimensional diffusion	$\frac{1}{2\alpha}$	$\alpha^2$
8. Two-dimensional diffusion	$\frac{1}{\ln(1 - \alpha)}$	$\alpha + (1 - \alpha)\ln(1 - \alpha)$
9. Three-dimensional diffusion (Jander equation) <sup>c,d</sup>	$\frac{3(1 - \alpha)^{2/3}}{2[1 - (1 - \alpha)^{1/3}]}$	$[1 - (1 - \alpha)^{1/3}]^2$
10. Three-dimensional diffusion (Ginstling-Brounshteinn equation)	$\frac{3}{2[(1 - \alpha)^{-1/3} - 1]}$	$1 - \frac{2}{3}\alpha - (1 - \alpha)^{2/3}$

<sup>a</sup>  $g(\alpha) = \int_0^\alpha \frac{d\alpha}{f(\alpha)}$

<sup>b</sup> Chemical reaction as rate determining step.

<sup>c</sup> Geometrically defined as contracting sphere or shrinking core model with topochemically occurring reaction.

<sup>d</sup> Diffusion of gas through product layer as rate determining step.

### 4.2.3 Determination of reduction activation energy

Reduction activation energy is determined via generalized Kissinger approach which correlates the change in reduction peak temperature with the change in heating rate

(Kissinger, 1957). Based on TPR pattern, maximum reduction rate occurs at peak maxima,  $T_{max}$  and the following equation holds:

$$\left| \frac{d}{dT} \left( \frac{d\alpha}{dT} \right) \right|_{T=T_{max}} = 0 \quad (4.14)$$

By combining Equation 4.7 with Equation 4.14, one can get Equation 4.15, 4.16 and 4.17:

$$\left| \frac{d}{dT} \left( \frac{A}{\beta} e^{-E/RT} f(\alpha) \right) \right|_{T=T_{max}} = 0 \quad (4.15)$$

$$\frac{A}{\beta} e^{-E/RT_{max}} \left| \frac{df(\alpha)}{dT} \right|_{T=T_{max}} + \frac{E}{RT_{max}^2} \left( \frac{A}{\beta} e^{-E/RT_{max}} f(\alpha) \right) = 0 \quad (4.16)$$

$$\left( \frac{d\alpha}{dT} \right)_{T=T_{max}} \left[ \frac{A}{\beta} e^{-E/RT_{max}} \left| \frac{df(\alpha)}{d\alpha} \right|_{T=T_{max}} + \frac{E}{RT_{max}^2} \right] = 0 \quad (4.17)$$

Since  $\left( \frac{d\alpha}{dT} \right)_{T=T_{max}}$  is non-zero, Equation 4.17 can be rewritten as:

$$\frac{\beta E}{ART_{max}^2} = -e^{-\frac{E}{RT_{max}}} \left| \frac{df(\alpha)}{d\alpha} \right|_{T=T_{max}} \quad (4.18)$$

By rearranging Equation 4.18 in natural logarithmic form, one can get:

$$\ln \left( \frac{\beta}{T_{max}^2} \right) + \ln \left( \frac{E}{AR} \right) = -\frac{E}{RT_{max}} + \ln \left( -\frac{df(\alpha)}{d\alpha} \right)_{T=T_{max}} \quad (4.19)$$

$$\ln \left( \frac{\beta}{T_{max}^2} \right) = -\frac{E}{R} \left( \frac{1}{T_{max}} \right) + \ln \left( \frac{AR}{E} \right) + \ln \left( -\frac{df(\alpha)}{d\alpha} \right)_{T=T_{max}} \quad (4.20)$$

where  $|df(\alpha)/d\alpha|_{T=T_{max}}$  was assumed as a non-zero constant since reduction mechanism is independent of the heating rate. From Equation 4.20, linear plot of  $\ln(\beta/T_{max}^2)$  versus  $1/T_{max}$  is an Arrhenius plot with its gradient equivalent to  $-E/R$ . Thus, it should be noted that reduction activation energy can be determined without any

prior knowledge of the reduction mechanism. Determination of  $A$  value is done by comparing a set of TPR patterns for each reduction mechanisms based on different suggested  $A$  values. TPR pattern of each reduction mechanism which has its calculated  $T_{max}$  value at the measured  $T_{max}$  value of experimental TPR pattern would then give the correct  $A$  value.

#### 4.2.4 Determination of reduction mechanism

Determination of reduction mechanism based on TPR patterns of catalysts could be done by using the approach as mentioned by Wimmers et al. (1986) Figure 4.1 shows the overall algorithm used to determine the reduction mechanism of Ag/TiO<sub>2</sub> catalyst. Firstly, reduction activation energy,  $E$  can be determined using the gradient of Equation 4.20,  $-E/R$ . By fixing the values of  $E$  and  $\beta$ , the respective  $A$  value of each reduction mechanism can be determined based on the set of TPR patterns which have their calculated  $T_{max}$  values being equivalent to the measured  $T_{max}$  values. By using Equation 4.13, a set of simulated TPR patterns are generated based on the corresponding  $A$  values for reduction mechanisms and the fixed values of  $E$ ,  $T_{max}$  and  $\beta$ . Simulated TPR patterns are then compared with the measured TPR pattern of catalyst in which the best-fitting simulated pattern would be the reduction model for the catalyst.



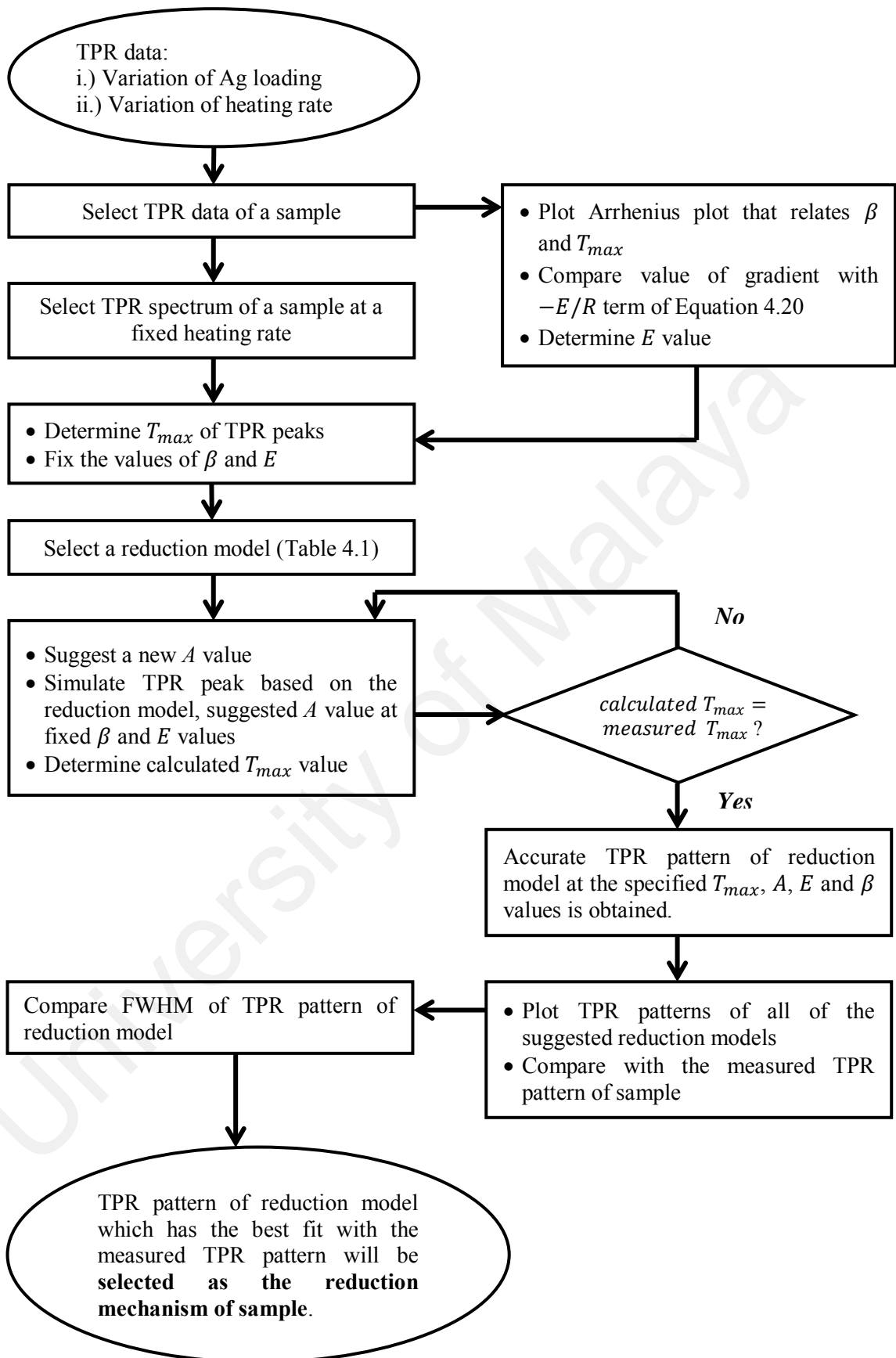


Figure 4.1: Algorithm for determination of Ag/TiO<sub>2</sub> reduction mechanism

### 4.3 Experimental

#### 4.3.1 Materials

Ag/TiO<sub>2</sub> catalysts of various silver loadings (1 wt%, 3 wt%, 5 wt% and 10 wt%) were prepared using dry impregnation method and labelled as Ag/TiO<sub>2</sub>-1, Ag/TiO<sub>2</sub>-3, Ag/TiO<sub>2</sub>-5 and Ag/TiO<sub>2</sub>-10. An aqueous solution of silver nitrate was added into the commercially available titanium dioxide (Sigma-Aldrich) under stirring. Samples were oven dried at 120 °C for 24 h and calcined in air at 400 °C for 24 h. ICP-OES, BET and TEM analyses were conducted to determine actual Ag loading, mean pore diameter and mean particle size of Ag/TiO<sub>2</sub> catalyst respectively (Table 4.2).

**Table 4.2: Physicochemical properties of Ag/TiO<sub>2</sub> catalyst**

Catalyst	Ag loading (wt%)	Mean pore diameter (nm)	Mean particle size (nm)
Ag/TiO <sub>2</sub> -1	0.779	10.77	97.45
Ag/TiO <sub>2</sub> -3	2.427	10.13	106.28
Ag/TiO <sub>2</sub> -5	3.981	10.07	110.03
Ag/TiO <sub>2</sub> -10	9.132	9.53	113.13

#### 4.3.2 Reduction experiments

TPR was performed using Micromeritics Chemisorb 2720 instrument and 5 vol% H<sub>2</sub>/N<sub>2</sub> gas as reducing gas. H<sub>2</sub> consumption was measured by thermal conductivity detector (TCD). A 50 mg of catalyst sample was loaded in quartz U-tube reactor for each TPR test. Samples were heated from 298 K to 573 K at heating rate of 20 K/min and held at 573 K for 30 min under 20 mL/min helium flow for sample outgassing. Outgassed samples were subsequently cooled down to 298 K. When TCD signal becomes stable, sample reduction was then conducted from 298 K to 773 K at heating rate of 20 K/min under 5 vol% H<sub>2</sub>/N<sub>2</sub> flow (20 mL/min). For Ag/TiO<sub>2</sub>-10 sample,

sample reduction was done at several heating rates (20, 30, 40 and 50 K/min) for determination of reduction activation energy and mechanism.

## 4.4 Results and discussion

### 4.4.1 Effect of metal loading and particle size

Figure 4.2a shows TPR patterns of TiO<sub>2</sub> and Ag/TiO<sub>2</sub> samples of different Ag loadings at 20 K/min heating rate. TPR patterns of Ag/TiO<sub>2</sub> samples exhibited two major peaks in which the first peak was within 385.5 K – 389.3 K temperature region while the second peak was within 464.3 K – 487.0 K temperature region (Table 4.3). Both peaks were attributed to Ag<sub>2</sub>O reduction in catalysts since both peaks were not observed in TiO<sub>2</sub> pattern. The first peak would be reduction of Ag<sub>2</sub>O particles to Ag as commonly reported to occur within temperature range of 353 K – 423 K (Dai et al., 2004; Zhang et al., 2015). As for the additional Ag<sub>2</sub>O reduction at higher temperature, there are two plausible reasons to this phenomenon: 1.) Variation in particle size of Ag<sub>2</sub>O species; 2.) Reduction variation between surface and bulk lattice oxygen species. The first explanation accounts for the possibility of having a portion of Ag<sub>2</sub>O aggregates existing in smaller particle sizes and better dispersion which in turn experienced a stronger metal-support interaction with TiO<sub>2</sub> support (Carnevillier et al., 2004; Cónsul et al., 2004; Hernández-Cristóbal et al., 2014). However, the result in this study (Figure 2b) showed that the slight increase in catalyst particle size had negligible effects on reduction phenomenon. Particle size distribution from TEM analysis also showed a good uniformity in particle size of each individual catalyst particle. The minute particle size deviation would certainly not be accountable for the additional reduction phenomenon which had a temperature difference of about 100 K. Contrariwise, additional reduction peak would be due to the difference in oxygen species, i.e. surface

and bulk lattice oxygen. Oxygen species difference was also due to different deposition of Ag aggregates on support. Results from BET and TEM analyses corroboratively showed significant Ag deposition in pores at lower loading (1, 3 wt%) and on support surface at higher loading (5, 10 wt%) which subsequently account for the respective existence of bulk and surface lattice oxygen species. Bulk lattice oxygen species within catalyst structure tend to be of lower mobility and of stronger metal-support interaction which account for their higher reduction temperature (Chen et al., 2017). For Ag/TiO<sub>2</sub>-10 sample, the minor peak splitting of second peak may be attributed to a slight heterogeneity of Ag<sub>2</sub>O aggregates.

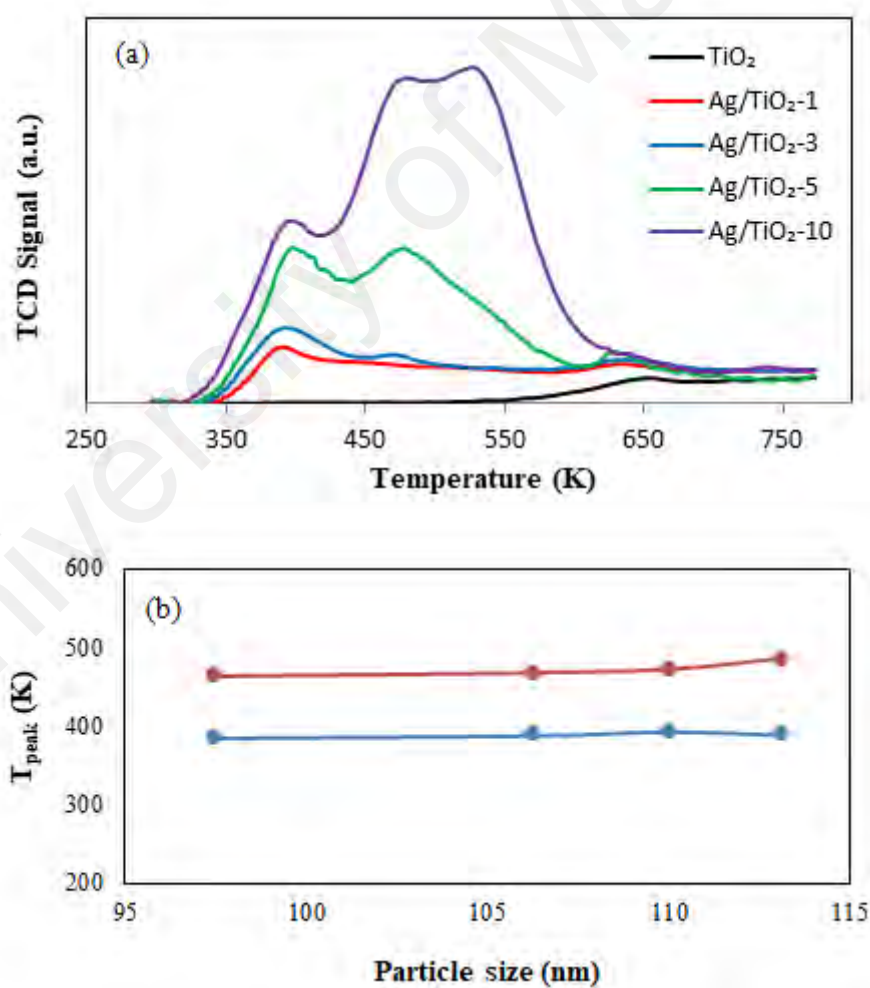


**Figure 4.2: (a) TPR profiles of TiO<sub>2</sub> and Ag/TiO<sub>2</sub> samples at 20 K/min heating rate. (b) Effect of particle size on reduction temperature**

**Table 4.3: TPR results of Ag/TiO<sub>2</sub> catalysts at 20/K min heating rate**

Catalysts	Ag loading <sup>a</sup> (wt%)	Peak temperature (K)		H <sub>2</sub> consumption amount (μmol/g)			H <sub>2</sub> /Ag <sup>c</sup> (mol/mol)	AOS of Ag <sup>d</sup>
		Peak 1 <sup>b</sup>	Peak 2 <sup>b</sup>	Peak 1	Peak 2	Total		
Ag/TiO <sub>2</sub> -1	0.779	385.5	464.3	19.11	16.99	36.10	0.50	0
Ag/TiO <sub>2</sub> -3	2.427	388.6	468.8	54.37	37.14	91.51	0.41	+0.18
Ag/TiO <sub>2</sub> -5	3.981	393.6	473.3	71.76	82.75	154.51	0.42	+0.16
Ag/TiO <sub>2</sub> -10	9.132	389.3	487.0	125.33	267.98	393.31	0.46	+0.08

<sup>a</sup> Actual Ag loading as determined by ICP analysis

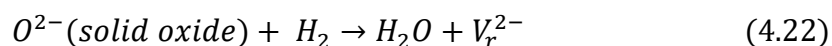
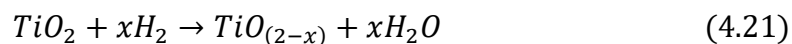
<sup>b</sup> Ag<sub>2</sub>O reduction peaks

<sup>c</sup> Molar ratio of H<sub>2</sub> consumed for reduction to Ag present in sample

<sup>d</sup> Average oxidation state of Ag after reduction

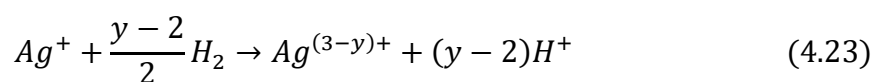
Hydrogen uptake at about 621 K – 657 K in TPR profile could be attributed to either reduction of residual Ag<sub>2</sub>O species or partial reduction of TiO<sub>2</sub> support. Partial TiO<sub>2</sub> reduction would likely be the cause since observation of reduction peak at this temperature range was also present in bare titania support. Likewise, past studies have shown TiO<sub>2</sub> to be one of the reducible transition metal oxides in which reduction of some Ti<sup>4+</sup> ions into Ti<sup>3+</sup> ions resulted in partially reduced TiO<sub>(2-x)</sub> during H<sub>2</sub> treatment (Tauster, 1987). The partially reduced TiO<sub>x</sub> was known to migrate to the surface of superjacent metal to form metal-Ti<sup>3+</sup> interactions. Presence of such interaction indicated that there is a slight electronic perturbation in the Ag metal particles by TiO<sub>2</sub> supports. This metal-support interaction would likely change the catalytic properties of Ag metal to a certain extent such as spreading of Ag metal particles over TiO<sub>(2-x)</sub> and higher hydrogen spillover flux within the locality of TiO<sub>(2-x)</sub> (Tauster et al., 1978). Hence, the classical view of metal particles remaining electronically unperturbed on a metal oxide support would not be the entirely accurate concept for Ag/TiO<sub>2</sub> catalyst. The partial reduction of TiO<sub>2</sub> was also reported in the Ag/TiO<sub>2</sub> catalysts synthesized by Zhang et al. (2015) for formaldehyde oxidation. For bare titania support, they observed the onset of this phenomenon at 822 K which is higher than in this study (657 K). The difference in onset temperature may likely be due to variations in TiO<sub>2</sub> samples; catalyst preparation and TPR settings. Nevertheless, both studies observed the effect of Ag metal in

facilitating partial TiO<sub>2</sub> reduction as evidenced by the decrease in TiO<sub>2</sub> reduction peak temperature upon Ag addition. Another issue to be considered would also be formation of oxygen vacant sites upon reduction of TiO<sub>2</sub> as according to the following reactions (Khader et al., 1993; Zhang et al., 2015):



where  $V_r^{2-}$  is oxygen vacant site. These generated oxygen vacancies were also reported by Khader et al. (1993) to favor further H<sub>2</sub> adsorption which would be beneficial for activation and adsorption of hydrogen during hydrodeoxygenation.

Based on Table 4.3, reduction peak temperature for the first peak was marginally affected by the increase in Ag loading while reduction peak temperature of the second peak was more significantly affected. Thus, the typical reduction of Ag<sub>2</sub>O aggregates by H<sub>2</sub> as accounted by the first peak was not really influenced by Ag loading. As for reduction of Ag<sub>2</sub>O with metal-support interaction (peak 2), the increase in Ag loading resulted in a greater extent of metal-support interaction which would increase the reduction temperature instead. When silver loading increased, H<sub>2</sub> consumption also increased in a fashion that it would be commensurate with the increase in silver loading as shown by the almost similar H<sub>2</sub>/Ag molar ratios. The extent of Ag reduction could be determined based on average oxidation states of Ag after reduction. By knowing the experimental molar ratios of H<sub>2</sub> consumption to actual silver loading of catalysts, average oxidation state of Ag after reduction can be determined based on the following reaction:



where  $(y - 2)/2$  is experimental molar consumption amount of  $H_2$  to reduce one mole of  $Ag^+$  ion and  $(3 - y)$  is average oxidation number of Ag after reduction. All samples were reported to have almost similar average oxidation states of Ag after reduction (0 to +0.18) despite the increase in Ag loading in catalyst. Thus, reducibility of  $Ag_2O$  aggregates is independent of the silver loading.

#### 4.4.2 Effect of heating rate

Figure 4.3 shows TPR profiles of  $Ag/TiO_2-10$  samples at different heating rates. Similar type and number of reduction peaks were observed at different heating rates. The changes in the peak height and width at higher heating rates would be attributed to instrumental peak broadening effect. This effect can be explained by the existence of thermal gradient in sample during its heating. During TPD test, a constant heat flux was supplied to the sample from furnace whereby heat was transferred to the U-tube wall and then to the sample via thermal conduction. Since thermal conduction requires a finite amount of time, this would create an internal temperature gradient within the sample which would cause a thermal lag in sample reduction. The thermal lag is observed when the higher temperature zones in sample undergo reduction first whereas the lower temperature zones undergo reduction later. The temperature gradient within sample becomes larger when higher heating rate or sample that is of larger mass and lower thermal conductivity was used. An increase in thermal lag due to larger internal temperature gradient within the sample would thus yield a TPR profile that is of larger peak width and higher peak temperature.

The presence of instrumental peak broadening effect on TPR profiles at higher heating rates may affect the resolution of peak reduction in such a way that there might be instances of peak overlapping if both peak temperatures are close to one another.

Hence, the use of lower heating rate would introduce smaller thermal gradient in sample heating which would give a set of more resolved and distinct peaks in such instances. However, the use of lower heating rates also has several drawbacks such as lower signal to noise ratios and decreased sensitivity (Günther et al., 2009). Hence, selection of appropriate heating rate is required to ensure TPR profiles have good resolution and sensitivity for analysis while thermal gradient is minimal. In this study, a higher range of heating rates (20 – 50 K/min) was used to enhance TPR measurement sensitivity. Selection of this range was also justified as small sample mass was used (50 mg) and peaks resolution were not compromised to the extent that they were indistinguishable. In addition, since Arrhenius plots in Figure 4.4 are straight lines, the independence of reduction mechanism from heating rate variation and the reliability of Kissinger approach in the determination of reduction activation energy can be established over the large range of heating rates in this study.

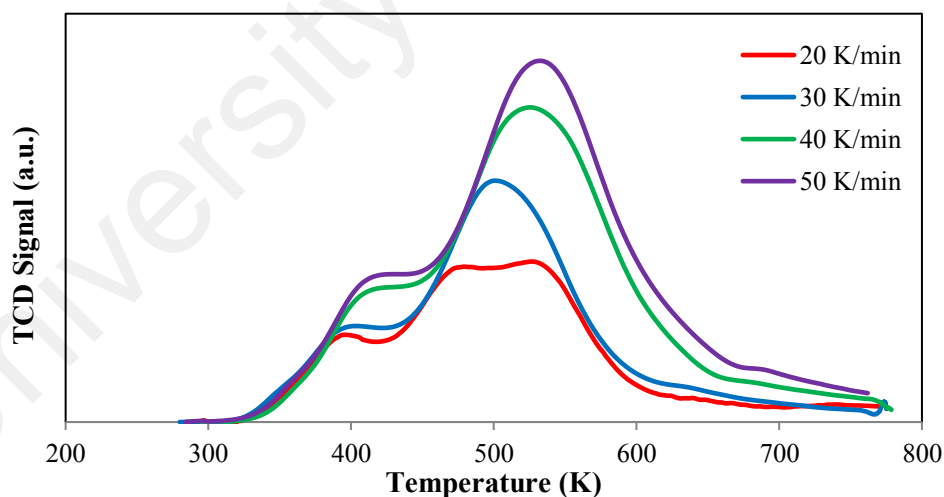


**Figure 4.3: TPR profiles of Ag/TiO<sub>2</sub>-10 catalyst with different heating rates**

Based on Arrhenius plots in Figure 4.4, activation energy,  $E$ , were determined for both reduction peaks based on the generalized Kissinger approach (Equation 4.20). The  $T_{max}$  values obtained from Figure 4.3 would correspond to the  $T_{max}$  values at which



reduction rates of Ag<sub>2</sub>O to Ag metal are maxima at different heating rates. The  $E$  values were reported to be 73.35 kJ/mol and 81.71 kJ/mol for surficial and pore-deposited Ag<sub>2</sub>O aggregates respectively. The higher reduction activation energy of the latter was due to the stronger metal-support interaction as experienced by its associated bulk lattice oxygen species. The activation energy for Ag<sub>2</sub>O reduction reported here should be treated as its apparent activation energy. This is because the apparent activation energy obtained via TPR analysis is also affected by the nature of raw material, sample preparation method, nature of reducing gas and temperature range besides being mainly affected by its bonding configuration. Likewise, the trend of varying apparent activation energies was also reported in other metal oxides such as iron oxide in which these studies were done using various TPR conditions (Pineau et al., 2006).

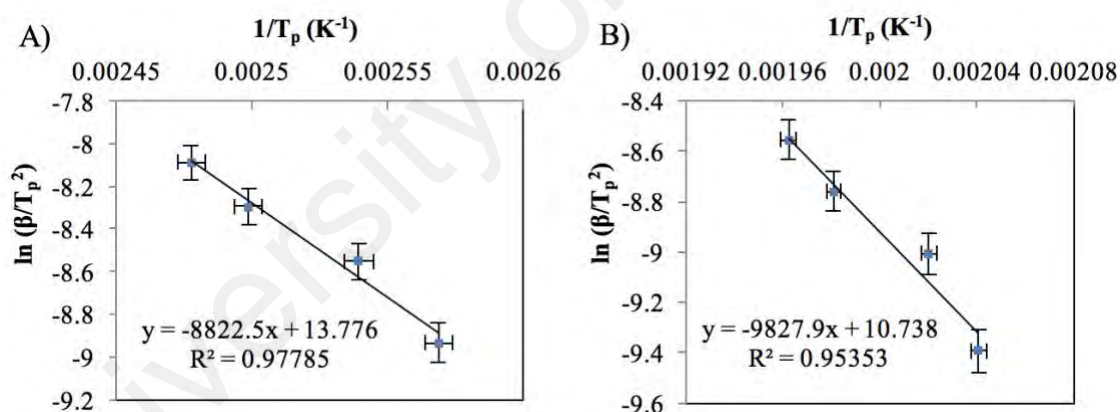


**Figure 4.4: Temperature-programmed “Arrhenius plots” for Ag<sub>2</sub>O reduction (Ag/TiO<sub>2</sub>-10): (A) first peak; (B) second peak**

#### 4.4.3 Reduction mechanism of Ag/TiO<sub>2</sub> catalyst

This present study shows that Ag metal is formed at 350 – 550 K from Ag<sub>2</sub>O reduction using 5% H<sub>2</sub> in N<sub>2</sub> gas. Other TPR studies on metal oxide such as cobalt oxide, chromium oxide, iron oxide and vanadium oxide were also reported in the literature (Kanervo et al., 2003; Kanervo & Krause, 2002; Lin & Chen, 2004; Lin et al.,

2003). However, we sought to determine the reduction mechanism of Ag<sub>2</sub>O to Ag metal for several reasons: i.) reduction mechanism and kinetics of Ag<sub>2</sub>O to Ag in supported Ag based catalyst is still a relatively new study, ii.) Ag/TiO<sub>2</sub> catalyst was proposed to be one of the catalysts for hydrodeoxygenation under H<sub>2</sub> condition in our study and thus the reduction mechanism of catalyst by H<sub>2</sub> serves as a pre-requisite for the understanding of its catalytic interaction in hydrodeoxygenation.

For the investigation of the reduction mechanism of Ag<sub>2</sub>O to Ag metal, TPR spectra of Ag/TiO<sub>2</sub>-10 catalyst at 30 K/min was used. This is because this data has the relatively largest sample size of Ag which gives the best approximation of an ideal packed bed and the most random selection of sample. Likewise, TPR pattern of lower heating rate was selected due to the lesser instrumental peak broadening effect but 30 K/min heating rate was preferred instead as the 20 K/min TPR pattern consists of minor heterogeneity in the second peak. Based on the  $T_{max}$ ,  $E$  and  $\beta$  values, the respective  $A$  values of the reduction models were determined as according to the procedures described in Section 4.2.4. Table 4.4 lists the reduction models with their respective full width at half maximum heights (FWHM) and  $A$  values that are unique solutions with physical significance for TPR interpretations. By knowing these  $A$  values, the calculated TPR patterns of reduction models were determined for each reduction peak. Juxtaposition of these TPR patterns in Figure 4.5 validated that significant discrimination could be made between these models. Preliminary analysis indicated that three-dimensional diffusion reduction model via Jander equation (curve 4.5f) is not representative of the TPR pattern of sample since the peak height of the former was too low as compared with the latter.

**Table 4.4:  $A$  and FWHM values of the two reduction peaks calculated by using  $E = 73.35$  kJ/mol,  $T_{max} = 393.8$  K for first peak;  $E = 81.71$  kJ/mol,  $T_{max} = 495$  K for second peak at  $\beta = 30$  K/min**

Reduction model	Peak 1		Peak 2	
	$A$ ( $s^{-1}$ )	FWHM <sup>a</sup> (K)	$A$ ( $s^{-1}$ )	FWHM <sup>a</sup> (K)
Unimolecular decay (Random nucleation)	$1.53 \times 10^8$	39.80	$8.33 \times 10^6$	59.11
Two-dimensional growth of nuclei (Avrami-Erofeev equation)	$1.58 \times 10^8$	17.92	$8.75 \times 10^6$	32.38
Three-dimensional growth of nuclei (Avrami-Erofeev equation)	$1.63 \times 10^8$	13.55	$8.58 \times 10^6$	16.25
Phase boundary controlled reaction (Contracting cylinder)	$1.67 \times 10^8$	30.56	$8.83 \times 10^6$	42.88
Phase boundary controlled reaction (Contracting sphere)	$1.58 \times 10^8$	35.17	$8.67 \times 10^6$	48.36
Three-dimensional diffusion (Jander equation)	$1.63 \times 10^7$	72.43	$8.00 \times 10^5$	95.28

<sup>a</sup> Full width at half maximum

By comparing the full width at half maximum heights (FWHM) of these TPR patterns with the measured TPR pattern of Ag/TiO<sub>2</sub>-10 sample, reduction mechanisms of Ag<sub>2</sub>O to Ag metal at both 393.8 K and 495 K were both best described by unimolecular decay model which is a first order kinetics with random nucleation. Figure 4.6 shows the comparison of the measured and calculated TPR patterns. Unimolecular decay model was shown to have a good fit with the deconvoluted experimental reduction peaks in terms of the peak profiling. However, FWHM deviations between measured and calculated TPR patterns were not marginal which can be attributed to peak broadening effect at 30 K/min heating rate. Similar observation was also reported in iron oxide TPR by Lin et al. (Lin et al., 2003) when heating rate was increased. Nevertheless, similarity in peak curvatures between the measured and calculated pattern in the presence of peak broadening effect at high heating rate could still give a firm validation on the explanation of Ag<sub>2</sub>O reduction to Ag metal via unimolecular decay model. The data would certainly give a higher accuracy of model validation at lower

heating rate but the selection of higher heating rate in this study was done to ensure the verified reduction model would fit even at higher range of heating rate.

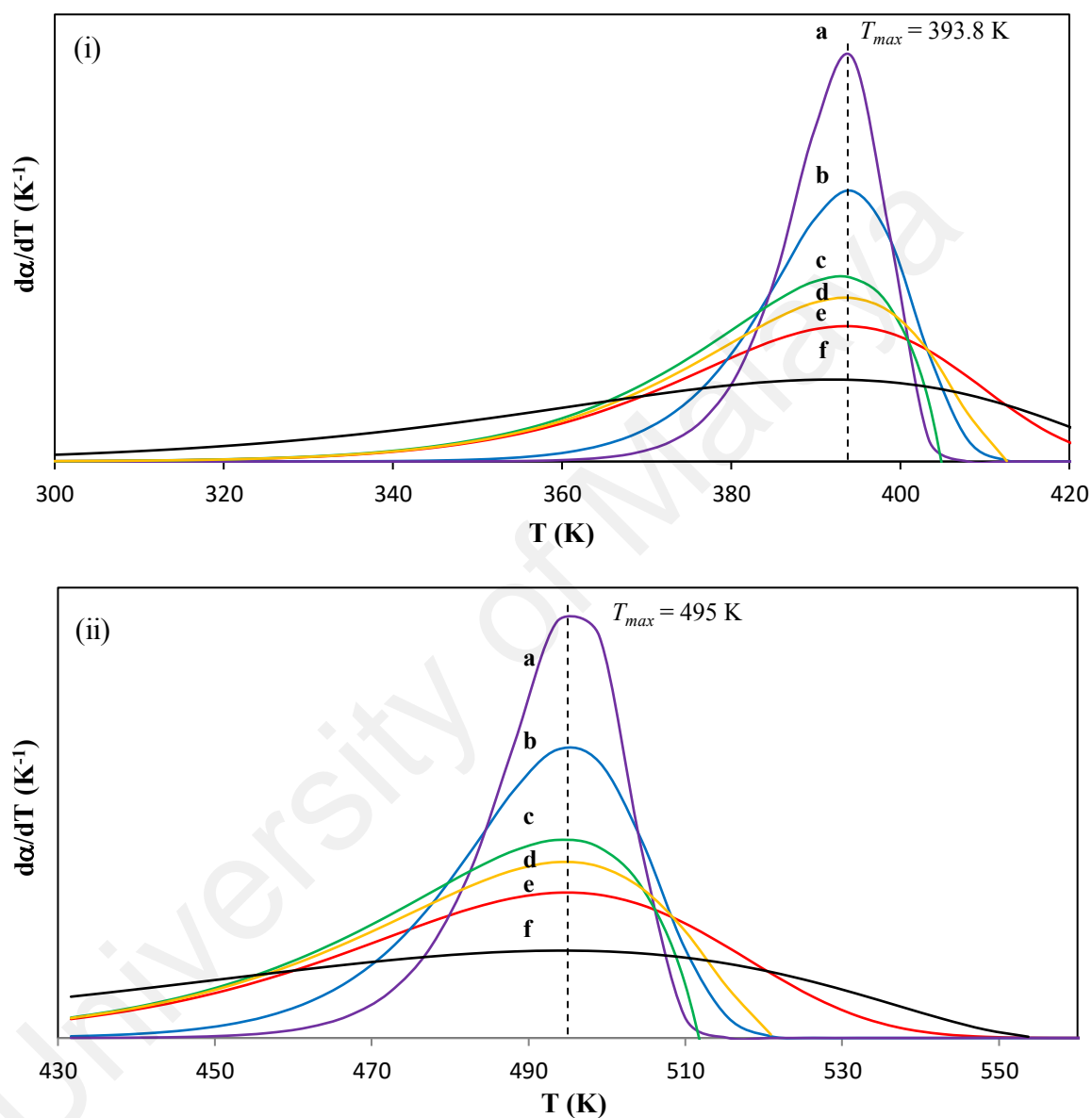


**Figure 4.5: Calculated TPR patterns for peak 1 (i) and 2 (ii) based on reduction models: (a) three-dimensional nucleation based on Avrami-Erofeev equation; (b) two-dimensional nucleation based on Avrami-Erofeev equation; (c) phase boundary controlled contracting cylinder; (d) phase boundary controlled contracting sphere; (e) unimolecular decay; (f) three-dimensional diffusion based on Jander equation**

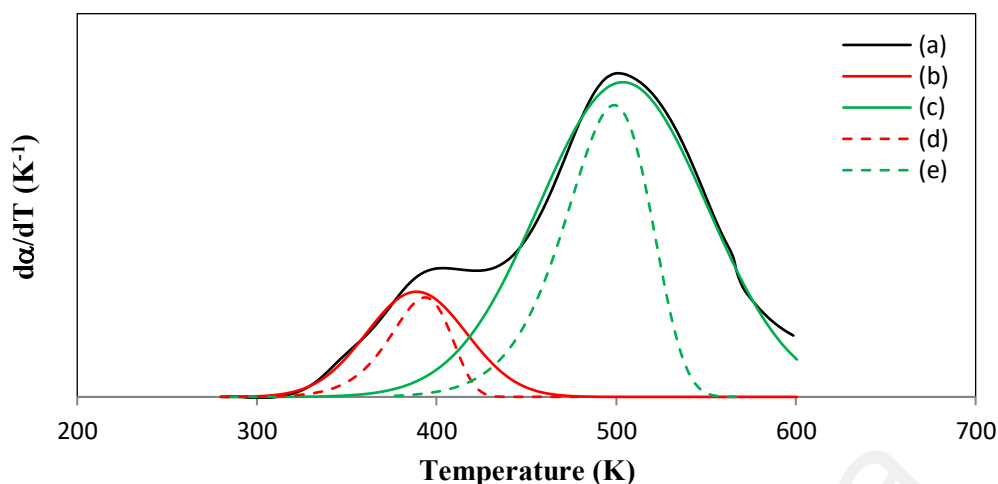


**Figure 4.6: Comparison of TPR patterns: (a) experimental result using Ag/TiO<sub>2</sub>-10 at 30 K/min, (b) first measured reduction peak obtained via peak deconvolution, (c) second measured reduction peak obtained via peak deconvolution, (d) simulation result of first peak using unimolecular decay model, (e) simulation result of second peak using unimolecular decay model**

For a typical reducible metal oxide, its reduction requires the adsorption of hydrogen on the surface of metal oxide as the first elementary step. Subsequently, removal of oxygen ions will be initiated by inward hydrogen diffusion to the metal-metal oxide interface or outward oxygen diffusion from the metal oxide to the metal-gas interface. The continuous removal of oxygen ions from the metal oxide lattice during reduction process would increase the concentration of oxygen vacancies (Gervasini, 2013). These oxygen vacancies would then be eliminated via lattice rearrangement to form new metal nuclei. Kinetic modeling of Ag<sub>2</sub>O reduction to Ag metal via unimolecular decay mechanism indicates that its rate determining step is a random nucleation process which has a uniform internal reduction characteristic. In addition, it can also be concluded that Ag<sub>2</sub>O reduction was not rate-limited by hydrogen adsorption and diffusion; oxygen diffusion and topochemical reaction at phase boundaries. The reduction kinetic parameters for both reduction peaks were also shown in Table 4.5. Bulk oxygen species are of stronger interaction with support than surface oxygen species, causing the

reduction of the former to be more difficult. As such, this phenomenon is validated by the observations of higher maximum reduction temperature and activation energy; lower rate constant and reduction rate (Table 4.5).

**Table 4.5: Reduction kinetic parameters of Ag/TiO<sub>2</sub>-10 at 20 K/min at maximum reduction rate**

Peak	Oxygen species	$T_{max}$ (K)	$A$ (s <sup>-1</sup> )	$E$ (kJ/mol)	$k$ (s <sup>-1</sup> )	$r$ (s <sup>-1</sup> )
1 ( <i>Surface deposits</i> )	Surface	389.3	$1.58 \times 10^8$	73.35	0.0220	0.0109
2 ( <i>Pore deposits</i> )	Bulk	490.0	$8.33 \times 10^6$	81.71	0.0162	0.0078

For nucleation model, an S-shaped isothermal reduction curve (degree of reduction against time) would be observed with a maximum reduction rate occurring at the middle range of the process. The initial rapid increase in reduction rate was attributed to formation and growth of new metal nuclei. Beyond the point where maximum reduction rate was observed, the steady decline in reduction rate would be caused by the decrease in reaction interface as coalescence of metal nuclei and consumption of metal oxide grains become more prominent at later phase of reduction. This phenomenon is akin to the contracting sphere or shrinking core model. However, the unique distinction between these models lies in the evolution of reaction interface in which the former model involves a steady increase in reaction interface to reach an optimized interface for maximum reduction rate and followed by a steady decrease in reaction interface whereas the latter model begins with an initial rapid nucleation that decreases over time as the reaction interface is constantly contracting throughout the reduction process. Even though both of these models had a bit of similarity in their mathematical interpretations, one must also consider that nucleation model is rate controlled by autocatalytic nucleation step whereas contracting sphere model is rate controlled by

topochemical reaction occurring at reaction interface which accounts for the variations in their physical interpretations on reduction mechanism. The autocatalytic nucleation step is attributed to the formation of Ag nuclei during the initial reduction phase on the boundaries of Ag<sub>2</sub>O particles which are autocatalytic for further Ag<sub>2</sub>O reduction (Shahcheraghi & Khayati, 2014a; Shahcheraghi & Khayati, 2014b).

Besides unimolecular decay mechanism, there are other nucleation models which can describe uniform internal reduction via different mathematical expressions. Examples of such models would be crackling core (Park & Levenspiel, 1975; Zhang & Ostrovski, 2001) and Avrami-Erofeev models. For crackling core model, it assumes that a non-porous particle becomes porous through crack formations which then enable uniform internal reduction. However, BET analysis of Ag/TiO<sub>2</sub> catalyst in this study showed that it is a mesoporous catalyst with type IV adsorption–desorption isotherm which would be inconsistent with the use of crackling core model. For Avrami-Erofeev model, it assumes random and homogeneous nucleation which would cease upon the overlapping of metal nuclei. Jelić et al. (2011) suggested Avrami-Erofeev model to describe Ag<sub>2</sub>O reduction by H<sub>2</sub> which has similar first order reaction model with unimolecular decay model. Even though Avrami-Erofeev model was noted to accurately model several reductions of metal oxides, its mathematical derivation via the concept of extended volume has been called into question in regard to its validity since the concept itself is more inclined towards a mathematically permitted construct instead of a physical basis (Van Sichen, 1996). Ag<sub>2</sub>O reduction studies were also done by other researchers with different Ag<sub>2</sub>O-based samples and methods (Table 4.6). In the preceding discussion of Section 4.4.1, negligible effect of particle size on reduction phenomenon was observed within the range of 97.45–113.13 nm. However, upon further increase of particle size to several orders of nm, the effects of particle size on Ag<sub>2</sub>O reduction model and reduction activation energy become significant. Reduction activation energy of Ag/TiO<sub>2</sub>

sample was slightly higher due to the use of TiO<sub>2</sub> support which introduced metal-support interaction. In this study, unimolecular decay model was selected among these models to describe Ag<sub>2</sub>O reduction as it has the closest fit to the sample TPR patterns besides having a simpler mathematical form for the calculation of the simulated TPR patterns.

**Table 4.6: Comparison of Ag<sub>2</sub>O reduction models**

Sample	Particle size (nm)	Method	Reduction model	E (kJ/mol)	Ref.
Ag/TiO <sub>2</sub>	97.45-113.13	TPR	Unimolecular decay	73.35	This work
Ag <sub>2</sub> MoO <sub>4</sub>	690	TGA	Shrinking core	64.0	(Juarez & Morales, 2008)
Ag <sub>2</sub> O	700-5000	TGA	Avrami-Erofeev	59.7	(Jelić et al., 2011)

Likewise, for uniform internal reduction to occur, the condition of random and homogeneous nucleation over the untransformed region of material must be valid. Thus, other mechanisms such as nucleation on regular lattice and clustered nucleation were not included in this study as these were non-random nucleation. With the change in particle size and reduction temperature, reduction model was noted to be unchanged. This observation would also indicate that nucleation as rate determining step for Ag<sub>2</sub>O reduction as compared with effects due to gaseous diffusion and topochemical reactions. Lastly, it is also worth noting that metal-support interaction may affect Ag<sub>2</sub>O reduction mechanism in certain ways. For instance, reduction of Ag<sub>2</sub>O particles dispersed on TiO<sub>2</sub> support can be viewed as heterogeneous nucleation with formation of new Ag nuclei over support surface. With the introduction of metal-support interaction, metal oxide supports were commonly known to cause spreading of active phase over its surface in which the spreading effect is somewhat correlated with the strength of the metal-support



interaction (Tauster, 1987). Likewise, the spreading effect would certainly alter the contact angle of the nuclei with surface, causing a change in the nucleation barrier,  $\Delta G^*$ . Since different metal oxides exhibit different metal-support interaction strengths, the idea of using different metal oxide supports to alter reduction process of  $\text{Ag}_2\text{O}$  may be postulated. However, further studies on this matter have to be done in near future for its verification.

#### 4.4.4 Mass transfer limitations

Effects of mass transfer limitations were also investigated to ensure the proposed reduction kinetics of  $\text{Ag}/\text{TiO}_2$  was not diffusion-limited. For external mass transfer, 5 vol%  $\text{H}_2/\text{N}_2$  flow was increased from 20 mL/min to 80 mL/min to determine its effect on hydrogen consumption rate while keeping other parameters constant. Similar hydrogen consumption rate was observed when hydrogen flow velocity was increased, indicating that reduction was not limited by external mass transfer. For internal mass transfer, the values of Thiele modulus, internal effectiveness factor and Weisz-Prater criterion were computed based on first order of reduction for  $\text{Ag}/\text{TiO}_2$  (Appendix A)

$$\phi_1 = R_{cat} \sqrt{\frac{k_R}{D_e}} \quad (4.24)$$

$$\eta = \frac{3}{\phi_1^2} (\phi_1 \coth \phi_1 - 1) \quad (4.25)$$

$$C_{W-P} = \eta \phi_1^2 \quad (4.26)$$

$$D_e = \frac{(D_K)_{\text{H}_2} \phi_p \sigma_c}{\tilde{\tau}} \quad (4.27)$$

$$(D_K)_{\text{H}_2} = \frac{d}{3} \sqrt{\frac{8RT}{\pi M_A}} \quad (4.28)$$

where  $\phi_1$  is Thiele modulus,  $\eta$  is internal effectiveness factor,  $C_{W-P}$  is Weisz-Prater criterion,  $R_{cat}$  is particle radius (56.57 nm for Ag/TiO<sub>2</sub>-10 sample),  $k_R$  is reduction rate constant,  $D_e$  is effective diffusivity,  $(D_K)_{H_2}$  is Knudsen diffusivity of H<sub>2</sub>,  $\phi_p$  is porosity (0.4),  $\sigma_c$  is constriction factor (0.8),  $\tilde{\tau}$  is tortuosity (3),  $d$  is pore diameter (9.53 nm),  $R$  is ideal gas constant,  $T$  is reduction temperature,  $M_A$  is molecular mass of H<sub>2</sub>. Based on these data, the values for  $\phi_1$ ,  $\eta$  and  $C_{W-P}$  are  $1.01 \times 10^{-5}$ , 1.00 and  $1.02 \times 10^{-10}$  for the first peak and  $8.2 \times 10^{-6}$ , 1.00 and  $6.72 \times 10^{-11}$  for the second peak at their respective reduction peak temperatures (389.3 K and 490 K). When  $\eta$  approaches unity and  $C_{W-P}$  is less than 0.3, internal diffusion rate is much higher than reaction rate (Fogler, 2006). Since these conditions were fulfilled, Ag/TiO<sub>2</sub> reduction had negligible internal mass transfer limitations, indicating that concentration gradient within catalyst particle is negligible.

#### 4.5 Conclusion

Reduction kinetics of titania-supported silver catalyst was analyzed using temperature-programmed reduction. A single-step reduction of Ag<sub>2</sub>O to Ag was observed in all samples at two reduction peaks. Reduction peak at higher temperature was due to reduction of pore-deposited Ag<sub>2</sub>O in which bulk lattice oxygen species experienced greater extent of metal-support interactions. All samples were shown to achieve high reducibility with AOS ranging from 0 to +0.18. The increase in Ag loading was noted to have no causal effects on catalyst reducibility and reduction mechanism. However, the increase in Ag loading has resulted in a marginal increase of reduction temperature and a proportional increase in reduction site amount. Apparent activation energies for Ag<sub>2</sub>O reduction to Ag metal were 73.35 kJ/mol and 81.71 kJ/mol for surficial and pore-deposited Ag<sub>2</sub>O aggregates respectively. Based on this study,

reduction mechanism of Ag/TiO<sub>2</sub> catalyst was best described using unimolecular decay model which has the characteristics of uniform internal reduction and random nucleation. Hence, this would also infer that the catalyst reduction is rate-limited by the nucleation of Ag metal instead of topochemical reaction and diffusion of hydrogen and oxygen molecules. By analyzing the reduction behavior of Ag/TiO<sub>2</sub> catalyst, interaction of hydrogen with active sites and formation of oxygen vacant sites can thus be elucidated. These insights would definitely further improve the understanding on hydrodeoxygenation process catalyzed by supported metal catalysts such as Ag/TiO<sub>2</sub>. Nevertheless, the possibility of reduction behavioral alteration by different metal oxide supports in supported Ag catalysts still remain a question to be addressed in future studies for further insights on reduction kinetics of supported Ag catalysts.

## **CHAPTER 5: DELAYED VOLATILES RELEASE PHENOMENON AT HIGHER TEMPERATURE IN TGA VIA SAMPLE ENCAPSULATION TECHNIQUE**

### **5.1 Introduction**

Thermogravimetry (TG) or thermogravimetric analysis (TGA) is a method used to measure mass change of a sample as a function of time or temperature while subjecting the sample in a controlled atmosphere and temperature program. By observing the precise mass change of sample, various reactions occurring within the sample such as decomposition, crystallization, combustion, reduction, oxidation, vaporization, desorption and adsorption can be investigated rigorously (Hatakeyama & Liu, 2000). Solid-gas reaction is one of the important fields covered in TGA in which pure samples or sample mixtures were often analyzed for their thermochemical reactivity or stability. As such, the current state of the art generally involves the use of thermal volatilization analysis (TVA) which requires TGA to measure physical changes such as weight, temperature, etc. and evolved gas analysis (EGA) or evolved gas detection (EGD) to measure chemical changes in the reaction system (Rosa et al., 2015). EGA and EGD instrumentations may consist of mass spectroscopy (MS), gas chromatography (GC) or infrared spectroscopy (IR), depending on the chemical properties—molecular weight, structural conformation, composition, etc.— of the evolved volatiles to be analyzed (Wendlandt, 1986). The use of volatile samples for solid-gas reaction remains a challenge in this field as the volatilization effect of these samples at lower temperatures may lead to issues such as substantial loss of sample prior to analysis and inaccurate account of the thermal stability and reactivity of sample.

The flow of gaseous sample through catalyst bed at a targeted temperature in catalytic gas-solid reaction is important as reaction temperature is an important

parameter in affecting reaction kinetics (Butt, 2000; Fogler, 2006; Houston, 2006). Significant pre-volatilization of volatile samples may thus pose difficulties in attaining kinetics data across various isotherms (Vlaev et al., 2015). Several existing techniques were well established in other previous works to mitigate this problem such as pulsed thermal analysis (Eigenmann et al., 2000; Gupta et al.; Maciejewski et al., 1999; Maciejewski et al., 1997) and the use of reactive gas streams in TG system (Hatakeyama & Liu, 2000; Speyer, 1994). PTA technique involves the injection of a specified quantity of gaseous reactant through the carrier gas stream which passes over the solid sample in TG crucible for gas-solid reactions (Brown, 2001; Wendlandt & Gallagher, 1981). This technique has the advantage that reaction occurs at a well-controlled temperature and reactant amount by ensuring the solid sample reaches to the desired temperature prior to the injection of known amount of gaseous reactant (Eigenmann et al., 2000; Maciejewski et al., 1997). However, this technique does not offer the feature of continuous flow of gaseous reactant through solid sample during non-isothermal reaction. The continuous feed of gaseous reactant can be accomplished through the simultaneous flow of reactive and inert gas streams into TG environment. However, the extent of reactant flux through the reaction zone was noted to be affected by crucible dimensions, hydrodynamics and direction of reactant flow in TG environment (Hatakeyama & Quinn, 1999; Speyer, 1994). This effect is undesirable, causing the reaction kinetics analysis to have mass transfer limitations.

In view of these challenges, sample encapsulation technique was proposed as an innovative method in this work. This method involves the physical confinement of sample within a metal capsule or pan covered with lid which is then being crimped at the edges to form hermetically sealed capsule. As temperature increases during TGA, the increasing sample volatilization rate will result in a greater accumulation of vapor pressure within the sealed capsule. As such, the progressive loosening of hermetic seals

over a range of elevated pressure will provide a continuous and delayed release of volatile samples over a range of higher temperature. With this technique, the continuous feed of gaseous reactant directly through the reaction zone of catalyst bed could be achieved at the defined temperatures and without the influence of crucible geometry and hydrodynamics of purge gas flow. The extension of this method in TGA by encapsulation of volatile samples such as fuel model compounds may lead to further opportunities in the area of thermochemical kinetics for fuel processing such as gasification, carbonization, reforming or petrochemical reactions that involve catalyst activation at high temperature and use of volatile samples.

In differential scanning calorimetry (DSC), metal capsule containing sample and empty capsule as reference were used to analyze physical or chemical phenomena of sample occurring within the capsule such as phase transitions, oxidation, reduction, decomposition, etc. (Berlin & Kliman, 1974; Brenman, 1974; Duswalt, 1974) Based on the determination of heat flux between sample and reference, quantitative parameters of these endothermic or exothermic processes can be determined (Parlouër, 2013; Wunderlich, 2005). However, in this TGA study, the chemical and physical phenomena of sample occurring within the sealed pan were not the main aspects of study. Rather, the metal capsules in this TGA study served as sealed containers to physically isolate the volatile sample from the purge gas environment and the other solid reactants present in TGA crucible. As such, pure liquid samples were used in this analysis to ensure boiling is the only physical phenomenon that would occur. Likewise, chemical and physical phenomena of sample are only analyzed when the evolved gas from capsule comes in contact with other solid reactants within TGA crucible. The focus of this work is on the effectiveness of metal capsules in retaining the vaporized sample and releasing it at higher temperature. The application of this proposed delayed volatile release via

sample encapsulation in enhancing catalytic gas-solid reactions was also examined in this work using catalytic phenol reduction.

## 5.2 Theory

### 5.2.1 Thermodynamics of vaporization

Vaporization is the phase transition of a substance from liquid to vapor phase which can be achieved through evaporation and boiling. Generally, both processes are endothermic because heat is absorbed by molecules in both instances to transit from liquid phase into gaseous phase which is of higher energy state. However, evaporation and boiling thermodynamics are very different. Evaporation is a surface phenomenon which involves vaporization of liquid from liquid surface into gaseous phase at temperatures below boiling point while boiling is a bulk phenomenon which involves the vaporization of liquid from the entire liquid phase into gaseous phase at boiling point (Atkins & Paula, 2010).

Evaporation is a vapor-liquid exchange process which involves the accumulation of escaped molecules at the vapor above the liquid. When the vapor phase is saturated, evaporation reaches to a thermodynamic equilibrium state. The pressure exerted by this saturated vapor phase is known as saturation vapor pressure which can be determined using Clausius-Clapeyron relation (Equation 5.1) or Antoine equation (Equation 5.2) (Felder & Rousseau, 2004):

$$\frac{d \ln p}{dT} = \frac{\Delta_{vap}H^o}{RT^2} \quad (5.1)$$

$$\log p = A - \frac{B}{C + T} \quad (5.2)$$

where  $p$  is saturation vapor pressure (mmHg for Equation 5.2),  $T$  is temperature of liquid (K for Equation 5.1 and °C for Equation 5.2),  $\Delta_{vap}H^\circ$  is standard latent heat of vaporization of liquid,  $R$  is ideal gas constant and  $A$ ,  $B$  and  $C$  are component-specific constants. Based on these equations, saturation vapor pressure increases with the increase in liquid temperature as more molecules acquire sufficient kinetic energy to escape from liquid surface into gaseous phase. Further increase in temperature will cause the saturation vapor pressure of liquid to further increase until it becomes equal with the ambient pressure. At this temperature, boiling of liquid would occur in which heat is absorbed to overcome the intermolecular attraction force of molecules within liquid phase to form bulk gaseous phase.

### **5.2.2 Release of vaporized volatiles at higher temperatures**

When volatile liquids are being left unperturbed in an open system, a significant amount of liquid can be vaporized easily at room temperature in the absence of heating due to their high volatilities and evaporation rates. Thus, when volatiles are being heated steadily to achieve their boiling states, a portion of volatile liquid may have been pre-vaporized thus creating an undesirable issue of volatile sample escape at early stage during thermogravimetric analysis. Based on Clausius-Clapeyron relation, it is thermodynamically possible to increase the boiling point of liquid sample by increasing the surrounding pressure. Pressurization of system may be useful in delaying the boiling process of liquid sample and shifting the evaporation equilibrium towards the liquid phase. However, specifications of conventional TGAs usually allow only thermal processes to be done at atmospheric or low pressures. For thermal analysis involving pressurization, high pressure thermogravimetric analysis equipment (HP-TGA) is required instead and is usually of higher cost and rarity (Kok et al., 1996; Yun & Lee,



1999). Likewise, the increase in boiling point of liquid sample via pressurization of system is not effective based on two reasons: 1.) Large pressure increase is needed to produce small increase in boiling point, 2.) Larger pressure increase is required for the same interval of boiling point increase at higher temperatures. For instance, the saturation pressures of water at 100, 120 and 140 °C are 101.42, 198.67 and 361.53 kPa respectively (Cengel & Boles, 2011). Thus, system pressurization for vaporization of volatiles at higher temperature in TGA analysis may not be effective due to its higher cost, rarity and risk.

In this study, encapsulation of liquid sample by hermetically sealed metal pan was proposed as an innovative method for the release of vaporized volatiles at higher temperatures and without pressurization of surroundings during TG analysis (Figure 5.1). The encapsulation involves the placement of liquid sample in a cylindrical pan which is then covered by a lid. The rims of both pan and lid are crimped together to form a sealed closure using a capsule sealing tool. This setup would physically confine the liquid sample to a closed system which prevents or minimizes the escape of evaporated sample. When the encapsulated sample is being heated, pressure build-up occurs due to the thermal expansion of trapped air layer and the increasing vapor pressure of liquid sample at higher temperature. In addition, the increase in internal pressure of capsule also causes the liquid sample to boil at higher temperature, thus remaining as liquid for a longer period of time. The internal pressure will progressively increase causing the crimped rim of capsule to rupture. The ruptured rim would then function as the outlet for the release of vaporized sample in a continuous flow into the surrounding at ambient pressure condition.

The delayed volatiles release phenomenon at higher temperature in TGA via sample encapsulation technique as proposed in this study may lead to new opportunities of

analyzing catalytic gas-solid reactions in TGA. For instance, consider an experimental setup of a typical catalytic gas-solid reaction in a TGA crucible which involves the passing of vaporized samples through a suspended catalyst bed at an elevated temperature (Figure 5.2). If the liquid sample is exposed to the internal environment of TGA furnace, the sample would vaporize at its atmospheric boiling point ( $T_{b,1 atm}$ ) and pass through the catalyst bed at this temperature. In heterogeneous catalytic study, catalyst activation at high temperature under a stream of air,  $H_2$ ,  $O_2$ , etc., is necessary to achieve the desired oxidation states of active sites, better dispersion of active sites, improved morphology and replenishment of surface and lattice species within the catalyst structure for better catalytic activity (Abon et al., 1995; Alayat et al., 2018; Butt & Petersen, 1988; Jana et al., 2013; McDaniel, 2010; Zardin & Perez-Lopez, 2017). With the use of volatile reactant, the vaporized sample may pass through the catalyst bed prior to its activation temperature. Thus, by physically confining the sample in capsule, it can release and allow the vaporized sample to pass through the catalyst bed at a higher temperature, i.e. catalyst activation temperature.

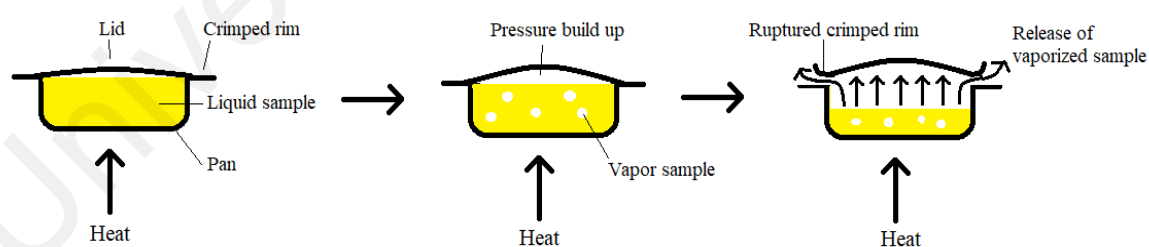


**Figure 5.1: Delayed release of vaporized sample via encapsulation**

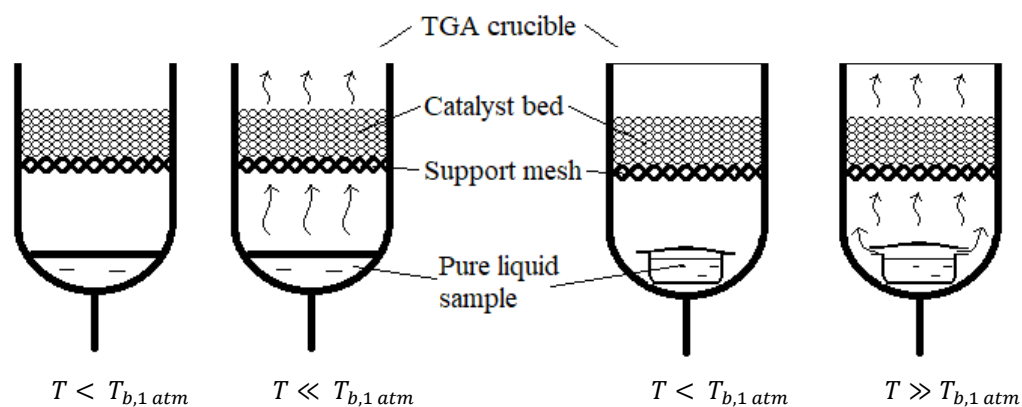


**Figure 5.2: Schematics of sample encapsulation concept for catalytic gas-solid reaction with standard sample (left) and encapsulated sample (right) in TGA where  $T$  is sample temperature and  $T_{b,1 atm}$  is atmospheric boiling point of sample**

## 5.3 Experimental

### 5.3.1 Materials

Phenol and guaiacol were purchased from Sigma-Aldrich and used as received without any purification. Purified nitrogen gas was purchased from Linde Malaysia Sdn. Bhd. Three types of Perkin-Elmer metal capsules were obtained which are tin pan, aluminium pan (Al pan) and tin cylindrical capsules. Table 5.1 shows the dimensions of capsules. The TGA crucible (Figure 5.2) as required for the setup was the 3.4 mL  $\text{Al}_2\text{O}_3$  crucible by NETZSCH. Dry impregnated  $\text{Ag}/\text{TiO}_2$  was used as the phenol reduction catalyst as part of the application study. The catalyst has silver loading of 9.13 wt%, specific surface area of  $8.69 \text{ m}^2/\text{g}$ , average pore diameter of 9.53 nm, average  $\text{TiO}_2$  particle size of 113.13 nm, acid site density of 0.2576 mmol/g and  $\text{H}_2$  uptake amount of 0.1129 mmol/g as determined by ICP-OES, BET, TEM,  $\text{NH}_3$ -TPD and  $\text{H}_2$ -TPD techniques.

**Table 5.1: Dimensions of metal capsules**

Capsule type	O.D. <sup>a</sup> (mm)	I.D. <sup>b</sup> (mm)	H <sub>o</sub> <sup>c</sup> (mm)	H <sub>i</sub> <sup>d</sup> (mm)	A/V <sup>e</sup> (mm <sup>-1</sup> )
Tin pan	4.30	4.20	2.00	1.10	0.909
Aluminium pan	5.90	5.40	2.30	1.40	0.714
Tin cylinder	2.80	2.50	7.00	5.80	0.172

<sup>a</sup> Outer diameter

<sup>b</sup> Inner diameter

<sup>c</sup> Outer height

<sup>d</sup> Inner height

<sup>e</sup> Surface area to volume of sample ratio

### 5.3.2 Sample encapsulation technique

A micropipette of 0.1  $\mu\text{L}$  precision was used to place liquid sample into metal capsule. The dispensed volume of liquid sample by micropipette corresponds exactly to the capacity volume of metal capsules to avoid liquid spillage. Corresponding lids were used to cover the top of the filled capsules. The rims of the capsule and lid were crimped firmly using pan crimper to form hermetic seal (Figure 5.3). As for the filled tin cylindrical capsules, its top end was pressed together without a lid instead to form the sealed closure. The weight of encapsulated liquid sample was determined based on the difference in weight of empty capsule with lid and weight of hermetically sealed capsule containing liquid sample (Shalaev & Steponkus, 2000). All weighing procedures were repeated for three times and the measurement errors were less than 4%. In order to examine the integrity of hermetic seals, the encapsulated sample was placed in TGA setup for 15 minutes under 20 mL/min  $\text{N}_2$  flow without any heating. The encapsulated samples are ensured to have good seal integrity to prevent liquid leakage or loss prior to volatilization test.



**Figure 5.3: Hermetically sealed pans containing liquid samples: Tin cylinder (left), Tin pan (middle) and Aluminum pan (right)**

### 5.3.3 Volatilization of encapsulated sample

Volatilization of encapsulated liquid samples was tested in a TGA-FTIR (Thermogravimetric-Fourier Transform Infrared Spectroscopy) coupling system. Each test consisted of the volatilization of a liquid sample that is encapsulated with a particular metal capsule. The encapsulated liquid sample was placed in the TGA  $\text{Al}_2\text{O}_3$  crucible of NETZSCH STA 443 Jupiter thermogravimetric analyzer. In each test, the sample was heated from 25 °C to 400 °C at a designated heating rate under 20 mL/min  $\text{N}_2$  purge flow. Each set of test was done in duplicates for the result reproducibility purposes. Effect of heating rate on volatilization was studied by performing the experiments at heating rates of 30, 40 and 50 K/min. Effect of sample boiling point was also investigated through the Al pan encapsulated phenol and guaiacol vaporizations at 50 K/min. Effect of metal capsule material and geometry was also studied by observing phenol vaporization at 50 K/min with different metal capsules such as tin cylinder, tin pan and aluminum pan (Figure 5.3). Phenol vaporization at 50 K/min was also done without sample encapsulation as blank test.

During heating, a 20 mL/min  $\text{N}_2$  flow was supplied in TGA to purge vaporized volatile samples into FTIR system via a 53-cm transfer line. Transfer line was maintained at 230 °C to prevent condensation of evolved vapor samples. In-situ evolved

gas analysis was performed by Bruker TENSOR 27 FT-IR spectrometer to identify and quantify the vaporized samples at a particular time interval. Scans were taken at resolution of  $4\text{ cm}^{-1}$  to give a theoretical data spacing of  $1.928\text{ cm}^{-1}$  ranging from  $650$  to  $4500\text{ cm}^{-1}$  wavenumbers. Spectral interferences by atmospheric  $\text{CO}_2$  and  $\text{H}_2\text{O}$  were eliminated through background scans. Volatilization of samples was also done in the absence of metal capsule as the standard calibration tests for the quantification of samples. Weights of metal capsules were also measured before and after volatilization to investigate for capsule degradation.

#### 5.3.4 Catalytic gas-solid reaction

Application of sample encapsulation for catalytic gas-solid reaction was investigated in gas-phase reduction of phenol over  $\text{Ag}/\text{TiO}_2$  catalyst. In the presence of supported metal catalyst, phenol will be reduced into benzene (He & Wang, 2012; Kay Lup et al., 2017a; Mortensen et al., 2011). The reaction was carried out in TG crucible via two different reactant setups as shown in Figure 5.4: 1.) Non-encapsulated liquid phenol which is subjected to conventional vaporization, 2.) Encapsulated liquid phenol which is subjected to delayed volatile release effect. Tin cylinder was used to encapsulate liquid phenol. Upon ramping up the temperature of reaction system, liquid phenol would vaporize and pass through  $\text{Ag}/\text{TiO}_2$  catalyst bed to be reduced into benzene. During the reduction, vapor products are continuously transferred to FTIR for evolved gas analysis. Both setups were done using the same amount of phenol (25 mg), catalyst (230 mg) and heating profile ( $25\text{ }^\circ\text{C}$  to  $400\text{ }^\circ\text{C}$  at  $50\text{ K}/\text{min}$ ) under a  $100\text{ mL}/\text{min}$  of  $5\%\text{ H}_2/\text{N}_2$  flow. A control experiment was also carried out in the absence of liquid phenol and no weight loss was observed, indicating the thermal stability of catalyst and reaction setup. Benzene yield was determined using the following equations:

$$\text{Benzene yield (mol\%)} = \frac{\text{Moles of benzene product}}{\text{Moles of initial phenol}} \times 100\% \quad (5.3)$$

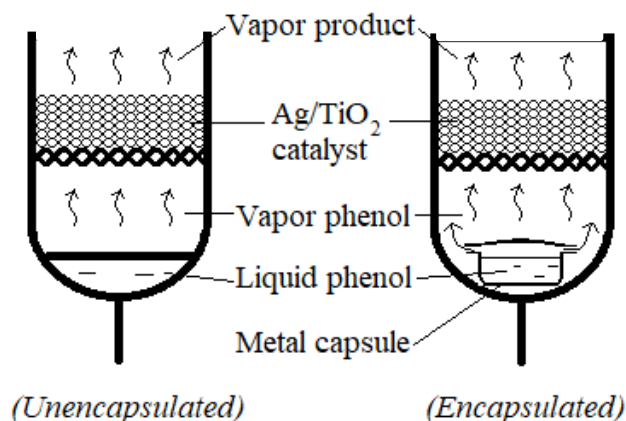


**Figure 5.4: Gas-phase reduction of phenol to benzene over Ag/TiO<sub>2</sub> catalyst without and with sample encapsulation technique**

## 5.4 Results and discussion

### 5.4.1 Post-vaporization conditions

Figure 5.5 shows the conditions of metal capsules before and after the volatilization of liquid samples in TGA. Both tin cylinder and aluminum pan retained their structures after the release of vaporized volatile samples at higher temperatures. The seal rupture was formed through the entire detachment of crimped rims between lid and capsule which contributed to the release of vaporized volatile samples. As for tin pan, its shrinkage into a sphere may be attributed to melting and re-solidification of tin during volatilization. Weight of capsule after volatilization was equivalent with the weight of stock capsule with a maximum deviation of  $\pm 2\%$ . This indicates that metal capsules were thermally inert and stable throughout the volatilization. Likewise, FTIR spectra showed only the respective functional groups of phenol and guaiacol on experiments with different phenolic samples. Hence, the total weight loss in TGA curve would be entirely attributed to the weight of vaporized volatile sample.

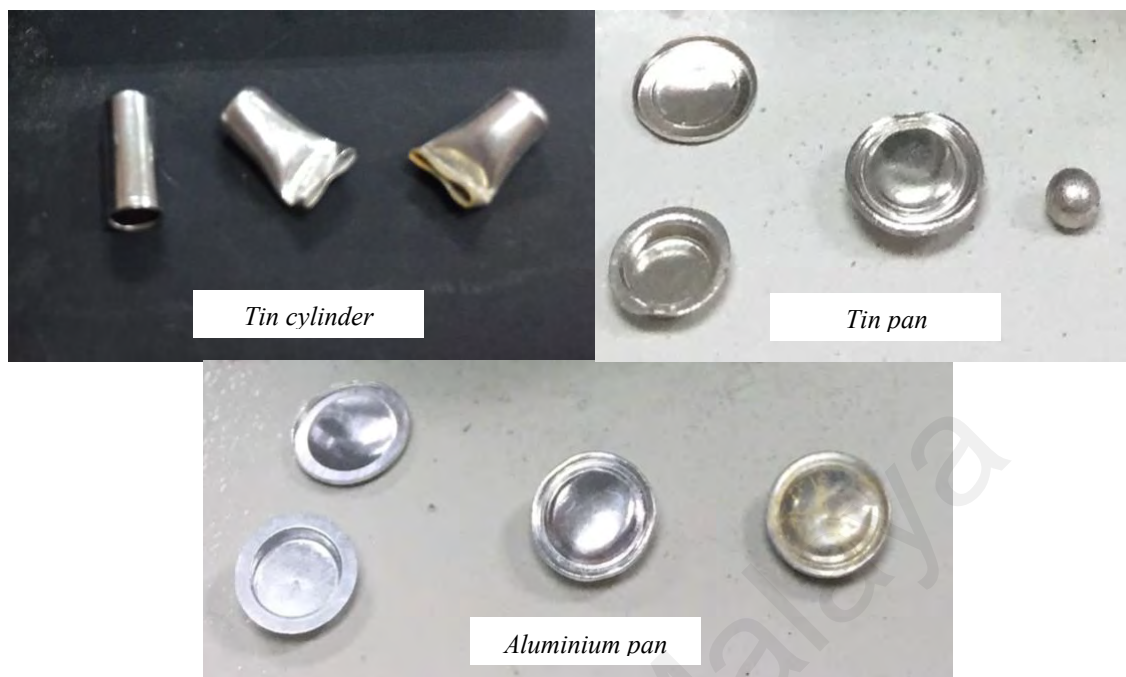


**Figure 5.5: Conditions of metal capsules: stock (left), before (middle) and after (right) experiment**

#### 5.4.2 Delayed volatile release via sample encapsulation

Figure 5.6 shows the TG and DTG curves of Al pan encapsulated guaiacol vaporization at heating rates of 30, 40 and 50 K/min. Based on DTG curve, two peaks were observed at 120 °C and 198 °C during guaiacol vaporization. The first peak accounts for evaporation of guaiacol which occurs below its boiling point (205 °C) while the second peak accounts for boiling of guaiacol. The maximum guaiacol vaporization rate (-3.79 %/s) occurred at 198 °C which corresponded to the boiling state of guaiacol. Further release of guaiacol vapor until 217 °C also indicated the retention ability of capsule in delaying the release of boiled guaiacol. Nevertheless, guaiacol vaporization at lower temperatures was observed despite the physical confinement of guaiacol in metal capsule. This is because the hermetic seal of metal capsule is formed via mechanical crimping of the rims of capsule and lid without any sealants. Thus, the



rupturing mechanism of the seal occurs through the progressive loosening of the mechanically crimped seal as it is continuously subjected to an increasing pressure or temperature. This seal would thus feature the steady delayed release of vapor over a range of higher temperatures rather than outburst of vapors via an instantaneous capsule rupturing, i.e. explosion. If it is an instantaneous capsule rupturing, there would be a sharp and total decline in the weight change readings at a specific temperature which was not observed in this case. This feature is necessary to ensure the delayed volatile release is achieved without affecting the stability of catalyst bed and TGA system. The possibility of catalyst bed shaking due to gas release was also excluded as TG readings showed a smooth and steady decline in weight change. The TGA instrument has a high gravimetric sensitivity of 0.025  $\mu\text{g}$  which is able to detect minute instability in catalyst bed and gas release. By increasing the heating rate from 30 K/min to 50 K/min, a greater portion of the vaporized sample was released at higher temperatures. For liquid sample physically confined in a hermetically sealed metal capsule, it will still undergo vaporization via evaporation before boiling point and boiling which is then being steadily released from the capsule via the progressive loosening of the hermetic seals over a range of elevated temperature. Thus, by increasing the heating rate, the initial volatile release of guaiacol via evaporation was reduced as guaiacol achieves its boiling state faster.

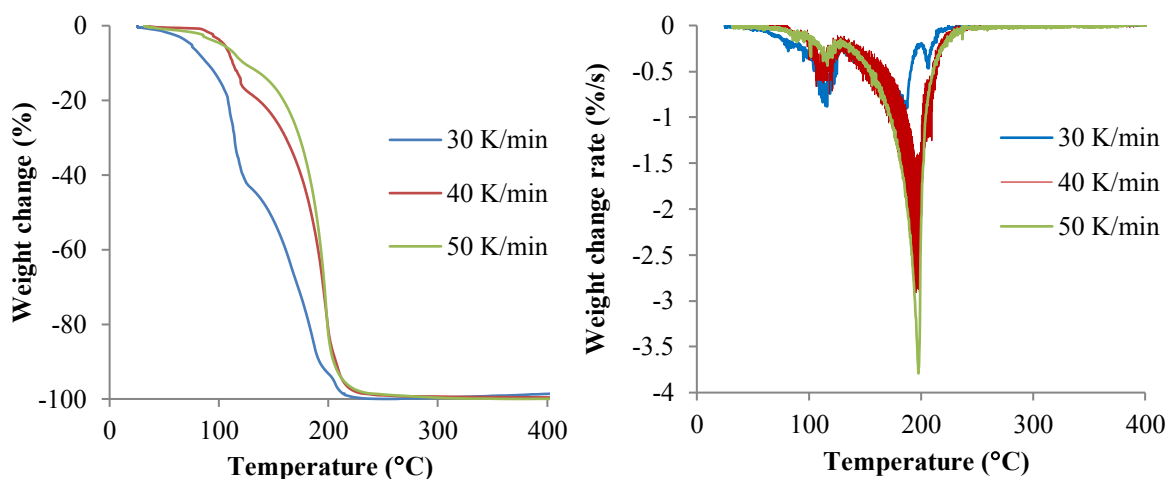


**Figure 5.6: TG (left) and DTG (right) curves of Al pan encapsulated guaiacol vaporization at different heating rates**

Figure 5.7 shows the vaporization of Al pan encapsulated phenol and guaiacol which occurred via evaporation and boiling at different temperatures and extents. Phenol exhibited two vaporization peaks at 165.7 °C and 192.4 °C with the respective maximum release rates of -2.33 %/s and -0.87 %/s whereas vaporization peaks of guaiacol were at 120 °C and 198 °C with respective maximum release rates of -0.25 %/s and -3.79 %/s. The vaporization peak of phenol was significant higher than guaiacol as phenol is more volatile than guaiacol. Besides that, vaporization of phenol also occurred at lower temperature due to its lower boiling point. The volatility and boiling point of a liquid sample are dependent on its saturation vapor pressure at a temperature. For instance, phenol has higher volatility and lower boiling point than guaiacol due to its higher saturation vapor pressure as computed from Antoine equation (Figure 5.8) (Dreisbach & Shrader, 1949; Stull, 1947). Hence, the accumulation of higher vapor pressure at lower temperature will expedite the rupturing of metal capsule as seen in the phenol vaporization case. For a non-encapsulation setup, the vapor release of phenol and guaiacol would occur until their respective boiling temperatures: 181.7 °C and 205 °C. However, with the encapsulation setup, the vapor release of phenol and guaiacol was managed to be extended up to temperatures of 209.8 °C and 217 °C respectively.

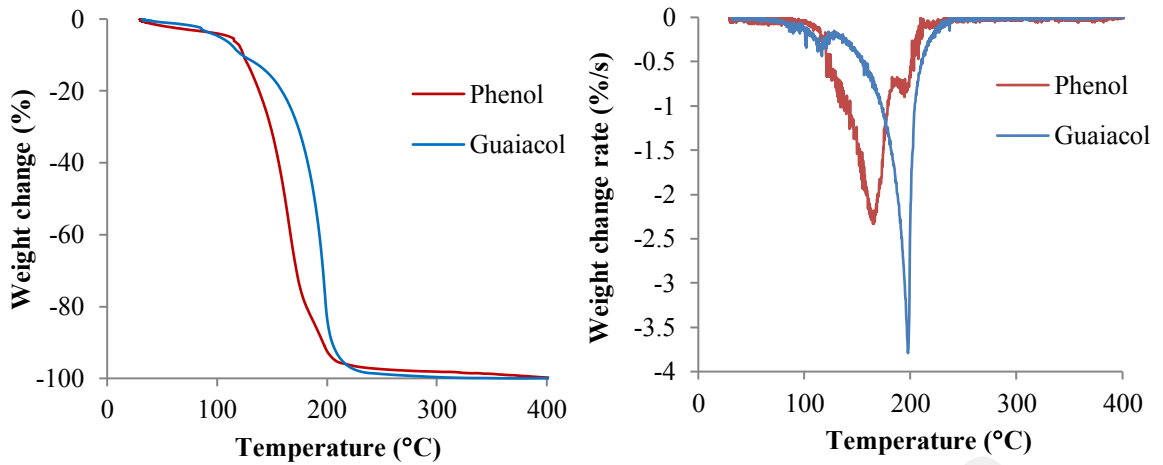


**Figure 5.7: TG (left) and DTG (right) curves of Al pan encapsulated phenol and guaiacol vaporization at 50 K/min**

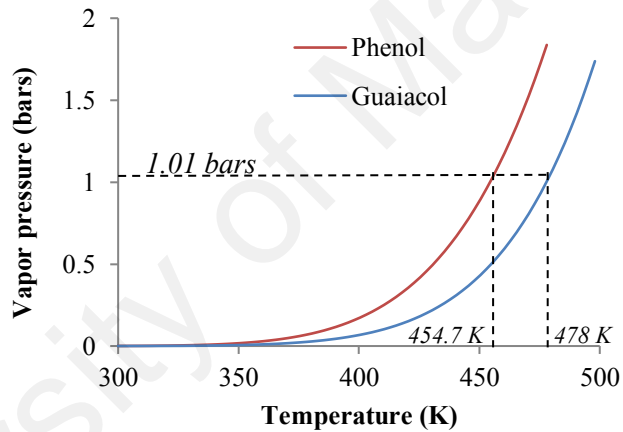


**Figure 5.8: Vapor pressure of phenol and guaiacol at different temperatures based on Antoine equation**

As for the release of guaiacol vapor, it occurred at higher temperature range due to its higher boiling point and lower volatility. However, its vapor release rate was observed to be higher than that of phenol. The release rate of vaporized sample is dependent on the pressure difference between the metal capsule interior and external surrounding. Likewise, a higher rate of pressure change would also increase the release rate of vaporized sample. By putting these into consideration, Clausius-Clapeyron relation (Equation 5.1) can be expressed in terms of the rate of temperature change of sample:

$$\frac{d \ln p}{dT} = \frac{d \ln p}{dt} \cdot \frac{dt}{dT} = \frac{1}{\beta} \frac{d \ln p}{dt} = \frac{\Delta_{vap} H^{\circ}}{RT^2} \quad (5.4)$$

$$\frac{d \ln p}{dt} = \beta \frac{\Delta_{vap} H^{\circ}}{RT^2} \quad (5.5)$$

where  $\beta = dT/dt$  is heating rate. The rate of sample temperature change was equated with heating rate with the assumption of negligible heat transfer limitation. Equation 5.5 indicates that the rate of saturation vapor pressure change (natural logarithmic form) increases when heating rate or latent heat of vaporization increases. Since guaiacol (62.6 kJ/mol) has a higher latent heat of vaporization than phenol (58.8 kJ/mol) (Chickos et al., 1995; Matos et al., 2003), the higher rate of saturation vapor pressure change of guaiacol would result in a higher release rate of guaiacol vapor as shown in DTG curve of Figure 5.7. Likewise, by increasing the heating rate used for vaporization of the same sample, it would also cause the release rate of sample vapor to be higher as indicated in DTG curve of Figure 5.6.

The vaporization trends of different metal capsules encapsulated phenol were shown in Figure 5.9. Among the three tested capsules, tin cylinder pan was noted to delay the release of vaporized phenol to the greatest extent. Based on the TG curves, all encapsulated phenol samples were shown to have a delayed onset in the loss of vaporized phenol as compared with vaporization of non-capsulated phenol in TG crucible. Tin cylinder and Al pan were observed to entirely delay the release of vaporized phenol by a temperature shift of 36 °C and 11 °C while such effect was not readily observed with the use of tin pan.

When equal mass of phenol was allowed to be vaporized in TG crucible under the same conditions and without encapsulation feature, 95 % of the initial phenol sample was observed to have been vaporized and escaped from the TG system prior to reaching

its boiling point. The high evaporation rate of phenol was due to several reasons: 1.) high vapor pressure which would result in substantial amount of evaporated phenol if heating process was slow; 2.) constant flow of purge gas in TG system would continuously sweep vaporized phenol from the system, thus resulting in the non-equilibrium state of vapor-liquid phenol system and a positive concentration gradient from liquid component to vapor component of phenol. Therefore, by encapsulating the volatile liquid samples during TG analysis, the release of vaporized samples could be delayed to a higher temperature exceeding their boiling points.

Based on the DTG curves of encapsulated phenol samples, capsule material and geometry were also noted to significantly affect its efficiency in retaining the volatile samples. By comparing tin and Al capsules that are of identical geometries, Al capsule was able to retain the vaporized phenol for another 8.9 °C temperature higher than the retention temperature limit of tin capsule. The retention efficiency of metal capsule lies in its ability to withstand the accumulated vapor pressure before rupturing. Therefore, metal hardness is an important physical property which aids in this retention ability. For instance, Al capsule was able to withstand a slightly higher vapor pressure than tin capsule prior to their rupturing as the Mohs hardness values of aluminium and tin were 2—2.9 and 1.5—1.8 respectively (Samsonov, 1968).

By comparing tin pan and cylindrical capsules, the latter managed to retain the vaporized phenol for another 49 °C temperature higher than the retention temperature limit of the former. Likewise, DTG curve of phenol encapsulated by tin cylindrical capsule also showed minimal loss of volatile sample via evaporation as most of the vaporized phenol sample was released at temperature starting from its boiling point. The minimal loss of volatile sample via evaporation in tin cylindrical capsule was due to its geometry which resulted in the lowest surface area to volume of liquid sample ratio

(Table 5.1). Thus, by minimizing the specific surface area of liquid sample, its evaporation can be reduced and the release of vaporized sample can be delayed to a higher temperature during TG analysis.

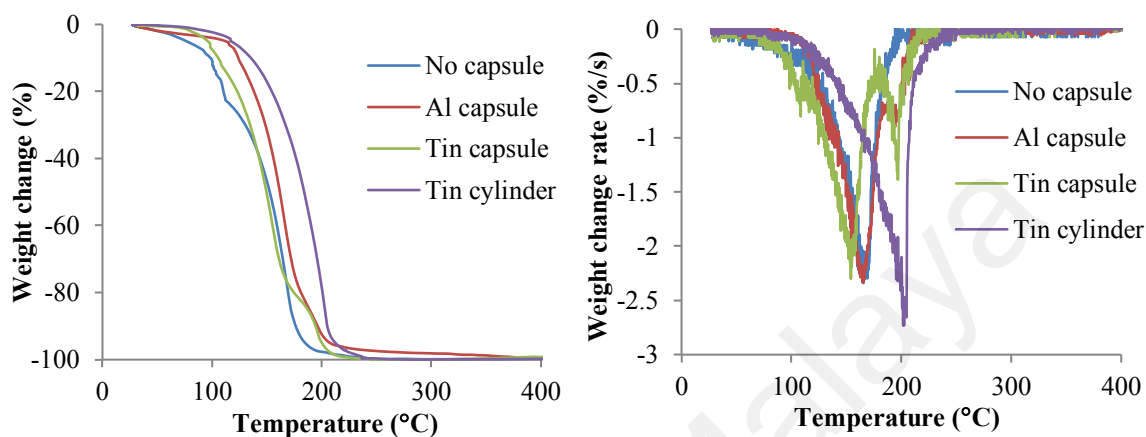


**Figure 5.9: TG (left) and DTG (right) curves of encapsulated phenol vaporization at 50 K/min**

The effectiveness of sample encapsulation is verily dependent on capsule material and geometry. In this study, hermetically sealed aluminum and tin capsules were assessed on their sample encapsulation effectiveness. However, hermetically sealed pans are also made of other high purity materials such as Au, Ag, Cu, Pt, stainless steels, etc. By making use of the varying material hardness, the sample release temperature can be varied and applied differently based on the analysis preference. These features of sample encapsulation can thus be applied to improve the existing analyses of solid-gas reactions via TGA. By altering the capsule configurations, different temperatures of sample release could also be obtained, which would enable solid-gas reactions to be carried out at different isotherms for a more comprehensive kinetic data acquisition. Hermetically sealed pans are generally able to withstand pressure of 2 atm before rupturing (Menczel et al., 2009). However, it was shown in this study that the rupturing onset of hermetic seal began at about 1.38 atm and progressed

up to its rupture design pressure due to the progressive loosening of the hermetic seal over a range of elevated pressure. Contrariwise, high pressure metal capsules are stainless steel based and involve screw sealants as part of their sealing mechanism, thus being able to withstand higher pressure of up to 200 atm before rupturing (Menczel et al., 2009). Thus, the use of high pressure metal capsules may be potentially applied in TG analysis that requires a more significant delay in release of volatile samples. However, further studies on this matter have to be done in near future for its verification.

#### **5.4.3 Catalytic gas-solid reaction**

The application of sample encapsulation in catalytic phenol reduction was done by encapsulating liquid phenol in tin cylinder. With the sample encapsulation technique, the temperature range for the release of vaporized phenol has increased by 49 °C as indicated in the phenol release rate graph in Figure 5.10. Product evolution trend in Figure 5.10 has also indicated higher benzene and lower unreacted phenol compositions in the vapor products of phenol reduction when sample encapsulation was applied. The delayed volatile phenomenon as induced by sample encapsulation has improved the efficiency of phenol reduction over Ag/TiO<sub>2</sub> catalyst. This is because the delayed release of phenol vapor enabled better activation of Ag/TiO<sub>2</sub> catalyst at higher temperature. In catalytic reactions, catalyst activation at sufficiently high temperatures is important to ensure the optimal catalytic activity of catalysts through the attainment of suitable oxidation states, active site dispersion, morphology and catalyst phase during catalyst activation (Abon et al., 1995; Alayat et al., 2018; Butt & Petersen, 1988; Jana et al., 2013; McDaniel, 2010; Zardin & Perez-Lopez, 2017). At temperatures below 100 °C, negligible benzene yield was observed in the non-capsulated setup even though

phenol vapor was passing through Ag/TiO<sub>2</sub> catalyst bed. Rather, the onset temperature of Ag/TiO<sub>2</sub> activation was at 100 °C and it was optimally activated at 150 °C onwards as shown in the significant increase in reduction activity from 150 °C to 200 °C. Besides that, the delayed release of vaporized phenol at higher temperatures also enabled the reduction of phenol at higher reaction temperatures. At higher reaction temperatures, phenol had higher kinetic energy to overcome the activation energy of reduction, causing a higher reduction rate of phenol into benzene (Fogler, 2006; Kay Lup et al., 2017b). Thus, without the use of sample encapsulation, unhindered volatilization effect of phenol at lower temperatures would adversely affect phenol reduction rate as more phenol vapor passed through Ag/TiO<sub>2</sub> catalyst bed at lower temperatures. By considering the reduction of phenol across the heating profile, the benzene yield was increased from 19.2 mol% to 46.5 mol% when sample encapsulation was employed. Beyond the maxima of vaporization peaks, all product evolution rates decreased significantly due to the depletion of phenol reactants.

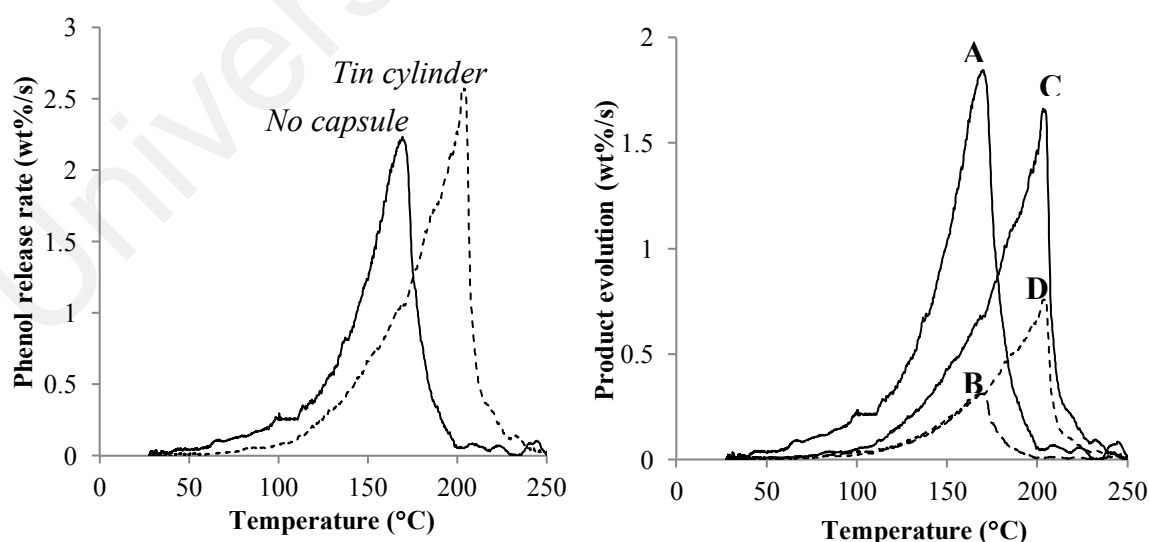


**Figure 5.10: Phenol release rates (left) and product evolution during phenol reduction (right): (A) unreacted phenol and (B) benzene without sample encapsulation; (C) unreacted phenol and (D) benzene with sample encapsulation**



## 5.5 Conclusion

The technique of sample encapsulation in TG analysis, as described in this work, enabled a controlled delay in the release of vaporized volatile samples at higher temperatures which can be used in studies such as catalytic gas-solid reactions and reactions that are temperature sensitive and require catalyst activation at high temperature. The delayed volatile release effect was achieved through the progressive loosening of the hermetic seal of metal capsule over the range of elevated temperature. Sample release temperature could also be altered by varying the material and geometry of pan or capsule. The result of this work indicated that the sample release temperature could be increased by using pan or capsule which is of higher material hardness to withstand higher internal pressure or geometry that has lower surface area to volume of sample to minimize evaporation. The described sample encapsulation method widens the application range of TGA technique to cater for reactions involving chemicals of high volatility. By encapsulating the volatile sample, pre-loss of volatile sample due to evaporation and purge flow environment can then be minimized which enable sufficient sample being available for analysis at the desired higher temperatures. Application of this method in catalytic phenol reduction has shown an increase in benzene yield from 19.2 mol% to 46.5 mol% when phenol is encapsulated by tin cylinder. Thus, these findings have formed the basis for more detailed studies on the sample encapsulation effectiveness of other hermetically sealed pans of various materials and geometries and high pressure metal capsules which would be the focus of future works.

# CHAPTER 6: ATMOSPHERIC HYDRODEOXYGENATION OF PHENOL AS PYROLYTIC OIL MODEL COMPOUND FOR HYDROCARBON PRODUCTION USING Ag/TiO<sub>2</sub> CATALYST

## 6.1 Introduction

Oxygen removal is a fundamental bio-oil or pyrolytic oil upgrading step to produce liquid fuel of higher heating value and lower oxygen content. The upgrading of bio-oil via oxygen removal process is often accomplished via hydrodeoxygenation (HDO) (Mortensen et al., 2011). It was further necessitated owing to the complex mixture of more than 400 O-containing compounds found within bio-oils which were produced during pyrolysis of lignocellulosic biomass (Bu et al., 2012). The compositions of oxygenated compounds in bio-oils are highly dependent on the biomass source (Mullen & Boateng, 2008; Shafaghat et al., 2016; Zhang et al., 2007) and the pyrolysis conditions (Abnisa & Wan Daud, 2014; Qureshi et al., 2018). These oxygenated compounds are commonly classified as phenolics, furans, acids, alcohols, carbonyls and ethers in which phenolics deoxygenation remained the toughest due to their high C—O bond dissociation energies (Furimsky, 2000; Huber et al., 2006).

There are various phenolic model compounds being studied for phenolic HDO such as guaiacol, cresol, anisole, vanillin, etc. Phenol is another important model compound being studied as it exhibits single functionality (Zhang et al., 2013b). Several supported Co, Fe, Mo, Ni, Pd, Pt, Rh and Ru based catalysts have been studied for phenol hydrodeoxygenation in liquid or gas phase (Badawi et al., 2013; Boullosa-Eiras et al., 2014; de Souza et al., 2015; Echeandia et al., 2014; Mortensen et al., 2015; Ohta et al., 2014; Platanitis et al., 2014; Shafaghat et al., 2016; Yang et al., 2009; Zhao et al., 2012b). Researchers have classified phenol HDO into three major reaction pathways: 1.) direct deoxygenation route (DDO), 2.) hydrogenation-dehydration route (HYD), 3.)

tautomerization-deoxygenation route (Boullosa-Eiras et al., 2014; de Souza et al., 2015; Nie & Resasco, 2014; Zhao et al., 2011). DDO pathway involves a direct cleavage of  $C_{AR}-OH$  bond from phenol to form benzene whereas HYD pathway requires phenyl ring hydrogenation prior to  $C_{AR}-OH$  bond scission to form cyclohexane. Likewise, phenolic tautomerization was also reported in some HDO studies to favor benzene formation (de Souza et al., 2014; Nelson et al., 2015; Nie et al., 2014; Robinson et al., 2016a). From an economical point of view, DDO is preferred instead of HYD as the former consumes lesser  $H_2$  (Hensley et al., 2015) and produces benzene which is a better fuel blending precursor (Mochizuki et al., 2014; Zanuttini et al., 2013). The selectivity of DDO and HYD pathways has been widely studied and is mainly dependent on thermodynamic limitations of  $H_2$  sorption, phenol adsorption modes and physicochemical properties of catalyst active sites (Kay Lup et al., 2017a).

Bifunctional metal-acid catalysts are instrumental in catalyzing phenol HDO via hydrogenation, hydrogenolysis and dehydration over its metal-acid sites (Furimsky, 2000; Mortensen et al., 2013). Mild acid supports such as  $TiO_2$ ,  $Al_2O_3$ ,  $ZrO_2$  and  $CeO_2$  are often used as they provide better coking resistance than zeolites besides having optimal acid sites for phenol hydrogenolysis. Oxidic supports such as  $TiO_2$  and  $ZrO_2$  are also known to be oxophilic which would enhance the activation of  $C-O$  bond in phenol (de Souza et al., 2014; de Souza et al., 2015). Co, Pd, Pt, Rh and Ru are the most commonly used noble metal catalyst for phenol HDO to produce aromatic and cyclic hydrocarbons. However, the high cost of these noble metals remained a challenge to their industrial applications. Transition metals such as Ag, Cu, Fe, Ni, and Zn may offer a more economical alternative for HDO catalyst though the study on phenol HDO over Ag has yet to be warranted. Ag metal may offer the possibility for oxygen removal as some studies have indicated of its excellent activity and selectivity for chemoselective reduction of styrene oxides, stilbene oxide, carbonyls, alcohols, nitro-aromatics and

epoxides (Dong et al., 2015; Du et al., 2012; Mikami et al., 2010; Mitsudome et al., 2010). Nevertheless, there are also several density functional theory (DFT) studies that predicted of the low turnover frequency of Ag for HDO of ethylene glycol and ethanol (Jalid et al., 2017; Lausche et al., 2014).

Therefore, the goal of this work is to assess the activity of phenol HDO over titania supported silver catalyst via experimental hydrodeoxygenation process of phenol. The analyses of reaction pathways, product distribution and kinetic modeling were done to shed some light on this matter.

## **6.2 Theoretical formalisms of elementary rate reaction**

Reaction kinetic analyses generally entail formulation of a reaction scheme that would explain the surface chemistry at catalytic sites as accurate as possible (Cortright & Dumesic, 2002). Thus, postulates which formed the basis of proposed reaction scheme are often reconciled with theoretical and experimental data to ensure the reaction scheme is accurate in its mathematical and physical interpretations (Stoltze, 2000). In this section, theoretical formalisms of rate constant estimation and elementary rate equation focused only on application of collision theory and transition state theory for a gas-phase bimolecular reaction on a catalyst surface i.e. gas-phase HDO of phenol over Ag/TiO<sub>2</sub> catalyst. The discussion on theory application for estimated rate constants will be presented along with experimental kinetic data in Section 6.4.4.

### **6.2.1 Collision theory**

In collision theory, the notion of reaction occurring between two molecules involves a collisional process in which sufficient collision energy is required to overcome energy

barrier for the rearrangement of valence electrons of reactants (Butt, 2000; Pilling & Seakins, 1995). Molecules are assumed to be hard and structureless spheres which are impenetrable and of no interactions upon their contacts. For a collision to occur, both molecules must be within the cross section of the reaction,  $\sigma_{ij}$ , which is the circular area with its radius,  $r_{ij}$ , as the sum of radii of both colliding molecules. When a system consists of species  $i$  and  $j$  molecules that have Maxwellian velocity distribution and collide with one another, number of collisions per unit time and volume,  $Z_{ij}$ , is expressed as:

$$Z_{ij} = \left(\frac{N_i}{V}\right) \left(\frac{N_j}{V}\right) \sigma_{ij} \bar{v}_r = N_A^2 C_i C_j r_{ij}^2 \sqrt{\frac{8\pi k_B T}{\mu_{ij}}} \quad (6.1)$$

where  $N_i$  and  $N_j$  are number of  $i$  and  $j$  molecules,  $C_i$  and  $C_j$  are molar concentrations of  $i$  and  $j$  molecules,  $V$  is volume of system,  $\sigma_{ij} = \pi r_{ij}^2$ , is cross section of reaction,  $N_A$  is Avogadro's constant,  $\bar{v}_r = \sqrt{8k_B T / \pi \mu_{ij}}$  as relative mean velocity of  $i$  and  $j$  molecules,  $k_B$  is Boltzmann's constant,  $T$  is absolute temperature and  $\mu_{ij} = m_i m_j / (m_i + m_j)$  as reduced mass of  $i$  and  $j$  molecules.

For a system of Maxwellian velocity distribution, only a fraction of  $e^{-E_a/RT}$  molecules have collision energies,  $E \gg E_a$ , which result in reactions. Thus, based on collision theory, rate of reaction can be formulated as:

$$-\frac{d(N_i/V)}{dt} = -N_A \frac{dC_i}{dt} = N_A^2 C_i C_j r_{ij}^2 \sqrt{\frac{8\pi k_B T}{\mu_{ij}}} e^{-E_a/RT} \quad (6.2)$$

Since  $-(dC_i/dt) = r_{rxn}$ :

$$r_{rxn} = \rho N_A C_i C_j r_{ij}^2 \sqrt{\frac{8\pi k_B T}{\mu_{ij}}} e^{-E_a/RT} = \rho \left( N_A r_{ij}^2 \sqrt{\frac{8\pi k_B T}{\mu_{ij}}} \right) e^{-E_a/RT} C_i C_j$$

$$= \rho A_{CT} e^{-E_a/RT} C_i C_j = A e^{-E_a/RT} C_i C_j = k_{CT}(T) C_i C_j \quad (6.3)$$

where  $\rho$  is steric factor,  $R = k_B N_A$  is ideal gas constant,  $E_a$  is activation energy,  $A_{CT} = N_A r_{ij}^2 \sqrt{8\pi k_B T / \mu_{ij}}$  as pre-exponential factor based on collision theory,  $A = \rho A_{CT}$ , as pre-exponential factor of Arrhenius equation and  $k_{CT}(T) = A e^{-E_a/RT}$  as rate constant based on collision theory. The rate constant of Equation 6.3 had similar form with rate constant of Arrhenius equation, i.e.  $k(T) = A e^{-E_a/RT}$  which gives a theoretical interpretation of  $A$  and  $E_a$  values based on collision theory.

Adsorption rate of reactant on catalyst surface,  $i_{(g)} + S \rightleftharpoons i \cdot S$ , can also be derived from collision theory using collision frequency,  $Z_{w,i}$ , which is number of collisions of  $i$  molecules with an area unit of catalyst surface per unit time.

$$Z_{w,i} = \frac{1}{4} \left( \frac{N_i}{V} \right) \bar{v}_i = \frac{1}{4} \left( \frac{N_i}{V} \right) \sqrt{\frac{8k_B T}{\pi m_i}} = \frac{1}{4} \left( \frac{p_i V}{V k_B T} \right) \sqrt{\frac{8k_B T}{\pi m_i}} = \frac{p_i}{\sqrt{2\pi m_i k_B T}} \quad (6.4)$$

Since collision must have energy of  $E \gg E_{ads}$  to result in adsorption and adsorption rate is also dependent on the coverage of vacant sites,  $\theta_S$ :

$$\begin{aligned} r_{ads} &= \sigma_i(\theta_S, T) Z_{w,i} = \rho \theta_S e^{-E_{ads}/RT} Z_{w,i} = \frac{\rho p_i \theta_S}{\sqrt{2\pi m_i k_B T}} e^{-E_{ads}/RT} \\ &= A_{ads} e^{-E_{ads}/RT} p_i \theta_S = k_{ads} p_i \theta_S \end{aligned} \quad (6.5)$$

The mathematical expression of desorption rate also has similar form:

$$r_{des} = k_{des} \theta_i \quad (6.6)$$

where  $p_i$  is partial pressure of species  $i$ ,  $\sigma_i(\theta_S, T)$  is sticking probability of species  $i$ ,  $E_{ads}$  is adsorption activation energy,  $A_{ads} = \rho / \sqrt{2\pi m_i k_B T}$  as pre-exponential factor of adsorption and  $k_{ads} = A_{ads} e^{-E_{ads}/RT}$  as adsorption rate constant. Chemisorption of

reactant on catalyst surface is a reversible process. Thus, at dynamic equilibrium, adsorption and desorption rates are equivalent:

$$k_{ads}p_i\theta_S = k_{des}\theta_i \quad (6.7)$$

$$K_i = \frac{k_{ads}}{k_{des}} = \frac{\theta_i}{p_i\theta_S} \quad (6.8)$$

where  $K_i$  is adsorption equilibrium constant of species  $i$ . Since  $\theta_i + \theta_S = 1$ , rearranging Equation 6.8 and solving for  $\theta_i$ :

$$\theta_i = \frac{K_i p_i}{1 + K_i p_i} \quad (6.9)$$

which is Langmuir isotherm equation for non-dissociative adsorption on catalyst surface.

Bimolecular surface reaction between two adsorbed species can also be described based on collision theory by considering adsorbed species as two-dimensional mobile species on catalyst surface. Thus, average relative mean velocity of  $i$  and  $j$  molecules in two dimensions is noted to be (Boudart, 1975):

$$\bar{v}_{r,2D} = \sqrt{\pi k_B T / 2\mu_{ij}} \quad (6.10)$$

Similarly, collision frequency can be expressed as:

$$Z_{2D} = \theta_i \theta_j r_{ij} \bar{v}_{r,2D} = \theta_i \theta_j r_{ij} \sqrt{\frac{\pi k_B T}{2\mu_{ij}}} \quad (6.11)$$

which is two-dimensional form of collision frequency in Equation 6.1. By using the same approach, surface reaction rate,  $r_{surf}$ , can be expressed as:

$$\begin{aligned}
r_{surf} &= \rho_{surf} C_S \theta_i \theta_j r_{ij} \sqrt{\frac{\pi k_B T}{2\mu_{ij}}} e^{-E_a/RT} = \rho_s \left( C_S r_{ij} \sqrt{\frac{\pi k_B T}{2\mu_{ij}}} \right) e^{-E_a/RT} \theta_i \theta_j \\
&= \rho_s A_{CT,surf} e^{-E_a/RT} \theta_i \theta_j = A_{surf} e^{-E_a/RT} \theta_i \theta_j = k_{surf} \theta_i \theta_j \quad (6.12)
\end{aligned}$$

where  $C_S$  is concentration of catalyst site;  $\theta_{i,S}$  and  $\theta_{j,S}$  are fractional coverages of adsorbed  $i$  and  $j$  species;  $\rho_s$ ,  $A_{surf}$  and  $k_{surf}$  are steric factor, pre-exponential factor and rate constant of surface reaction respectively.

### 6.2.2 Transition state theory

Transition state theory (TST) postulates that a reaction between  $i$  and  $j$  species proceeds via formation of an activated transition state complex,  $ij^\ddagger$ , which exists in a quasi-equilibrium state with reactants (Hänggi et al., 1990; Laidler & Christine King, 1983; Truhlar et al., 1996). The activated complex would then undergo unimolecular decay to form products C and D.



Rate of reaction,  $r_{rxn}$ , which is the rate at which activated complex breaks apart into products is dependent on its concentration,  $C_{ij^\ddagger}$ , and vibration frequency,  $\nu$ .

$$r_{rxn} = \nu C_{ij^\ddagger} \quad (6.14)$$

Since quasi-equilibrium constant,  $K^\ddagger$ , is defined as:

$$K^\ddagger = \frac{C_{ij^\ddagger}}{C_i C_j} \quad (6.15)$$

and one vibrational degree of freedom of the complex which causes the bond breaking is of loose vibration with average energy in the order of  $k_B T$ :



$$v = \frac{k_B T}{h} \quad (6.16)$$

rate of reaction can be rewritten as:

$$r_{rxn} = \frac{k_B T}{h} K^\ddagger C_i C_j = k C_i C_j \quad (6.17)$$

where  $h$  is Planck's constant,  $C_i$  and  $C_j$  are concentrations of reactant  $i$  and  $j$  respectively and  $k = (k_B T/h)K^\ddagger$ , is TST-derived rate constant. Theoretical rate constant can be calculated if  $K^\ddagger$  value is known. The  $K^\ddagger$  can be formulated via microscopic and macroscopic approaches. Microscopic formulation expresses  $K^\ddagger$  in terms of molecular partition functions while macroscopic formulation expresses  $K^\ddagger$  in terms of thermodynamic functions.

### 6.2.2.1 Microscopic formulation

By using statistical thermodynamics, thermodynamic property of a system such as Gibbs energy,  $G$ , can be expressed in its total canonical partition function,  $Q$ :

$$G - G(0) = -k_B T \ln Q + nRT \quad (6.18)$$

For gas-phase reaction system with indistinguishable molecules, canonical partition function can be expressed in terms of molecular partition function,  $q$ , as:

$$Q = \frac{q^N}{N!} \quad (6.19)$$

where  $G(0)$  is Gibbs energy at reference state,  $n$  is number of moles in system,  $N$  is number of molecules in system. By substituting  $Q = q^N/N!$  into Equation 6.18 and using Stirling's approximation ( $\ln N! = N \ln N - N$ ), Equation 6.18 becomes:

$$\begin{aligned}
G - G(0) &= -k_B T \ln \left( \frac{q^N}{N!} \right) + nRT = -Nk_B T \ln q + k_B T \ln N! + nRT \\
&= -nRT \ln q + k_B T (N \ln N - N) + nRT \\
&= -nRT \ln \left( \frac{q}{N} \right) = -nRT \ln \left( \frac{q_m}{N_A} \right) \quad (6.20)
\end{aligned}$$

where  $q_m = q/n$  is molar partition function. For an equilibrium reaction, i.e. formation of activated complex from reactant, molar Gibbs energy of activation,  $\Delta_r G_m^\ddagger$ , is:

$$\begin{aligned}
\Delta_r G_m^\ddagger &= G_m(ij^\ddagger) - G_m(i) - G_m(j) \\
&= G_m(ij^\ddagger, 0) - G_m(i, 0) - G_m(j, 0) - RT \left\{ \ln \left( \frac{q_{ij^\ddagger, m}}{N_A} \right) - \ln \left( \frac{q_{i, m}}{N_A} \right) - \ln \left( \frac{q_{j, m}}{N_A} \right) \right\} \\
&= -RT \left\{ -\frac{\Delta_r E_{m, 0}^\ddagger}{RT} + \ln \left( \frac{N_A q_{ij^\ddagger, m}}{q_{i, m} q_{j, m}} \right) \right\} \quad (6.21)
\end{aligned}$$

where  $\Delta_r E_{m, 0}^\ddagger = G_m(ij^\ddagger, 0) - G_m(i, 0) - G_m(j, 0)$  is activation energy of activated complex formation,  $q_{ij^\ddagger, m}$ ,  $q_{i, m}$  and  $q_{j, m}$  are molar partition functions of complex  $ij^\ddagger$ , reactants  $i$  and  $j$ . Since  $\Delta_r G_m^\ddagger = -RT \ln (K^\ddagger a)$  for an ideal system ( $K_\gamma = 1$ ), this gives:

$$\ln(K^\ddagger a) = \left\{ -\frac{\Delta_r E_{m, 0}^\ddagger}{RT} + \ln \left( \frac{N_A q_{ij^\ddagger, m}}{q_{i, m} q_{j, m}} \right) \right\} \quad (6.22a)$$

$$K^\ddagger = \frac{N_A}{a} \left( \frac{q_{ij^\ddagger, m}}{q_{i, m} q_{j, m}} \right) e^{-\frac{\Delta_r E_{m, 0}^\ddagger}{RT}} \quad (6.22b)$$

where  $a$  has the value of unity and a reciprocal unit of  $K^\ddagger$  to preserve dimensional homogeneity of equation. Thus, based on microscopic formulation of TST, rate constant can be written as:

$$k = \frac{RT}{ha} \left( \frac{q_{ij^\ddagger, m}}{q_{i, m} q_{j, m}} \right) e^{-\frac{\Delta_r E_{m, 0}^\ddagger}{RT}} = \frac{k_B T}{ha} \left( \frac{q_{ij^\ddagger}}{q_i q_j} \right) e^{-\frac{\Delta_r E_{m, 0}^\ddagger}{RT}} \quad (6.23)$$

which has similar form with rate constant from Arrhenius' equation.

For a system with  $N$  molecules and total energy of  $E$ , a portion of  $n_r$  molecules can have energy at  $r^{\text{th}}$  energy level,  $\varepsilon_r$ , with a probability distribution by Boltzmann's law:

$$n_r \propto g_r e^{-\frac{\varepsilon_r}{k_B T}} = g_r e^{-\beta \varepsilon_r} \quad (6.24)$$

where  $g_r$  is degeneracy of state which is the number of states which have same energy,  $\varepsilon_r$  and  $\beta = 1/k_B T$  is thermodynamic beta. Thus, partition function is the weighted sum of all energy levels occupied by molecules at a given temperature (Atkins & Paula, 2010).

$$q = \sum_{r=0}^{\infty} g_r e^{-\beta \varepsilon_r} \quad (6.25)$$

For a molecule at gaseous state, its total molecular energy consists of translational (T), rotational (R), vibrational (V) and electronic (El) energies. Based on Born-Oppenheimer approximation, total molecular energy can be resolved into these independent components with their respective independent degeneracies:

$$\varepsilon_r = \sum_i \varepsilon_r^i = \varepsilon_r^T + \varepsilon_r^R + \varepsilon_r^V + \varepsilon_r^{El} \quad (6.26)$$

$$g_r = \prod_i g_r^i = g_r^T g_r^R g_r^V g_r^{El} \quad (6.27)$$

Based on these two properties, partition function can be factorized as:

$$\begin{aligned} q &= \sum_{r^T}^{\infty} \sum_{r^R}^{\infty} \sum_{r^V}^{\infty} \sum_{r^{El}}^{\infty} (g_r^T g_r^R g_r^V g_r^{El}) (e^{-\beta \varepsilon_r^T} \cdot e^{-\beta \varepsilon_r^R} \cdot e^{-\beta \varepsilon_r^V} \cdot e^{-\beta \varepsilon_r^{El}}) \\ &= \sum_{r^T}^{\infty} g_r^T e^{-\beta \varepsilon_r^T} \sum_{r^R}^{\infty} g_r^R e^{-\beta \varepsilon_r^R} \sum_{r^V}^{\infty} g_r^V e^{-\beta \varepsilon_r^V} \sum_{r^{El}}^{\infty} g_r^{El} e^{-\beta \varepsilon_r^{El}} = q^T q^R q^V q^{El} \end{aligned} \quad (6.28)$$

which is a product of independent translational, rotational, vibrational and electronic partition functions. Partition functions of each mode and their respective approximate

order of magnitude are listed in Table 6.1. Based on these information, molecular partition functions of activated complex,  $q_{ij^\ddagger}$ , reactant species,  $q_i$  and  $q_j$ , can then be calculated for determination of  $K^\ddagger$ .

**Table 6.1: Partition function of each mode (Upadhyay, 2006)**

Modes	Degree of freedom	Partition function*	Order of magnitude
1. Translational	3	$(2\pi mk_B T)^{3/2}/h^3$	$10^{24} - 10^{25}$
2. Rotational			
<i>Linear</i>	2	$8\pi^2 I k_B T / \sigma h^2$	$10 - 10^2$
<i>Non-linear</i>	3	$8\pi^2 (8\pi^3 I_A I_B I_C) (k_B T)^3 / \sigma h^3$	$10^2 - 10^3$
3. Vibrational			
<i>Linear</i>	$j = 3N - 5$	$\prod_j (1 - e^{(-h\nu_j/k_B T)})^{-1}$	$1 - 10^j$
<i>Non-linear</i>	$j = 3N - 6$		
4. Electronic	-	$\sum_{r, El} g_r^{El} e^{-\beta \epsilon_{El}}$	1

\*  $I, I_A, I_B$  and  $I_C$  are moments of inertia,  $\sigma$  is symmetry factor,  $N$  is number of atoms in a molecule

### 6.2.2.2 Macroscopic formulation

Analyses of  $K^\ddagger$  via statistical mechanical formulation of partition functions tend to be laborious when it comes to reactions of larger molecules. Thus, thermodynamic functions were often preferred in determining  $K^\ddagger$  of more complex reaction systems (Benson & Golden, 1975; Pilling & Seakins, 1995). By using definitions of  $\Delta_r G_m^\ddagger = -RT \ln(K^\ddagger a)$  and  $\Delta_r G_m^\ddagger = \Delta_r H_m^\ddagger - T \Delta_r S_m^\ddagger$  (Gibbs-Helmholtz relation),

$$K^\ddagger a = e^{-\Delta_r G_m^\ddagger / RT} = e^{-(\Delta_r H_m^\ddagger - T \Delta_r S_m^\ddagger) / RT} = e^{-\Delta_r H_m^\ddagger / RT} e^{\Delta_r S_m^\ddagger / R} \quad (6.29)$$

which is Eyring equation that relates quasi-equilibrium concentration constant with two macroscopic thermodynamic properties: molar enthalpy change of activation,  $\Delta_r H_m^\ddagger$ , and molar entropy change of activation,  $\Delta_r S_m^\ddagger$ . Thus, based on macroscopic formulation of TST, rate constant can be written as:

$$k = \frac{k_B T}{h} K^\ddagger = \frac{k_B T}{h a} e^{-\Delta_r H_m^\ddagger / RT} e^{\Delta_r S_m^\ddagger / R} \quad (6.30)$$

which has similar form with rate constant of Arrhenius equation. By expressing Equation 6.30 in natural logarithmic form and differentiating it with respect to  $T$ , it becomes:

$$\frac{d(\ln k)}{dT} = \frac{1}{T} + \frac{d(\ln K^\ddagger)}{dT} \quad (6.31)$$

Similarly, for Arrhenius equation:

$$\frac{d(\ln k)}{dT} = \frac{E_a}{RT^2} \quad (6.32)$$

By equating both equations and using Van't Hoff equation,

$$E_a = RT + RT^2 \frac{d(\ln K^\ddagger)}{dT} = RT + \Delta_r E_m^\ddagger \quad (6.33)$$

Based on 1<sup>st</sup> law of thermodynamics and assuming ideal gas behavior,

$$\Delta_r H_m^\ddagger = \Delta_r E_m^\ddagger + \Delta(PV) = \Delta_r E_m^\ddagger + (\Delta n)RT = E_a - 2RT \quad (6.34)$$

where  $\Delta n = -1$  for bimolecular reactions. Thus, rate constant can be expressed in terms of  $E_a$  instead of  $\Delta_r H_m^\ddagger$ :

$$k = \frac{k_B T e^2}{h a} e^{\Delta_r S_m^\ddagger / R} e^{-E_a / RT} = A e^{-E_a / RT} \quad (6.35)$$

where  $A = (k_B T e^2 / h a) e^{\Delta_r S_m^\ddagger / R}$  is pre-exponential factor based on thermodynamic formulation of TST.

### 6.2.2.3 Surface reactions

TST for surface reactions remains equally applicable with gas-phase reactions (Houston, 2006; Pitt et al., 1994; Pitt et al., 1995a; Pitt et al., 1995b). However, partition functions for surface species are now expressed in per unit surface area. For gas-phase molecule adsorption on catalyst site,  $i_{(g)} + S \rightleftharpoons [i \cdot S]^\ddagger \rightarrow i \cdot S$ , adsorption rate equation can be expressed in terms of partition or thermodynamic functions.

$$r_{ads,i} = \frac{k_B T C_T}{h} \left( \frac{q_{[i \cdot S]^\ddagger}}{q_i q_S} \right) e^{-\frac{E_{ads,i}}{RT}} p_i \theta_S = \frac{k_B T C_T e^2}{h} e^{\frac{\Delta S_{ads}^\ddagger}{R}} e^{-\frac{E_{ads,i}}{RT}} p_i \theta_S \quad (6.36)$$

Similarly, for desorption,  $i \cdot S \rightleftharpoons [i \cdot S]^\ddagger \rightarrow i_{(g)} + S$ , desorption rate equation becomes:

$$r_{des,i} = \frac{k_B T C_T}{h} \left( \frac{q_{[i \cdot S]^\ddagger}}{q_{i \cdot S}} \right) e^{-\frac{E_{des,i}}{RT}} \theta_{i \cdot S} = \frac{k_B T C_T e}{h} e^{\frac{\Delta S_{des}^\ddagger}{R}} e^{-\frac{E_{des,i}}{RT}} \theta_{i \cdot S} \quad (6.37)$$

and rate equation for bimolecular surface reaction,  $i \cdot S + j \cdot S \rightleftharpoons [S \cdot i - j \cdot S]^\ddagger \rightarrow M \cdot S + N \cdot S$ , becomes:

$$r_{surf,i} = \frac{k_B T C_T^2}{h} \left( \frac{q_{[S \cdot i - j \cdot S]^\ddagger}}{q_{i \cdot S} q_{j \cdot S}} \right) e^{-\frac{E_a}{RT}} \theta_{i \cdot S} \theta_{j \cdot S} = \frac{k_B T C_T^2 e^2}{h} e^{\frac{\Delta S_{surf}^\ddagger}{R}} e^{-\frac{E_a}{RT}} \theta_{i \cdot S} \theta_{j \cdot S} \quad (6.38)$$

where  $C_T$  is concentration of total surface sites;  $\Delta S_{ads}^\ddagger$ ,  $\Delta S_{des}^\ddagger$  and  $\Delta S_{surf}^\ddagger$  are entropy changes of activation for adsorption, desorption and surface reaction.

## 6.3 Experimental

### 6.3.1 Chemicals

All chemicals were obtained from Sigma-Aldrich supplier: phenol (99.5%), benzene (99%), cyclohexane (99%), cyclohexene (99%), cyclohexanone (99%), cyclohexanol (99%), silver nitrate (ACS reagent) and titanium (IV) dioxide (technical,  $\geq 97\%$ ). Gases

used in this study: He (>99.999%), N<sub>2</sub> (>99.999%), gas mixtures of 10% NH<sub>3</sub>/He and 5% H<sub>2</sub>/N<sub>2</sub> were purchased from Linde Malaysia Sdn. Bhd.

### 6.3.2 Catalyst preparation

Titania-supported silver catalyst with 10 wt% silver loading was used to investigate the mechanism of phenol hydrodeoxygenation reaction. Catalyst was prepared by dry impregnation of pure anatase TiO<sub>2</sub> (100 g, BET surface area: 10.5 m<sup>2</sup>/g) with an aqueous solution (10 mL) of silver nitrate (18.6 g). Impregnation mixture was stirred at room temperature for 1 h, dried at 120 °C for 24 h and calcined in air at 400 °C for 24 h. The prepared catalyst is henceforth denoted as Ag/TiO<sub>2</sub>.

### 6.3.3 Catalyst characterization

Actual silver loading of catalyst was determined using a Perkin Elmer Optima 5300V ICP-OES. Specific surface area was obtained via BET method using a Micromeritics ASAP 2020. Scanning electron micrograph (SEM) and transmission electron micrograph (TEM) images were respectively collected on ZEISS GeminiSEM 300 and TEM LEO 912 Omega. 120 particles were sampled for size calculation.

Acidity of catalyst was studied by ammonia temperature programmed desorption (NH<sub>3</sub>-TPD) using Micromeritics Chemisorb 2720 with a 10 vol% NH<sub>3</sub>/He gas flow. 50 mg of catalyst was loaded in TPD cell and heated from 25 °C to 300 °C with heating rate of 20 °C/min and was held at 300 °C for 30 min in a 20 mL/min stream of He. Sample was cooled down to 25 °C and ammonia was adsorbed by sample for 30 min by changing He flow to 10 vol% NH<sub>3</sub>/He flow. Physisorbed molecules on sample were

removed by purging it with He for 30 min. Ammonia desorption measurement was done from 100 °C to 900 °C with heating rate of 30 °C/min under 20 mL/min He flow.

Hydrogen chemisorption on catalyst surface was performed by hydrogen temperature programmed desorption (H<sub>2</sub>-TPD) using Micromeritics Chemisorb 2720. 50 mg of catalyst was pretreated in 20 mL/min 5 vol% H<sub>2</sub>/N<sub>2</sub> flow at 300 °C for 30 min and then cooled down to 25 °C for 30 min of hydrogen adsorption. Hydrogen desorption measurement was done from 25 °C to 700 °C with heating rate of 30 °C/min under 20 mL/min He flow. Hydrogen chemisorbed on Ag was determined using chemisorption stoichiometry of H/Ag<sub>surf</sub> = 1.

### **6.3.4 Catalytic measurement**

#### **6.3.4.1 Kinetic tests**

Experimental studies were done using a continuous-flow microreactor (I.D. 15.6 mm and length 20.2 mm) with on-line TGA-FTIR coupling system, in which catalyst of 250-300 mesh size was packed. Prior to the reactions, the catalyst was activated by in-situ reduction under a 20 mL/min of 5% H<sub>2</sub>/N<sub>2</sub> flow at 400 °C for 2 h. All HDO reactions were carried out at atmospheric pressure under 5% H<sub>2</sub>/N<sub>2</sub> gas flow and 3.457 μmol/s phenol flow rate for 1 h. For HDO kinetic tests, fresh catalyst samples were used for each experiment. For the study of H<sub>2</sub> flow rate effect on phenol HDO over Ag/TiO<sub>2</sub>, reaction was conducted at different H<sub>2</sub> flow rates of 1, 2, 5 and 10 mL/min. Effect of weight hourly space velocity (WHSV) was investigated by varying the ratios of phenol mass flow rate with catalyst weight during reaction, using different catalyst weights (50, 230 and 350 mg). Effect of reaction temperature was also studied by conducting reaction at 454, 495, 530 and 553 K.



Vapor products from reaction system were analyzed by evolved gas analysis (EGA) of Bruker TENSOR 27 FTIR spectrometer. Evolved gaseous products were swept by purge gas from TGA through a 53 cm-transfer line into FTIR gas cell which is heated up to 200 °C. Transfer line was maintained at 230 °C to prevent product condensation. FTIR gas cell with 123 mm path length and 8.7 mL volume functioned as the detection chamber of evolved gaseous products using liquid nitrogen-cooled MCT (Mercury Cadmium Telluride) detector. Scans were taken at resolution of 4 cm<sup>-1</sup> to give a theoretical data spacing of 1.928 cm<sup>-1</sup> ranging from 650 to 4500 cm<sup>-1</sup> wavenumbers. Background scans were done beforehand to eliminate peak interference from atmospheric CO<sub>2</sub> and H<sub>2</sub>O. FTIR gas cell was purged with pure N<sub>2</sub> before collecting FTIR spectra. FTIR spectra were collected at an interval of 7.027 s and each spectrum was obtained based on the average of 16 scans. TGA-FTIR coupling system was also purged with N<sub>2</sub> flow to ensure a clean environment for next experiment.

Reaction products were also analyzed off-line by GC-MS (Shimadzu QP 2010, DB-5 30 m x 0.25 mm x 0.25 mm) coupled with flame ionization detection. 2-isopropylphenol was used as the internal standard and the NIST (National Institute of Standards and Technology) library was used for product identification. All experiments were repeated twice and result deviations were less than ±3%. The mass balance in each experiment was within ±2% deviation. Conversion of phenol and selectivity of products in this study were calculated based on the following equations:

$$\text{Conversion (\%)} = \frac{\text{Mol of reacted phenol}}{\text{Mol of initial phenol}} \times 100 \quad (6.39)$$

$$\text{Selectivity (\%)} = \frac{\text{Mol of a product}}{\text{Mol of all products}} \times 100 \quad (6.40)$$

#### 6.3.4.2 Catalyst stability study

For catalyst stability testing, phenol hydrodeoxygenation was tested on three recycling runs using the same catalyst sample after the first experimental run. The catalyst recycling procedure was as followed: 3.457  $\mu\text{mol/s}$  phenol vapor flow was passed through catalyst bed (2.0 g, 250-300 mesh size) in the same reactor and then reacted at 553 K and 1 atm in a 200 mL/min 5%  $\text{H}_2/\text{N}_2$  gas flow. The products were analyzed using GC-MS when reaction reached steady state condition. After each experimental run, the spent catalyst was washed using acetone and water, dried at 403 K. About 0.1 g of spent catalyst was sampled to be characterized using XRD, BET, TEM and TGA. Prior to its reuse in the next run, the dried spent catalyst was calcined in air at 400 °C and activated again by  $\text{H}_2$  at 400 °C.

### 6.4 Results and discussion

#### 6.4.1 Characterization of catalysts under study

Physicochemical properties of  $\text{Ag}/\text{TiO}_2$  catalyst determined by  $\text{N}_2$  isothermal adsorption-desorption, TEM, ICP-OES,  $\text{NH}_3$ -TPD and  $\text{H}_2$ -TPD are summarized in Table 6.2. Based on Figure 6.1,  $\text{Ag}/\text{TiO}_2$  is a mesoporous catalyst with type IV isotherm and H1 hysteresis loop. The H1 hysteresis loop indicates that  $\text{Ag}/\text{TiO}_2$  contains mesoporous cylindrical channels with uniform size and shape (Leofanti et al., 1998). Pore volume of  $\text{TiO}_2$  was higher than that of Ag impregnated  $\text{TiO}_2$  as Ag metal species were deposited inside the catalytic pores and reduced the pore volume. Similarly, silver loading has also reduced the BET surface area of catalyst. The actual silver loading determined via ICP-OES was lower than the stoichiometric silver loading (10 wt%) intended during catalyst synthesis. This is attributed to the slight sample loss during the preparation, synthesis and calcination of catalyst (Leofanti et al., 1997).

Based on SEM micrograph (Figure 6.2A), the catalyst morphology was shown to be in the stacking form of multiple circular TiO<sub>2</sub> slabs with an average TiO<sub>2</sub> slab size of 113 nm. A miniscule amount of Ag metal was deposited on catalyst surface while most of them were deposited in catalytic pores as shown in the TEM micrograph (Figure 6.2B). The average particle size of Ag was determined from TEM images to be 7.45 ± 2.38 nm. The estimated Ag particle size based on its metal dispersion from H<sub>2</sub> chemisorption is quite close to the TEM-measured particle size.

**Table 6.2: Physicochemical properties of Ag/TiO<sub>2</sub> catalyst**

Physical properties		Chemical properties	
S <sub>BET</sub> (m <sup>2</sup> /g)	8.69	Ag loading (wt%)	9.13
Pore volume (cm <sup>3</sup> /g)	0.0296	Acidity (mmol/g) <sup>c</sup>	0.2576
Pore size (nm)	9.53	H <sub>2</sub> uptake by Ag (mmol/g) <sup>d</sup>	0.0861
Ag particle size (nm)	6.39 <sup>a</sup> 7.45 <sup>b</sup>	Ag metal dispersion <sup>d</sup>	0.204
TiO <sub>2</sub> particle size (nm)	113 <sup>b</sup>		

<sup>a</sup> Calculated using equation: Ag particle size = 1.3/(Ag metal dispersion) (Seyedmonir et al., 1990)

<sup>b</sup> Determined by TEM images

<sup>c</sup> Determined by NH<sub>3</sub>-TPD

<sup>d</sup> Determined by H<sub>2</sub>-TPD

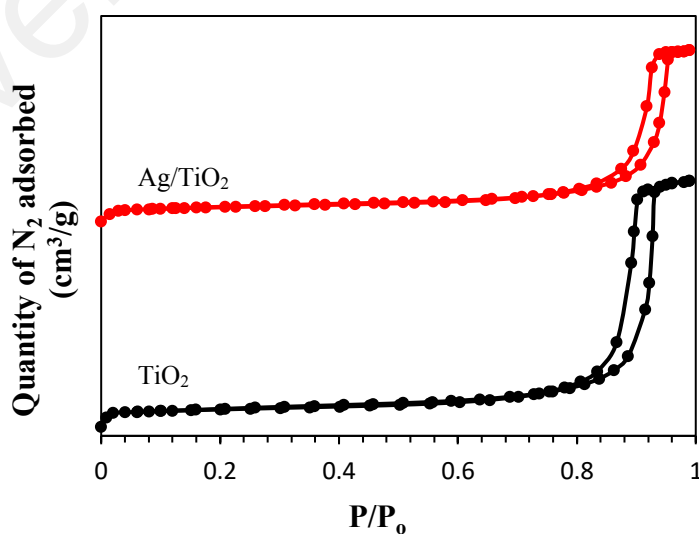


**Figure 6.1: N<sub>2</sub> adsorption-desorption isotherms of Ag/TiO<sub>2</sub> and TiO<sub>2</sub>**

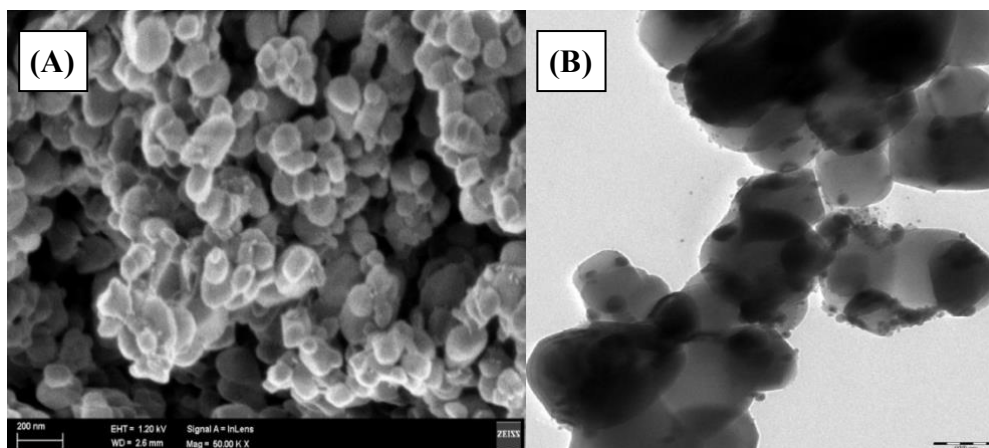


**Figure 6.2: (A) SEM and (B) TEM images of Ag/TiO<sub>2</sub> catalyst**

#### **6.4.2 Hydrodeoxygenation of phenol**

Phenol hydrodeoxygenation reaction scheme is shown in Figure 6.3 which consists of phenol hydrogenolysis (Step 1), phenol hydrogenation (Step 2), cyclohexanol dehydration (Step 3), cyclohexene hydrogenation (Step 4) and benzene hydrogenation (Step 5). Step 1 is commonly known as direct deoxygenation pathway (DDO) while Step 2, 3, and 4 are belonged to hydrogenation-dehydration pathway (HYD) (Badawi et al., 2013; He & Wang, 2012). These HDO pathways were also commonly reported with the use of various supported transition metal catalysts such as Co (Platanitis et al., 2014; Yang et al., 2009), Fe (Shafaghat et al., 2016), Mo (Badawi et al., 2013; Boullosa-Eiras et al., 2014; Mortensen et al., 2015), Ni (Shafaghat et al., 2016; Zhao et al., 2012b), Pd (Echeandia et al., 2014) and Pt (Ohta et al., 2014). In the overall gas-phase reaction, the metal sites catalyzed phenol hydrogenolysis and the hydrogenations of phenol, benzene and cyclohexene while the acid sites catalyzed the dehydration of cyclohexanol intermediate into cyclohexene (He & Wang, 2012; Kay Lup et al., 2017a). The proposed phenol HDO reaction network over Ag/TiO<sub>2</sub> catalyst was made based on the product analyses via in-situ IR spectroscopy and GC-MS.

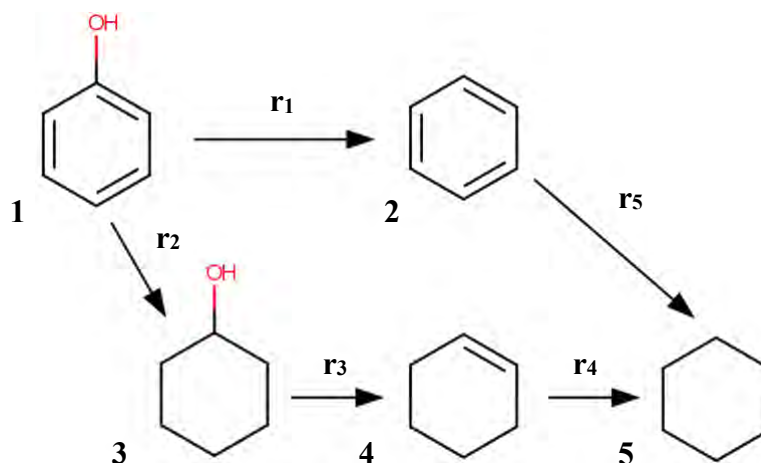


**Figure 6.3: Reaction scheme of phenol hydrodeoxygenation**

The comparison of IR spectra (Figure 6.4) between HDO product mixtures measured during phenol hydrodeoxygenation over Ag/TiO<sub>2</sub> catalyst with a phenol standard mainly showed the presence of phenol functional groups. The analysis of HDO product IR spectrum alone is not conclusive enough to show the formation of benzene to phenol as both also had overlapping peaks for their aromatic rings (Table 6.3). However, by comparing it with phenol IR spectrum, it can be observed that peak intensities at 3649 cm<sup>-1</sup> (O—H stretching, phenol) and 3060 cm<sup>-1</sup> (benzenic C—H stretching) were decreased due to O—H bond dissociation in phenol and conversion of benzene ring into cyclic ring respectively. The small peaks at 2985 cm<sup>-1</sup> and 2871 cm<sup>-1</sup> due to C—H stretching in cyclic ring indicated the presence of cyclic products such as cyclohexanol, cyclohexene and cyclohexane in trace amount. Likewise, peak intensities at 1603 cm<sup>-1</sup> (C=C ring stretching), 1184 cm<sup>-1</sup> (C—H bending) and 748 cm<sup>-1</sup> (C—H wagging) by benzene ring were increased through the formation of an additional C—H bond in aromatic ring as phenol was converted to benzenic products. The characteristic peak of cyclohexanone product at 1715 cm<sup>-1</sup> (C=O stretching) was not detected by IR as GC-MS showed only a negligible amount of cyclohexanone.

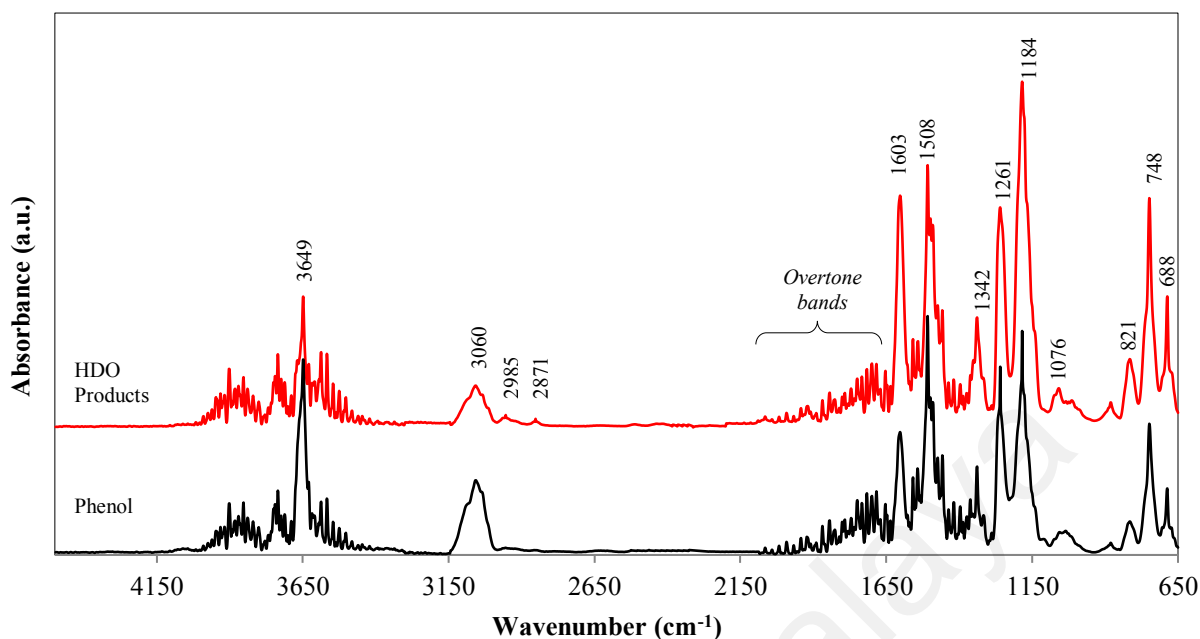


**Figure 6.4: FTIR absorbance spectra for phenol and HDO product mixtures. HDO conditions: 553 K, 1 atm,  $W_{\text{cat}} = 0.23$  g,  $WHSV = 5.09$  h<sup>-1</sup>, 5 mL/min H<sub>2</sub> flow.**

**Table 6.3: IR bands for functional group identification (Larkin, 2011; Robinson et al., 2005)**

Wavenumber (cm <sup>-1</sup> )	Bond vibration	Functional group
4000—3400	O—H (stretching)	Phenol/Water vapor
3150—3000	C—H (stretching)	Benzene ring
2999—2700	C—H (stretching)	Cyclic ring
2000—1645	<i>Benzene ring overtones</i>	
1715	C=O (stretching)	Cyclohexanone
1600	C=C ring (stretching)	Benzene ring
1500	C=C semicircle ring deformation	Benzene ring
1360—1340	C—O—H (bending)	Benzene ring
1260—1238	C—O (stretching)	Phenol
1200—1000	C—H (bending)	Benzene ring
1000—680	C—H (wagging)	Benzene ring

Based on the IR analysis, formation of benzene, cyclohexanol, cyclohexene and cyclohexane were postulated as the products during phenol HDO over Ag/TiO<sub>2</sub> catalyst. HDO product mixtures were further analyzed via GC-MS to confirm the products formation and their respective compositions. Distribution of products from phenol hydrodeoxygenation over Ag/TiO<sub>2</sub> catalyst is summarized in Table 6.4. Water as by-

product was detected during HDO. Its yield was equivalent ( $\pm 4\%$  deviation) with the cumulative yield of deoxygenated products (benzene, cyclohexane and cyclohexene). This is because scission of C—OH bond during phenol hydrogenolysis or cyclic intermediates dehydration will produce a stoichiometric amount of water. Other by-products such as CO or CO<sub>2</sub> were not detected as C—C scission based reaction pathways such as decarbonylation, decarboxylation or ring opening were not observed during the phenol HDO over Ag/TiO<sub>2</sub> catalyst.

The phenol conversion range for Ag/TiO<sub>2</sub> was within 25.2 mol% to 75.5 mol% for 454—553 K which is lower than other supported Co, Fe, Mo, Ni, Pd and Pt based catalysts that had phenol conversion above 80 mol% (Kay Lup et al., 2017b). For atmospheric HDO of phenol over Ag/TiO<sub>2</sub>, direct deoxygenation of phenol to benzene was observed to be the major reaction pathway. The higher benzene selectivity was due to the lower H<sub>2</sub> consumption of phenol hydrogenolysis as compared with phenol hydrogenation. Similar trend was also reported in HDO of *m*-cresol to toluene over Ni/SiO<sub>2</sub> (Chen et al., 2015a), Pt/SiO<sub>2</sub> (Chen et al., 2015a; Nie & Resasco, 2014), Fe/SiO<sub>2</sub> (Nie et al., 2014) and Ga/HBeta (Ausavasukhi et al., 2012); anisole to benzene over Pt/SiO<sub>2</sub> (Zhu et al., 2011); guaiacol to benzene over Co/Al-MCM-41 (Tran et al., 2016) and Fe/SiO<sub>2</sub> (Olcese et al., 2012) which indicated that atmospheric or low H<sub>2</sub> pressure HDO had higher selectivity for deoxygenated aromatics.

In several DFT studies, Ag has been reported to have low catalytic rate for HDO reactions due to its high C—O bond breaking energy and low carbon and oxygen binding energies (Jalid et al., 2017; Lausche et al., 2014). For instance, Jalid et al. (2017) has shown that the activity for ethanol conversion to ethane at 523 K over (211) metal surfaces has the order of: Co > Ru > Ir > Rh > Ni > Fe > Pt > Pd > Cu > Re > Ag > Au. Similarly, Lausche et al. (2014) reported on the Gibbs free energy of C—O bond

splitting over (211) surfaces of Ag, Pt and Ru during ethylene glycol hydrodeoxygenation at 650 K and noted the order of energy barrier as: Ag (3.19 eV) > Pt (2.58 eV) > Ru (1.66 eV). Lausche et al. (2014) also proposed a strategy for better activation of C—O bond by supporting metals on oxophilic materials (ZrO<sub>2</sub>, TiO<sub>2</sub>) which can activate the oxygen end of C—O bond. In this study, with the introduction of TiO<sub>2</sub> as reducible and oxophilic support, phenol hydrodeoxygenation over Ag was able to be enhanced as TiO<sub>2</sub> was reported to be one of the excellent supports for HDO catalyst (de Souza et al., 2015; Kay Lup et al., 2017b; Mortensen et al., 2013). The effect of oxophilic support materials in improving HDO activity and yield of deoxygenated aromatics was also seen in the studies of phenol hydrodeoxygenation over Pd/HY (Echeandia et al., 2014) and Pd/ZrO<sub>2</sub> (de Souza et al., 2015) catalysts at 573 K. Both studies showed a stark difference in Pd catalytic performance in which the former mainly catalyzed cyclohexane formation (20% conversion, 58% selectivity) while the use of oxophilic support in the latter resulted in benzene formation as the major product (75% conversion, 54% selectivity)



**Table 6.4: HDO products of phenol over Ag/TiO<sub>2</sub> as determined by GC-MS<sup>a</sup>**

	Reaction temperature (K)						
	454	495		553		600	
Conversion (mol%)							
Phenol	25.2 <sup>b</sup>	19.2 <sup>b</sup>	41.8	21.6 <sup>b</sup>	75.5	19.5 <sup>b</sup>	99.3
Yield (mol%)							
Benzene	23.49	17.39	39.86	19.70	74.75	17.90	98.62
Cyclohexanol	1.06	1.12	1.08	1.01	0.36	0.85	0.36
Cyclohexene	0.39	0.41	0.47	0.50	0.19	0.39	0.17
Cyclohexane	0.25	0.28	0.38	0.38	0.17	0.36	0.15
Cyclohexanone	< 0.01	< 0.01	< 0.01	< 0.02	< 0.02	< 0.01	< 0.01
Benzenediols	< 0.01	< 0.01	< 0.01	< 0.01	< 0.01	< 0.01	< 0.01
Selectivity (%)							
Benzene	93.21	90.56	95.37	91.21	99.01	91.78	99.32
Cyclohexanol	4.21	5.81	2.58	4.67	0.48	4.34	0.36
Cyclohexene	1.55	2.12	1.12	2.32	0.25	1.98	0.17
Cyclohexane	0.99	1.48	0.90	1.77	0.23	1.87	0.15
Cyclohexanone	< 0.03	< 0.02	< 0.02	< 0.02	< 0.02	< 0.01	< 0.01
Benzenediols	< 0.01	< 0.01	< 0.01	< 0.01	< 0.01	< 0.01	< 0.01

<sup>a</sup> Reaction conditions: 1 atm, 230 mg catalyst, 5 mL/min H<sub>2</sub> flow, WHSV = 5.09 h<sup>-1</sup>

<sup>b</sup> Low HDO conversion experiment

### 6.4.3 Effect of reaction conditions

#### 6.4.3.1 Effect of temperature

Product distributions from Ag/TiO<sub>2</sub> catalyst at 454, 495 and 553 K, 1 atm, 5.09 h<sup>-1</sup> WHSV and 100 mL/min 5% H<sub>2</sub>/N<sub>2</sub> flow were measured (Table 6.4). By increasing the reaction temperature from 454 K to 553 K, phenol conversion was increased from 25.2 mol% to 75.5 mol%. The higher HDO activity of Ag/TiO<sub>2</sub> was made possible through the higher energy input at higher reaction temperature to overcome the activation energy of phenol HDO. At higher temperature, benzene selectivity (DDO) was increased while cyclohexane selectivity (HYD) was decreased. The cleavage of C<sub>AR</sub>(sp<sup>2</sup>)—OH and C<sub>cyclic</sub>(sp<sup>3</sup>)—OH bonds in the respective DDO and HYD pathways had bond energies of 468 and 385 kJ/mol which would be enhanced at higher temperatures (Furimsky, 2000; Nie et al., 2014). However, the dominance of DDO pathway at higher temperature was

seen due to the thermodynamic limitations of aromatic ring hydrogenation and H<sub>2</sub> adsorption at higher temperatures (Derrouiche & Bianchi, 2004; Nimmanwudipong et al., 2011a). Since H<sub>2</sub> adsorption decreases with temperature increase and HYD pathway is dependent on coverage of adsorbed hydrogen on catalyst surface (Gutierrez et al., 2009), DDO pathway would be favored due to its lower H<sub>2</sub> consumption. Similar trend was also observed when temperature for phenol HDO over Ag/TiO<sub>2</sub> was increased with a different set of reaction conditions (Figure 6.5 and 6.6).

#### 6.4.3.2 Effect of H<sub>2</sub> flow rate

Effect of H<sub>2</sub> flow rate on product selectivity and phenol conversion is shown in Figure 6.5A and 6.5B respectively. By increasing H<sub>2</sub> flow rate from 1 mL/min to 10 mL/min at 454 K, benzene selectivity decreased from 96.1 mol% to 85 mol% and cyclohexane selectivity increased from 0.3 mol% to 3.7 mol%, as more H<sub>2</sub> is readily available for the HYD pathway which requires higher H<sub>2</sub> consumption for phenyl ring hydrogenation. At 454 K, an increase in H<sub>2</sub> flow rate from 1 mL/min to 5 mL/min resulted in an increase in phenol conversion from 5.6% to 23.6%. A further increase in H<sub>2</sub> flow rate resulted in a marginal increase of phenol conversion to 24.7% at 10 mL/min as seen from the plateau region of the curve. Similar trends were also observed at different HDO reaction temperatures. This can be explained on the basis that C—OH bond hydrogenolysis of phenol requires H<sub>2</sub> and thus the initial increase in H<sub>2</sub> concentration would enable more phenol to be hydrodeoxygenated. Hydrodeoxygenation of phenol has a minimum phenol to H<sub>2</sub> stoichiometric ratio of 1:1 (Kay Lup et al., 2017a). Thus, the minimum H<sub>2</sub> flow rate required for an optimum phenol HDO with average phenol flow rate of 3.457 μmol/s would be 3.457 μmol/s which is also equivalent to 4.98 mL/min of H<sub>2</sub> flow. Any further increase in H<sub>2</sub> flow

would increase cyclohexane to benzene selectivity ratio while having a marginal increase in phenol conversion as phenol remained as the limiting reactant.

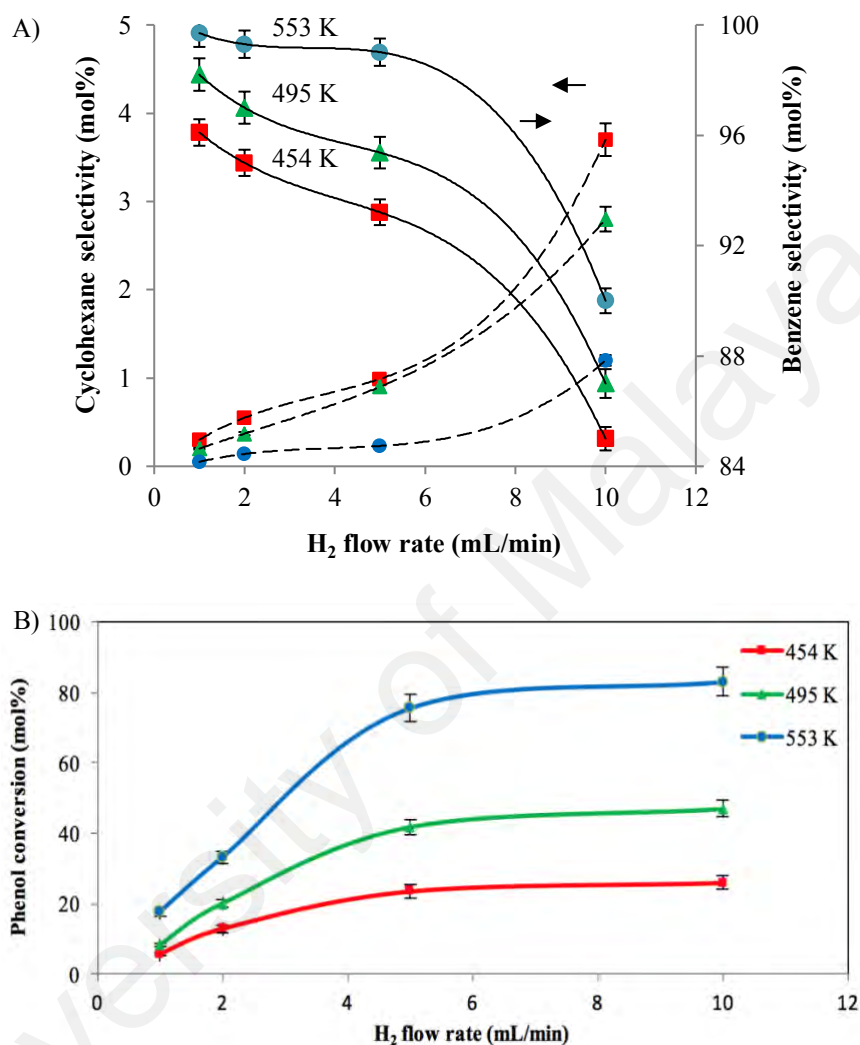


**Figure 6.5: Effect of H<sub>2</sub> flow rate on A) cyclohexane and benzene selectivity, B) phenol conversion at 454, 495 and 553 K. HDO conditions: 1 atm, 230 mg catalyst, 5.09 h<sup>-1</sup> WHSV**

### 6.4.3.3 Effect of WHSV

Effect of WHSV on phenol conversion is shown in Figure 6.6. In this study, WHSV is the ratio of phenol mass flow rate with mass of Ag/TiO<sub>2</sub> catalyst bed. The WHSV values were decreased by increasing the mass of catalyst used while maintaining phenol mass flow rate. For instance, with a fixed phenol mass flow rate of 0.325 mg/s (3.457

$\mu\text{mol/s}$ ), WHSVs of 23.4, 5.1 and  $3.3 \text{ h}^{-1}$  would be obtained with the use of 50, 230 and 350 mg catalyst weights. By decreasing WHSV from  $23.4 \text{ h}^{-1}$  to  $3.3 \text{ h}^{-1}$ , phenol conversion was increased from 18 mol% to 28.4 mol% at 454 K. The increase in phenol conversion with the decrease in WHSV was also observed with other reaction temperatures. This is because a lower WHSV enabled a longer contact time of phenol with active sites for HDO reaction (Fogler, 2006; Wang et al., 2015a). Average contact time can be determined as follow:

$$\text{Contact time (s)} = \frac{\text{Quantity of active sites } (\mu\text{mol/g}) \times \text{Catalyst weight (g)}}{\text{Average reactant flowrate } (\mu\text{mol/s})} \quad (6.41)$$

Based on  $\text{H}_2$  chemisorption analysis,  $\text{Ag/TiO}_2$  catalyst has a 0.0861 mmol/g of Ag active sites. With WHSVs of 23.4, 5.1 and  $3.3 \text{ h}^{-1}$ , the contact times were 1.25, 5.73 and 8.72 s in which the increase of contact time by 700% has resulted in the increase of phenol conversion by 158, 192 and 217% for 454, 495 and 530 K respectively. Similarly, the observation on the increase of phenol conversion with catalyst weight could also be understood that the total amount of available active sites for phenol HDO was higher.

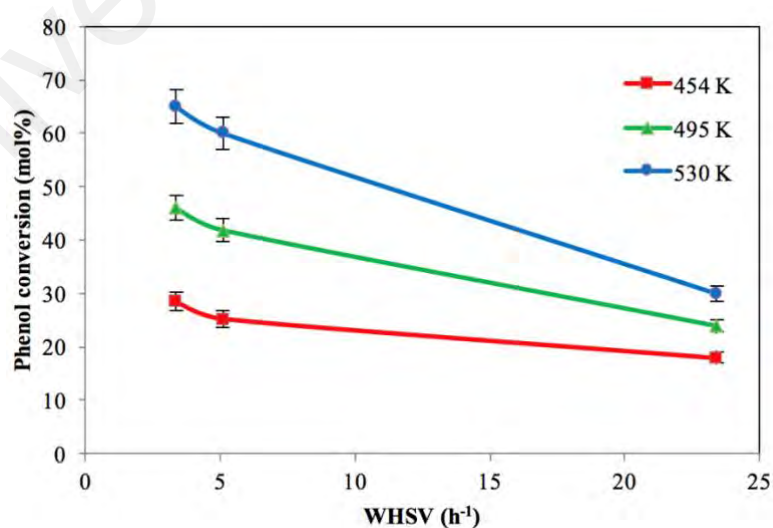


**Figure 6.6: Effect of WHSV on phenol conversion at 454, 495 and 530 K. HDO conditions: 1 atm, 5 mL/min  $\text{H}_2$  flow.**

#### 6.4.4 Mechanisms and kinetics

The partial pressures of reactants and products with respect to their measured reaction rates were analyzed using non-linear regression analysis by the POLYMATH 6.10 program to determine the contribution of each individual reaction to the overall mechanism. Langmuir-Hinshelwood model was proposed as the formalism to describe the reaction system kinetics for the overall reaction scheme (Figure 6.3). This model is subjected to several assumptions:

1. Sorption reactions are in quasi-equilibrium
2. Catalyst sites are identical, independent and evenly distributed.
3. Number of catalyst sites is constant under all reaction conditions.
4. Surface reactions are irreversible and rate determining steps.

and the reaction rate equations in this model can be expressed as:

$$r_i = \frac{k_i (K_H p_{H_2})^{n/2} K_X p_X}{(1 + \sqrt{K_H p_{H_2}})^n (1 + \sum_{i=1}^5 K_X p_X)} \quad (6.42)$$

where  $r_i$  is rate of  $i$ -th reaction based on Figure 6.3,  $k_i$  is its respective rate constant,  $p$  is partial pressure,  $K$  is adsorption coefficient,  $n$  is the number of moles of hydrogen atom used in  $i$ -th reaction step and index  $X$  indicates the reactant of  $i$ -th reaction step. The  $n$  values for reaction step 1, 2, 3, 4 and 5 are 2, 6, 0, 2, and 6 respectively.

To ensure the surface reactions are rate limiting steps, effect of mass transfer limitation was investigated based on Weisz-Prater criterion value,  $C_{W-P}$ . The  $C_{W-P}$  value was determined based on the following equations (Appendix A):

$$C_{W-P} = \frac{(-r_{HDO})_{exp} R_{cat}^2}{C_s D_e} \ll 0.3 \quad (6.43)$$

$$D_e = \frac{(D_K)_{phenol} \phi_p \sigma_c}{\tilde{\tau}} \quad (6.44)$$

$$(D_K)_{phenol} = \frac{d}{3} \sqrt{\frac{8RT}{\pi M_A}} \quad (6.45)$$

where  $(-r_{HDO})_{exp}$  is overall experimental HDO reaction rate,  $R_{cat}$  is catalyst particle radius (56.5 nm for Ag/TiO<sub>2</sub> sample),  $C_s$  is surface concentration of reactant,  $D_e$  is effective diffusivity,  $(D_K)_{phenol}$  is Knudsen diffusivity of phenol,  $\phi_p$  is porosity (0.4),  $\sigma_c$  is constriction factor (0.8),  $\tilde{\tau}$  is tortuosity (3),  $d$  is pore diameter (9.53 nm),  $R$  is ideal gas constant,  $T$  is reaction temperature,  $M_A$  is molecular mass of phenol (94 g/mol) (Fogler, 2006). To find the largest  $C_{W-P}$  value in this kinetic study, internal diffusion of the heaviest reactant, i.e. phenol was selected for this criterion at the reference temperature (454 K). The  $C_{W-P}$  value was calculated to be  $9.64 \times 10^{-16}$  which is considerably less than 0.3 and the kinetics are not limited by mass transfers.

The proposed model (Equation 6.42) has several physical implications. Firstly, the reaction rates are dependent on the stoichiometric ratio of hydrogen atoms required in each reaction step that is determined by the  $n$  value. This model also indicates that phenol HDO over Ag/TiO<sub>2</sub> involves the catalytic role of two distinct active sites for dissociative hydrogen adsorption and adsorption of reactants. The Ag metal site functioned as Lewis acid site for hydrogen adsorption and activation while the metal-support interface or support site functioned as Brønsted acid site for reactant adsorption and activation (He & Wang, 2012; Moberg et al., 2010). When hydrogen activation sites are saturated, activated hydrogen species undergo spillover to Brønsted acid sites for the phenyl ring hydrogenation or hydrogenolysis of C<sub>AR</sub>—O bond in reaction intermediates. This proposed reaction mechanism is also in corroboration with the findings of numerous phenolic HDO studies involving other supported transition metal catalysts (Foster et al., 2012; Hong et al., 2014a; Moberg et al., 2010; Nelson et al., 2015; Nimmanwudipong et al., 2011a; Olcese et al., 2012).

Optimum values of kinetic parameters as estimated via regression analysis for phenol HDO network on Ag/TiO<sub>2</sub> catalyst are shown in Table 6.5 and 6.6. The reaction rate

and adsorption equilibrium constants were respectively parameterized by Arrhenius and Van't Hoff equations.

$$k_i = (k_i)_0 e^{(-E_i/R)(1/T-1/T_0)} \quad (6.46)$$

$$K_i = (K_i)_0 e^{(-\Delta H_i/R)(1/T-1/T_0)} \quad (6.47)$$

where  $k_i$  and  $K_i$  are reaction rate and adsorption equilibrium constants at an absolute temperature,  $T$ ,  $(k_i)_0$  and  $(K_i)_0$  are reaction rate and adsorption equilibrium constants at reference temperature,  $T_0$  (454 K),  $E_i$  is activation energy and  $\Delta H_i$  is adsorption enthalpy. When the reaction rates of step 1—5 were compared, it can be seen that phenol hydrodeoxygenation over Ag/TiO<sub>2</sub> has reaction rates with the following order:  $r_1$  (phenol hydrogenolysis) <  $r_2$  (phenol hydrogenation) <  $r_5$  (benzene hydrogenation) <  $r_3$  (cyclohexanol dehydration) <  $r_4$  (cyclohexene hydrogenation). Both phenol hydrogenolysis and hydrogenation steps are the respective rate-limiting steps for DDO and HYD pathways of phenol hydrodeoxygenation over Ag/TiO<sub>2</sub> as their reaction rates were 10<sup>3</sup>—10<sup>6</sup> times slower as compared with other reaction steps. Activation energy of phenol hydrogenolysis was lower than phenol hydrogenation in this case which can be attributed to the preferential activation of C—O bond by oxophilic TiO<sub>2</sub>.

**Table 6.5: Kinetic data for gas-phase phenol hydrodeoxygenation network on Ag/TiO<sub>2</sub> catalyst with their 95% confidence intervals. HDO conditions: 454 K, 1 atm, WHSV = 5.1 h<sup>-1</sup>, H<sub>2</sub>/phenol molar ratio = 1**

Reaction steps	$(k_i)_0$ (mol/dm <sup>3</sup> .s)	$E_a$ (kJ/mol)	$(\Delta S_i^\ddagger)_0$ (J/mol.K)	$(r_i)_0$ (mol/dm <sup>3</sup> .s)
Step 1: Phenol hydrogenolysis	$2.39 \times 10^{-6} \pm 2.4 \times 10^{-9}$	$46.4 \pm 1.9$	$-270.4 \pm 1.2$	$2.03 \times 10^{-10}$
Step 2: Phenol hydrogenation	$1.82 \times 10^{-1} \pm 2.2 \times 10^{-4}$	$66.4 \pm 2.8$	$-133.0 \pm 0.7$	$4.54 \times 10^{-7}$
Step 3: Cyclohexanol dehydration	$6.95 \times 10^{-4} \pm 7.1 \times 10^{-7}$	$50.1 \pm 2.1$	$-215.2 \pm 3.8$	$3.85 \times 10^{-4}$
Step 4: Cyclohexene hydrogenation	$1.13 \times 10^{-2} \pm 7.5 \times 10^{-6}$	$18.2 \pm 0.8$	$-262.3 \pm 5.7$	$5.34 \times 10^{-4}$
Step 5: Benzene hydrogenation	$1.58 \times 10^{-1} \pm 1.6 \times 10^{-4}$	$45.2 \pm 1.9$	$-180.8 \pm 1.4$	$1.31 \times 10^{-4}$

**Table 6.6: Adsorption equilibrium parameters for reactants in phenol hydrodeoxygenation network on Ag/TiO<sub>2</sub> catalyst and their 95% confidence intervals at 454 K**

X	1 (Phenol)	2 (Benzene)	3 (Cyclohexanol)	4 (Cyclohexene)	5 (Cyclohexane)	H (Hydrogen)
(K <sub>X</sub> ) <sub>0</sub> (kPa <sup>-1</sup> )	1.38 ± 0.01	1.94 × 10 <sup>3</sup> ± 3.8 × 10 <sup>2</sup>	1.45 × 10 <sup>5</sup> ± 3.1 × 10 <sup>3</sup>	1.96 × 10 <sup>5</sup> ± 1.1 × 10 <sup>3</sup>	6.79 × 10 <sup>3</sup> ± 1.1 × 10 <sup>3</sup>	0.11 ± 0.002
ΔH <sub>x</sub> (kJ/mol)	-3.9 ± 0.2	-8.7 ± 0.4	-25.2 ± 0.4	-51.5 ± 1.5	-32.5 ± 3.3	-1.6 ± 0.3

The entropy changes of activation for the reaction steps, ΔS<sub>i</sub><sup>‡</sup>, were also determined based on the rate equations derived using transition state theory (TST) (Equation 6.48). The TST-derived rate equation for bimolecular surface reaction, i.e. A · S + B · S ⇌ [S · A ... B · S]<sup>‡</sup> → C · S + D · S, can be expressed in terms of partition function (microscopic formulation) or thermodynamic function (macroscopic formulation):

$$r_i = \frac{k_B T C_T^2}{h} \left( \frac{q_{[S \cdot A \dots B \cdot S]^\ddagger}}{q_{A \cdot S} q_{B \cdot S}} \right) e^{-E_a/RT} \theta_{A \cdot S} \theta_{B \cdot S} = \frac{k_B T C_T^2 e^2}{h} e^{\Delta S_i^\ddagger/R} e^{-E_a/RT} \theta_{A \cdot S} \theta_{B \cdot S} \quad (6.48)$$

where  $r_i$  is rate of  $i$ -th reaction,  $k_B$  is Boltzmann constant,  $h$  is Planck constant,  $T$  is absolute temperature,  $C_T$  is concentration of total surface sites ( $S$ ),  $q$  is molar partition function of reaction species,  $A$  and  $B$  are reactants,  $C$  and  $D$  products, ΔS<sub>i</sub><sup>‡</sup> is entropy change of activation for  $i$ -th reaction and  $\theta$  is fractional coverage of adsorbed reactant.

All entropy changes of activation in this kinetic model were noted to be negative. A clear distinction to be noted here is that entropy change of activation is neither equivalent nor interchangeable with entropy change of reaction as the former is on the entropy change from reactant to activated complex whereas the latter is on the entropy change from reactant to product. Thus, entropy change of activation provides only the thermodynamic state of activated complex instead of product. The state of activated complex involved in each reaction step gives further insight on the bonding configuration of reaction intermediates in each reaction step. For in this case, negative



entropy changes of activation indicated that the reactants formed activated complexes which had more orderly bonding configurations prior to the hydrogenolysis, hydrogenation and dehydration steps. The overall quality of the fit of kinetic model to HDO experimental data can be examined from the parity plots in Figure 6.7. An acceptable agreement between experimental and calculated reaction rates was obtained with deviations not more than 10%. In general, the proposed reaction model is able to satisfactorily predict the observed phenol HDO rates within the range of reaction conditions in this study.

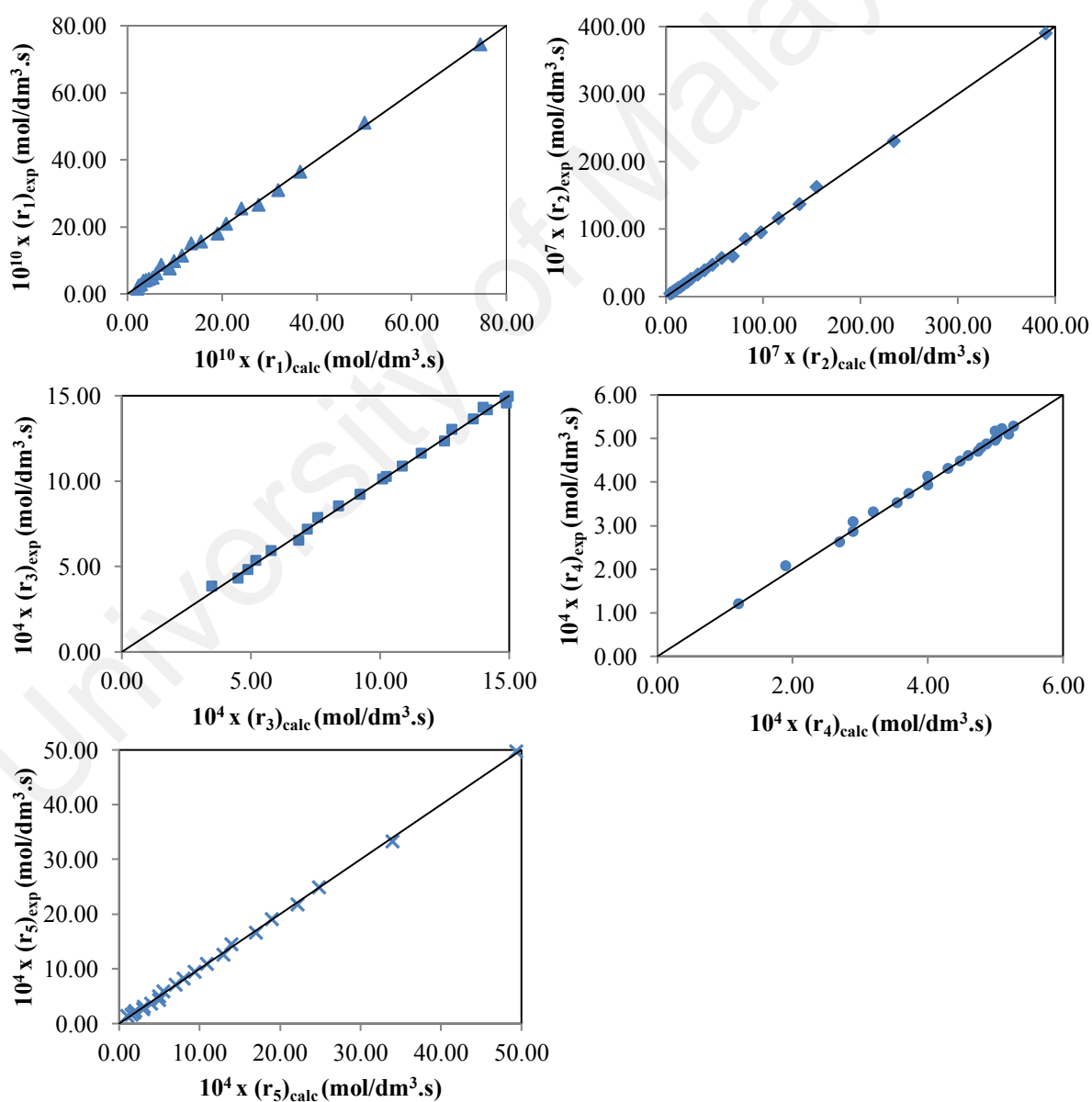


**Figure 6.7: Parity plots of experimental and calculated reaction rates of Step 1, 2, 3, 4 and 5.**

## 6.4.5 Catalyst recycling test

### 6.4.5.1 Catalyst stability

It has been observed that after each HDO run at 553 K for 1 h, the spent Ag/TiO<sub>2</sub> catalyst turned slightly black in color. When the spent catalyst was calcined in air and activated again by H<sub>2</sub> at 400 °C for its next recycling run, it regained its initial gray color. This observation is attributed to the surface oxidation of Ag metallic species and the carbon deposition on catalyst during reaction. The air calcination and H<sub>2</sub> activation of spent catalyst were monitored using TGA. Based on the gravimetric parameters in Table 6.7, it can be noted that the spent catalyst contained a small consistent amount of oxidized Ag and cokes produced in every run which are accountable for the change in catalyst appearance. With air calcination and H<sub>2</sub> activation at 400 °C, the catalyst was able to be regenerated close to its initial state with a trace amount of coke residuals (0.03 mg/g<sub>cat</sub>).

**Table 6.7: Total coke and oxidized silver contents of spent catalyst as obtained from TGA. HDO conditions of each 1 h run: 553 K, 1 atm, W<sub>cat</sub> = 2.0 g, WHSV = 0.59 h<sup>-1</sup>, 200 mL/min 5% H<sub>2</sub>/N<sub>2</sub> gas flow**

Gravimetric parameters	Number of experimental run			
	1 <sup>st</sup>	2 <sup>nd</sup>	3 <sup>rd</sup>	4 <sup>th</sup>
Weight gain after <i>n</i> <sup>th</sup> reaction (mg)	13.77	13.33	13.49	14.06
Oxidized silver amount after <i>n</i> <sup>th</sup> reaction (mg/g <sub>cat</sub> )	3.66	3.72	3.55	3.69
Coke amount after <i>n</i> <sup>th</sup> reaction (mg/g <sub>cat</sub> )	3.18	2.90	3.15	3.29
Coke amount after calcination (mg/g <sub>cat</sub> )	0.033	0.030	0.033	0.034
Coke removal efficiency (%)	98.96	98.97	98.95	98.97

Several important physicochemical properties of spent Ag/TiO<sub>2</sub> catalyst on its catalytic stability during HDO were summarized in Table 6.8. After 4 h of HDO runs (4 experimental runs), pore volume and size of spent Ag/TiO<sub>2</sub> were marginally decreased due to the formation of trace coke residuals within catalyst pores. BET surface area and

particle sizes of Ag and TiO<sub>2</sub> spent catalyst were also reported to be almost similar with that of the fresh catalyst, indicating minimal sintering effect. No significant agglomeration of Ag and TiO<sub>2</sub> particles were observed as shown in TEM image (Figure 6.8). Sintering was minimized in this study as the reaction temperature, i.e. 553 K was well below Hüttig temperature of TiO<sub>2</sub> (825.9 K). This is because at temperature above Hüttig temperature of a particular material, the atoms exhibit significant mobility which leads to atomic migration and agglomeration (Kay Lup et al., 2017b; Moulijn et al., 2001). ICP-OES analysis showed that metal leaching from catalyst was negligible after four experimental HDO runs. Comparison between XRD patterns of fresh and spent Ag/TiO<sub>2</sub> (Figure 6.9) showed negligible structural and crystallographic modification of Ag and TiO<sub>2</sub>. Oxidized Ag metal phase in spent catalyst which was reported in TGA was not detected by XRD owing to its trace amount and well dispersion.

**Table 6.8: Physicochemical properties of spent Ag/TiO<sub>2</sub> catalyst after 4 h of reaction**

Properties	Value
S <sub>BET</sub> (m <sup>2</sup> /g)	8.61
Pore volume (cm <sup>3</sup> /g)	0.0288
Pore size (nm)	9.2
Ag particle size (nm)	8.37
TiO <sub>2</sub> particle size (nm)	114.2
Ag loading (wt%)	9.11

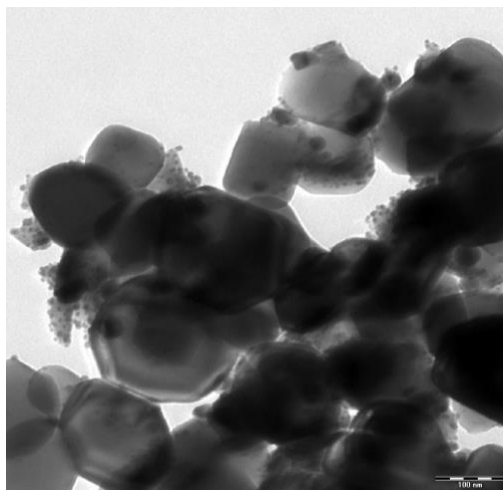


**Figure 6.8: TEM images of spent Ag/TiO<sub>2</sub> catalyst after 4 h of reaction**

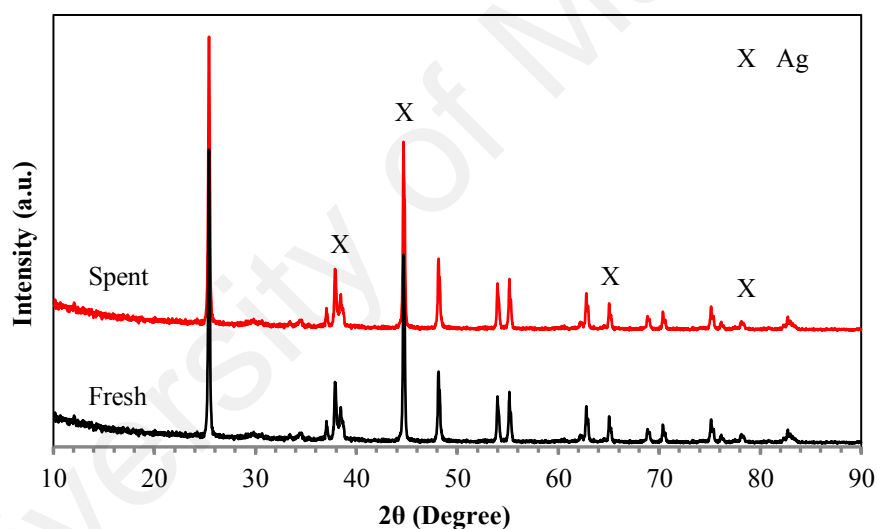


**Figure 6.9: XRD diffractograms of fresh and spent Ag/TiO<sub>2</sub> catalysts**

#### 6.4.5.2 Catalyst activity

The results of Ag/TiO<sub>2</sub> catalyst recycling shown in Table 6.9 indicated that its catalytic activity was slightly decreased after four experimental runs. Catalytic regeneration via air calcination and H<sub>2</sub> activation was done before each recycling run to stabilize its catalytic performance. Nevertheless, the cumulative deposition of coke residuals on catalyst in trace amount resulted in the slight decrease of its catalytic

activity. This suggests that the coke formation on catalyst surfaces was the origin of its minuscule deactivation (Li et al., 2015c; Srifa et al., 2015). In these catalyst recycling test, 4 h of recycling HDO runs were done in order to understand the initial deactivation and catalyst stability during initial HDO runs. Further recycling studies at about 100 h are recommended in order to test its catalyst lifespan at industrial application and to derive accurate deactivation model.

**Table 6.9: Product analysis of each HDO run. HDO conditions of each 1 h run: 553 K, 1 atm,  $W_{\text{cat}} = 2.0$  g,  $WHSV = 0.59$  h<sup>-1</sup>, 200 mL/min 5% H<sub>2</sub>/N<sub>2</sub> gas flow**

Run	Phenol conversion (mol%)	Yield of deoxygenated products (mol%) <sup>a</sup>	Yield of oxygenated products (mol%) <sup>b</sup>
1	75.5	75.32	0.18
2	75.2	75.02	0.18
3	74.8	74.61	0.19
4	74.2	74.03	0.17

<sup>a</sup> Yield of benzene, cyclohexane and cyclohexene

<sup>b</sup> Yield of cyclohexanol, cyclohexanone, benzenediols

## 6.5 Conclusion

Silver catalysts with titania support was found to have mediocre phenol conversion for its hydrodeoxygenation due to the high C—O bond breaking energy and low carbon and oxygen binding energies of Ag metal. However, phenol hydrogenolysis to benzene was made possible through the use of oxophilic TiO<sub>2</sub> support which enhanced the activation of oxygen end of C—O bond. At atmospheric pressure condition, phenol HDO was found to favor benzene formation via DDO pathway owing to its lower H<sub>2</sub> consumption. The proposed kinetic model for the phenol HDO network over Ag/TiO<sub>2</sub> confirmed the occurrence of phenol hydrogenolysis and hydrogenation; cyclohexanol dehydration and hydrogenation of benzene and cyclohexene. The reaction rates increase with the following order:  $r_1$  (phenol hydrogenolysis) <  $r_2$  (phenol hydrogenation) <  $r_5$  (benzene hydrogenation) <  $r_3$  (cyclohexanol dehydration) <  $r_4$  (cyclohexene

hydrogenation). Both phenol hydrogenolysis and hydrogenation steps are the respective rate-limiting steps for DDO and HYD pathways of phenol hydrodeoxygenation over Ag/TiO<sub>2</sub>. Successive hydrodeoxygenation runs (4 h) showed no significant degradation in catalytic and physicochemical properties of Ag/TiO<sub>2</sub> catalyst. The accumulation of oxidized Ag metal species and coke deposits on Ag/TiO<sub>2</sub> catalyst after each HDO run can be removed via H<sub>2</sub>-activation and calcination in air at 553 K with at least 98.9% removal efficiency.

University of Malaya

## CHAPTER 7: CONCLUSIONS AND RECOMMENDATIONS

### 7.1 Conclusions

Hydrodeoxygenation is an important deoxygenation step required to upgrade bio-oil into liquid fuel of lower oxygen content and to valorize biomass precursors into high-added value chemicals. By considering the hydrodeoxygenation mechanism occurring at the catalyst surface, properties of supported metal catalyst such as high H<sub>2</sub> sticking coefficient, optimal metal-oxygen bond strength and suitable acid strength from support play a significant role in enabling facile scission of C—O bonds and activation of H<sub>2</sub> and O-containing compounds. This overall work was done to investigate the potential of titania supported silver catalyst as HDO catalyst; the interaction of Ag/TiO<sub>2</sub> catalyst with H<sub>2</sub> and the kinetic modeling of phenol HDO over Ag/TiO<sub>2</sub> catalyst in TGA-FTIR based microreactor. Based on the findings of these work, there are several important thematic conclusions to be noted here to convey the overall significance of this work.

The results from the first objective showed that Ag/TiO<sub>2</sub> catalyst had the fundamental properties: oxophilicity, acidity, hydrogen sticking probability and reducibility for phenol HDO catalysis. The metal-support interaction of Ag/TiO<sub>2</sub> enabled hydrogen spillover phenomenon and synergistic interaction of metal-acid sites. The observed properties within Ag/TiO<sub>2</sub> catalyst would infer its catalytic ability for the adsorption and activation of phenol and hydrogen during HDO. Among the titania supported silver catalysts of different silver loadings in this study, Ag/TiO<sub>2</sub>-10 (9.13 wt% Ag) catalyst was the most optimal choice due to higher hydrogen spillover ratio. At silver loadings above 5 wt%, prominent silver deposition on surface also promoted formation of more Lewis acid sites which are required for HDO.

Results from the second objective showed that the Ag/TiO<sub>2</sub> catalyst interacted with hydrogen through the reduction of Ag<sub>2</sub>O into Ag metal. This reduction phenomenon

occurred via a single step reduction of  $\text{Ag}_2\text{O}$  to Ag by  $\text{H}_2$  in Ag/ $\text{TiO}_2$  catalyst to achieve average final oxidation state of 0 to +0.18. The high reducibility of Ag/ $\text{TiO}_2$  catalyst enabled facile formation of oxygen vacant sites within the catalyst, thus being useful for the  $\text{H}_2$ -aided oxygen removal mechanism from phenol. The reduction mechanism of Ag/ $\text{TiO}_2$  catalyst was proposed to be unimolecular decay model based on kinetic fittings. This model would indicate that the reduction has the characteristics of uniform internal reduction and random nucleation besides being rate-limited by the nucleation of Ag metal.

The study on sample encapsulation in TGA also verified the possibility of delaying volatilization of liquid sample at higher range of temperature through the physical confinement of liquid sample during heating process. The proposed technique of encapsulating samples, i.e. phenol in metal capsules, was able to lengthen the release of phenol vapor through the catalyst bed over an extended range of temperature. This delayed volatiles release phenomenon was enhanced by using metal capsule with higher material hardness and smaller surface area for sample evaporation. By using this technique, results has shown better reaction performance for catalytic gas-solid reaction due to the passing of vapor through the catalyst bed at higher temperature. Thus, this finding has enabled the analysis of kinetic study in TGA-FTIR based microreactor to be done over a larger range of reaction temperature and to achieve better catalyst activation.

The kinetic study of gas-phase phenol HDO over Ag/ $\text{TiO}_2$  catalyst showed the conversion of phenol into benzene as major product via direct deoxygenation pathway at atmospheric condition. The proposed kinetic model for the phenol HDO network over Ag/ $\text{TiO}_2$  confirmed the occurrence of phenol hydrogenolysis and hydrogenation; cyclohexanol dehydration and hydrogenation of benzene and cyclohexene. The



proposed kinetic model was in good agreement with the quantitative and the qualitative observations in this study. The reaction rates increase with the following order:  $r_1$  (phenol hydrogenolysis)  $< r_2$  (phenol hydrogenation)  $< r_5$  (benzene hydrogenation)  $< r_3$  (cyclohexanol dehydration)  $< r_4$  (cyclohexene hydrogenation). Both phenol hydrogenolysis and hydrogenation steps are the respective rate-limiting steps for DDO and HYD pathways of phenol hydrodeoxygenation over Ag/TiO<sub>2</sub>. With the use of oxophilic TiO<sub>2</sub> support, phenol hydrogenolysis to benzene was made possible through the enhanced activation of oxygen end at phenolic C—O bond. Ag/TiO<sub>2</sub> catalyst remained catalytically stable after 4 h of successive hydrodeoxygenation runs. After each HDO run, accumulation of oxidized Ag metal species and coke deposits on Ag/TiO<sub>2</sub> were observed and can be removed via H<sub>2</sub>-activation and calcination in air at 553 K with at least 98.9% removal efficiency. Nevertheless, testing of Ag/TiO<sub>2</sub> catalyst performance at extended duration (~100 h) may be required in future studies in order to assess its catalyst lifespan at industrial scale.

With these model compound studies on phenol HDO over Ag/TiO<sub>2</sub> catalyst, these findings can be further used in the model compound studies of other phenolics present in bio-oil. By the extrapolation of these findings and the kinetic models, the phenolics would be predicted to have undergone similar reaction pathways such as DDO and HYD over Ag/TiO<sub>2</sub> catalyst to form deoxygenated products owing to the presence of identical C—OH functional group within these phenolics. However, the presence of other functional groups within these phenolics may pose various reaction alterations physically due to steric hindrance by HDO-inert functional groups or chemically through participation of these HDO-active functional groups in causing secondary HDO reactions. These insights are required to be verified in future HDO model compound studies of other phenolics. This understanding of phenolics HDO mechanism would furnish important kinetics and mechanistic information to account for the phenolic

contribution during the total deoxygenation within bio-oil. The total deoxygenation process of bio-oil involves the deoxygenation of various O-containing functional groups from various O-containing compounds via different deoxygenation pathways. Therefore, the interaction of these parallel deoxygenation reactions with HDO remains an important matter to be addressed in future works on the understanding of bio-oil deoxygenation kinetics and mechanism.

## **7.2 Recommendations for future works**

This work has reported of the successful use of titania supported silver catalyst for a model compound study on the hydrodeoxygenation of phenol into benzene via a TGA-FTIR based microreactor. Nevertheless, there are still several recommendations that can be considered for future studies. Based on these recommendations, further findings on enhancement of process design for bio-oil upgrading and surface chemistry of HDO process can be obtained.

- i. Studies on the catalyst preparation process and the catalyst supports in affecting the HDO activity of silver based catalysts.
- ii. Studies on application and optimization of sample encapsulation technique for catalytic solid-gas reaction involving gas-phase deoxygenation processes of other oxygen-containing model compounds or real bio-oil samples.
- iii. Utilizing computational modeling (Density functional theory), surface spectroscopic techniques and real time in-situ observation technique, i.e. femtosecond laser spectroscopy for further validation of the activated complexes during HDO.

- iv. Deactivation studies at longer HDO duration with order of 100 h in order to evaluate catalyst lifespan at industrial scale and to derive accurate deactivation models.

University of Malaya

## REFERENCES

- Abdul-Wahab, M. I. and Jackson, S. D. (2013). Hydrogenation of 3-nitroacetophenone over rhodium/silica catalysts: Effect of metal dispersion and catalyst support. *Applied Catalysis A: General*, 462-463: 121-128.
- Abnisa, F. and Wan Daud, W. M. A. (2014). A review on co-pyrolysis of biomass: An optional technique to obtain a high-grade pyrolysis oil. *Energy Conversion and Management*, 87: 71-85.
- Abnisa, F., Wan Daud, W. M. A., Arami-Niya, A., Ali, B. S. and Sahu, J. N. (2014). Recovery of liquid fuel from the aqueous phase of pyrolysis oil using catalytic conversion. *Energy & Fuels*, 28: 3074-3085.
- Abon, M., Bere, K. E., Tuel, A. and Delichere, P. (1995). Evolution of a VPO catalyst in *n*-butane oxidation reaction during the activation time. *Journal of Catalysis*, 156: 28-36.
- Alayat, A., McIlroy, D. N. and McDonald, A. G. (2018). Effect of synthesis and activation methods on the catalytic properties of silica nanospring (NS)-supported iron catalyst for Fischer-Tropsch synthesis. *Fuel Processing Technology*, 169: 132-141.
- Alharbi, K., Alharbi, W., Kozhevnikova, E. F. and Kozhevnikov, I. V. (2016). Deoxygenation of ethers and esters over bifunctional Pt-heteropoly acid catalyst in the gas phase. *ACS Catalysis*, 6: 2067-2075.
- Alharbi, K., Kozhevnikova, E. F. and Kozhevnikov, I. V. (2015). Hydrogenation of ketones over bifunctional Pt-heteropoly acid catalyst in gas phase. *Applied Catalysis A: General*, 504: 457-462.
- Alloncle, G., Gilon, N., Lienemann, C.-P. and Morin, S. (2009). A new method for quantitative analysis of metal content in heterogeneous catalysts: Laser ablation-ICP-AES. *Comptes Rendus Chimie*, 12: 637-646.
- Alotaibi, M. A., Kozhevnikova, E. F. and Kozhevnikov, I. V. (2012a). Deoxygenation of propionic acid on heteropoly acid and bifunctional metal-loaded heteropoly acid catalysts: Reaction pathways and turnover rates. *Applied Catalysis A: General*, 447-448: 32-40.

- Alotaibi, M. A., Kozhevnikova, E. F. and Kozhevnikov, I. V. (2012b). Hydrogenation of methyl isobutyl ketone over bifunctional Pt-zeolite catalyst. *Journal of Catalysis*, 293: 141-144.
- Amada, Y., Shinmi, Y., Koso, S., Kubota, T., Nakagawa, Y. and Tomishige, K. (2011). Reaction mechanism of the glycerol hydrogenolysis to 1,3-propanediol over Ir-ReO<sub>x</sub>/SiO<sub>2</sub> catalyst. *Applied Catalysis B: Environmental*, 105: 117-127.
- Ambursa, M. M., Ali, T. H., Voon, L. H., Sudarsanam, P., Bhargava, S. K. and Hamid, S. B. A. (2016). Hydrodeoxygenation of dibenzofuran to bicyclic hydrocarbons using bimetallic Cu-Ni catalysts supported on metal oxides. *Fuel*, 180: 767-776.
- Arun, N., Sharma, R. V. and Dalai, A. K. (2015). Green diesel synthesis by hydrodeoxygenation of bio-based feedstocks: Strategies for catalyst design and development. *Renewable and Sustainable Energy Reviews*, 48: 240-255.
- Asadieraghi, M., Wan Daud, W. M. A. and Abbas, H. F. (2014). Model compound approach to design process and select catalysts for in-situ bio-oil upgrading. *Renewable and Sustainable Energy Reviews*, 36: 286-303.
- Assary, R. S., Curtiss, L. A. and Dumesic, J. A. (2013). Exploring Meerwein-Ponndorf-Verley reduction chemistry for biomass catalysis using a first-principles approach. *ACS Catalysis*, 3: 2694-2704.
- Atkins, P. and Paula, J. D. (2010). *Physical chemistry* (9th ed.). Great Britain: Oxford University Press.
- Auneau, F., Noël, S., Aubert, G., Besson, M., Djakovitch, L. and Pinel, C. (2011). On the role of the atmosphere in the catalytic glycerol transformation over iridium-based catalysts. *Catalysis Communications*, 16: 144-149.
- Ausavasukhi, A., Huang, Y., To, A. T., Sooknoi, T. and Resasco, D. E. (2012). Hydrodeoxygenation of *m*-cresol over gallium-modified beta zeolite catalysts. *Journal of Catalysis*, 290: 90-100.
- Ausavasukhi, A., Sooknoi, T. and Resasco, D. E. (2009). Catalytic deoxygenation of benzaldehyde over gallium-modified ZSM-5 zeolite. *Journal of Catalysis*, 268: 68-78.
- Ayodele, O. B., Abbas, H. F. and Wan Daud, W. M. A. (2014). Catalytic upgrading of oleic acid into biofuel using Mo modified zeolite supported Ni oxalate catalyst

functionalized with fluoride ion. *Energy Conversion and Management*, 88: 1111-1119.

Badawi, M., Paul, J.-F., Payen, E., Romero, Y., Richard, F., Brunet, S., Popov, A., Kondratieva, E., Gilson, J.-P., Mariey, L., Travert, A. and Maugé, F. (2013). Hydrodeoxygenation of phenolic compounds by sulfided (Co)Mo/Al<sub>2</sub>O<sub>3</sub> catalysts, a combined experimental and theoretical study. *Oil & Gas Science and Technology*, 68: 829-840.

Baertsch, C. D., Komala, K. T., Chua, Y.-H. and Iglesia, E. (2002). Genesis of Brønsted acid sites during dehydration of 2-butanol on tungsten oxide catalysts. *Journal of Catalysis*, 205: 44-57.

Bayahia, H., Kozhevnikova, E. F. and Kozhevnikov, I. V. (2015). Ketonisation of carboxylic acids over Zn-Cr oxide in the gas phase. *Applied Catalysis B: Environmental*, 165: 253-259.

Bejblová, M., Zámotný, P., Červený, L. and Čejka, J. (2005). Hydrodeoxygenation of benzophenone on Pd catalysts. *Applied Catalysis A: General*, 296: 169-175.

Benson, S. W. and Golden, D. M. (1975). Methods for the estimation of rate parameters of elementary processes. In Eyring, H. (Ed.), *Physical chemical: An advanced treatise* (pp. 57-124). USA: Academic Press.

Berlin, E. and Kliman, P. G. (1974). Effect of dehydration on the specific heat of cheese whey. In Porter, R. S. & Johnson, J. F. (Eds.), *Analytical calorimetry* (pp. 497-504). New York: Plenum Press.

Bernas, H., Eränen, K., Simakova, I., Leino, A.-R., Kordás, K., Myllyoja, J., Mäki-Arvela, P., Salmi, T. and Murzin, D. Y. (2010). Deoxygenation of dodecanoic acid under inert atmosphere. *Fuel*, 89: 2033-2039.

Biscardi, J. A. and Iglesia, E. (1996). Structure and function of metal cations in light alkane reactions catalyzed by modified H-ZSM5. *Catalysis Today*, 31: 207-231.

Boda, L., Onyestyák, G., Solt, H., Lónyi, F., Valyon, J. and Thernesz, A. (2010). Catalytic hydroconversion of tricaprylin and caprylic acid as model reaction for biofuel production from triglycerides. *Applied Catalysis A: General*, 374: 158-169.

Bond, G. C. and Webb, G. (1962). Ruthenium and osmium as hydrogenation catalysts. *Platinum Metals Review*, 6: 12-19.

- Boronat, M., Corma, A. and Renz, M. (2006). Mechanism of the Meerwein-Ponndorf-Verley-Oppnenauer (MPVO) redox equilibrium on Sn- and Zr-Beta zeolite catalysts. *Journal of Physical Chemistry B*, 110: 21168-21174.
- Boudart, M. (1975). Heterogeneous catalysis. In Eyring, H. (Ed.), *Physical chemistry: An advanced treatise* (pp. 349-411). USA: Academic Press.
- Boullosa-Eiras, S., Lødeng, R., Bergem, H., Stöcker, M., Hannevold, L. and Blekkan, E. A. (2014). Catalytic hydrodeoxygenation (HDO) of phenol over supported molybdenum carbide, nitride, phosphide and oxide catalysts. *Catalysis Today*, 223: 44-53.
- Brenman, W. P. (1974). Application of differential scanning calorimetry for the study of phase transitions. In Porter, R. S. & Johnson, J. F. (Eds.), *Analytical Calorimetry* (pp. 103-117). New York: Springer.
- Brown, M. E. (2001). *Introduction to Thermal Analysis: Techniques and Applications* (2nd ed.). USA: Kluwer Academic Publishers.
- Bruycker, R. D., Anthonykutti, J. M., Linnekoski, J., Harlin, A., Lehtonen, J., Van Geem, K. M., Räsänen, J. and Marin, G. B. (2014). Assessing the potential of crude tall oil for the production of green-base chemicals: An experimental and kinetic modeling study. *Industrial & Engineering Chemistry Research*, 53: 18430-18442.
- Bu, Q., Lei, H., Zacher, A. H., Wang, L., Ren, S., Liang, J., Wei, Y., Liu, Y., Tang, J., Zhang, Q. and Ruan, R. (2012). A review of catalytic hydrodeoxygenation of lignin-derived phenols from biomass pyrolysis. *Bioresource Technology*, 124: 470-477.
- Buckles, G. J. and Hutchings, G. J. (1996). Aromatisation of propane over Ga/H-ZSM-5: comments on the activation of propane. *Catalysis Today*, 31: 233-246.
- Bunch, A. Y. and Ozkan, U. S. (2002). Investigation of the reaction network of benzofuran hydrodeoxygenation over sulfided and reduced Ni-Mo/Al<sub>2</sub>O<sub>3</sub> catalysts. *Journal of Catalysis*, 206: 177-187.
- Butt, J. B. (2000). *Reaction kinetics and reactor design* USA: Marcel Dekker.
- Butt, J. B. and Petersen, E. E. (1988). *Activation, deactivation and poisoning of catalysts* London: Academic Press.

- Bykova, M. V., Ermakov, D. Y., Kaichev, V. V., Bulavchenko, O. A., Saraev, A. A., Lebedev, M. Y. and Yakovlev, V. A. (2012). Ni-based sol-gel catalysts as promising systems for crude bio-oil upgrading: Guaiacol hydrodeoxygenation study. *Applied Catalysis B: Environmental*, 113-114: 296-307.
- Bykova, M. V., Ermakov, D. Y., Khromova, S. A., Smirnov, A. A., Lebedev, M. Y. and Yakovlev, V. A. (2014). Stabilized Ni-based catalysts for bio-oil hydrotreatment: Reactivity studies using guaiacol. *Catalysis Today*, 220-222: 21-31.
- Cárdenas-Lizana, F., Wang, X., Lamey, D., Li, M., Keane, M. A. and Kiwi-Minsker, L. (2014). An examination of catalyst deactivation in *p*-chloronitrobenzene hydrogenation over supported gold. *Chemical Engineering Journal*, 255: 695-704.
- Carnevillier, C., Epron, F. and Marecot, P. (2004). Controlled preparation and characterization of plurimetallic Pt-Sn and Pt-Ir-Sn/Al<sub>2</sub>O<sub>3</sub> reforming catalysts. *Applied Catalysis A: General*, 275: 25-33.
- Cecilia, J. A., Infantes-Molina, A., Rodríguez-Castellón, E., Jiménez-López, A. and Oyama, S. T. (2013). Oxygen-removal of dibenzofuran as a model compound in biomass derived bio-oil on nickel phosphide catalysts: Role of phosphorus. *Applied Catalysis B: Environmental*, 136-137: 140-149.
- Cengel, Y. A. and Boles, M. A. (2011). *Thermodynamics: An engineering approach* (7th ed.). London: McGraw-Hill Education.
- Chaudhari, R. V., Torres, A., Jin, X. and Subramaniam, B. (2013). Multiphase catalytic hydrogenolysis/hydrodeoxygenation processes for chemicals from renewable feedstocks: Kinetics, mechanism, and reaction engineering. *Industrial & Engineering Chemistry Research*, 52: 15226-15243.
- Chen, C., Chen, G., Yang, F., Wang, H., Han, J., Ge, Q. and Zhu, X. (2015a). Vapor phase hydrodeoxygenation and hydrogenation of *m*-cresol on silica supported Ni, Pd and Pt catalysts. *Chemical Engineering Science*, 135: 145-154.
- Chen, D., He, D., Lu, J., Zhong, L., Liu, F., Liu, J., Yu, J., Wan, G., He, S. and Luo, Y. (2017). Investigation of the role of surface lattice oxygen and bulk lattice oxygen migration of cerium-based oxygen carriers: XPS and designed H<sub>2</sub>-TPR characterization. *Applied Catalysis B: Environmental*, 218: 249-259.



- Chen, H., Tan, J., Zhu, Y. and Li, Y. (2016a). An effective and stable Ni<sub>2</sub>P/TiO<sub>2</sub> catalyst for the hydrogenation of dimethyl oxalate to methyl glycolate. *Catalysis Communications*, 73: 46-49.
- Chen, J., Sun, L., Wang, R. and Zhang, J. (2009). Hydrodechlorination of chlorobenzene over Ni<sub>2</sub>P/SiO<sub>2</sub> catalysts: Influence of Ni<sub>2</sub>P loading. *Catalysis Letters*, 133: 346.
- Chen, K., Koso, S., Kubota, T., Nakagawa, Y. and Tomishige, K. (2010). Chemoselective hydrogenolysis of tetrahydropyran-2-methanol to 1,6-hexanediol over rhenium-modified carbon-supported rhodium catalysts. *ChemCatChem*, 2: 547-555.
- Chen, K., Mori, K., Watanabe, H., Nakagawa, Y. and Tomishige, K. (2012a). C-O bond hydrogenolysis of cyclic ethers with OH groups over rhenium-modified supported iridium catalysts. *Journal of Catalysis*, 294: 171-183.
- Chen, L., Li, Y., Zhang, X., Zhang, Q., Wang, T. and Ma, L. (2014). Mechanistic insights into the effects of support on the reaction pathway for aqueous-phase hydrogenation of carboxylic acid over the supported Ru catalysts. *Applied Catalysis A: General*, 478: 117-128.
- Chen, L., Zhu, Y., Zheng, H., Zhang, C. and Li, Y. (2012b). Aqueous-phase hydrodeoxygenation of propanoic acid over the Ru/ZrO<sub>2</sub> and Ru-Mo/ZrO<sub>2</sub> catalysts. *Applied Catalysis A: General*, 411-412: 95-104.
- Chen, L., Zhu, Y., Zheng, H., Zhang, C., Zhang, B. and Li, Y. (2011). Aqueous-phase hydrodeoxygenation of carboxylic acids to alcohols or alkanes over supported Ru catalysts. *Journal of Molecular Catalysis A: Chemical*, 351: 217-227.
- Chen, N., Gong, S., Shirai, H., Watanabe, T. and Qian, E. W. (2013). Effects of Si/Al ratio and Pt loading on Pt/SAPO-11 catalysts in hydroconversion of Jatropha oil. *Applied Catalysis A: General*, 466: 105-115.
- Chen, N., Ren, Y. and Qian, E. W. (2016b). Elucidation of the active phase in PtSn/SAPO-11 for hydrodeoxygenation of methyl palmitate. *Journal of Catalysis*, 334: 79-88.
- Chen, W., Bao, H., Wang, D., Wang, X., Li, Y. and Hu, Y. (2015b). Chemoselective hydrogenation of nitrobenzyl ethers to aminobenzyl ethers catalyzed by palladium-nickel bimetallic nanoparticles. *Tetrahedron*, 71: 9240-9244.

- Chen, Y., Choi, S. and Thompson, L. T. (2016c). Ethyl formate hydrogenolysis over Mo<sub>2</sub>C-based catalysts: Towards low temperature CO and CO<sub>2</sub> hydrogenation to methanol. *Catalysis Today*, 259: 285-291.
- Cheng, Y.-T. and Huber, G. W. (2011). Chemistry of furan conversion into aromatics and olefins over HZSM-5: A model biomass conversion reaction. *ACS Catalysis*, 1: 611-628.
- Chia, M., Pagán-Torres, Y. J., Hibbitts, D., Tan, Q., Pham, H. N., Datye, A. K., Neurock, M., Davis, R. J. and Dumesic, J. A. (2011). Selective hydrogenolysis of polyols and cyclic ethers over bifunctional surface sites on rhodium-rhenium catalysts. *Journal of the American Chemical Society*, 133: 12675-12689.
- Chickos, J. S., Hosseini, S. and Hesse, D. G. (1995). Determination of vaporization enthalpies of simple organic molecules by correlations of changes in gas chromatographic net retention times. *Thermochimica Acta*, 249: 41-62.
- Choudhary, T. V. and Phillips, C. B. (2011). Renewable fuels via catalytic hydrodeoxygenation. *Applied Catalysis A: General*, 397: 1-12.
- Chouhan, A. P. S. and Sarma, A. K. (2011). Modern heterogeneous catalysts for biodiesel production: A comprehensive review. *Renewable and Sustainable Energy Reviews*, 15: 4378-4399.
- Chu, Y., Yu, Z., Zheng, A., Fang, H., Zhang, H., Huang, S.-J., Liu, S.-B. and Deng, F. (2011). Acidic strengths of Brønsted and Lewis acid sites in solid acids scaled by <sup>31</sup>P NMR chemical shifts of adsorbed trimethylphosphine. *Journal of Physical Chemistry C*, 115: 7660-7667.
- Conner, W. C. and Falconer, J. L. (1995). Spillover in heterogeneous catalysis. *Chemical Reviews*, 95: 759-788.
- Cónsul, J. M. D., Thiele, D., Baibich, I. M. and Veses, R. C. (2004). Selective Reduction of NO<sub>x</sub> by Propylene Over Silver Catalyst Under Oxidative Conditions. *Journal of the Brazilian Chemical Society*, 15: 556-562.
- Corma, A., Domine, M. E., Nemeth, L. and Valencia, S. (2002). Al-free Sn-Beta zeolite as a catalyst for the selective reduction of carbonyl compounds (Meerwein-Ponndorf-Verley reaction). *Journal of the American Chemical Society*, 124: 3194-3195.

- Corma, A., Domine, M. E. and Valencia, S. (2003). Water-resistant solid Lewis acid catalysts: Meerwein-Ponndorf-Verley and Oppenauer reactions catalyzed by tin-beta zeolite. *Journal of Catalysis*, 215: 294-304.
- Corradini, S. A. d. S., Lenzi, G. G., Lenzi, M. K., Soares, C. M. F. and Santos, O. A. A. (2008). Characterization and hydrogenation of methyl oleate over Ru/TiO<sub>2</sub>, Ru-Sn/TiO<sub>2</sub> catalysts. *Journal of Non-Crystalline Solids*, 354: 4865-4870.
- Cortright, R. D. and Dumesic, J. A. (2002). Kinetics of heterogeneous catalytic reactions: Analysis of reaction schemes. In Gates, B. C. & Knözinger, H. (Eds.), *Advances in catalysis* (pp. 161-264). USA: Academic Press.
- Crevier, T. J. and Mayer, J. M. (1997). C-O bond homolysis in a tungsten alkoxide: The mechanism of alcohol deoxygenation by WCl<sub>2</sub>(PMe<sub>3</sub>)<sub>4</sub> and WH<sub>2</sub>Cl<sub>2</sub>(PMe<sub>3</sub>)<sub>4</sub>. *Journal of the American Chemical Society*, 119: 8485-8491.
- Currall, K. and Jackson, S. D. (2014). Hydrogenation of 4-nitroacetophenone over Rh/silica. *Applied Catalysis A: General*, 484: 59-63.
- Dai, W.-L., Cao, Y., Ren, L.-P., Yang, X.-L., Xu, J.-H., Li, H.-X., He, H.-Y. and Fan, K.-N. (2004). Ag-SiO<sub>2</sub>-Al<sub>2</sub>O<sub>3</sub> composite as highly active catalyst for the formation of formaldehyde from the partial oxidation of methanol. *Journal of Catalysis*, 228: 80-91.
- Danuthai, T., Sooknoi, T., Jongpatiwut, S., Rirksomboon, T., Osuwan, S. and Resasco, D. E. (2011). Effect of extra-framework cesium on the deoxygenation of methylester over CsNaX zeolites. *Applied Catalysis A: General*, 409-410: 74-81.
- De Jong, K. P. (2010). Deposition precipitation. In De Jong, K. P. (Ed.), *Synthesis of solid catalysts* (pp. 111-132). Germany: Wiley-VCH.
- De, S., Saha, B. and Luque, R. (2015). Hydrodeoxygenation processes: Advances on catalytic transformations of biomass-derived platform chemicals into hydrocarbon fuels. *Bioresource Technology*, 178: 108-118.
- de Souza, P. M., Nie, L., Borges, L. E. P., Noronha, F. B. and Resasco, D. E. (2014). Role of oxophilic supports in the selective hydrodeoxygenation of *m*-cresol on Pd catalysts. *Catalysis Letters*, 144: 2005-2011.
- de Souza, P. M., Rabelo-Neto, R. C., Borges, L. E. P., Jacobs, G., Davis, B. H., Sooknoi, T., Resasco, D. E. and Noronha, F. B. (2015). Role of keto

intermediates in the hydrodeoxygenation of phenol over Pd on oxophilic supports. *ACS Catalysis*, 5: 1318-1329.

Derrouiche, S. and Bianchi, D. (2004). Heats of adsorption using temperature programmed adsorption equilibrium: Application to the adsorption of CO on Cu/Al<sub>2</sub>O<sub>3</sub> and H<sub>2</sub> on Pt/Al<sub>2</sub>O<sub>3</sub>. *Langmuir*, 20: 4489-4497.

Dhandapani, B., Clair, T. S. and Oyama, S. T. (1998). Simultaneous hydrodesulfurization, hydrodeoxygenation, and hydrogenation with molybdenum carbide. *Applied Catalysis A: General*, 168: 219-228.

Di, W., Cheng, J., Tian, S., Li, J., Chen, J. and Sun, Q. (2016). Synthesis and characterization of supported copper phyllosilicate catalysts for acetic acid hydrogenation to ethanol. *Applied Catalysis A: General*, 510: 244-259.

Dickinson, J. G., Poberezny, J. T. and Savage, P. E. (2012). Deoxygenation of benzofuran in supercritical water over a platinum catalyst. *Applied Catalysis B: Environmental*, 123-124: 357-366.

Dickinson, J. G. and Savage, P. E. (2014). Stability and activity of Pt and Ni catalysts for hydrodeoxygenation in supercritical water. *Journal of Molecular Catalysis A: Chemical*, 388-389: 56-65.

Diebold, J. P. (2000). A review of the chemical and physical mechanisms of the storage stability of fast pyrolysis bio-oils. *NREL/SR-570-27613, Colorado, USA*,

Dines, T. J., Rochester, C. H. and Ward, A. M. (1991). Infrared and Raman study of the surface acidity of titania-supported vanadia catalysts. *Journal of the Chemical Society, Faraday Transactions*, 87: 1611-1616.

Ding, R., Wu, Y., Chen, Y., Liang, J., Liu, J. and Yang, M. (2015). Effective hydrodeoxygenation of palmitic acid to diesel-like hydrocarbons over MoO<sub>2</sub>/CNTs catalyst. *Chemical Engineering Science*, 135: 517-525.

Dong, X.-Y., Gao, Z.-W., Yang, K.-F., Zhang, W.-Q. and Xu, L.-W. (2015). Nanosilver as a new generation of silver catalysts in organic transformations for efficient synthesis of fine chemicals. *Catalysis Science & Technology*, 5: 2554-2574.

Dongil, A. B., Rivera-Cárcamo, C., Pastor-Pérez, L., Sepúlveda-Escribano, A. and Reyes, P. (2015). Ir supported over carbon materials for the selective hydrogenation of chloronitrobenzenes. *Catalysis Today*, 249: 72-78.

- Doyle, C. D. (1961). Kinetic analysis of thermogravimetric data. *Journal of Applied Polymer Science*, 5: 285-292.
- Dragu, A., Kinayyigit, S., García-Suárez, E. J., Florea, M., Stepan, E., Velea, S., Tanase, L., Collière, V., Philippot, K., Granger, P. and Parvulescu, V. I. (2015). Deoxygenation of oleic acid: Influence of the synthesis route of Pd/mesoporous carbon nanocatalysts onto their activity and selectivity. *Applied Catalysis A: General*, 504: 81-91.
- Dreisbach, R. R. and Shrader, S. A. (1949). Vapor pressure-temperature data on some organic compounds. *Industrial & Engineering Chemistry*, 41: 2879-2880.
- Du, X., He, J., Zhu, J., Sun, L. and An, S. (2012). Ag-deposited silica-coated Fe<sub>3</sub>O<sub>4</sub> magnetic nanoparticles catalyzed reduction of *p*-nitrophenol. *Applied Surface Science*, 258: 2717-2723.
- Duan, J., Kim, Y. T., Lou, H. and Huber, G. W. (2014). Hydrothermally stable regenerable catalytic supports for aqueous-phase conversion of biomass. *Catalysis Today*, 234: 66-74.
- Durán-Martín, D., Ojeda, M., López Granados, M., Fierro, J. L. G. and Mariscal, R. (2013). Stability and regeneration of Cu-ZrO<sub>2</sub> catalysts used in glycerol hydrogenolysis to 1,2-propanediol. *Catalysis Today*, 210: 98-105.
- Duswalt, A. A. (1974). Novel methods for gas generating reactions. In Porter, R. S. & Johnson, J. F. (Eds.), *Analytical Calorimetry* (pp. 137-146). New York: Springer.
- Echeandia, S., Pawelec, B., Barrio, V. L., Arias, P. L., Cambra, J. F., Loricera, C. V. and Fierro, J. L. G. (2014). Enhancement of phenol hydrodeoxygenation over Pd catalysts supported on mixed HY zeolite and Al<sub>2</sub>O<sub>3</sub>. An approach to O-removal from bio-oils. *Fuel*, 117: 1061-1073.
- Echeverri, D. A., Marín, J. M., Restrepo, G. M. and Rios, L. A. (2009). Characterization and carbonylic hydrogenation of methyl oleate over Ru-Sn/Al<sub>2</sub>O<sub>3</sub>: Effects of metal precursor and chlorine removal. *Applied Catalysis A: General*, 366: 342-347.
- Edelman, M. C., Maholland, M. K., Baldwin, R. M. and Cowley, S. W. (1988). Vapor-phase catalytic hydrodeoxygenation of benzofuran. *Journal of Catalysis*, 111: 243-253.

- Eigenmann, F., Maciejewski, M. and Baiker, A. (2000). Gas adsorption studied by pulse thermal analysis. *Thermochimica Acta*, 359: 131-141.
- Emmett, P. H. and Skau, N. (1943). The catalytic hydrogenation of benzene over metal catalysts. *Journal of the American Chemical Society*, 65: 1029-1035.
- Evans, M. G. and Polanyi, M. (1936). Further considerations on the thermodynamics of chemical equilibria and reaction rates. *Transactions of the Faraday Society*, 32: 1333-1360.
- Everson, D. A., Shrestha, R. and Weix, D. J. (2010). Nickel-catalyzed reductive cross-coupling of aryl halides with alkyl halides. *Journal of the American Chemical Society*, 132: 920-921.
- Faba, L., Díaz, E. and Ordóñez, S. (2014). Hydrodeoxygenation of acetone-furfural condensation adducts over alumina-supported noble metal catalysts. *Applied Catalysis B: Environmental*, 160-161: 436-444.
- Fanchiang, W.-L. and Lin, Y.-C. (2012). Catalytic fast pyrolysis of furfural over H-ZSM-5 and Zn/H-ZSM-5 catalysts. *Applied Catalysis A: General*, 419-420: 102-110.
- Felder, R. M. and Rousseau, R. W. (2004). *Elementary principles of chemical processes* (3rd ed.). USA: Wiley.
- Feng, J., Fu, H., Wang, J., Li, R., Chen, H. and Li, X. (2008). Hydrogenolysis of glycerol to glycols over ruthenium catalysts: Effect of support and catalyst reduction temperature. *Catalysis Communications*, 9: 1458-1464.
- Feng, Y., Yin, H., Wang, A., Shen, L., Yu, L. and Jiang, T. (2011). Gas phase hydrogenolysis of glycerol catalyzed by Cu/ZnO/MO<sub>x</sub> (MO<sub>x</sub> = Al<sub>2</sub>O<sub>3</sub>, TiO<sub>2</sub>, and ZrO<sub>2</sub>) catalysts. *Chemical Engineering Journal*, 168: 403-412.
- Firouzabadi, H., Iranpoor, N. and Jafarpour, M. (2005). Rapid, highly efficient and stereoselective deoxygenation of epoxides by ZrCl<sub>4</sub>/NaI. *Tetrahedron Letters*, 46: 4107-4110.
- Fogler, H. S. (2006). *Elements of chemical reaction engineering* (4th ed.). United States: Pearson Education.

- Foster, A. J., Do, P. T. M. and Lobo, R. F. (2012). The synergy of the support acid function and the metal function in the catalytic hydrodeoxygenation of *m*-cresol. *Topics in Catalysis*, 55: 118-128.
- Föttinger, K., Halwax, E. and Vinek, H. (2006). Deactivation and regeneration of Pt containing sulfated zirconia and sulfated zirconia. *Applied Catalysis A: General*, 301: 115-122.
- Furimsky, E. (1983). Mechanism of catalytic hydrodeoxygenation of tetrahydrofuran. *Industrial & Engineering Chemistry Product Research and Development*, 22: 31-34.
- Furimsky, E. (2000). Catalytic hydrodeoxygenation. *Applied Catalysis A: General*, 199: 147-190.
- Galadima, A. and Muraza, O. (2015). Catalytic upgrading of vegetable oils into jet fuels range hydrocarbons using heterogeneous catalysts: A review. *Journal of Industrial and Engineering Chemistry*, 29: 12-23.
- Galan-Fereres, M., Alemany, L. J., Mariscal, R., Banares, M. A., Anderson, J. A. and Fierro, J. L. G. (1995). Surface acidity and properties of titania-silica catalysts. *Chemistry of Materials*, 7: 1342-1348.
- Garner, W. E. and Reeves, L. W. (1954). The thermal decomposition of silver oxide. *Transactions of the Faraday Society*, 50: 254-260.
- Gervasini, A. (2013). Temperature Programmed Reduction/Oxidation (TPR/TPO) Methods. In Auroux, A. (Ed.), *Calorimetry and Thermal Methods in Catalysis* (pp. 175-196). Berlin: Springer.
- Goldstein, J. I., Newbury, D., Joy, D., Lyman, C., Echlin, P., Lifshin, E., Sawyer, L. and Michael, J. R. (2003). *Scanning electron microscopy and X-ray microanalysis* (3rd). New York: Kluwer Academic/Plenum Publishers.
- González-Borja, M. A. and Resasco, D. E. (2011). Anisole and guaiacol hydrodeoxygenation over monolithic Pt-Sn catalysts. *Energy & Fuels*, 25: 4155-4162.
- Gosselink, R. W., Stellwagen, D. R. and Bitter, J. H. (2013). Tungsten-based catalysts for selective deoxygenation. *Angewandte Chemie*, 125: 5193-5196.

- Grilc, M., Veryasov, G., Likozar, B., Jesih, A. and Levec, J. (2015). Hydrodeoxygenation of solvolysed lignocellulosic biomass by unsupported MoS<sub>2</sub>, MoO<sub>2</sub>, Mo<sub>2</sub>C and WS<sub>2</sub> catalysts. *Applied Catalysis B: Environmental*, 163: 467-477.
- Guenard, R. L., Fernández-Torres, L. C., Kim, B.-I., Perry, S. S., Frantz, P. and Didziulis, S. V. (2002). Selective surface reactions of single crystal metal carbides: Alkene production from short chain alcohols on titanium carbide and vanadium carbide. *Surface Science*, 515: 103-116.
- Günther, E., Hiebler, S., Mehling, H. and Redlich, R. (2009). Enthalpy of phase change materials as a function of temperature: Required accuracy and suitable measurement methods. *International Journal of Thermophysics*, 30: 1257-1269.
- Guo, X., Guan, J., Li, B., Wang, X., Mu, X. and Liu, H. (2015). Conversion of biomass-derived sorbitol to glycols over carbon materials supported Ru-based catalysts. *Scientific Reports*, 5: 16451-16459.
- Guo, X., Wang, X., Guan, J., Chen, X., Qin, Z., Mu, X. and Xian, M. (2014). Selective hydrogenation of D-glucose to D-sorbitol over Ru/ZSM-5 catalysts. *Chinese Journal of Catalysis*, 35: 733-740.
- Gupta, P., Colvin, V. L. and George, S. M. (1988). Hydrogen desorption kinetics from monohydride and dihydride species on silicon surfaces. *Physical Review B*, 37: 8234-8243.
- Gutierrez, A., Kaila, R. K., Honkela, M. L., Slioor, R. and Krause, A. O. I. (2009). Hydrodeoxygenation of guaiacol on noble metal catalysts. *Catalysis Today*, 147: 239-246.
- Hammett, L. P. (1937). The effect of structure upon the reactions of organic compounds. Benzene derivatives. *Journal of the American Chemical Society*, 59: 96-103.
- Hänggi, P., Talkner, P. and Borkovec, M. (1990). Reaction-rate theory: Fifty years after Kramers. *Reviews of Modern Physics*, 62: 251-341.
- Hatakeyama, T. and Liu, Z. (2000). *Handbook of thermal analysis* England: John Wiley & Sons Ltd.
- Hatakeyama, T. and Quinn, F. X. (1999). *Thermal analysis: Fundamentals and applications to polymer science* (2nd ed.). England: Wiley.



- He, L., Li, X., Lin, W., Li, W., Cheng, H., Yu, Y., Fujita, S., Arai, M. and Zhao, F. (2014). The selective hydrogenation of ethyl stearate to stearyl alcohol over Cu/Fe bimetallic catalysts. *Journal of Molecular Catalysis A: Chemical*, 392: 143-149.
- He, Z. and Wang, X. (2012). Hydrodeoxygenation of model compounds and catalytic systems for pyrolysis bio-oils upgrading. *Catalysis for Sustainable Energy*, 1: 28-52.
- Heidebrecht, P., Galvita, V. and Sundmacher, K. (2008). An alternative method for parameter identification from temperature programmed reduction (TPR) data. *Chemical Engineering Science*, 63: 4776-4788.
- Hellinger, M., Carvalho, H. W. P., Baier, S., Wang, D., Kleist, W. and Grunwaldt, J.-D. (2015). Catalytic hydrodeoxygenation of guaiacol over platinum supported on metal oxides and zeolites. *Applied Catalysis A: General*, 490: 181-192.
- Hengst, K., Schubert, M., Carvalho, H. W. P., Lu, C., Kleist, W. and Grunwaldt, J.-D. (2015). Synthesis of  $\gamma$ -valerolactone by hydrogenation of levulinic acid over supported nickel catalysts. *Applied Catalysis A: General*, 502: 18-26.
- Hensley, A. J. R., Hong, Y., Zhang, R., Zhang, H., Sun, J., Wang, Y. and McEwen, J.-S. (2014a). Enhanced Fe<sub>2</sub>O<sub>3</sub> reducibility via surface modification with Pd: Characterizing the synergy with Pd/Fe catalysts for hydrodeoxygenation reactions. *ACS Catalysis*, 4: 3381-3392.
- Hensley, A. J. R., Wang, Y. and McEwen, J.-S. (2014b). Adsorption of phenol on Fe (110) and Pd (111) from first principles. *Surface Science*, 630: 244-253.
- Hensley, A. J. R., Wang, Y. and McEwen, J.-S. (2015). Phenol deoxygenation mechanisms on Fe(110) and Pd(111). *ACS Catalysis*, 5: 523-536.
- Herley, P. J. and Prout, E. G. (1960). The thermal decomposition of silver oxide. *Journal of the American Chemical Society*, 82: 1540-1543.
- Hernández-Cristóbal, O., Díaz, G. and Gómez-Cortés, A. (2014). Effect of the Reduction Temperature on the Activity and Selectivity of Titania-Supported Iridium Nanoparticles for Methylcyclopentane Reaction. *Industrial & Engineering Chemistry Research*, 53: 10097-10104.

- Hernandez-Tamargo, C. E., Roldan, A. and de Leeuw, N. H. (2017). Density functional theory study of zeolite-mediated tautomerization of phenol and catechol. *Molecular Catalysis*, 433: 334-345.
- Hong, Y.-K., Lee, D.-W., Eom, H.-J. and Lee, K.-Y. (2014a). The catalytic activity of Pd/WO<sub>x</sub>/γ-Al<sub>2</sub>O<sub>3</sub> for hydrodeoxygenation of guaiacol. *Applied Catalysis B: Environmental*, 150-151: 438-445.
- Hong, Y., Zhang, H., Sun, J., Ayman, K. M., Hensley, A. J. R., Gu, M., Engelhard, M. H., McEwen, J.-S. and Wang, Y. (2014b). Synergistic catalysis between Pd and Fe in gas phase hydrodeoxygenation of *m*-cresol. *ACS Catalysis*, 4: 3335-3345.
- Horsley, J. A., Wachs, I. E., Brown, J. M., Via, G. H. and Hardcastle, F. D. (1987). Structure of surface tungsten oxide species in WO<sub>x</sub>/Al<sub>2</sub>O<sub>3</sub> supported oxide system from X-ray absorption near-edge spectroscopy and Raman spectroscopy. *Journal of Physical Chemistry*, 91: 4014-4020.
- Houston, P. L. (2006). *Chemical kinetics and reaction dynamics* New York: Dover Publications.
- Hu, T., Yin, H., Zhang, R., Wu, H., Jiang, T. and Wada, Y. (2007). Gas phase hydrogenation of maleic anhydride to γ-butyrolactone by Cu-Zn-Ti catalysts. *Catalysis Communications*, 8: 193-199.
- Huang, X., Zhang, Q., Wang, T., Liu, Q., Ma, L. and Zhang, Q. (2012). Production of jet fuel intermediates from furfural and acetone by aldol condensation over MgO/NaY. *Journal of Fuel Chemistry and Technology*, 40: 973-978.
- Huber, G. W. and Dumesic, J. A. (2006). An overview of aqueous-phase catalytic processes for production of hydrogen and alkanes in a biorefinery. *Catalysis Today*, 111: 119-132.
- Huber, G. W., Iborra, S. and Corma, A. (2006). Synthesis of transportation fuels from biomass: Chemistry, catalysts and engineering. *Chemical Reviews*, 106: 4044-4098.
- Hurst, N. W., Gentry, S. J., Jones, A. and McNicol, B. D. (1982). Temperature Programmed Reduction. *Catalysis Reviews: Science and Engineering*, 24: 233-309.

- Iino, A., Cho, A., Takagaki, A., Kikuchi, R. and Ted Oyama, S. (2014). Kinetic studies of hydrodeoxygenation of 2-methyltetrahydrofuran on a Ni<sub>2</sub>P/SiO<sub>2</sub> catalyst at medium pressure. *Journal of Catalysis*, 311: 17-27.
- Ishikawa, M., Tamura, M., Nakagawa, Y. and Tomishige, K. (2016). Demethoxylation of guaiacol and methoxybenzenes over carbon-supported Ru-Mn catalyst. *Applied Catalysis B: Environmental*, 182: 193-203.
- Jacobson, K., Maheria, K. C. and Dalai, A. K. (2013). Bio-oil valorization: A review. *Renewable and Sustainable Energy Reviews*, 23: 91-106.
- Jalid, F., Khan, T. S., Mir, F. Q. and Haider, M. A. (2017). Understanding trends in hydrodeoxygenation reactivity of metal and bimetallic alloy catalysts from ethanol reaction on stepped surface. *Journal of Catalysis*, 353: 265-273.
- Jammaer, J., Aerts, A., D'Haen, J., Seo, J. W. and Martens, J. A. (2009). Convenient synthesis of ordered mesoporous silica at room temperature and quasi-neutral pH. *Journal of Materials Chemistry*, 19: 8290-8293.
- Jammaer, J., van Erp, T. S., Aerts, A., Kirschhock, C. E. A. and Martens, J. A. (2011). Continuous synthesis process of hexagonal nanoplates of *P6m* ordered mesoporous silica. *Journal of the American Chemical Society*, 133: 13737-13745.
- Jana, P., de la Peña O'Shea, V. A., Coronado, J. M. and Serrano, D. P. (2013). H<sub>2</sub> production by CH<sub>4</sub> decomposition over metallic cobalt nanoparticles: Effect of the catalyst activation. *Applied Catalysis A: General*, 467: 371-379.
- Jang, H., Kim, S.-H., Lee, D., Shim, S. E., Baeck, S.-H., Kim, B. S. and Chang, T. S. (2013). Hydrogenation of lactic acid to propylene glycol over a carbon-supported ruthenium catalyst. *Journal of Molecular Catalysis A: Chemical*, 380: 57-60.
- Jelić, D., Penavin-Škundrić, J., Majstorović, D. and Mentus, S. (2011). The thermogravimetric study of silver(I) oxide reduction by hydrogen. *Thermochimica Acta*, 526: 252-256.
- Jeong, H., Kim, T. H., Kim, K. I. and Cho, S. H. (2006). The hydrogenation of maleic anhydride to  $\gamma$ -butyrolactone using mixed metal oxide catalysts in a batch-type reactor. *Fuel Processing Technology*, 87: 497-503.

- Jiang, H., Yang, H., Hawkins, R. and Ring, Z. (2007). Effect of palladium on sulfur resistance in Pt-Pd bimetallic catalysts. *Catalysis Today*, 125: 282-290.
- Jin, S., Xiao, Z., Li, C., Chen, X., Wang, L., Xing, J., Li, W. and Liang, C. (2014). Catalytic hydrodeoxygenation of anisole as lignin model compound over supported nickel catalysts. *Catalysis Today*, 234: 125-132.
- Jin, X., Dang, L., Lohrman, J., Subramaniam, B., Ren, S. and Chaudhari, R. V. (2013). Lattice-matched bimetallic CuPd-graphene nanocatalysts for facile conversion of biomass-derived polyols to chemicals. *ACS Nano*, 7: 1309-1316.
- Joshi, N. and Lawal, A. (2012). Hydrodeoxygenation of acetic acid in a microreactor. *Chemical Engineering Science*, 84: 761-771.
- Jozwiak, W. K., Kaczmarek, E., Maniecki, T. P., Ignaczak, W. and Maniukiewicz, W. (2007). Reduction behavior of iron oxides in hydrogen and carbon monoxide atmospheres. *Applied Catalysis A: General*, 326: 17-27.
- Juarez, J. C. and Morales, R. (2008). Reduction kinetics of  $\text{Ag}_2\text{MoO}_4$  by hydrogen. *Metallurgical and Materials Transactions B*, 39: 738-745.
- Jung, S. M., Godard, E., Jung, S. Y., Park, K.-C. and Choi, J. U. (2003). Liquid-phase hydrogenation of maleic anhydride over Pd-Sn/SiO<sub>2</sub>. *Catalysis Today*, 87: 171-177.
- Kaewpengkrow, P., Atong, D. and Sricharoenchaikul, V. (2014). Effect of Pd, Ru, Ni and ceramic supports on selective deoxygenation and hydrogenation of fast pyrolysis *Jatropha* residue vapors. *Renewable Energy*, 65: 92-101.
- Kanervo, J. M., Elina Harlin, M., Krause, A. O. I. and Banares, M. A. (2003). Characterisation of alumina-supported vanadium oxide catalysts by kinetic analysis of H<sub>2</sub>-TPR data. *Catalysis Today*, 78: 171-180.
- Kanervo, J. M. and Krause, A. O. I. (2002). Characterisation of supported chromium oxide catalysts by kinetic analysis of H<sub>2</sub>-TPR data. *Journal of Catalysis*, 207: 57-65.
- Kang, K. H., Hong, U. G., Bang, Y., Choi, J. H., Kim, J. K., Lee, J. K., Han, S. J. and Song, I. K. (2015). Hydrogenation of succinic acid to 1,4-butanediol over Re-Ru bimetallic catalysts supported on mesoporous carbon. *Applied Catalysis A: General*, 490: 153-162.

- Kang, K. H., Hong, U. G., Jun, J. O., Song, J. H., Bang, Y., Choi, J. H., Han, S. J. and Song, I. K. (2014). Hydrogenation of succinic acid to  $\gamma$ -butyrolactone and 1,4-butanediol over mesoporous rhenium-copper-carbon composite catalyst. *Journal of Molecular Catalysis A: Chemical*, 395: 234-242.
- Karim, W., Spreafico, C., Kleibert, A., Gobrecht, J., VandeVondele, J., Ekinici, Y. and van Bokhoven, J. A. (2017). Catalyst support effects on hydrogen spillover. *Nature*, 541: 68-71.
- Karimi, E., Teixeira, I. F., Ribeiro, L. P., Gomez, A., Lago, R. M., Penner, G., Kycia, S. W. and Schlaf, M. (2012). Ketonization and deoxygenation of alkanolic acids and conversion of levulinic acid to hydrocarbons using a Red Mud bauxite mining waste as the catalyst. *Catalysis Today*, 190: 73-88.
- Kay Lup, A. N., Abnisa, F., Wan Daud, W. M. A. and Aroua, M. K. (2017a). A review on reaction mechanisms of metal-catalyzed deoxygenation process in bio-oil model compounds. *Applied Catalysis A: General*, 541: 87-106.
- Kay Lup, A. N., Abnisa, F., Wan Daud, W. M. A. and Aroua, M. K. (2017b). A review on reactivity and stability of heterogeneous metal catalysts for deoxygenation of bio-oil model compounds. *Journal of Industrial and Engineering Chemistry*, 56: 1-34.
- Kay Lup, A. N., Abnisa, F., Wan Daud, W. M. A. and Aroua, M. K. (2018a). Acidity, oxophilicity and hydrogen sticking probability of supported metal catalysts for hydrodeoxygenation process. *IOP Conference Series: Materials Science and Engineering*, 334: 1-6.
- Kay Lup, A. N., Abnisa, F., Wan Daud, W. M. A. and Aroua, M. K. (2018b). Delayed volatiles release phenomenon at higher temperature in TGA via sample encapsulation technique. *Fuel*, 234: 422-429.
- Kazansky, V. B., Subbotina, I. R., van Santen, R. A. and Hensen, E. J. M. (2004). DRIFTS study of the chemical state of modifying gallium ions in reduced Ga/ZSM-5 prepared by impregnation I. Observation of gallium hydrides and application of CO adsorption as a molecular probe for reduced gallium ions. *Journal of Catalysis*, 227: 263-269.
- Keane, M. A. and Patterson, P. M. (1999). The role of hydrogen partial pressure in the gas-phase hydrogenation of aromatics over supported nickel. *Industrial & Engineering Chemistry Research*, 38: 1295-1305.

- Kepp, K. P. (2016). A quantitative scale of oxophilicity and thiophilicity. *Inorganic Chemistry*, 55: 9461-9470.
- Khader, M. M., Kheiri, F. M.-N., El-Anadouli, B. E. and Ateya, B. G. (1993). Mechanism of Reduction of Rutile with Hydrogen. *Journal of Physical Chemistry*, 97: 6074-6077.
- Kim, J. K., Lee, J. K., Kang, K. H., Song, J. C. and Song, I. K. (2015). Selective cleavage of C-O bond in benzyl phenyl ether to aromatics over Pd-Fe bimetallic catalyst supported on ordered mesoporous carbon. *Applied Catalysis A: General*, 498: 142-149.
- Kim, Y. T., Dumesic, J. A. and Huber, G. W. (2013). Aqueous-phase hydrodeoxygenation of sorbitol: A comparative study of Pt/Zr phosphate and Pt-ReO<sub>x</sub>/C. *Journal of Catalysis*, 304: 72-85.
- Kissinger, H. E. (1957). Reaction Kinetics in Differential Thermal Analysis. *Analytical Chemistry*, 29: 1702-1706.
- Kok, M. V., Hughes, R. and Price, D. (1996). High pressure TGA analysis of crude oils. *Thermochimica Acta*, 287: 91-99.
- Krasovskiy, A., Duplais, C. and Lipshutz, B. H. (2009). Zn-mediated, Pd-catalyzed cross-couplings in water at room temperature without prior formation of organozinc reagents. *Journal of the American Chemical Society*, 131: 15592-15593.
- Kubička, D. and Kaluža, L. (2010). Deoxygenation of vegetable oils over sulfided Ni, Mo and NiMo catalysts. *Applied Catalysis A: General*, 372: 199-208.
- Kuklin, S., Maximov, A., Zolotukhina, A. and Karakhanov, E. (2016). New approach for highly selective hydrogenation of phenol to cyclohexanone: Combination of rhodium nanoparticles and cyclodextrins. *Catalysis Communications*, 73: 63-68.
- Kumar, P., Yenumala, S. R., Maity, S. K. and Shee, D. (2014). Kinetics of hydrodeoxygenation of stearic acid using supported nickel catalysts: Effects of supports. *Applied Catalysis A: General*, 471: 28-38.
- Kuwahara, Y., Magatani, Y. and Yamashita, H. (2015). Ru nanoparticles confined in Zr-containing spherical mesoporous silica containers for hydrogenation of levulinic acid and its esters into  $\gamma$ -valerolactone at ambient conditions. *Catalysis Today*, 258: 262-269.

- L'vov, B. V. (1999). Kinetics and mechanism of thermal decomposition of silver oxide. *Thermochimica Acta*, 333: 13-19.
- Laidler, K. J. and Christine King, M. (1983). The development of transition-state theory. *Journal of Physical Chemistry*, 87: 2657-2664.
- Landau, M. V. (2010). Sol-gel processing. In de Jong, K. P. (Ed.), *Synthesis of solid catalysts* (pp. 83-109). Germany: Wiley-VCH.
- Larkin, P. (2011). *Infrared and Raman Spectroscopy: Principles and Spectral Interpretation* USA: Elsevier.
- Lausche, A. C., Falsig, H., Jensen, A. D. and Studt, F. (2014). Trends in the hydrodeoxygenation activity and selectivity of transition metal surfaces. *Catalysis Letters*, 144: 1968-1972.
- Lazaridis, P. A., Karakoulia, S., Delimitis, A., Coman, S. M., Parvulescu, V. I. and Triantafyllidis, K. S. (2015). D-Glucose hydrogenation/hydrogenolysis reactions on noble metal (Ru, Pt)/activated carbon supported catalysts. *Catalysis Today*, 257: 281-290.
- Lee, C.-L. and Ollis, D. F. (1984). Catalytic hydrodeoxygenation of benzofuran and *o*-ethylphenol. *Journal of Catalysis*, 87: 325-331.
- Lee, D. W. and Yoo, B. R. (2014). Advanced metal oxide (supported) catalysts: Synthesis and applications. *Journal of Industrial and Engineering Chemistry*, 20: 3947-3959.
- Lee, E. H., Park, R.-s., Kim, H., Park, S. H., Jung, S.-C., Jeon, J.-K., Kim, S. C. and Park, Y.-K. (2016a). Hydrodeoxygenation of guaiacol over Pt loaded zeolitic materials. *Journal of Industrial and Engineering Chemistry*, 37: 18-21.
- Lee, S., Yu, Z., Zaborenko, N. and Varma, A. (2016b). Acetophenone hydrogenation on Rh/Al<sub>2</sub>O<sub>3</sub> catalyst: Intrinsic reaction kinetics and effects of internal diffusion. *Chemical Engineering Journal*, 288: 711-723.
- Lee, W.-S., Wang, Z., Wu, R. J. and Bhan, A. (2014). Selective vapor-phase hydrodeoxygenation of anisole to benzene on molybdenum carbide catalysts. *Journal of Catalysis*, 319: 44-53.

- Leiva, K., Martinez, N., Sepulveda, C., García, R., Jiménez, C. A., Laurenti, D., Vrinat, M., Geantet, C., Fierro, J. L. G., Ghampson, I. T. and Escalona, N. (2015a). Hydrodeoxygenation of 2-methoxyphenol over different Re active phases supported on SiO<sub>2</sub> catalysts. *Applied Catalysis A: General*, 490: 71-79.
- Leiva, K., Sepulveda, C., García, R., Laurenti, D., Vrinat, M., Geantet, C. and Escalona, N. (2015b). Kinetic study of the conversion of 2-methoxyphenol over supported Re catalysts: Sulfide and oxide state. *Applied Catalysis A: General*, 505: 302-308.
- Leofanti, G., Padovan, M., Tozzola, G. and Venturelli, B. (1998). Surface area and pore texture of catalysts. *Catalysis Today*, 41: 207-219.
- Leofanti, G., Tozzola, G., Padovan, M., Petrini, G., Bordiga, S. and Zecchina, A. (1997). Catalyst characterization: Characterization techniques. *Catalysis Today*, 34: 307-327.
- Li, K., Wang, R. and Chen, J. (2011). Hydrodeoxygenation of anisole over silica-supported Ni<sub>2</sub>P, MoP, and NiMoP catalysts. *Energy & Fuels*, 25: 854-863.
- Li, W., Ye, L., Chen, J., Duan, X., Lin, H. and Yuan, Y. (2015a). FeSBA-15-supported ruthenium catalyst for the selective hydrogenolysis of carboxylic acids to alcoholic chemicals. *Catalysis Today*, 251: 53-59.
- Li, X., Su, H., Ren, G. and Wang, S. (2016). The role of MgO in the performance of Pd/SiO<sub>2</sub>/cordierite monolith catalyst for the hydrogenation of 2-ethyl-anthraquinone. *Applied Catalysis A: General*, 517: 168-175.
- Li, Y., Huang, X., Zhang, Q., Chen, L., Zhang, X., Wang, T. and Ma, L. (2015b). Hydrogenation and hydrodeoxygenation of difurfurylidene acetone to liquid alkanes over Raney Ni and the supported Pt catalysts. *Applied Energy*, 160: 990-998.
- Li, Y., Zhang, C., Liu, Y., Hou, X., Zhang, R. and Tang, X. (2015c). Coke deposition on Ni/HZSM-5 in bio-oil hydrodeoxygenation processing. *Energy & Fuels*, 29: 1722-1728.
- Lin, H.-Y. and Chen, Y.-W. (2004). The mechanism of reduction of cobalt by hydrogen. *Materials Chemistry and Physics*, 85: 171-175.
- Lin, H.-Y., Chen, Y.-W. and Li, C. (2003). The mechanism of reduction of iron oxide by hydrogen. *Thermochimica Acta*, 400: 61-67.



- Liu, S., Okuyama, Y., Tamura, M., Nakagawa, Y., Imai, A. and Tomishige, K. (2016). Catalytic conversion of sorbitol to gasoline-ranged products without external hydrogen over Pt-modified Ir-ReO<sub>x</sub>/SiO<sub>2</sub>. *Catalysis Today*, 269: 122-131.
- Liu, Y., Chen, J. and Zhang, J. (2007). Effects of the supports on activity of supported nickel catalysts for hydrogenation of *m*-dinitrobenzene to *m*-phenylenediamine. *Chinese Journal of Chemical Engineering*, 15: 63-67.
- Lok, M. (2010). Coprecipitation. In De Jong, K. P. (Ed.), *Synthesis of solid catalysts* (pp. 135-149). Germany: Wiley-VCH.
- Lopez, R. M., Hays, D. S. and Fu, G. C. (1997). Bu<sub>3</sub>SnH-catalyzed Barton-McCombie deoxygenation of alcohols. *Journal of the American Chemical Society*, 119: 6949-6950.
- Lu, J. and Heyden, A. (2015). Theoretical investigation of the reaction mechanism of the hydrodeoxygenation of guaiacol over a Ru (0001) model surface. *Journal of Catalysis*, 321: 39-50.
- Lugo-José, Y. K., Monnier, J. R. and Williams, C. T. (2014). Gas phase, catalytic hydrodeoxygenation of propanoic acid, over supported group VIII noble metals: Metal and support effects. *Applied Catalysis A: General*, 469: 410-418.
- Luo, Y.-R. (2007). *Comprehensive handbook of chemical bond energies* Boca Raton, FL: CRC Press.
- Luo, Z., Wang, Y., He, M. and Zhao, C. (2016). Precise oxygen scission of lignin derived aryl ethers to quantitatively produce aromatic hydrocarbons in water. *Green Chemistry*, 18: 433-441.
- Luo, Z. and Zhao, C. (2016). Mechanistic insights into selective hydrodeoxygenation of lignin-derived β-O-4 linkage to aromatic hydrocarbons in water. *Catalysis Science & Technology*, 6: 3476-3484.
- Maciejewski, M., Emmerich, W. D. and Baiker, A. (1999). Pulse thermal analysis a new range of opportunities. *Journal of Thermal Analysis and Calorimetry*, 56: 627-637.
- Maciejewski, M., Müller, C. A., Tschan, R., Emmerich, W. D. and Baiker, A. (1997). Novel pulse thermal analysis method and its potential for investigating gas-solid reactions. *Thermochimica Acta*, 295: 167-182.

- Mäki-Arvela, P., Kumar, N., Nasir, A., Salmi, T. and Murzin, D. Y. (2005). Selectivity enhancement by catalyst deactivation in three-phase hydrogenation of nerol. *Industrial & Engineering Chemistry Research*, 44: 9376-9383.
- Mäki-Arvela, P., Snåre, M., Eränen, K., Myllyoja, J. and Murzin, D. Y. (2008). Continuous decarboxylation of lauric acid over Pd/C catalyst. *Fuel*, 87: 3543-3549.
- Marceau, E., Carrier, X. and Che, M. (2010). Impregnation and drying. In De Jong, K. P. (Ed.), *Synthesis of solid catalysts* (pp. 59-82). Germany: Wiley-VCH.
- Maris, E. P. and Davis, R. J. (2007). Hydrogenolysis of glycerol over carbon-supported Ru and Pt supported catalysts. *Journal of Catalysis*, 249: 328-337.
- Martens, J. A., Jammaer, J., Bajpe, S., Aerts, A., Lorgouilloux, Y. and Kirschhock, C. E. A. (2011). Simple synthesis recipes of porous materials. *Microporous and Mesoporous Materials*, 140: 2-8.
- Martin, C., Martin, I., del Moral, C. and Rives, V. (1994). FT-IR assessment through pyridine adsorption of the surface acidity of alkali-doped MoO<sub>3</sub>/TiO<sub>2</sub>. *Journal of Catalysis*, 146: 415-421.
- Massoth, F. E., Politzer, P., Concha, M. C., Murray, J. S., Jakowski, J. and Simons, J. (2006). Catalytic hydrodeoxygenation of methyl-substituted phenols: Correlations of kinetic parameters with molecular properties. *Journal of Physical Chemistry B*, 110: 14283-14291.
- Matos, M. A. R., Miranda, M. S. and Morais, V. M. F. (2003). Thermochemical study of the methoxy- and dimethoxyphenol isomers. *Journal of Chemical & Engineering Data*, 48: 669-679.
- McDaniel, M. P. (2010). A review of the Phillips supported chromium catalyst and its commercial use for ethylene polymerization. In Gates, B. C. & Knözinger, H. (Eds.), *Advances in catalysis* (pp. 123-606). USA: Academic Press.
- McManus, J. R., Martono, E. and Vohs, J. M. (2013). Selective deoxygenation of aldehydes: The reaction of acetaldehyde and glycolaldehyde on Zn/Pt(111) bimetallic surfaces. *ACS Catalysis*, 3: 1739-1750.
- McManus, J. R. and Vohs, J. M. (2014). Deoxygenation of glycolaldehyde and furfural on Mo<sub>2</sub>C/Mo(100). *Surface Science*, 630: 16-21.

- Meller, E., Green, U., Aizenshtat, Z. and Sasson, Y. (2014). Catalytic deoxygenation of castor oil over Pd/C for the production of cost effective biofuel. *Fuel*, 133: 89-95.
- Menczel, J. D., Judovits, L., Bruce Prime, R., Bair, H. E., Reading, M. and Swier, S. (2009). Differential scanning calorimetry (DSC). In Menczel, J. D. & Bruce Prime, R. (Eds.), *Thermal analysis of polymers: Fundamentals and applications* (pp. 7-240). New Jersey: John Wiley & Sons, Inc.
- Miao, C., Marin-Flores, O., Davidson, S. D., Li, T., Dong, T., Gao, D., Wang, Y., Garcia-Pérez, M. and Chen, S. (2016). Hydrothermal catalytic deoxygenation of palmitic acid over nickel catalyst. *Fuel*, 166: 302-308.
- Mikami, Y., Noujima, A., Mitsudome, T., Mizugaki, T., Jitsukawa, K. and Kaneda, K. (2010). Selective deoxygenation of styrene oxides under a CO atmosphere using silver nanoparticle catalyst. *Tetrahedron Letters*, 51: 5466-5468.
- Miller, J. T., Meyers, B. L., Modica, F. S., Lane, G. S., Vaarkamp, M. and Koningsberger, D. C. (1993). Hydrogen temperature-programmed desorption (H<sub>2</sub> TPD) of supported platinum catalysts. *Journal of Catalysis*, 143: 395-408.
- Mitsudome, T., Mikami, Y., Matoba, M., Mizugaki, T., Jitsukawa, K. and Kaneda, K. (2012). Design of a Silver-Cerium Dioxide Core-Shell Nanocomposite Catalyst for Chemoselective Reduction Reactions. *Angewandte Chemie*, 51: 136-139.
- Mitsudome, T., Noujima, A., Mikami, Y., Mizugaki, T., Jitsukawa, K. and Kaneda, K. (2010). Supported Gold and Silver Nanoparticles for Catalytic Deoxygenation of Epoxides into Alkenes. *Angewandte Chemie*, 122: 5677-5680.
- Miyake, T., Makino, T., Taniguchi, S., Watanuki, H., Niki, T., Shimizu, S., Kojima, Y. and Sano, M. (2009). Alcohol synthesis by hydrogenation of fatty acid methyl esters on supported Ru-Sn and Rh-Sn catalysts. *Applied Catalysis A: General*, 364: 108-112.
- Moberg, D. R., Thibodeau, T. J., Amar, F. G. and Frederick, B. G. (2010). Mechanism of hydrodeoxygenation of acrolein over a cluster model of MoO<sub>3</sub>. *Journal of Physical Chemistry C*, 114: 13782-13795.
- Mochizuki, T., Chen, S.-Y., Toba, M. and Yoshimura, Y. (2014). Deoxygenation of guaiacol and woody tar over reduced catalysts. *Applied Catalysis B: Environmental*, 146: 237-243.

- Montes, A. and Giannetto, G. (2000). A new way to obtain acid or bifunctional catalysts V. Considerations on bifunctionality of the propane aromatization reaction over [Ga,Al]-ZSM-5 catalysts. *Applied Catalysis A: General*, 197: 31-39.
- Morgan, T., Santillan-Jimenez, E., Harman-Ware, A. E., Ji, Y., Grubb, D. and Crocker, M. (2012). Catalytic deoxygenation of triglycerides to hydrocarbons over supported nickel catalysts. *Chemical Engineering Journal*, 189-190: 346-355.
- Morris, M. C., McMurdie, H. F., Evans, E. H., Paretzkin, B., Parker, H. S. and Panagiotopoulos, N. C., National Bureau of Standards Monograph, 25, *Standard X-ray Diffraction Powder Patterns* 18 United States Department of Commerce Washington D.C. 1981
- Mortensen, P. M., Carvalho, H. W. P., Grunwaldt, J.-D., Jensen, P. A. and Jensen, A. D. (2015). Activity and stability of Mo<sub>2</sub>C/ZrO<sub>2</sub> as catalyst for hydrodeoxygenation of mixtures of phenol and 1-octanol. *Journal of Catalysis*, 328: 208-215.
- Mortensen, P. M., Grunwaldt, J.-D., Jensen, P. A. and Jensen, A. D. (2013). Screening of catalysts for hydrodeoxygenation of phenol as a model compound for bio-oil. *ACS Catalysis*, 3: 1774-1785.
- Mortensen, P. M., Grunwaldt, J.-D., Jensen, P. A., Knudsen, K. G. and Jensen, A. D. (2011). A review of catalytic upgrading of bio-oil to engine fuels. *Applied Catalysis A: General*, 407: 1-19.
- Moulijn, J. A., Diepen, A. E. V. and Kapteijin, F. (2001). Catalyst deactivation: Is it predictable? What to do? *Applied Catalysis A: General*, 212: 3-16.
- Mu, W., Ben, H., Du, X., Zhang, X., Hu, F., Liu, W., Ragauskas, A. J. and Deng, Y. (2014). Noble metal catalyzed aqueous phase hydrogenation and hydrodeoxygenation of lignin-derived pyrolysis oil and related model compounds. *Bioresource Technology*, 173: 6-10.
- Mullen, C. A. and Boateng, A. A. (2008). Chemical composition of bio-oils produced by fast pyrolysis of two energy crops. *Energy & Fuels*, 22: 2104-2109.
- Munnik, P., de Jongh, P. E. and de Jong, K. P. (2015). Recent developments in the synthesis of supported catalysts. *Chemical Reviews*, 115: 6687-6718.
- Nakabayashi, T. (1960). Studies on the mechanism of Clemmensen reduction. III. The relation of Clemmensen reduction to electrochemical reduction. *Journal of the American Chemical Society*, 82: 3909-3913.

- Nakagawa, Y., Ning, X., Amada, Y. and Tomishige, K. (2012). Solid acid co-catalyst for the hydrogenolysis of glycerol to 1,3-propanediol over Ir-ReO<sub>x</sub>/SiO<sub>2</sub>. *Applied Catalysis A: General*, 433-434: 128-134.
- Nakagawa, Y., Shinmi, Y., Koso, S. and Tomishige, K. (2010). Direct hydrogenolysis of glycerol into 1,3-propanediol over rhenium-modified iridium catalyst. *Journal of Catalysis*, 272: 191-194.
- Nakagawa, Y., Tamura, M. and Tomishige, K. (2013). Catalytic reduction of biomass-derived furanic compounds with hydrogen. *ACS Catalysis*, 3: 2655-2668.
- Nelson, R. C., Baek, B., Ruiz, P., Goundie, B., Brooks, A., Wheeler, M. C., Frederick, B. G., Grabow, L. C. and Austin, R. N. (2015). Experimental and theoretical insights into the hydrogen-efficient direct hydrodeoxygenation mechanism of phenol over Ru/TiO<sub>2</sub>. *ACS Catalysis*, 5: 6509-6523.
- Nie, L., de Souza, P. M., Noronha, F. B., An, W., Sooknoi, T. and Resasco, D. E. (2014). Selective conversion of *m*-cresol to toluene over bimetallic Ni-Fe catalysts. *Journal of Molecular Catalysis A: Chemical*, 388-389: 47-55.
- Nie, L. and Resasco, D. E. (2014). Kinetics and mechanism of *m*-cresol hydrodeoxygenation on a Pt/SiO<sub>2</sub> catalyst. *Journal of Catalysis*, 317: 22-29.
- Nimmanwudipong, T., Runnebaum, R. C., Block, D. E. and Gates, B. C. (2011a). Catalytic conversion of guaiacol catalyzed by platinum supported on alumina: Reaction network including hydrodeoxygenation reactions. *Energy & Fuels*, 25: 3417-3427.
- Nimmanwudipong, T., Runnebaum, R. C., Tay, K., Block, D. E. and Gates, B. C. (2011b). Cyclohexanone conversion catalyzed by Pt/ $\gamma$ -Al<sub>2</sub>O<sub>3</sub>: Evidence of oxygen removal and coupling reactions. *Catalysis Letters*, 141: 1072-1078.
- Nowak, I., Quartararo, J., Derouane, E. G. and Védrine, J. C. (2003). Effect of H<sub>2</sub>-O<sub>2</sub> pre-treatments on the state of gallium in Ga/H-ZSM-5 propane aromatisation catalysts. *Applied Catalysis A: General*, 251: 107-120.
- Odebunmi, E. O. and Ollis, D. F. (1983a). Catalytic hydrodeoxygenation I. Conversions of *o*-, *p*-, and *m*-cresols. *Journal of Catalysis*, 80: 56-64.
- Odebunmi, E. O. and Ollis, D. F. (1983b). Catalytic hydrodeoxygenation II. Interactions between catalytic hydrodeoxygenation of *m*-cresol and hydrodesulfurization of benzothiophene and dibenzothiophene. *Journal of Catalysis*, 80: 65-75.

- Ohta, H., Feng, B., Kobayashi, H., Hara, K. and Fukuoka, A. (2014). Selective hydrodeoxygenation of lignin-related 4-propylphenol into *n*-propylbenzene in water by Pt-Re/ZrO<sub>2</sub> catalysts. *Catalysis Today*, 234: 139-144.
- Olcese, R., Bettahar, M. M., Malaman, B., Ghanbaja, J., Tibavizco, L., Petitjean, D. and Dufour, A. (2013a). Gas-phase hydrodeoxygenation of guaiacol over iron-based catalysts. Effect of gases composition, iron load and supports (silica and activated carbon). *Applied Catalysis B: Environmental*, 129: 528-538.
- Olcese, R. N., Bettahar, M., Petitjean, D., Malaman, B., Giovanella, F. and Dufour, A. (2012). Gas-phase hydrodeoxygenation of guaiacol over Fe/SiO<sub>2</sub> catalyst. *Applied Catalysis B: Environmental*, 115-116: 63-73.
- Olcese, R. N., Francois, J., Bettahar, M. M., Petitjean, D. and Dufour, A. (2013b). Hydrodeoxygenation of guaiacol, a surrogate of lignin pyrolysis vapors, over iron based catalysts: Kinetics and modeling of the lignin to aromatics integrated process. *Energy & Fuels*, 27: 975-984.
- Onfroy, T., Clet, G., Bukallah, S. B., Visser, T. and Houalla, M. (2006). Acidity of titania-supported tungsten or niobium oxide catalysts: Correlation with catalytic activity. *Applied Catalysis A: General*, 298: 80-87.
- Onyestyák, G., Harnos, S., Kaszonyi, A., Štolcová, M. and Kalló, . (2012). Acetic acid hydroconversion to ethanol over novel InNi/Al<sub>2</sub>O<sub>3</sub> catalysts. *Catalysis Communications*, 27: 159-163.
- Pan, Q., Ramanathan, A., Snavely, W. K., Chaudhari, R. V. and Subramaniam, B. (2013). Synthesis and dehydration activity of novel Lewis acidic ordered mesoporous silicate: Zr-KIT-6. *Industrial & Engineering Chemistry Research*, 52: 15481-15487.
- Pan, Q., Ramanathan, A., Snavely, W. K., Chaudhari, R. V. and Subramaniam, B. (2014). Intrinsic kinetics of ethanol dehydration over Lewis acidic ordered mesoporous silicate, Zr-KIT-6. *Topics in Catalysis*, 57: 1407-1411.
- Pan, Z., Wang, R., Li, M., Chu, Y. and Chen, J. (2015). Deoxygenation of methyl laurate to hydrocarbons on silica-supported Ni-Mo phosphides: Effect of calcination temperatures of precursor. *Journal of Energy Chemistry*, 24: 77-86.
- Panchenko, V. N., Zaytseva, Y. A., Simonov, M. N., Simakova, I. L. and Paukshtis, E. A. (2014). DRIFTS and UV-vis DRS study of valeric acid ketonization mechanism over ZrO<sub>2</sub> in hydrogen atmosphere. *Journal of Molecular Catalysis A: Chemical*, 388-389: 133-140.

- Parida, K. and Mishra, H. K. (1999). Catalytic ketonisation of acetic acid over modified zirconia 1. Effect of alkali-metal cations as promoter. *Journal of Molecular Catalysis A: Chemical*, 139: 73-80.
- Park, J. Y. and Levenspiel, O. (1975). The crackling core model for the reaction of solid particles. *Chemical Engineering Science*, 30: 1207-1214.
- Parlouër, P. L. (2013). Thermal analysis and calorimetry techniques for catalytic investigations. In Auroux, A. (Ed.), *Calorimetry and thermal methods in catalysis* (pp. 51-102). Berlin: Springer.
- Pearson, R. G. (1985). The transition-metal-hydrogen bond. *Chemical Reviews*, 85: 41-49.
- Peng, B., Zhao, C., Mejía-Centeno, I., Fuentes, G. A., Jentys, A. and Lercher, J. A. (2012). Comparison of kinetics and reaction pathways for hydrodeoxygenation of C<sub>3</sub> alcohols on Pt/Al<sub>2</sub>O<sub>3</sub>. *Catalysis Today*, 183: 3-9.
- Peng, Y., Zhongyi, L., Wanqing, Z., Haijie, S. and Shouchang, L. (2010). Cu-Zn/Al<sub>2</sub>O<sub>3</sub> catalyst for the hydrogenation of esters to alcohols. *Chinese Journal of Catalysis*, 31: 769-775.
- Peralta, M. A., Sooknoi, T., Danuthai, T. and Resasco, D. E. (2009). Deoxygenation of benzaldehyde over CsNaX zeolites. *Journal of Molecular Catalysis A: Chemical*, 312: 78-86.
- Pestman, R., Koster, R. M., Pieterse, J. A. Z. and Ponec, V. (1997). Reactions of carboxylic acids on oxides 1. Selective hydrogenation of acetic acid to acetaldehyde. *Journal of Catalysis*, 168: 255-264.
- Pham, T. N., Shi, D., Sooknoi, T. and Resasco, D. E. (2012). Aqueous-phase ketonization of acetic acid over Ru/TiO<sub>2</sub>/carbon catalysts. *Journal of Catalysis*, 295: 169-178.
- Pillai, U. R., Sahle-Demessie, E. and Young, D. (2003). Maleic anhydride hydrogenation over Pd/Al<sub>2</sub>O<sub>3</sub> catalyst under supercritical CO<sub>2</sub> medium. *Applied Catalysis B: Environmental*, 43: 131-138.
- Pilling, M. J. and Seakins, P. W. (1995). *Reaction Kinetics* United States: Oxford University Press.

- Pineau, A., Kanari, N. and Gaballah, I. (2006). Kinetics of reduction of iron oxides by H<sub>2</sub> Part I: Low temperature reduction of hematite. *Thermochimica Acta*, 447: 89-100.
- Pitt, I. G., Gilbert, R. G. and Ryan, K. R. (1994). Application of transition-state theory to gas-surface reactions: Barrierless adsorption on clean surfaces. *Journal of Physical Chemistry*, 98: 13001-13010.
- Pitt, I. G., Gilbert, R. G. and Ryan, K. R. (1995a). The application of transition state theory to gas-surface reactions III. Lattice gas systems with adsorbate interactions. *Surface Science*, 326: 361-369.
- Pitt, I. G., Gilbert, R. G. and Ryan, K. R. (1995b). The application of transition state theory to gas-surface reactions in Langmuir systems. *Journal of Chemical Physics*, 102: 3461-3473.
- Platanitis, P., Panagiotou, G. D., Bourikas, K., Kodulis, C. and Lycourghiotis, A. (2014). Hydrodeoxygenation of phenol over hydrotreatment catalysts in their reduced and sulfided states. *Open Catalysis Journal*, 7: 18-25.
- Pokrovski, G. S., Schott, J., Hazemann, J.-L., Farges, F. and Pokrovsky, O. S. (2002). An X-ray absorption fine structure and nuclear magnetic resonance spectroscopy study of gallium-silica complexes in aqueous solution. *Geochimica et Cosmochimica Acta*, 66: 4203-4222.
- Poutsma, M. and Wolthuis, E. (1959). Clemmensen reduction of acetophenone. *Journal of Organic Chemistry*, 24: 875-877.
- Prasomsri, T., Nimmanwudipong, T. and Román-Leshkov, Y. (2013). Effective hydrodeoxygenation of biomass-derived oxygenates into unsaturated hydrocarbons by MoO<sub>3</sub> using low H<sub>2</sub> pressures. *Energy & Environmental Science*, 6: 1732-1738.
- Prasomsri, T., Shetty, M., Murugappan, K. and Román-Leshkov, Y. (2014). Insights into the catalytic activity and surface modification of MoO<sub>3</sub> during the hydrodeoxygenation of lignin-derived model compounds into aromatic hydrocarbons under low hydrogen pressures. *Energy & Environmental Science*, 7: 2660-2669.
- Prasomsri, T., To, A. T., Crossley, S., Alvarez, W. E. and Resasco, D. E. (2011). Catalytic conversion of anisole over HY and HZSM-5 zeolites in the presence of different hydrocarbon mixtures. *Applied Catalysis B: Environmental*, 106: 204-211.



- Procházková, D., Zámotný, P., Bejblova, M., Červený, L. and Čejka, J. (2007). Hydrodeoxygenation of aldehydes catalyzed by supported palladium catalysts. *Applied Catalysis A: General*, 332: 56-64.
- Puértolas, B., Keller, T. C., Mitchell, S. and Pérez-Ramírez, J. (2016). Deoxygenation of bio-oil over solid base catalysts: From model to realistic feeds. *Applied Catalysis B: Environmental*, 184: 77-86.
- Qian, E. W., Chen, N. and Gong, S. (2014). Role of support in deoxygenation and isomerization of methyl stearate over nickel-molybdenum catalysts. *Journal of Molecular Catalysis A: Chemical*, 387: 76-85.
- Qin, H., Guo, C., Sun, C. and Zhang, J. (2015). Influence of the support composition on the hydrogenation of methyl acetate over Cu/MgO-SiO<sub>2</sub> catalysts. *Journal of Molecular Catalysis A: Chemical*, 409: 79-84.
- Qin, L.-Z., Song, M.-J. and Chen, C.-L. (2010). Aqueous-phase deoxygenation of glycerol to 1,3-propanediol over Pt/WO<sub>3</sub>/ZrO<sub>2</sub> catalysts in a fixed-bed reactor. *Green Chemistry*, 12: 1466-1472.
- Qureshi, K. M., Kay Lup, A. N., Khan, S., Abnisa, F. and Wan Daud, W. M. A. (2018). A technical review on semi-continuous and continuous pyrolysis process of biomass to bio-oil. *Journal of Analytical and Applied Pyrolysis*, 131: 52-75.
- Ramanathan, A., Subramaniam, B., Maheswari, R. and Hanefeld, U. (2013). Synthesis and characterization of zirconium incorporated ultra large pore mesoporous silicate, Zr-KIT-6. *Microporous and Mesoporous Materials*, 167: 207-212.
- Redhead, P. A. (1962). Thermal desorption of gases. *Vacuum*, 12: 203-211.
- Ren, H., Chen, Y., Huang, Y., Deng, W., Vlachos, D. G. and Chen, J. G. (2014). Tungsten carbides as selective deoxygenation catalysts: experimental and computational studies of converting C<sub>3</sub> oxygenates to propene. *Green Chemistry*, 16: 761-769.
- Resasco, D. E. and Crossley, S. P. (2015). Implementation of concepts derived from model compound studies in the separation and conversion of bio-oil to fuel. *Catalysis Today*, 257: 185-199.
- Rezaei, P. S., Shafaghat, H. and Wan Daud, W. M. A. (2015). Origin of catalyst deactivation in atmospheric hydrogenolysis of *m*-cresol over Fe/HBeta. *RSC Advances*, 5: 51278-51285.

- Rismanchian, A., Chen, Y.-W. and Chuang, S. S. C. (2016). In situ infrared study of photoreaction of ethanol on Au and Ag/TiO<sub>2</sub>. *Catalysis Today*, 264: 16-22.
- Robinson, A., Ferguson, G. A., Gallagher, J. R., Cheah, S., Beckham, G. T., Schaidle, J. A., Hensley, J. E. and Medlin, J. W. (2016a). Enhanced hydrodeoxygenation of *m*-cresol over bimetallic Pt-Mo catalysts through an oxophilic metal-induced tautomerization pathway. *ACS Catalysis*, 6: 4356-4368.
- Robinson, A. M., Hensley, J. E. and Medlin, J. W. (2016b). Bifunctional catalysts for upgrading of biomass-derived oxygenated: A review. *ACS Catalysis*, 6: 5026-5043.
- Robinson, J. W., Skelly Frame, E. M. and Frame II, G. M. (2005). *Undergraduate Instrumental Analysis* (6th ed.). New York: Marcel Dekker.
- Romero, A., Alonso, E., Sastre, Á. and Nieto-Márquez, A. (2016). Conversion of biomass into sorbitol: Cellulose hydrolysis on MCM-48 and D-glucose hydrogenation on Ru/MCM-48. *Microporous and Mesoporous Materials*, 224: 1-8.
- Romero, Y., Richard, F. and Brunet, S. (2010). Hydrodeoxygenation of 2-ethylphenol as a model compound of bio-crude over sulfided Mo-based catalysts: Promoting effect and reaction mechanism. *Applied Catalysis B: Environmental*, 98: 213-223.
- Romero, Y., Richard, F., Renème, Y. and Brunet, S. (2009). Hydrodeoxygenation of benzofuran and its oxygenated derivatives (2,3-dihydrobenzofuran and 2-ethylphenol) over NiMoP/Al<sub>2</sub>O<sub>3</sub> catalyst. *Applied Catalysis A: General*, 353: 46-53.
- Rosa, D. D. S., Passatore, C. R. and de Macedo, J. R. N. (2015). The use of thermal volatilization analysis of polylactic acid and its blends with starch. In Tiwari, A. & Raj, B. (Eds.), *Reactions and mechanisms in thermal analysis of advanced materials* (pp. 269-284). Canada: Scrivener Publishing.
- Ruinart de Brimont, M., Dupont, C., Daudin, A., Geantet, C. and Raybaud, P. (2012). Deoxygenation mechanisms on Ni-promoted MoS<sub>2</sub> bulk catalysts: A combined experimental and theoretical study. *Journal of Catalysis*, 286: 153-164.
- Sá, J. and Śrębowata, A. (2016). *Hydrogenation with low-cost transition metals* Boca Raton: CRC Press.

- Sad, M. E., Neurock, M. and Iglesia, E. (2011). Formation of C-C and C-O bonds and oxygen removal in reactions of alkanediols, alkanols, and alkanals on copper catalysts. *Journal of the American Chemical Society*, 133: 20384-20398.
- Saidi, M., Rostami, P., Rahimpour, H. R., Fallah, M. A. R., Rahimpour, M. R., Gates, B. C. and Raeissi, S. (2015). Kinetics of upgrading of anisole with hydrogen catalyzed by platinum supported on alumina. *Energy & Fuels*, 29: 4990-4997.
- Samanya, J., Hornung, A., Apfelbacher, A. and Vale, P. (2012). Characteristics of the upper phase of bio-oil obtained from co-pyrolysis of sewage sludge with wood, rapeseed and straw. *Journal of Analytical and Applied Pyrolysis*, 94: 120-125.
- Samsonov, G. V. (1968). *Handbook of the physicochemical properties of the elements* New York: IFI/Plenum.
- Santiago, C. B., Milo, A. and Sigman, M. S. (2016). Developing a modern approach to account for steric effects in Hammett-type correlations. *Journal of the American Chemical Society*, 138: 13424-13430.
- Santillan-Jimenez, E., Morgan, T., Shoup, J., Harman-Ware, A. E. and Crocker, M. (2014). Catalytic deoxygenation of triglycerides and fatty acids to hydrocarbons over Ni-Al layered double hydroxide. *Catalysis Today*, 237: 136-144.
- Sapunov, V. N., Stepacheva, A. A., Sulman, E. M., Wärnå, J., Mäki-Arvela, P., Sulman, M. G., Sidorov, A. I., Stein, B. D., Murzin, D. Y. and Matveeva, V. G. (2017). Stearic acid hydrodeoxygenation over Pd nanoparticles embedded in mesoporous hypercrosslinked polystyrene. *Journal of Industrial and Engineering Chemistry*, 46: 426-435.
- Sautet, P. and Delbecq, F. (2010). Catalysis and surface organometallic chemistry: A view from theory and simulations. *Chemical Reviews*, 110: 1788-1806.
- Schabel, T., Belger, C. and Plietker, B. (2013). A mild chemoselective Ru-catalyzed reduction of alkynes, ketones, and nitro compounds. *Organic Letters*, 15: 2858-2861.
- Schimming, S. M., LaMont, O. D., König, M., Rogers, A. K., D'Amico, A. D., Yung, M. M. and Sievers, C. (2015). Hydrodeoxygenation of guaiacol over ceria-zirconia catalysts. *ChemSusChem*, 8: 2073-2083.
- Şenol, O. İ., Ryymin, E.-M., Viljava, T.-R. and Krause, A. O. I. (2007). Effect of hydrogen sulphide on the hydrodeoxygenation of aromatic and aliphatic

oxygenates on sulphided catalysts. *Journal of Molecular Catalysis A: Chemical*, 277: 107-112.

Şenol, O. İ., Viljava, T.-R. and Krause, A. O. I. (2005). Hydrodeoxygenation of methyl esters on sulphided NiMo/ $\gamma$ -Al<sub>2</sub>O<sub>3</sub> and CoMo/ $\gamma$ -Al<sub>2</sub>O<sub>3</sub> catalysts. *Catalysis Today*, 100: 331-335.

Sepulveda, C., Escalona, N., García, R., Laurenti, D. and Vrinat, M. (2012). Hydrodeoxygenation and hydrodesulfurization co-processing over ReS<sub>2</sub> supported catalysts. *Catalysis Today*, 195: 101-105.

Serrano-Ruiz, J. C., Pineda, A., Balu, A. M., Luque, R., Campelo, J. M., Romero, A. A. and Ramos-Fernández, J. M. (2012). Catalytic transformations of biomass-derived acids into advanced biofuels. *Catalysis Today*, 195: 162-168.

Serrano-Ruiz, J. C., Wang, D. and Dumesic, J. A. (2010). Catalytic upgrading of levulinic acid to 5-nonanone. *Green Chemistry*, 12: 574-577.

Šesták, J. and Berggren, G. (1971). Study of the kinetics of the mechanism of solid-state reactions at increasing temperatures. *Thermochimica Acta*, 3: 1-12.

Seyedmonir, S. R., Plischke, J. K., Vannice, M. A. and Young, H. W. (1990). Ethylene oxidation over small silver crystallites. *Journal of Catalysis*, 123: 534-549.

Seyedmonir, S. R., Strohmayer, D. E., Guskey, G. J., Geoffroy, G. L. and Vannice, M. A. (1985). Characterization of supported silver catalysts. III. Effects of support, pretreatment, and gaseous environment on the dispersion of Ag. *Journal of Catalysis*, 93: 288-302.

Shafaghat, H., Rezaei, P. S. and Wan Daud, W. M. A. (2016). Catalytic hydrodeoxygenation of simulated phenolic bio-oil to cycloalkanes and aromatic hydrocarbons over bifunctional metal/acid catalysts of Ni/HBeta, Fe/HBeta and NiFe/HBeta. *Journal of Industrial and Engineering Chemistry*, 35: 268-276.

Shahcheraghi, S. H. and Khayati, G. R. (2014a). Arrhenius parameters determination in non-isothermal conditions for mechanically activated Ag<sub>2</sub>O-graphite mixture. *Transactions of Nonferrous Metals Society of China*, 24: 3994-4003.

Shahcheraghi, S. H. and Khayati, G. R. (2014b). Kinetics analysis of non-isothermal decomposition of Ag<sub>2</sub>O-graphite mixture. *Transactions of Nonferrous Metals Society of China*, 24: 2991-3000.

- Shalaev, E. Y. and Steponkus, P. L. (2000). Correction of the sample weight in hermetically sealed DSC pans. *Thermochimica Acta*, 345: 141-143.
- Shen, W., Tompsett, G. A., Hammond, K. D., Xing, R., Dogan, F., Grey, C. P., Curtis Connor Jr., W., Auerbach, S. M. and Huber, G. W. (2011). Liquid phase aldol condensation reactions with MgO-ZrO<sub>2</sub> and shape-selective nitrogen-substituted NaY. *Applied Catalysis A: General*, 392: 57-68.
- Shi, H., Chen, J., Yang, Y. and Tian, S. (2014). Catalytic deoxygenation of methyl laurate as a model compound to hydrocarbons on nickel phosphide catalysts: Remarkable support effect. *Fuel Processing Technology*, 118: 161-170.
- Shi, Y., Zhang, X.-L., Feng, G., Chen, X. and Lu, Z.-H. (2015). Ag-SiO<sub>2</sub> nanocomposites with plum-pudding structure as catalyst for hydrogenation of 4-nitrophenol. *Ceramics International*, 41: 14660-14667.
- Shim, J., Jeong, D., Jang, W., Jeon, K., Jeon, B., Cho, S. Y., Roh, H., Na, J., Ko, C. H., Oh, Y. and Han, S. S. (2014). Deoxygenation of oleic acid over Ce<sub>(1-x)</sub>Zr<sub>(x)</sub>O<sub>2</sub> catalysts in hydrogen environment. *Renewable Energy*, 65: 36-40.
- Shiner, V. J. and Whittaker, D. (1969). A kinetic study of the Meerwein-Ponndorf-Verley reaction. *Journal of the American Chemical Society*, 91: 394-398.
- Silva, L. N., Fortes, I. C. P., de Sousa, F. P. and Pasa, V. M. D. (2016). Biokerosene and green diesel from macauba oils via catalytic deoxygenation over Pd/C. *Fuel*, 164: 329-338.
- Simakova, I., Simakova, O., Mäki-Arvela, P., Simakov, A., Estrada, M. and Murzin, D. Y. (2009). Deoxygenation of palmitic and stearic acid over supported Pd catalysts: Effect of metal dispersion. *Applied Catalysis A: General*, 355: 100-108.
- Simakova, I. L. and Murzin, D. Y. (2016). Transformation of bio-derived acids into fuel-like alkanes via ketonic decarboxylation and hydrodeoxygenation: Design of multifunctional catalyst, kinetic and mechanistic aspects. *Journal of Energy Chemistry*, 25: 208-224.
- Sitthisa, S., An, W. and Resasco, D. E. (2011a). Selective conversion of furfural to methylfuran over silica-supported Ni-Fe bimetallic catalysts. *Journal of Catalysis*, 284: 90-101.

- Sitthisa, S., Pham, T., Prasomsri, T., Sooknoi, T., Mallinson, R. G. and Resasco, D. E. (2011b). Conversion of furfural and 2-methylpentanal on Pd/SiO<sub>2</sub> and Pd-Cu/SiO<sub>2</sub> catalysts. *Journal of Catalysis*, 280: 17-27.
- Sitthisa, S. and Resasco, D. E. (2011). Hydrodeoxygenation of furfural over supported metal catalysts: A comparative study of Cu, Pd and Ni. *Catalysis Letters*, 141: 784-791.
- Sitthisa, S., Sooknoi, T., Ma, Y., Balbuena, P. B. and Resasco, D. E. (2011c). Kinetics and mechanism of hydrogenation of furfural on Cu/SiO<sub>2</sub> catalysts. *Journal of Catalysis*, 277: 1-13.
- Smirnov, A. A., Khromova, S. A., Ermakov, D. Y., Bulavchenko, O. A., Saraev, A. A., Aleksandrov, P. V., Kaichev, V. V. and Yakovlev, V. A. (2016). The composition of Ni-Mo phases obtained by NiMoO<sub>x</sub>-SiO<sub>2</sub> reduction and their catalytic properties in anisole hydrogenation. *Applied Catalysis A: General*, 514: 224-234.
- Soares, A. V. H., Salazar, J. B., Falcone, D. D., Vasconcellos, F. A., Davis, R. J. and Passos, F. B. (2016). A study of glycerol hydrogenolysis over Ru-Cu/Al<sub>2</sub>O<sub>3</sub> and Ru-Cu/ZrO<sub>2</sub> catalysts. *Journal of Molecular Catalysis A: Chemical*, 415: 27-36.
- Song, H., Gong, J., Song, H. and Li, F. (2015). A novel surface modification approach for synthesizing supported nickel phosphide catalysts with high activity for hydrodeoxygenation of benzofuran. *Applied Catalysis A: General*, 505: 267-275.
- Sooknoi, T., Danuthai, T., Lobban, L. L., Mallinson, R. G. and Resasco, D. E. (2008). Deoxygenation of methylesters over CsNaX. *Journal of Catalysis*, 258: 199-209.
- Speyer, R. F. (1994). *Thermal analysis of materials* USA: Marcel Dekker, Inc.
- Spivey, J. J., Roberts, G. W., Goodwin Jr., J. G., Kim, S. and Rhodes, W. D. (2004). Turnover frequencies in metal catalysis: Meanings, functionalities and relationships. In Spivey, J. J. & Roberts, G. W. (Eds.), *Catalysis* (pp. 320-348). UK: Royal Society of Chemistry.
- Srifa, A., Viriya-empikul, N., Assabumrungrat, S. and Faungnawakij, K. (2015). Catalytic behaviors of Ni/γ-Al<sub>2</sub>O<sub>3</sub> and Co/γ-Al<sub>2</sub>O<sub>3</sub> during the hydrodeoxygenation of palm oil. *Catalysis Science & Technology*, 5: 3693-3705.

- Stellwagen, D. R. and Bitter, J. H. (2015). Structure-performance relations of molybdenum- and tungsten carbide catalysts for deoxygenation. *Green Chemistry*, 17: 582-593.
- Stoltze, P. (2000). Microkinetic simulation of catalytic reactions. *Progress in Surface Science*, 65: 65-150.
- Stottlemeyer, A. L., Kelly, T. G., Meng, Q. and Chen, J. G. (2012). Reactions of oxygen-containing molecules on transition metal carbides: Surface science insight into potential applications in catalysis and electrocatalysis. *Surface Science Reports*, 67: 201-232.
- Stull, D. R. (1947). Vapor pressure of pure substances. Organic and inorganic compounds. *Industrial & Engineering Chemistry*, 39: 517-540.
- Su, C., Chen, C.-C., Tsai, C.-S., Lin, J.-L. and Lin, J.-C. (2006). The adsorption, thermal desorption and photochemistry of methyl iodide on an Ag-covered TiO<sub>2</sub>(110) surface. *Journal of the Chinese Chemical Society*, 53: 803-813.
- Sullivan, M. M., Chen, C.-J. and Bhan, A. (2016). Catalytic deoxygenation on transition metal carbide catalysts. *Catalysis Science & Technology*, 6: 602-616.
- Swanson, H. E., McMurdie, H. F., Morris, M. C. and Evans, E. H., National Bureau of Standards Monograph, 25, *Standard X-ray Diffraction Powder Patterns 7* United States Department of Commerce Washington D.C. 1969
- Taft, R. W. (1952a). Linear free energy relationships from rates of esterification and hydrolysis of aliphatic and ortho-substituted benzoate esters. *Journal of the American Chemical Society*, 74: 2729-2732.
- Taft, R. W. (1952b). Polar and steric substituent constants for aliphatic and *o*-benzoate groups from rates of esterification and hydrolysis of esters. *Journal of the American Chemical Society*, 74: 3120-3128.
- Tahara, K., Nagahara, E., Itoi, Y., Nishiyama, S., Tsuruya, S. and Masai, M. (1997). Liquid-phase hydrogenation of carboxylic acid on supported bimetallic Ru-Sn-alumina catalysts. *Applied Catalysis A: General*, 154: 75-86.
- Tanaka, K. (2010). Unsolved problem in catalysis. *Catalysis Today*, 154: 105-112.

- Taniguchi, S., Makino, T., Watanuki, H., Kojima, Y., Sano, M. and Miyake, T. (2011). Effect of Pt addition to Ru-Sn/Al<sub>2</sub>O<sub>3</sub> catalyst on hydrogenation of methyl laurate. *Applied Catalysis A: General*, 397: 171-173.
- Tauster, S. J. (1987). Strong metal-support interactions. *Accounts of Chemical Research*, 20: 389-394.
- Tauster, S. J., Fung, S. C. and Garten, R. L. (1978). Strong Metal-Support Interactions. Group 8 Noble Metals Supported on TiO<sub>2</sub>. *Journal of the American Chemical Society*, 100: 170-175.
- Tiernan, M. J., Barnes, P. A. and Parkes, G. M. B. (2001). Reduction of Iron Oxide Catalysts: The Investigation of Kinetic Parameters Using Rate Perturbation and Linear Heating Thermoanalytical Techniques. *Journal of Physical Chemistry B*, 105: 220-228.
- To, A. T. and Resasco, D. E. (2014). Role of a phenolic pool in the conversion of *m*-cresol to aromatics over HY and HZSM-5 zeolites. *Applied Catalysis A: General*, 487: 62-71.
- To, A. T. and Resasco, D. E. (2015). Hydride transfer between a phenolic surface pool and reactant paraffins in the catalytic cracking of *m*-cresol/hexanes mixtures over an HY zeolite. *Journal of Catalysis*, 329: 57-68.
- Tran, N. T. T., Uemura, Y., Chowdhury, S. and Ramli, A. (2016). Vapor-phase hydrodeoxygenation of guaiacol on Al-MCM-41 supported Ni and Co catalysts. *Applied Catalysis A: General*, 512: 93-100.
- Truhlar, D. G., Garrett, B. C. and Klippenstein, S. J. (1996). Current status of transition-state theory. *Journal of Physical Chemistry*, 100: 12771-12800.
- Turáková, M., Salmi, T., Eränen, K., Wärnå, J., Murzin, D. Y. and Králik, M. (2015). Liquid phase hydrogenation of nitrobenzene. *Applied Catalysis A: General*, 499: 66-76.
- Upadhyay, S. K. (2006). *Chemical kinetics and reaction dynamics* India: Anamaya Publishers.
- Upare, D. P., Park, S., Kim, M. S., Jeon, Y.-P., Kim, J., Lee, D., Lee, J., Chang, H., Choi, S., Choi, W., Park, Y.-K. and Lee, C. W. (2017). Selective hydrocracking of pyrolysis fuel oil into benzene, toluene and xylene over CoMo/beta zeolite catalyst. *Journal of Industrial and Engineering Chemistry*, 46: 356-363.



- Upare, P. P., Lee, M., Lee, S.-K., Yoon, J. W., Bae, J., Hwang, D. W., Lee, U.-H., Chang, J.-S. and Hwang, Y. K. (2016). Ru nanoparticles supported graphene oxide catalyst for hydrogenation of bio-based levulinic acid to cyclic ethers. *Catalysis Today*, 265: 174-183.
- Van Sice, C. D. (1996). Random nucleation and growth kinetics. *Physical Review B*, 54: 11845-11848.
- Vilcoq, L., Cabiac, A., Especel, C., Lacombe, S. and Duprez, D. (2014). New insights into the mechanism of sorbitol transformation over an original bifunctional catalytic system. *Journal of Catalysis*, 320: 16-25.
- Vlaev, L. T., Georgieva, V. G. and Tavlieva, P. (2015). On the kinetic mechanism of non-isothermal degradation of solids. In Tiwari, A. & Raj, B. (Eds.), *Reactions and mechanisms in thermal analysis of advanced materials* (pp. 547-578). Canada: Scrivener Publishing.
- Vuurman, M. A. and Wachs, I. E. (1992). In situ Raman spectroscopy of alumina-supported metal oxide catalysts. *Journal of Physical Chemistry*, 96: 5008-5016.
- Wachs, I. E. (1996). Raman and IR studies of surface metal oxide species on oxide supports: Supported metal oxide catalysts. *Catalysis Today*, 27: 437-455.
- Wang, H.-Y., Jiao, T.-T., Li, Z.-X., Li, C.-S., Zhang, S.-J. and Zhang, J.-L. (2015a). Study on palm oil hydrogenation for clean fuel over Ni-Mo-W/ $\gamma$ -Al<sub>2</sub>O<sub>3</sub>-ZSM-5 catalyst. *Fuel Processing Technology*, 139: 91-99.
- Wang, L., Wan, H., Jin, S., Chen, X., Li, C. and Liang, C. (2015b). Hydrodeoxygenation of dibenzofuran over SiO<sub>2</sub>, Al<sub>2</sub>O<sub>3</sub>/SiO<sub>2</sub> and ZrO<sub>2</sub>/SiO<sub>2</sub> supported Pt catalysts. *Catalysis Science & Technology*, 5: 465-474.
- Wang, L., Yuan, F., Liu, L., Mominou, N., Li, S., Li, C. and Wang, W. (2015c). Transformations of phenol into fuel over TiO<sub>2</sub>-CeO<sub>2</sub>/ZSM-5 aided by ultrasound and ultraviolet. *Journal of Industrial and Engineering Chemistry*, 21: 494-499.
- Wang, L., Zhang, M., Zhang, M., Sha, G. and Liang, C. (2013). Hydrodeoxygenation of dibenzofuran over mesoporous silica COK-12 supported palladium catalysts. *Energy & Fuels*, 27: 2209-2217.
- Wang, W., Li, L., Wu, K., Zhang, K., Jie, J. and Yang, Y. (2015d). Preparation of Ni-Mo-S catalysts by hydrothermal method and their hydrodeoxygenation properties. *Applied Catalysis A: General*, 495: 8-16.

- Wang, W., Yang, Y., Bao, J. and Luo, H.-A. (2009). Characterization and catalytic properties of Ni-Mo-B amorphous catalysts for phenol hydrodeoxygenation. *Catalysis Communications*, 11: 100-105.
- Wang, W., Zhang, K., Li, L., Wu, K., Liu, P. and Yang, Y. (2014a). Synthesis of highly active Co-Mo-S unsupported catalysts by a one-step hydrothermal method for *p*-cresol hydrodeoxygenation. *Industrial & Engineering Chemistry Research*, 53: 19001-19009.
- Wang, Z., Li, G., Liu, X., Huang, Y., Wang, A., Chu, W., Wang, X. and Li, N. (2014b). Aqueous phase hydrogenation of acetic acid to ethanol over Ir-MoO<sub>x</sub>/SiO<sub>2</sub> catalyst. *Catalysis Communications*, 43: 38-41.
- Wang, Z., Pholjaroen, B., Li, M., Dong, W., Li, N., Wang, A., Wang, X., Cong, Y. and Zhang, T. (2014c). Chemoselective hydrogenolysis of tetrahydrofurfuryl alcohol to 1,5-pentanediol over Ir-MoO<sub>x</sub>/SiO<sub>2</sub> catalyst. *Journal of Energy Chemistry*, 23: 427-434.
- Waterhouse, G. I. N., Bowmaker, G. A. and Metson, J. B. (2001). The thermal decomposition of silver (I, III) oxide: A combined XRD, FT-IR and Raman spectroscopic study. *Physical Chemistry Chemical Physics*, 3: 3838-3845.
- Wei, K., Li, W., Koike, K. and Nikaido, T. (2005). Cobalt(II)-catalyzed intermolecular Diels-Alder reaction of piperine. *Organic Letters*, 7: 2833-2835.
- Wendlandt, W. W. (1986). *Thermal Analysis* (3rd ed.). USA: Wiley.
- Wendlandt, W. W. and Gallagher, P. K. (1981). Instrumentation. In Turi, E. A. (Ed.), *Thermal characterization of polymeric materials* (pp. USA: Academic Press, Inc.
- Wettstein, S. G., Bond, J. Q., Alonso, D. M., Pham, H. N., Datye, A. K. and Dumesic, J. A. (2012). RuSn bimetallic catalysts for selective hydrogenation of levulinic acid to  $\gamma$ -valerolactone. *Applied Catalysis B: Environmental*, 117-118: 321-329.
- Widayatno, W. B., Guan, G., Rizkiana, J., Yang, J., Hao, X., Tsutsumi, A. and Abudula, A. (2016). Upgrading of bio-oil from biomass pyrolysis over Cu-modified  $\beta$ -zeolite catalyst with high selectivity and stability. *Applied Catalysis B: Environmental*, 186: 166-172.

- Wimmers, O. J., Arnoldy, P. and Moulijn, J. A. (1986). Determination of the Reduction Mechanism by Temperature-Programmed Reduction: Application to Small Fe<sub>2</sub>O<sub>3</sub> Particles. *Journal of Physical Chemistry*, 90: 1331-1337.
- Wu, Q., Zhang, C., Zhang, B., Li, X., Ying, Z., Liu, T., Lin, W., Yu, Y., Cheng, H. and Zhao, F. (2016). Highly selective Pt/ordered mesoporous TiO<sub>2</sub>-SiO<sub>2</sub> catalysts for hydrogenation of cinnamaldehyde: The promoting role of Ti<sup>2+</sup>. *Journal of Colloid and Interface Science*, 463: 75-82.
- Wu, S.-K., Lai, P.-C., Lin, Y.-C., Wan, H.-P., Lee, H.-T. and Chang, Y.-H. (2013). Atmospheric hydrodeoxygenation of guaiacol over alumina-, zirconia-, and silica-supported nickel phosphide catalysts. *ACS Sustainable Chemistry & Engineering*, 1: 349-358.
- Wunderlich, B. (2005). *Thermal analysis of polymeric materials* Netherlands: Springer.
- Xin, B., Jing, L., Ren, Z., Wang, B. and Fu, H. (2005). Effects of simultaneously doped and deposited Ag on the photocatalytic activity and surface states of TiO<sub>2</sub>. *Journal of Physical Chemistry B*, 109: 2805-2809.
- Xing, S., Lv, P., Fu, J., Wang, J., Fan, P., Yang, L. and Yuan, Z. (2017). Direct synthesis and characterization of pore-broadened Al-SBA-15. *Microporous and Mesoporous Materials*, 239: 316-327.
- Xiong, K., Yu, W. and Chen, J. G. (2014). Selective deoxygenation of aldehydes and alcohols on molybdenum carbide (Mo<sub>2</sub>C) surfaces. *Applied Surface Science*, 323: 88-95.
- Xiong, W., Wang, K.-J., Liu, X.-W., Hao, F., Xiao, H.-Y., Liu, P.-L. and Luo, H.-A. (2016). 1,5-Dinitronaphthalene hydrogenation to 1,5-diaminonaphthalene over carbon nanotube supported non-noble metal catalysts under mild conditions. *Applied Catalysis A: General*, 514: 126-134.
- Yang, H., Huang, C., Yang, F., Yang, X., Du, L. and Liao, S. (2015). Mesoporous silica nanoparticle supported PdIr bimetal catalyst for selective hydrogenation, and the significant promotional effect of Ir. *Applied Surface Science*, 357: 558-563.
- Yang, Y., Gilbert, A. and Xu, C. (2009). Hydrodeoxygenation of bio-crude in supercritical hexane with sulfided CoMo and CoMoP catalysts supported on MgO: A model compound study using phenol. *Applied Catalysis A: General*, 360: 242-249.

- Yang, Y., Ochoa-Hernández, C., de la Peña O'Shea, V. A., Pizarro, P., Coronado, J. M. and Serrano, D. P. (2014). Effect of metal-support interactions on the selective hydrodeoxygenation of anisole to aromatics over Ni-based catalysts. *Applied Catalysis B: Environmental*, 145: 91-100.
- Ye, C.-L., Guo, C.-L. and Zhang, J.-L. (2016). Highly active and stable CeO<sub>2</sub>-SiO<sub>2</sub> supported Cu catalysts for the hydrogenation of methyl acetate to ethanol. *Fuel Processing Technology*, 143: 219-224.
- Yildiz, G., Lathouwers, T., Toraman, H. E., Van Geem, K. M., Marin, G. B., Ronsse, F., van Duren, R., Kersten, S. R. A. and Prins, W. (2014). Catalytic fast pyrolysis of pine wood: Effect of successive catalyst regeneration. *Energy & Fuels*, 28: 4560-4572.
- Yoon, K. J. and Albert Vannice, M. (1983). Benzene hydrogenation over iron: II. Reaction model over unsupported and supported catalysts. *Journal of Catalysis*, 82: 457-468.
- Yoosuk, B., Tumnantong, D. and Prasassarakich, P. (2012). Amorphous unsupported Ni-Mo sulfide prepared by one step hydrothermal method for phenol hydrodeoxygenation. *Fuel*, 91: 246-252.
- Yu, W., Xiong, K., Ji, N., Porosoff, M. D. and Chen, J. G. (2014). Theoretical and experimental studies of the adsorption geometry and reaction pathways of furfural over FeNi bimetallic model surfaces and supported catalysts. *Journal of Catalysis*, 317: 253-262.
- Yun, Y. and Lee, G.-B. (1999). Effects of pressure in coal pyrolysis observed by high pressure TGA. *Korean Journal of Chemical Engineering*, 16: 798-803.
- Zabeti, M., Wan Daud, W. M. A. and Aroua, M. K. (2009). Activity of solid catalysts for biodiesel production: A review. *Fuel Processing Technology*, 90: 770-777.
- Zaccheria, F., Ravasio, N., Ercoli, M. and Allegrini, P. (2005). Heterogeneous Cu-catalysts for the reductive deoxygenation of aromatic ketones without additives. *Tetrahedron Letters*, 46: 7743-7745.
- Zanuttini, M. S., Dalla Costa, B. O., Querini, C. A. and Peralta, M. A. (2014). Hydrodeoxygenation of *m*-cresol with Pt supported over mild acid materials. *Applied Catalysis A: General*, 482: 352-361.

- Zanuttini, M. S., Lago, C. D., Querini, C. A. and Peralta, M. A. (2013). Deoxygenation of *m*-cresol on Pt/ $\gamma$ -Al<sub>2</sub>O<sub>3</sub> catalysts. *Catalysis Today*, 213: 9-17.
- Zanuttini, M. S., Peralta, M. A. and Querini, C. A. (2015). Deoxygenation of *m*-cresol: Deactivation and regeneration of Pt/ $\gamma$ -Al<sub>2</sub>O<sub>3</sub> catalysts. *Industrial & Engineering Chemistry Research*, 54: 4929-4939.
- Zardin, L. and Perez-Lopez, O. W. (2017). Hydrogen production by methane decomposition over Co-Al mixed oxides derived from hydrotalcites: Effect of the catalyst activation with H<sub>2</sub> or CH<sub>4</sub>. *International Journal of Hydrogen Energy*, 42: 7895-7907.
- Zhang, C., Chen, L., Cheng, H., Zhu, X. and Qi, Z. (2016). Atomically dispersed Pd catalysts for the selective hydrogenation of succinic acid to  $\gamma$ -butyrolactone. *Catalysis Today*, 276: 55-61.
- Zhang, D., Yin, H., Ge, C., Xue, J., Jiang, T., Yu, L. and Shen, Y. (2009). Selective hydrogenation of maleic anhydride to  $\gamma$ -butyrolactone and tetrahydrofuran by Cu-Zn-Zr catalyst in the presence of ethanol. *Journal of Industrial and Engineering Chemistry*, 15: 537-543.
- Zhang, G. and Ostrovski, O. (2001). Kinetic Modeling of Titania Reduction by a Methane-Hydrogen-Argon Gas Mixture. *Metallurgical and Materials Transactions B*, 32: 465-473.
- Zhang, H., Lin, H. and Zheng, Y. (2014). The role of cobalt and nickel in deoxygenation of vegetable oils. *Applied Catalysis B: Environmental*, 160-161: 415-422.
- Zhang, J., Ellis, L. D., Wang, B., Dzara, M. J., Sievers, C., Pylypenko, S., Nikolla, E. and Medlin, J. W. (2018). Control of interfacial acid-metal catalysis with organic monolayers. *Nature Catalysis*, 1: 148-155.
- Zhang, J., Li, Y., Zhang, Y., Chen, M., Wang, L., Zhang, C. and He, H. (2015). Effect of support on the activity of Ag-based catalysts for formaldehyde oxidation. *Scientific Reports*, 5: 12950-12959.
- Zhang, J., Wang, B., Nikolla, E. and Medlin, J. W. (2017). Directing reaction pathways through controlled reactant binding at Pd-TiO<sub>2</sub> interfaces. *Angewandte Chemie*, 56: 1-6.

- Zhang, Q., Jie, C., Wang, T. and Xu, Y. (2007). Review of biomass pyrolysis oil properties and upgrading research. *Energy Conversion and Management*, 48: 87-92.
- Zhang, R., Yin, H., Zhang, D., Qi, L., Lu, H., Shen, Y. and Jiang, T. (2008). Gas phase hydrogenation of maleic anhydride to tetrahydrofuran by Cu/ZnO/TiO<sub>2</sub> catalysts in the presence of *n*-butanol. *Chemical Engineering Journal*, 140: 488-496.
- Zhang, S., Duan, X., Ye, L., Lin, H., Xie, Z. and Yuan, Y. (2013a). Production of ethanol by gas phase hydrogenation of acetic acid over carbon nanotube-supported Pt-Sn nanoparticles. *Catalysis Today*, 215: 260-266.
- Zhang, X., Wang, T., Ma, L., Zhang, Q., Huang, X. and Yu, Y. (2013b). Production of cyclohexane from lignin degradation compounds over Ni/ZrO<sub>2</sub>-SiO<sub>2</sub> catalysts. *Applied Energy*, 112: 533-538.
- Zhang, X., Zhang, Q., Wang, T., Ma, L., Yu, Y. and Chen, L. (2013c). Hydrodeoxygenation of lignin-derived phenolic compounds to hydrocarbons over Ni/SiO<sub>2</sub>-ZrO<sub>2</sub> catalysts. *Bioresource Technology*, 134: 73-80.
- Zhao, C., Camaioni, D. M. and Lercher, J. A. (2012a). Selective catalytic hydroalkylation and deoxygenation of substituted phenols to bicycloalkanes. *Journal of Catalysis*, 288: 92-103.
- Zhao, C., He, J., Lemonidou, A. A., Li, X. and Lercher, J. A. (2011). Aqueous-phase hydrodeoxygenation of bio-derived phenols to cycloalkanes. *Journal of Catalysis*, 280: 8-16.
- Zhao, C., Kasakov, S., He, J. and Lercher, J. A. (2012b). Comparison of kinetics, activity and stability of Ni/HZSM-5 and Ni/Al<sub>2</sub>O<sub>3</sub>-HZSM-5 for phenol hydrodeoxygenation. *Journal of Catalysis*, 296: 12-23.
- Zhao, X., Wei, L., Cheng, S., Cao, Y., Julson, J. and Gu, Z. (2015). Catalytic cracking of carinata oil for hydrocarbon biofuel over fresh and regenerated Zn/Na-ZSM-5. *Applied Catalysis A: General*, 507: 44-55.
- Zhao, Z. and Yang, H. (2015). Ni-W<sub>2</sub>C/mpg-C<sub>3</sub>N<sub>4</sub> as a promising catalyst for selective hydrogenation of nitroarenes to corresponding aryl amines in the presence of Lewis acid. *Journal of Molecular Catalysis A: Chemical*, 398: 268-274.
- Zhu, J., Wu, F., Li, M., Zhu, J., van Ommen, J. G. and Lefferts, L. (2015). Influence of internal diffusion on selective hydrogenation of 4-carboxybenzaldehyde over

palladium catalysts supported on carbon nanofiber coated monolith. *Applied Catalysis A: General*, 498: 222-229.

Zhu, X., Lobban, L. L., Mallinson, R. G. and Resasco, D. E. (2011). Bifunctional transalkylation and hydrodeoxygenation of anisole over a Pt/HBeta catalyst. *Journal of Catalysis*, 281: 21-29.

University of Malaya

## LIST OF PUBLICATIONS AND PAPERS PRESENTED

### ISI-indexed academic journals (Published)

- Kay Lup, A. N.,** Abnisa, F., Wan Daud, W. M. A. and Aroua, M. K. (2019). Atmospheric hydrodeoxygenation of phenol as pyrolytic oil model compound for hydrocarbon production using Ag/TiO<sub>2</sub> catalyst. *Asia-Pacific Journal of Chemical Engineering*, DOI: 10.1002/apj.2293
- Kay Lup, A. N.,** Abnisa, F., Wan Daud, W. M. A. and Aroua, M. K. (2018). Synergistic interaction of metal-acid sites for phenol hydrodeoxygenation over bifunctional Ag/TiO<sub>2</sub> nanocatalyst. *Chinese Journal of Chemical Engineering*, DOI: 10.1016/j.cjche.2018.08.028
- Kay Lup, A. N.,** Abnisa, F., Wan Daud, W. M. A. and Aroua, M. K. (2018). Delayed volatiles release phenomenon at higher temperature in TGA via sample encapsulation technique. *Fuel*, 234: 422-429.
- Kay Lup, A. N.,** Abnisa, F., Wan Daud, W. M. A. and Aroua, M. K. (2017). A review on reaction mechanism of metal-catalyzed deoxygenation process in bio-oil model compounds. *Applied Catalysis A: General*, 541: 87-106.
- Kay Lup, A. N.,** Abnisa, F., Wan Daud, W. M. A. and Aroua, M. K. (2017). A review on reactivity and stability of heterogeneous metal catalysts for deoxygenation of bio-oil model compounds. *Journal of Industrial and Engineering Chemistry*, 56: 1-34.

### ISI-indexed academic journals (Received in revised form)

- Kay Lup, A. N.,** Abnisa, F., Wan Daud, W. M. A. and Aroua, M. K. Temperature programmed reduction of silver(I) oxide in titania supported silver catalyst under H<sub>2</sub> atmosphere (*Journal of the Chinese Chemical Society*)

### Conference proceedings

- Kay Lup, A. N.,** Abnisa, F., Wan Daud, W. M. A. and Aroua, M. K. (2018). Acidity, oxophilicity and hydrogen sticking probability of supported metal catalysts for hydrodeoxygenation process. *IOP Conference Series: Materials Science and Engineering*, 334: 1-6.

### Intellectual property rights (Patent)

- Kay Lup, A. N. (main inventor),** Abnisa, F. and Wan Daud, W. M. A. Device for thermogravimetric analysis of catalytic gas-solid reactions, PI2018002656.



## **Research and publication awards**

**1<sup>st</sup> Runner up (Overall) and Gold medalist** in Malaysia National Nanotechnology Olympiad 2018 by Ministry of Energy, Science, Technology, Environment and Climate Change (MESTECC), *National level*.

**2<sup>nd</sup> Runner up** in Young Persons' World Lecture Competition 2018 by The Institute of Materials, Minerals and Mining (IOM<sup>3</sup>), *International level*, Malaysia finalist.

**1<sup>st</sup> place** in Materials Lecture Competition 2018 by Institute of Materials Malaysia (IMM), *National level*, University of Malaya finalist.

**1<sup>st</sup> place** in Materials Lecture Competition 2018 by Centre of Advanced Materials (CAM), *University level*.

**Top 15 PhD research project** in Nanotechnology Innovation Research Project Competition 2018 by Ministry of Energy, Science, Technology, Environment and Climate Change (MESTECC), *National level*.

**National finalist** of 3-Minute Thesis Competition 2018.

**2<sup>nd</sup> Runner up** in 3-Minute Thesis Competition 2018 by University of Malaya, *University level*, Faculty finalist

**1<sup>st</sup> place** in 3-Minute Thesis Competition 2018 by Faculty of Engineering, University of Malaya, *Faculty level*.

**National finalist** of Falling Walls Lab Malaysia 2018.

**Silver medalist** in Olympiad Nanotechnology Malaysia 2017 by Ministry of Science, Technology and Innovation (MOSTI), *National level*.

**Best oral presenter award** in Chemical Reaction Engineering, Polymer & Composite Materials in the 3<sup>rd</sup> International Conference on Chemical Engineering Sciences and Applications 2017 (ICChESA), *International level*.



# Atmospheric hydrodeoxygenation of phenol as pyrolytic-oil model compound for hydrocarbon production using Ag/TiO<sub>2</sub> catalyst

Andrew Ng Kay Lup<sup>1</sup> | Faisal Abnisa<sup>2</sup> | Wan Mohd Ashri Wan Daud<sup>1</sup> | Mohamed Kheireddine Aroua<sup>3,4</sup>

<sup>1</sup>Department of Chemical Engineering, Faculty of Engineering, University of Malaya, Kuala Lumpur, Malaysia

<sup>2</sup>Department of Chemical and Material Engineering, Faculty of Engineering, King Abdulaziz University, Jeddah, Saudi Arabia

<sup>3</sup>Centre for Carbon Dioxide Capture and Utilization, School of Science and Technology, Sunway University, Petaling Jaya, Malaysia

<sup>4</sup>Department of Engineering, Lancaster University, Lancaster, UK

## Correspondence

Andrew Ng Kay Lup, Department of Chemical Engineering, Faculty of Engineering, University of Malaya, 50603 Kuala Lumpur, Malaysia.  
Email: drewanyak@hotmail.com

## Funding information

University of Malaya, Grant/Award Number: MO008-2015

## Abstract

Hydrodeoxygenation (HDO) kinetics of phenol over Ag/TiO<sub>2</sub> catalyst was investigated at 415–600 K and 1 atm. The use of oxophilic TiO<sub>2</sub> support has improved phenol conversion due to its preferential activation of C–O bond. Product analysis confirmed the occurrence of direct deoxygenation (DDO) and hydrogenation–dehydration (HYD) pathways to produce benzene and cyclohexane, respectively. Both phenol hydrogenolysis and hydrogenation steps are the respective rate-limiting steps for DDO and HYD pathways of phenol HDO over Ag/TiO<sub>2</sub>. Based on the transition state theory, negative entropy changes of activation during HDO indicated that the HDO reactants formed activated complexes that had more orderly bonding configurations prior to the hydrogenolysis, hydrogenation, and dehydration steps. Under the present conditions, the catalyst was stable after 4 hr of HDO runs and able to be regenerated via H<sub>2</sub>-activation and calcination in air at 553 K with at least 98.9% removal efficiency to remove coke deposits and reform Ag metal species after HDO.

## KEYWORDS

Gas-phase hydrodeoxygenation, Kinetic modeling, Phenol, Silver catalyst, Titania support

## 1 | INTRODUCTION

Oxygen removal is a fundamental bio-oil or pyrolytic oil-upgrading step to produce liquid fuel of higher heating value and lower oxygen content. This is because bio-oil generally has high oxygen content which leads to its deficiencies in being used as liquid fuel. Issues such as thermal instability, high corrosivity, and low heating value were often due to the oxygenated compounds within bio-oil. Bio-oil contains a complex mixture of more than 400 O-containing compounds that were produced during pyrolysis of lignocellulosic biomass.<sup>1</sup> When lignocellulosic biomass is pyrolyzed, lignin-, cellulose-

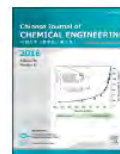
and hemicellulose-based components within the biomass undergo fragmentation and depolymerization to form oxygenated compounds such as phenolics, furans, acids, alcohols, carbonyls, and ethers. The compositions of these oxygenated compounds in bio-oils are highly dependent on the biomass source<sup>2–4</sup> and the pyrolysis conditions.<sup>5,6</sup> Among these oxygenated compounds, phenolics deoxygenation remained the toughest due to their high C–O bond dissociation energies.<sup>7,8</sup>

Phenolics deoxygenation is often accomplished via hydrodeoxygenation (HDO).<sup>9</sup> There are various phenolic model compounds being studied for phenolic HDO such as guaiacol, cresol, anisole, and vanillin. Phenol is



Contents lists available at ScienceDirect

Chinese Journal of Chemical Engineering

journal homepage: [www.elsevier.com/locate/CJChE](http://www.elsevier.com/locate/CJChE)

## Article

Synergistic interaction of metal–acid sites for phenol hydrodeoxygenation over bifunctional Ag/TiO<sub>2</sub> nanocatalystAndrew Ng Kay Lup<sup>1</sup>, Faisal Abnisa<sup>1,\*</sup>, Wan Mohd Ashri Wan Daud<sup>1,\*</sup>, Mohamed Kheireddine Aroua<sup>2,3</sup><sup>1</sup> Department of Chemical Engineering, Faculty of Engineering, University of Malaya, 50603 Kuala Lumpur, Malaysia<sup>2</sup> Centre for Carbon Dioxide Capture and Utilization, School of Science and Technology, Sunway University, Bandar Sunway, 47500 Petaling Jaya, Malaysia<sup>3</sup> Department of Engineering, Lancaster University, Lancaster LA1 4YW, UK

## ARTICLE INFO

## Article history:

Received 28 February 2018

Received in revised form 31 July 2018

Accepted 28 August 2018

Available online xxxxx

## Keywords:

Silver based catalyst

Physicochemical properties

Hydrogen spillover

Metal–acid sites

Hydrodeoxygenation

## ABSTRACT

The use of silver metal for hydrodeoxygenation (HDO) applications is scarce and different studies have indicated of its varying HDO activity. Several computational studies have reported of silver having almost zero turnover frequency for HDO owing to its high C–O bond breaking energy barrier and low carbon and oxygen binding energies. Herein this work, titania supported silver catalysts were synthesized and firstly used to examine its phenol HDO activity via experimental reaction runs. BET, XRD, FESEM, TEM, EDX, ICP–OES, Pyridine-FTIR, NH<sub>3</sub>-TPD and H<sub>2</sub>-TPD analyses were done to investigate its physicochemical properties. Phenomena of hydrogen spillover and metal–acid site synergy were examined in this study. With the aid of TiO<sub>2</sub> reducible support, hydrogen spillover and metal–acid site interactions were observed to a certain extent but were not as superior as other Pt, Pd, Ni-based catalysts used in other HDO studies. The experimental findings showed that Ag/TiO<sub>2</sub> catalyst has mediocre phenol conversion but high benzene selectivity which confirms the explanation from other computational studies.

© 2018 The Chemical Industry and Engineering Society of China, and Chemical Industry Press. All rights reserved.

## 1. Introduction

The use of bifunctional metal–acid catalyst has been known to be effective for hydrodeoxygenation (HDO) of phenolic compounds in bio-oil [1,2]. These catalysts contain metal and acid sites which are instrumental in catalyzing several reactions occurring in hydrodeoxygenation. For instance, metal sites catalyze hydrogenation and hydrogenolysis reactions while acid sites catalyze dehydration, transalkylation, isomerization, alkylation and condensation reactions [3,4]. Likewise, metal sites promote hydrogen adsorption and activation whereas acid sites promote adsorption and activation of O-containing model compounds through formation of oxygen vacancies [5,6]. For phenolic HDO, removal of hydroxyl group (–OH) from phenolics could occur through: (i) direct hydrogenolysis of C<sub>aromatic</sub>–OH bond to form deoxygenated aromatics; (ii) phenyl ring hydrogenation to form cycloalcohol intermediate which dehydrates and hydrogenates to form cycloalkane; (iii) phenolic tautomerization to form keto intermediates that undergoes –C=O hydrogenation and dehydration to form deoxygenated aromatics [1].

The catalytic roles of acid and metal sites of HDO catalyst were well established in past studies. For HDO catalyst to exhibit excellent HDO activity, validation of the existence and nature of acid and metal sites

in catalyst is not suffice. In fact, the synergistic interactions of both sites had to be analyzed in order to further understand the HDO mechanism occurring at both sites within the catalyst. Synergy of acid and metal sites is also important for the surface migration of activated hydrogen species from metal site to acid site which is known as hydrogen spillover [7]. Hydrogen spillover is commonly made more possible by having both sides existing in close proximity. Nevertheless, physicochemical properties of the selected metal and support are also important in influencing chemisorption and activation of phenolics in the presence of hydrogen. Therefore, proper designing of a bifunctional catalyst model for HDO is necessary to ensure efficient hydrogen spillover and optimal surface acidity for excellent hydrogenolysis of C–OH bond in phenolics.

Metal-promoted zeolite is one of the bifunctional metal–acid catalysts reported to have good HDO activity owing to the presence of metal sites and high surface acidity [8]. However, high surface acidity has also been known to favor secondary condensation reactions which would lead to severe catalytic coking [9]. Thus, mild acid supports such as Al<sub>2</sub>O<sub>3</sub>, TiO<sub>2</sub>, ZrO<sub>2</sub> and CeO<sub>2</sub> may offer better coking resistance while having optimal acid sites for hydrogenolysis in HDO. Among these, TiO<sub>2</sub> has been increasingly studied on due to its support reducibility, metal–support interaction and higher oxophilicity for C–O bond scission [10–13]. Besides using acidic metal oxides as HDO catalyst supports, they have also been used as promoters [14] and ligands [15] which were respectively reported to improve hydrogenolysis activity and to tune the Brønsted acid strength of catalyst. Likewise, many

\* Corresponding authors.

E-mail addresses: [drewanyak@hotmail.com](mailto:drewanyak@hotmail.com) (A.N. Kay Lup), [faisalabnisa@um.edu.my](mailto:faisalabnisa@um.edu.my), [faisalabnisa@gmail.com](mailto:faisalabnisa@gmail.com) (F. Abnisa), [ashri@um.edu.my](mailto:ashri@um.edu.my) (W.M.A.W. Daud), [kheireddinea@sunway.edu.my](mailto:kheireddinea@sunway.edu.my) (M.K. Aroua).<https://doi.org/10.1016/j.cjche.2018.08.028>

1004-9541/© 2018 The Chemical Industry and Engineering Society of China, and Chemical Industry Press. All rights reserved.

Please cite this article as: A.N. Kay Lup, et al., Synergistic interaction of metal–acid sites for phenol hydrodeoxygenation over bifunctional Ag/TiO<sub>2</sub> nanocatalyst, *Chin. J. Chem. Eng.* (2018), <https://doi.org/10.1016/j.cjche.2018.08.028>



## Full Length Article

## Delayed volatiles release phenomenon at higher temperature in TGA via sample encapsulation technique

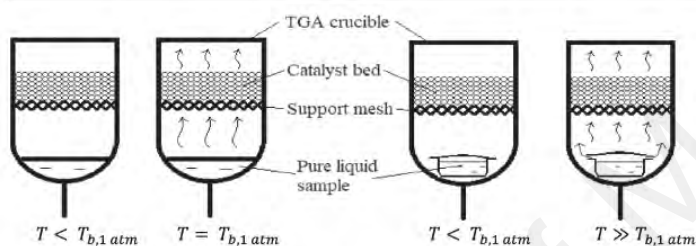
Andrew Ng Kay Lup<sup>a</sup>, Faisal Abnisa<sup>a,\*</sup>, Wan Mohd Ashri Wan Daud<sup>a,\*</sup>,  
Mohamed Kheireddine Aroua<sup>b,c</sup>

<sup>a</sup> Department of Chemical Engineering, Faculty of Engineering, University of Malaya, 50603 Kuala Lumpur, Malaysia

<sup>b</sup> Centre for Carbon Dioxide Capture and Utilization (CCDCU), School of Science and Technology, Sunway University, Bandar Sunway, 47500 Petaling Jaya, Malaysia

<sup>c</sup> Department of Engineering, Lancaster University, Lancaster LA1 4YW, UK

## GRAPHICAL ABSTRACT



## ARTICLE INFO

## Keywords:

Sample encapsulation  
Hermetically sealed pan  
Volatile sample  
Thermogravimetric analysis  
Catalytic solid-gas reaction

## ABSTRACT

Thermogravimetric analysis (TGA) for solid-gas reactions is well formalized and of ubiquitous use. However, the use of volatile samples in TGA often results in pre-loss of volatile sample by evaporation prior to reaching the specified thermal conditions of analysis. Therefore, sample encapsulation method was proposed as an innovative technique to address this issue. This technique was shown to provide a continuous and delayed release of vaporized samples over the range of elevated temperature through the progressive loosening of the hermetic seal of metal capsule. This effect can be enhanced by using capsule with higher material hardness and smaller surface area for sample evaporation. Application of this method in catalytic phenol reduction has shown an increase in benzene yield from 19.2 mol% to 46.5 mol% when phenol is encapsulated by tin cylinder. Based on these findings, delayed volatiles release phenomenon may lead to further opportunities in the area of thermochemical kinetics study for fuel processing such as gasification, carbonization, reforming or petrochemical reactions that involve catalyst activation at high temperature and use of volatile samples such as fuel model compounds in TGA setup.

## 1. Introduction

Thermogravimetry (TG) or thermogravimetric analysis (TGA) is a

method used to measure mass change of a sample as a function of time or temperature while subjecting the sample in a controlled atmosphere and temperature program. By observing the precise mass change of

\* Corresponding authors.

E-mail addresses: [drewanyak@hotmail.com](mailto:drewanyak@hotmail.com) (A.N. Kay Lup), [faisal.abnisa@um.edu.my](mailto:faisal.abnisa@um.edu.my), [faisal.abnisa@gmail.com](mailto:faisal.abnisa@gmail.com) (F. Abnisa), [ashri@um.edu.my](mailto:ashri@um.edu.my) (W.M.A. Wan Daud), [kheireddinea@sunway.edu.my](mailto:kheireddinea@sunway.edu.my) (M.K. Aroua).

<https://doi.org/10.1016/j.fuel.2018.06.120>

Received 18 January 2018; Received in revised form 27 June 2018; Accepted 29 June 2018  
0016-2361/ © 2018 Elsevier Ltd. All rights reserved.



## A review on reaction mechanisms of metal-catalyzed deoxygenation process in bio-oil model compounds



Andrew Ng Kay Lup, Faisal Abnisa\*, Wan Mohd Ashri Wan Daud, Mohamed Kheireddine Aroua

Department of Chemical Engineering, Faculty of Engineering, University of Malaya, Kuala Lumpur 50603, Malaysia

### ARTICLE INFO

**Keywords:**  
Bio-oil  
Deoxygenation  
Model compound  
Reaction mechanism  
Kinetics

### ABSTRACT

Bio-oil is a potential liquid fuel source which can be produced through the pyrolysis of biomass. Catalytic deoxygenation is an instrumental step for the defunctionalization of bio-oil which will result in liquid fuel which is of lower oxygen content and higher heating value. Numerous studies were done to investigate the deoxygenation mechanisms and the kinetics of various bio-oil model compounds. In this review, heterogeneous metal-catalyzed deoxygenation mechanisms of oxygenated model compounds with functional groups such as phenolics, furans, ethers, carboxylic acids, aldehydes, ketones and alcohols were compared and discussed. The limitations, benefits and feasibilities of such mechanisms were also presented in this article. The discussions on the classes of model compounds and the bonding configurations of oxygenated compounds have also shown that there is a strong correlation between these parameters and the reaction pathways. Hence, this review presented a summary of the model compound based approach researches which would be useful in correlating such knowledge with the actual bio-oil deoxygenation process. Several outlooks on the deoxygenation reactivity of model compounds were also presented in this article based on the studies on the literatures.

### 1. Introduction

Biomass is a renewable energy source which has been extensively researched on and utilized over these several decades. The high demand of energy resources, the search for an environmentally friendlier energy source and the abundance of biomass feedstock were some of the major reasons for the rapid development of biomass-based energy industry. Lignocellulosic biomass is a common biomass feedstock used to produce bio-oil through pyrolysis process. The pyrolysis process involves thermal decomposition of biomass feedstock in the absence of oxygen [1]. During pyrolysis, biomass components such as cellulose, hemicellulose and lignin undergo thermal degradation to form a complex mixture of oxygen-containing compounds. The complex mixture of O-containing compounds within bio-oil could contain more than 400 different compounds such as phenolics, furans, acids, alcohols, carbonyls, esters and ethers [2].

Bio-oil has the prospect of being used as a viable source for liquid fuel. However, a typical bio-oil has high oxygen content which leads to its deficiencies in being used as liquid fuel. Issues such as high corrosivity, low heating value and thermal instability were often attributed to the presence of oxygenated compounds within bio-oil. Therefore, bio-oil upgrading process is an essential step required to convert bio-oil into a deoxygenated liquid fuel which is comparable to

fossil fuels. In addition, bio-oil upgrading process is also important as it functions as a platform for the valorization of precursors into high-added value products which are of great importance to other industries [3]. Bio-oil upgrading process can be achieved through deoxygenation which is a process of removing oxygen atoms from a chemical compound. Unlike crude oil which requires hydrodesulfurization treatment due to its high sulfur content, bio-oil has negligible sulfur content and only requires deoxygenation treatment to reduce its oxygen content. The deoxygenation treatment of bio-oil is challenging as it involves oxygen removal from O-containing compounds with minimal hydrogen consumption and maximised retention of carbon in deoxygenated products [4]. These requirements were necessary to ensure the treatment is economical and the upgraded bio-oil has a high fuel rating.

In the light of this matter, extensive studies were done by numerous researchers on the deoxygenation of various model compounds of bio-oil over assorted kinds of metal catalysts. The studies involved the investigation of the nature of deoxygenation process itself and also the performances of metal catalysts. The study of the nature of deoxygenation process involved the discovery and the understanding of reaction pathways, reaction kinetics or mechanisms, and product compositions [5]. Likewise, the study of metal catalyst performance entailed the analyses of the catalytic effects, electronic interactions by metal and

\* Corresponding author.

E-mail addresses: [drewanyak@hotmail.com](mailto:drewanyak@hotmail.com) (A.N. Kay Lup), [faisal.abnisa@gmail.com](mailto:faisal.abnisa@gmail.com) (F. Abnisa), [ashri@um.edu.my](mailto:ashri@um.edu.my) (W.M.A.W. Daud), [mk\\_roua@um.edu.my](mailto:mk_roua@um.edu.my) (M.K. Aroua).

<http://dx.doi.org/10.1016/j.apcata.2017.05.002>

Received 27 January 2017; Received in revised form 2 May 2017; Accepted 5 May 2017

Available online 08 May 2017

0926-860X/ © 2017 Elsevier B.V. All rights reserved.



## Review

## A review on reactivity and stability of heterogeneous metal catalysts for deoxygenation of bio-oil model compounds



Andrew Ng Kay Lup<sup>a</sup>, Faisal Abnisa<sup>a,b</sup>, Wan Mohd Ashri Wan Daud<sup>a,\*</sup>,  
Mohamed Kheireddine Aroua<sup>c</sup>

<sup>a</sup>Department of Chemical Engineering, Faculty of Engineering, University of Malaya, 50603, Kuala Lumpur, Malaysia

<sup>b</sup>Department of Chemical Engineering, Faculty of Engineering, University of Malikussaleh, Lhokseumawe 24351, Indonesia

<sup>c</sup>School of Science and Technology, Sunway University, No.5 Jalan Universiti, 47500 Selangor Darul Ehsan, Malaysia

## ARTICLE INFO

## Article history:

Received 7 March 2017

Received in revised form 6 June 2017

Accepted 25 June 2017

Available online 4 July 2017

## Keywords:

Bio-oil

Metal catalyst

Deoxygenation

Catalytic deactivation

Catalytic regeneration

## ABSTRACT

Catalytic deoxygenation is a fundamental process for bio-oil upgrading due to its high oxygen content which will result in lower heating value, corrosion and instability issues. The discovery of an excellent heterogeneous deoxygenation metal catalyst with high deoxygenation activity is a necessary breakthrough for an optimized bio-oil catalytic deoxygenation. For an effective deoxygenation supported metal catalyst, properties such as high H<sub>2</sub> sticking coefficient, optimal metal-oxygen bond strength and suitable acid strength from support are needed to ensure facile scission of C–O bonds and activation of H<sub>2</sub> and O-containing compounds. Metals such as Fe, Ru, Sn, W, Zr and supports such as C, TiO<sub>2</sub>, ZrO<sub>2</sub> which are oxophilic were also observed to enhance direct removal of oxygen from O-containing compounds due to their high C–O and C=O bond affinities. The choice of support is important to ensure it has optimal physicochemical properties for facile deoxygenation and the optimal acid strength to enhance C–O hydrogenolysis activity while minimizing coke formation. The choice of metal is dependent on the type of model compound since different metals catalyze different reaction pathways of the deoxygenation of model compounds. This review presents on the use of heterogeneous metal catalysts in the deoxygenation of bio-oil model compounds through several perspectives which are catalytic properties, reaction conditions, deactivation and regeneration of metal catalysts. In addition, several outlooks on the feasible range of reaction condition for catalytic deoxygenation and criteria of excellent deoxygenation supported metal catalysts were also expressed in this article based on the studies on the literatures.

© 2017 The Korean Society of Industrial and Engineering Chemistry. Published by Elsevier B.V. All rights reserved.

## Contents

Introduction	2
Metal catalysts in deoxygenation process	2
Effect of metal element	3
Pt-based catalyst	3
Ni-based catalyst	3
Pd-based catalyst	6
Cu-based catalyst	6
Mo-based catalyst	8
Co-based catalyst	10
Zn-based catalyst	12
Ru-based catalyst	12
Re-based catalyst	13
Ir-based catalyst	14

\* Corresponding author. Fax: +60 379675319.

E-mail addresses: [drewanyak@hotmail.com](mailto:drewanyak@hotmail.com) (A.N. Kay Lup), [faisal.abnisa@gmail.com](mailto:faisal.abnisa@gmail.com) (F. Abnisa), [ashri@um.edu.my](mailto:ashri@um.edu.my) (W.M.A. Wan Daud), [kheireddinea@sunway.edu.my](mailto:kheireddinea@sunway.edu.my) (M.K. Aroua).

<http://dx.doi.org/10.1016/j.jiec.2017.06.049>

1226-086X/© 2017 The Korean Society of Industrial and Engineering Chemistry. Published by Elsevier B.V. All rights reserved.

## Acidity, oxophilicity and hydrogen sticking probability of supported metal catalysts for hydrodeoxygenation process

A Ng K Lup<sup>1</sup>, F Abnisa<sup>1,2,4</sup>, W M A W Daud<sup>1</sup> and M K Aroua<sup>3</sup>

<sup>1</sup> Department of Chemical Engineering, Faculty of Engineering, University of Malaya, 50603 Kuala Lumpur, Malaysia

<sup>2</sup> Department of Chemical Engineering, Faculty of Engineering, University of Malikussaleh, Lhokseumawe 24351, Indonesia

<sup>3</sup> School of Science and Technology, Sunway University, No.5 Jalan Universiti, 47500 Selangor Darul Ehsan, Malaysia

E-mail: faisal.abnisa@gmail.com

**Abstract.** Hydrodeoxygenation is an oxygen removal process that occurs in the presence of hydrogen and catalysts. This study has shown the importance of acidity, oxophilicity and hydrogen sticking probability of supported metal catalysts in having high hydrodeoxygenation activity and selectivity. These properties are required to ensure the catalyst has high affinity for C-O or C=O bonds and the capability for the adsorption and activation of H<sub>2</sub> and O-containing compounds. A theoretical framework of temperature programmed desorption technique was also discussed for the quantitative understanding of these properties. By using NH<sub>3</sub>-TPD, the nature and abundance of acid sites of catalyst can be determined. By using H<sub>2</sub>-TPD, the nature and abundance of metallic sites can also be determined. The desorption activation energy could also be determined based on the Redhead analysis of TPD spectra with different heating rates.

### 1. Introduction

Bio-oil has been extensively researched on for its application as one of the sources for liquid fuel. Bio-oil is produced through the pyrolysis of lignocellulosic biomass. However, bio-oil contains significant amount of oxygen-containing compounds due to depolymerization and defragmentation of cellulose, hemicellulose and lignin within biomass feedstock during pyrolysis[1]. The high oxygen content of bio-oil would cause issues such as low heating value, thermal instability and corrosivity that might affect its performance as liquid fuel [2, 3]. Thus, hydrodeoxygenation is often employed as an upgrading treatment for bio-oil in producing liquid fuel of low oxygen content and for the valorization of oxygen-containing compounds into high-added value products [4].

Hydrodeoxygenation (HDO) is a deoxygenation reaction which involves oxygen abstraction from the compound in the presence of hydrogen. The reaction is commonly catalyzed by zeolites and supported metal catalysts of various forms such as carbide, sulfide, nitride, phosphide and oxide. Numerous studies on HDO process using various oxygen-containing compounds and catalysts were done by researchers. The HDO studies using various oxygenated model compounds are instrumental in the understanding of the reaction mechanisms with respect to the functionalities of model

<sup>4</sup> To whom any correspondence should be addressed.



## APPENDIX

### Appendix A: Evaluation of internal mass transfer effects using Weisz-Prater criterion

When internal effectiveness factor,  $\eta$ , approaches unity and Weisz-Prater criterion,  $C_{W-P}$ , is less than 0.3, the following implications apply (Fogler, 2006):

- Internal pore diffusion rate is much higher than surface reaction rate and surface reaction is the rate limiting step
- Reaction rate at catalyst is equivalent with surface reaction rate and the entire catalyst surface is fully active

#### i.) Reduction of Ag<sub>2</sub>O to Ag in Ag/TiO<sub>2</sub> catalyst

The values of Thiele modulus, internal effectiveness factor and Weisz-Prater criterion were computed based on the first order of reduction for Ag/TiO<sub>2</sub>. For first order Thiele modulus,  $\phi_1$ , it was determined as:

$$\phi_1 = R_{cat} \sqrt{\frac{k_R}{D_e}} \quad (A1)$$

where  $R_{cat}$  is particle radius (56.57 nm for Ag/TiO<sub>2</sub>-10 sample),  $k_R$  is reduction rate constant and  $D_e$  is effective diffusivity.

Effective diffusivity is defined as:

$$D_e = \frac{(D_K)_{H_2} \phi_p \sigma_c}{\tilde{\tau}} \quad (A2)$$

where  $(D_K)_{H_2}$  is Knudsen diffusivity of H<sub>2</sub>,  $\phi_p$  is porosity (0.4),  $\sigma_c$  is constriction factor (0.8) and  $\tilde{\tau}$  is tortuosity (3).



Knudsen diffusivity of H<sub>2</sub> is defined as:

$$(D_K)_{H_2} = \frac{d}{3} \sqrt{\frac{8RT}{\pi M_A}} \quad (A3)$$

where  $d$  is pore diameter (9.53 nm),  $R$  is ideal gas constant,  $T$  is reduction temperature and  $M_A$  is molecular mass of H<sub>2</sub>.

Based on Table 4.5, the 1<sup>st</sup> reduction peak at 389.3 K has reduction rate constant of 0.0220 s<sup>-1</sup>. At 389.3 K, Knudsen diffusivity of H<sub>2</sub> has the value of:

$$\begin{aligned} (D_K)_{H_2} &= \frac{9.53 \text{ nm}}{3} \sqrt{\frac{8(8.314 \frac{\text{J}}{\text{mol}} \cdot \text{K})(389.3 \text{ K})}{\pi(2 \frac{\text{g}}{\text{mol}})}} \quad (A4) \\ &= \frac{9.53 \times 10^{-9} \text{ m}}{3} \sqrt{\frac{8(8.314 \frac{\text{kg} \cdot \text{m}^2/\text{s}^2}{\text{mol}} \cdot \text{K})(389.3 \text{ K})}{\pi(0.002 \frac{\text{kg}}{\text{mol}})}} \\ &= 6.45 \times 10^{-6} \text{ m}^2/\text{s} \end{aligned}$$

Effective diffusivity has the value of:

$$\begin{aligned} D_e &= \frac{(6.45 \times 10^{-6} \text{ m}^2/\text{s})(0.4)(0.8)}{3} \quad (A5) \\ &= 6.88 \times 10^{-7} \text{ m}^2/\text{s} \end{aligned}$$

Thiele modulus has the value of:

$$\begin{aligned} \phi_1 &= (56.57 \times 10^{-9} \text{ m}) \sqrt{\frac{0.022 \text{ s}^{-1}}{6.88 \times 10^{-7} \frac{\text{m}^2}{\text{s}}}} \quad (A6) \\ &= 1.01 \times 10^{-5} \end{aligned}$$

The internal effectiveness factor is determined as:

$$\eta = \frac{3}{\phi_1^2} (\phi_1 \coth \phi_1 - 1) \quad (A7)$$

where  $\eta \rightarrow 1$  when  $\phi_1 = 1.01 \times 10^{-5} \rightarrow 0$

Weisz-prater criterion becomes:

$$\begin{aligned} C_{W-P} &= (1)(1.01 \times 10^{-5})^2 \\ &= 1.02 \times 10^{-10} \ll 0.3 \end{aligned} \quad (A8)$$

Based on Table 4.5, the 2<sup>nd</sup> reduction peak at 490 K has reduction rate constant of 0.0162 s<sup>-1</sup>. At 490 K, Knudsen diffusivity of H<sub>2</sub> has the value of:

$$\begin{aligned} (D_K)_{H_2} &= \frac{9.53 \text{ nm}}{3} \sqrt{\frac{8(8.314 \frac{\text{J}}{\text{mol}} \cdot \text{K})(490 \text{ K})}{\pi(2 \frac{\text{g}}{\text{mol}})}} \\ &= \frac{9.53 \times 10^{-9} \text{ m}}{3} \sqrt{\frac{8(8.314 \frac{\text{kg} \cdot \text{m}^2/\text{s}^2}{\text{mol}} \cdot \text{K})(490 \text{ K})}{\pi(0.002 \frac{\text{kg}}{\text{mol}})}} \\ &= 7.23 \times 10^{-6} \text{ m}^2/\text{s} \end{aligned} \quad (A9)$$

Effective diffusivity has the value of:

$$\begin{aligned} D_e &= \frac{(7.23 \times 10^{-6} \text{ m}^2/\text{s})(0.4)(0.8)}{3} \\ &= 7.71 \times 10^{-7} \text{ m}^2/\text{s} \end{aligned} \quad (A10)$$

Thiele modulus has the value of:

$$\begin{aligned} \phi_1 &= (56.57 \times 10^{-9} \text{ m}) \sqrt{\frac{0.0162 \text{ s}^{-1}}{7.71 \times 10^{-7} \frac{\text{m}^2}{\text{s}}}} \\ &= 8.2 \times 10^{-6} \end{aligned} \quad (A11)$$

The internal effectiveness factor is determined as:

$$\eta = \frac{3}{\phi_1^2} (\phi_1 \coth \phi_1 - 1) \quad (A7)$$

where  $\eta \rightarrow 1$  when  $\phi_1 = 8.2 \times 10^{-6} \rightarrow 0$

Weisz-prater criterion becomes:

$$\begin{aligned} C_{W-P} &= (1)(8.2 \times 10^{-6})^2 \\ &= 6.72 \times 10^{-11} \ll 0.3 \end{aligned} \quad (A12)$$

Based on these data, the values for  $\phi_1$ ,  $\eta$  and  $C_{W-P}$  are  $1.01 \times 10^{-5}$ , 1.00 and  $1.02 \times 10^{-10}$  for the first reduction peak and  $8.2 \times 10^{-6}$ , 1.00 and  $6.72 \times 10^{-11}$  for the second reduction peak at their respective reduction peak temperatures of 389.3 K and 490 K. Thus, the aforementioned implications on internal mass transfer is valid for reduction of Ag<sub>2</sub>O to Ag in Ag/TiO<sub>2</sub> catalyst.

ii.) Phenol HDO reaction over Ag/TiO<sub>2</sub> catalyst

The  $C_{W-P}$  value was determined based on the following equations:

$$C_{W-P} = \frac{(-r_{HDO})_{exp} R_{cat}^2}{C_s D_e} \quad (A13)$$

$$D_e = \frac{(D_K)_{phenol} \phi_p \sigma_c}{\bar{\tau}} \quad (A14)$$

$$(D_K)_{phenol} = \frac{d}{3} \sqrt{\frac{8RT}{\pi M_A}} \quad (A15)$$

where  $(-r_{HDO})_{exp}$  is overall experimental HDO reaction rate,  $C_s$  is surface concentration of reactant,  $(D_K)_{phenol}$  is Knudsen diffusivity of phenol,  $M_A$  is molecular mass of phenol (94 g/mol).

At 454 K, Knudsen diffusivity of phenol has the value of:

$$(D_K)_{phenol} = \frac{9.53 \text{ nm}}{3} \sqrt{\frac{8(8.314 \frac{\text{J}}{\text{mol} \cdot \text{K}})(454 \text{ K})}{\pi(94 \frac{\text{g}}{\text{mol}})}} \quad (A16)$$

$$\begin{aligned}
&= \frac{9.53 \times 10^{-9} \text{ m}}{3} \sqrt{\frac{8(8.314 \frac{\text{kg} \cdot \text{m}^2/\text{s}^2}{\text{mol}} \cdot \text{K})(454 \text{ K})}{\pi(0.094 \frac{\text{kg}}{\text{mol}})}} \\
&= 3.05 \times 10^{-6} \text{ m}^2/\text{s}
\end{aligned}$$

Effective diffusivity has the value of:

$$\begin{aligned}
D_e &= \frac{(3.05 \times 10^{-6} \text{ m}^2/\text{s})(0.4)(0.8)}{3} & (A17) \\
&= 3.25 \times 10^{-7} \text{ m}^2/\text{s}
\end{aligned}$$

$(-r_{HDO})_{exp}$  is dependent on the slowest reaction step which is phenol hydrogenolysis (Table 6.5). Thus,

$$\begin{aligned}
C_{W-P} &= \frac{(2.03 \times 10^{-10} \text{ mol/dm}^3 \cdot \text{s})(56.57 \times 10^{-9} \text{ m})^2}{(0.0020742 \text{ mol/dm}^3)(3.25 \times 10^{-7} \text{ m}^2/\text{s})} & (A18) \\
&= 9.64 \times 10^{-16} \ll 0.3
\end{aligned}$$

The aforementioned implications on internal mass transfer are valid for phenol HDO over Ag/TiO<sub>2</sub> catalyst.

## Appendix B: Derivation of phenol HDO kinetic model

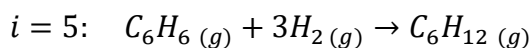
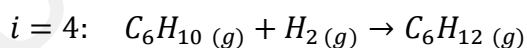
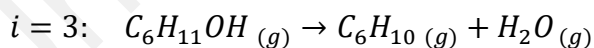
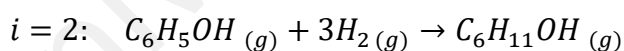
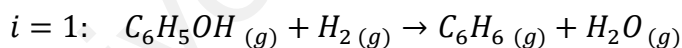
The following HDO kinetics is derived based on the postulated reaction pathways of phenol HDO (Figure 6.3). Langmuir-Hinshelwood model was proposed as the formalism to describe the reaction system kinetics for the overall reaction scheme. This model is subjected to several assumptions:

1. Sorption reactions are in quasi-equilibrium
2. Catalyst sites are identical, independent and evenly distributed.
3. Number of catalyst sites is constant under all reaction conditions.
4. Surface reactions are irreversible and rate determining steps.

The following are the labels of the reaction species and the reactions steps (Figure 6.3):

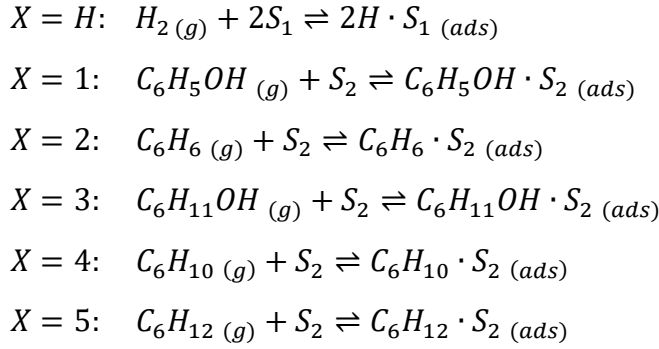
Index $X$	$X$ -th reaction species	Index $i$	$i$ -th reaction step
1	Phenol, $C_6H_5OH$	1	Phenol hydrogenolysis
2	Benzene, $C_6H_6$	2	Phenol hydrogenation
3	Cyclohexanol, $C_6H_{11}OH$	3	Cyclohexanol dehydration
4	Cyclohexene, $C_6H_{10}$	4	Cyclohexene hydrogenation
5	Cyclohexane, $C_6H_{12}$	5	Cyclohexane hydrogenation

The overall  $i$ -th reaction steps are as follow:

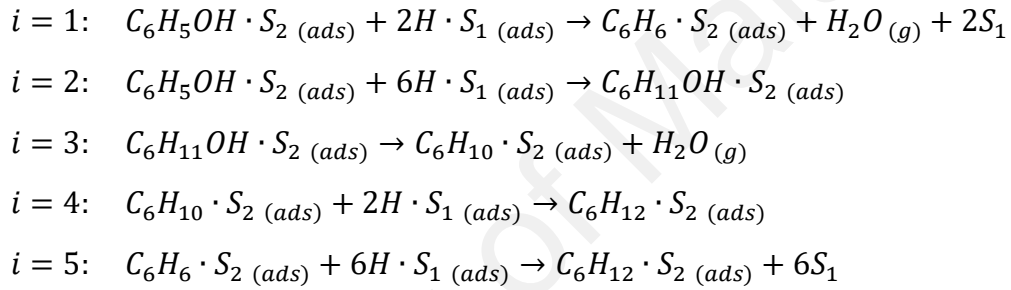


The Langmuir-Hinshelwood mechanism of each  $i$ -th reaction step consists of sorption of reaction species and surface reactions. Sorption of reaction species occurs over two distinct catalytic sites: metal sites ( $S_1$ ) for H atom and support site ( $S_2$ ) for phenol,

benzene, cyclohexanol, cyclohexene and cyclohexane. Dissociative adsorption for hydrogen was postulated. The sorption equilibria for  $X$ -th reaction species are as follow:



Surface reactions of  $i$ -th reaction steps are as follow:



The rate equations were expressed in terms of partial pressures of reaction species via ideal gas law to correlate with the concentrations of gaseous reaction species. The rate equations for sorption equilibria are as follow:

$$\begin{aligned}
 X = H: & \quad r_{ads,H} = k_H p_{H_2} C_{S_1}^2 - k_{-H} C_{H \cdot S_1}^2 = k_H (p_{H_2} C_{S_1}^2 - \frac{C_{H \cdot S_1}^2}{K_H}) \\
 X = 1: & \quad r_{ads,1} = k_1 p_1 C_{S_2} - k_{-1} C_{1 \cdot S_2} = k_1 (p_1 C_{S_2} - \frac{C_{1 \cdot S_2}}{K_1}) \\
 X = 2: & \quad r_{ads,2} = k_2 p_2 C_{S_2} - k_{-2} C_{2 \cdot S_2} = k_2 (p_2 C_{S_2} - \frac{C_{2 \cdot S_2}}{K_2}) \\
 X = 3: & \quad r_{ads,3} = k_3 p_3 C_{S_2} - k_{-3} C_{3 \cdot S_2} = k_3 (p_3 C_{S_2} - \frac{C_{3 \cdot S_2}}{K_3}) \\
 X = 4: & \quad r_{ads,4} = k_4 p_4 C_{S_2} - k_{-4} C_{4 \cdot S_2} = k_4 (p_4 C_{S_2} - \frac{C_{4 \cdot S_2}}{K_4}) \\
 X = 5: & \quad r_{ads,5} = k_5 p_5 C_{S_2} - k_{-5} C_{5 \cdot S_2} = k_5 (p_5 C_{S_2} - \frac{C_{5 \cdot S_2}}{K_5})
 \end{aligned}$$

where  $K_X = k_X/k_{-X}$ . Since  $r_{des,X} = -r_{ads,X}$ ,  $r_{des,X} = k_{-X}(C_{X \cdot S_2} - K_X p_X C_{S_2})$  for  $X = 1$  to 5 and  $r_{des,H} = k_{-H}(C_{H \cdot S_1}^2 - K_H p_H C_{S_1}^2)$  for  $X = H$ .

Surface rate equations are expressed as:

$$i = 1: \quad r_{s1} = k_{s1} C_{1 \cdot S_2} C_{H \cdot S_1}^2$$

$$i = 2: \quad r_{s2} = k_{s2} C_{1 \cdot S_2} C_{H \cdot S_1}^6$$

$$i = 3: \quad r_{s3} = k_{s3} C_{3 \cdot S_2}$$

$$i = 4: \quad r_{s4} = k_{s4} C_{4 \cdot S_2} C_{H \cdot S_1}^2$$

$$i = 5: \quad r_{s5} = k_{s5} C_{2 \cdot S_2} C_{H \cdot S_1}^6$$

Since surface reactions are the rate-limiting steps,  $k_X \gg k_{si}$  and  $k_{-X} \gg k_{si}$  are both valid and thus:

$$\frac{r_{ads,X}}{k_X} \approx 0, \quad \frac{r_{des,X}}{k_{-X}} \approx 0$$

Therefore, the sorption rate equations can be expressed in the following form:

$$X = 1: \quad C_{H \cdot S_1} = \sqrt{K_H p_{H_2} C_{S_1}}$$

$$X = 1: \quad C_{1 \cdot S_2} = K_1 p_1 C_{S_2}$$

$$X = 2: \quad C_{2 \cdot S_2} = K_2 p_2 C_{S_2}$$

$$X = 3: \quad C_{3 \cdot S_2} = K_3 p_3 C_{S_2}$$

$$X = 4: \quad C_{4 \cdot S_2} = K_4 p_4 C_{S_2}$$

$$X = 5: \quad C_{5 \cdot S_2} = K_5 p_5 C_{S_2}$$

By working on metal and support site balances:

$$C_{T_1} = C_{S_1} + C_{H \cdot S_1} = C_{S_1} + \sqrt{K_H p_{H_2} C_{S_1}}$$

$$\Rightarrow C_{S_1} = C_{T_1} / (1 + \sqrt{K_H p_{H_2}})$$

$$C_{T_2} = C_{S_2} + \sum_{X=1}^5 C_{X \cdot S_1} = C_{S_2} + \sum_{X=1}^5 K_X p_X C_{S_2}$$

$$\Rightarrow C_{S_2} = C_{T_2} / (1 + \sum_{X=1}^5 K_X p_X)$$

Thus, surface rate equations are now expressed as:

$$\begin{aligned} i = 1: \quad r_{s1} &= k_{s1} K_1 p_1 C_{S_2} \left( \sqrt{K_H p_{H_2} C_{S_1}} \right)^2 \\ &= \frac{k_{s1} C_{T_2} C_{T_1}^2 K_H p_{H_2} K_1 p_1}{(1 + \sqrt{K_H p_{H_2}})^2 (1 + \sum_{X=1}^5 K_X p_X)} \end{aligned}$$

$$\begin{aligned} i = 2: \quad r_{s2} &= k_{s2} K_1 p_1 C_{S_2} \left( \sqrt{K_H p_{H_2} C_{S_1}} \right)^6 \\ &= \frac{k_{s2} C_{T_2} C_{T_1}^6 (K_H p_{H_2})^3 K_1 p_1}{(1 + \sqrt{K_H p_{H_2}})^6 (1 + \sum_{X=1}^5 K_X p_X)} \end{aligned}$$

$$\begin{aligned} i = 3: \quad r_{s3} &= k_{s3} K_3 p_3 C_{S_2} \\ &= \frac{k_{s3} C_{T_2} K_3 p_3}{(1 + \sum_{X=1}^5 K_X p_X)} \end{aligned}$$

$$\begin{aligned} i = 4: \quad r_{s4} &= k_{s4} K_4 p_4 C_{S_2} \left( \sqrt{K_H p_{H_2} C_{S_1}} \right)^2 \\ &= \frac{k_{s4} C_{T_2} C_{T_1}^2 K_H p_{H_2} K_4 p_4}{(1 + \sqrt{K_H p_{H_2}})^2 (1 + \sum_{X=1}^5 K_X p_X)} \end{aligned}$$

$$\begin{aligned} i = 5: \quad r_{s5} &= k_{s5} K_2 p_2 C_{S_2} \left( \sqrt{K_H p_{H_2} C_{S_1}} \right)^6 \\ &= \frac{k_{s5} C_{T_2} C_{T_1}^6 (K_H p_{H_2})^3 K_2 p_2}{(1 + \sqrt{K_H p_{H_2}})^6 (1 + \sum_{X=1}^5 K_X p_X)} \end{aligned}$$

which have the general formula of:

$$r_{si} = \frac{k_i (K_H p_{H_2})^{n/2} K_X p_X}{(1 + \sqrt{K_H p_{H_2}})^n (1 + \sum_{X=1}^5 K_X p_X)}$$

$$k_i = k_{si} C_{T_2} C_{T_1}^n$$

where  $n$  is the number of moles of hydrogen atoms used in the  $i$ -th reaction step.



The overall reaction rates,  $r_i$ , are equivalent to the rate-limiting steps which are the surface rate reactions,  $r_{si}$ . Thus, the reaction rate equations in this model can be expressed as:

$$r_i = \frac{k_i(K_H p_{H_2})^{n/2} K_X p_X}{(1 + \sqrt{K_H p_{H_2}})^n (1 + \sum_{i=1}^5 K_X p_X)}$$

where  $r_i$  is rate of  $i$ -th reaction based on Figure 6.3,  $k_i$  is its respective rate constant,  $p$  is partial pressure,  $K$  is adsorption coefficient,  $n$  is the number of moles of hydrogen atom used in  $i$ -th reaction step and index  $X$  indicates the reactant of  $i$ -th reaction step. The  $n$  values for reaction step 1, 2, 3, 4 and 5 are 2, 6, 0, 2, and 6 respectively.